https://doi.org/10.15388/vu.thesis.752
https://orcid.org/0009-0009-9464-9524

VILNIUS UNIVERSITY
CENTER FOR PHYSICAL SCIENCES AND TECHNOLOGY

Agnė Kizalaitė

Dissolution-Precipitation Synthesis of Magnesium and Transition Metal Whitlockite

DOCTORAL DISSERTATION

Natural Sciences,
Chemistry (N 003)

VILNIUS 2025

The dissertation was prepared between 2020 and 2024 at Vilnius University. The research was supported by Research Council of Lithuania.

Academic Supervisor – Prof. Dr. Aleksej Žarkov (Vilnius University, Natural Sciences, Chemistry, N 003).
Academic Consultant – Assoc. Prof. Dr. Vytautas Klimavičius (Vilnius University, Natural Sciences, Physics, N 002).

This doctoral dissertation will be defended in a public meeting of the Dissertation Defense Panel:

Chairman – Prof. Dr. Rasa Pauliukaitė (Center for Physical Sciences and Technology, Natural Sciences, Chemistry, N 003).
Members:
Prof. Dr. Artūras Katelnikovas (Vilnius University, Natural Sciences, Chemistry, N 003),
Dr. Germanas Peleckis (University of Wollongong, Natural Sciences, Chemistry, N 003),
Dr. Milda Petrulevičienė (Center for Physical Sciences and Technology, Natural Sciences, Chemistry, N 003),
Prof. Dr. Almira Ramanavičienė (Vilnius University, Natural Sciences, Chemistry, N 003).

The dissertation shall be defended at a public meeting of the Dissertation Defense Panel at 14:00 on 8th of May 2025 in Inorganic chemistry auditorium (141 aud.) of the Faculty of Chemistry and Geosciences, Vilnius University.
Address: Naugarduko st. 24, LT – 03225, Vilnius, Lithuania
Tel. +37052193105; e-mail: info@chgf.vu.lt

The text of this dissertation can be accessed at the library of Vilnius University, as well as on the website of Vilnius University:
www.vu.lt/lt/naujienos/ivykiu-kalendorius

https://doi.org/10.15388/vu.thesis.752
https://orcid.org/0009-0009-9464-9524

VILNIAUS UNIVERSITETAS
FIZINIŲ IR TECHNOLOGIJOS MOKSLŲ CENTRAS

Agnė Kizalaitė

Magnio ir pereinamųjų metalų vitlokito sintezė tirpinimo-nusodinimo metodu

DAKTARO DISERTACIJA

Gamtos mokslai,
Chemija (N 003)

VILNIUS 2025

Disertacija rengta 2020–2024 metais Vilniaus universitete.
Mokslinius tyrimus rėmė Lietuvos mokslo taryba.

Mokslinis vadovas – Prof. dr. Aleksej Žarkov (Vilniaus universitetas, gamtos mokslai, chemija, N 003).
Mokslinis konsultantas – Doc. dr. Vytautas Klimavičius (Vilniaus universitetas, gamtos mokslai, fizika, N 002).

Gynimo taryba:
Pirmininkė – Prof. dr. Rasa Pauliukaitė (Fizinių ir technologijos mokslų centras, gamtos mokslai, chemija, N 003).
Nariai:
Prof. dr. Artūras Katelnikovas (Vilniaus universitetas, gamtos mokslai, chemija, N 003),
Dr. Germanas Peleckis (Wollongong universitetas, gamtos mokslai, chemija, N 003),
Dr. Milda Petrulevičienė (Fizinių ir technologijos mokslų centras, gamtos mokslai, chemija, N 003),
Prof. dr. Almira Ramanavičienė (Vilniaus universitetas, gamtos mokslai, chemija, N 003).

Disertacija ginama viešame Gynimo tarybos posėdyje 2025 m. gegužės mėn. 8 d. 14 val. Vilniaus Universiteto Chemijos ir geomokslų fakulteto Neorganinės chemijos auditorijoje (141 aud.).
Adresas: Naugarduko g. 24, LT – 03225, Vilnius, Lietuva.
Tel. +37052193105; el. paštas info@chgf.vu.lt

Disertaciją galima peržiūrėti Vilniaus universiteto bibliotekoje ir VU interneto svetainėje adresu:
https://www.vu.lt/naujienos/ivykiu-kalendorius

ACKNOWLEDGEMENTS

First of all, I would like to express my deep gratitude to my supervisor, Prof. Dr. Aleksej Žarkov, for all his help and support throughout the years. Your insights, dedication, and knowledge were invaluable in the creation of this dissertation.

Also, I would like to thank my consultant Assoc. Prof. Dr. Vytautas Klimavičius, as well as all other people who were involved in my research. Thank you for your collaboration, insights, remarks, and contributions which allowed me to improve the quality of my research. A special thank you goes to Assoc. Prof. Dr. Inga Grigoravičiūtė – the founder of this area of research in our faculty and a great advisor.

I am endlessly grateful to my colleagues who helped and supported me in this long journey. A special thanks goes to present and past colleagues and friends from the Department of Analytical and Environmental Chemistry as well as the Center of Didactics. You created such a warm and welcoming atmosphere that is always a pleasure to come back to. Thank you for making my days brighter, even when the times were hard.

Finally, I would like to thank all my friends and family for staying with me throughout this journey and encouraging me to seek a scientific path while reminding me to enjoy life and helping me find balance. For my mum and husband – this dissertation is as much yours as it is mine. This quest has been challenging, but your belief in me is what made it possible. Thank you all for being in my life for so many years, and I hope you'll stay for so many more.

 And a special thank you to my cat Mamba – sometimes a simple *meow* comes a long way.

The real treasure is the friends we made along the way!

LIST OF ABBREVIATIONS

3D – three-dimensional;
ACP – amorphous calcium phosphate;
ATP – adenosine triphosphate;
BET – Brunauer–Emmett–Teller analysis;
CCK-8 – cell counting kit-8;
CDHA – calcium deficient hydroxyapatite;
CP – calcium phosphate;
CPP – calcium pyrophosphate ($Ca_2P_2O_7$);
CP MAS – cross polarization magic angle spinning;
DC – direct current;
DCPA – dicalcium phosphate anhydrous ($CaHPO_4$);
DCPD – dicalcium phosphate dihydrate ($CaHPO_4 \cdot 2H_2O$);
EDX – energy dispersive X-ray spectroscopy;
FBS – fetal bovine serum;
FC – field-cooled;
FTIR – Fourier transform infrared spectroscopy;
HAP – hydroxyapatite ($Ca_{10}(PO_4)_6(OH)_2$);
ICP-OES – inductively coupled plasma optical emission spectrometry;
MAS – magic angle spinning;
MCP – monocalcium phosphate ($Ca(H_2PO_4)_2$);
MR – merrillite ($Ca_{18}Mg_2Na_2(PO_4)_{14}$);
MRI – magnetic resonance imaging;
NIR – near-infrared spectroscopy;
NMR – nuclear magnetic resonance;
OCP – octacalcium phosphate ($Ca_8(HPO_4)_2(PO_4)_4 \cdot 5H_2O$);
PTFE – polytetrafluoroethylene;
ROS – reactive oxygen species;
SBF – simulated body fluid;
SEM – scanning electron microscopy;
TCP – tricalcium phosphate ($Ca_3(PO_4)_2$);
TEM – transmission electron microscopy;
TTCP – tetracalcium phosphate ($Ca_4(PO_4)_2O$);
WH – whitlockite ($Ca_{18}M_2H_2(PO_4)_{14}$);
XPS – X-ray photoelectron spectroscopy;
XRD – X-ray diffraction;
ZFC – zero-field cooled.

TABLE OF CONTENTS

INTRODUCTION

Bone tissue can be damaged by trauma, inflammation, cancer, and a wide range of degenerative diseases, such as osteoporosis. Every year these conditions affect more and more people, especially elderly people, who tend to have higher rates of bone-related diseases and are more susceptible to injuries due to a decrease in bone density and overall bone mass loss. Even though, under normal circumstances, bone tissue is capable of repairing itself, this ability can be impaired depending on the extent of damage and its type. Furthermore, bone tissue can heal improperly or take a long time to heal fully. Therefore, scientific research developing new materials for bone replacement and repair is essential in biomedicine of today.

Inorganic matrix of bone is mostly composed of calcium phosphates (CPs). Therefore, in terms of bone regeneration, CPs are the most promising and widely used materials due to their chemical and structural similarities to natural bone tissue [1]. One of the members of the CPs family is magnesium whitlockite (Mg-WH: $Ca_{18}Mg_2H_2(PO_4)_{14}$). This material can be considered as a Mg-substituted CP, which naturally occurs in the human body. Mg-WH is known to be the second most abundant biomineral in human hard tissues, constituting around 20–35 wt.% of the total inorganic components of bone [2]. Unfortunately, a lot is still unknown about the role and formation of this material in the human body. However, Mg-WH is known for its bioactivity and biocompatibility. Also, this mineral has osteogenic properties uncharacteristic of most CPs [3]. The comparative study on *in vitro* and *in vivo* biocompatibility of Mg-WH, hydroxyapatite (HAP: $Ca_{10}(PO_4)_6(OH)_2$) and β-tricalcium phosphate (β-TCP) revealed that Mg-WH-containing scaffolds facilitated bone-specific differentiation in comparison with HAP-reinforced composite scaffolds [3].

Although CPs are highly biocompatible and have already demonstrated high efficiency, one of the directions of research aimed at achieving the superior performance of CP-based materials considers the partial replacement of Ca by other ions [4]. The ion substitution strategy allows combining the characteristics of CPs with newly obtained substitution-induced properties: antibacterial, optical, magnetic, etc. This approach leads to the development of biocompatible multifunctional materials with a wider application range [5].

Despite the fact that the first-row transition metal ions are of comparable size with Mg^{2+} ions [6], we found only 2 papers on the synthesis of transition metal WH, namely Fe-WH [7] and accidentally synthesized Mn-WH [8]. Zn is known to be an essential and biologically active ion, which is involved in many biological processes in the human body, and its' deficiency leads to a number of skeletal anomalies [9]. Zn-containing CPs are known for their superior biological performance and antibacterial properties [10, 11]. Cu-doped CPs demonstrate antibacterial properties, provide angiogenic ability, and favor osteogenesis [12]. Various Mn-substituted CPs, such as HAP [13], amorphous calcium phosphate (ACP) [14] and others can be used for magnetic resonance imaging (MRI) due to their magnetic properties. Additionally, same as Cu and Zn, Mn-containing biomaterials were shown to have antibacterial properties [15] and demonstrated a positive effect on osteogenesis [16].

Compared to other CPs, WH is quite a poorly investigated material both in terms of biological performance, crystal structure, and thermal stability. It was assumed for a long time that the synthesis of phase-pure Mg-WH is a challenging task due to the formation of other CP. However, this issue was overcome in recent years, and different successful synthesis approaches were demonstrated [17-19].

Depending on specific purpose, different forms of CPs can be used in regenerative medicine. Mg-WH has already been prepared in the form of powders [18], granules [20], coating on TCP ceramics [21], and different composites [22-24]. However, there is no data on the fabrication of ceramics. Conventional ceramic routes consider sintering at high temperatures, which is needed for the densification of material. Of course, such an approach is limited by thermal stability of materials. Therefore, the basic knowledge of the thermal degradation of the material is crucial as preparation work for the fabrication of ceramics. Mg-WH is assumed to be thermally unstable; however, the mechanism of thermal decomposition and phase evolution was not comprehensively investigated so far.

The aim of this study was to synthesize and comprehensively characterize magnesium and transition metal (Zn, Cu, Mn) WH as potential materials for bone regeneration.

The objectives of this study:

- To develop a reliable dissolution-precipitation process for the synthesis of Mg-, Zn-, and Cu-WH powders under hydrothermal conditions.
- To employ an aqueous dissolution-precipitation process for the synthesis of Zn-, and Mn-WH powders under ambient pressure.
- To comprehensively characterize synthesized products in terms of structural, physical, morphological, and biological properties as well as thermal stability.

1. LITERATURE OVERVIEW

1.1. Bone tissue

1.1.1. Structure

Bone is a rigid connective tissue consisting of relatively few cells embedded in a large amount of hard intercellular matrix. This tissue is important for a wide range of functions such as hematopoiesis, locomotion, support and protection of soft tissues, muscle attachment, storage of phosphate, calcium, and other micro- and macroelements necessary for a variety of metabolic functions [25, 26].

The bone is composed of a dense outer layer, called compact bone, surrounded by a lower-density porous tissue (Fig. 1) [27]. Porosity is a vital bone property that enables cells and bodily fluids to travel to various regions of the tissue [26]. Surrounded by porous tissue lays gel-like tissue known as bone marrow. On a microscopic level, bone is composed of an extracellular matrix comprised of a collagen fiber network and inorganic minerals, as well as bone tissue cells [2].

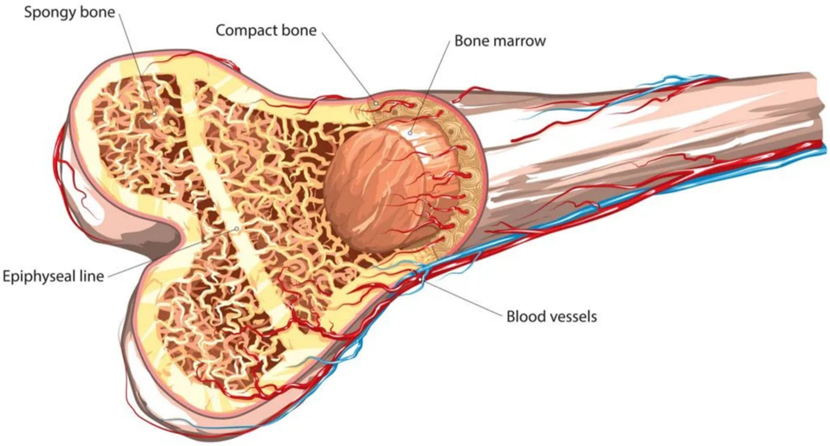

Fig. 1. Anatomy of long bone [28].

A relatively small percentage of bone tissue is composed of cells however they are vital for the function and repair of this tissue. Human bone tissue consists of four major types of cells – osteoblasts, osteocytes, osteogenic cells, and osteoclasts (Fig. 2) [12]. These cells are involved in all stages of bone formation and remodeling process. Osteogenesis is a circular process comprised of 3 main phases [29, 30]. First, old, injured or otherwise unneeded bone is dissolved by cells responsible for the resorption of bone tissue – osteoclasts. Then, a transitional phase occurs where bone resorption is replaced by the formation of new bone. The third phase is a new bone formation by osteoblasts – a cell type responsible for the growth of the new bone. The ongoing balance between osteoblastic and osteoclastic action is a major factor in bone tissue homeostasis.

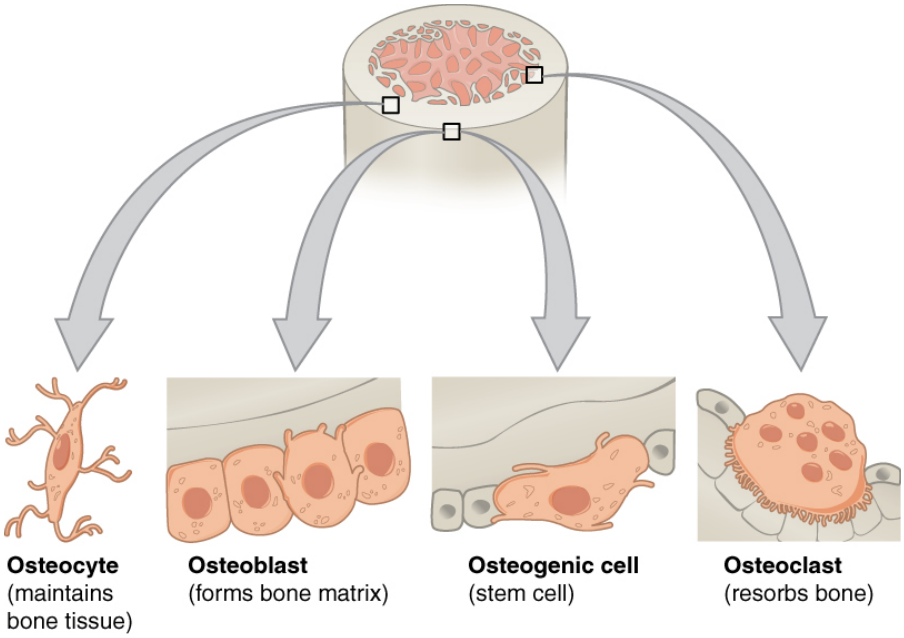

Fig. 2. Major types of cells found within bone tissue [31].

A major part of human bone is its extracellular matrix. One of its major components are collagen fibers. Collagen provides a scaffolding surface to which CP crystals can adhere. It also gives the bone a certain level of flexibility and makes it less fragile. Collagen fibers are 80–100 nm thick and have lengths of a few to tens of microns [26]. The dominant type of collagen is type I [32]. Cylindrically shaped collagen fibrils are formed by self-assembling collagen triple helices [33].

Roughly about 70% of human bone consists of inorganic matter, which is mostly composed of CPs [1]. This part of the extracellular matrix gives bone compressive strength and sturdiness. The CP crystals in natural bone are always plate-like and thin, so they can insert themselves parallelly into the collagen fibrils. The orientation of CPs crystals parallel to the long axes of an organic framework is a general feature of the overall CP biomineralization process in all vertebrates [26].

The dominant CP in bone tissue is HAP or more precisely – calcium deficient hydroxyapatite (CDHA). HAP can be formed even if large number of defects are present and is prone to both cationic and anionic substitution. CDHA is a variant of HAP, where part of Ca^{2+} crystallographic sites are vacancies. In biological systems this compound exists only in its partially substituted form [34]. Ca^{2+} ions are most likely to be substituted by Na^{+}, K^{+}, Mg^{2+}, Sr^{2+}, phosphate ions – by CO_3^{2-}, and OH^{-} ions – by F^{-}, Cl^{-}, CO_3^{2-} [26]. Partially substituted CDHA is also known as biological apatite. However, CDHA and HAP never precipitates directly *in vivo* – first, the intermediate phase of CP has to form that undergoes phase transformation and mineralization into biological apatite [35, 36].

1.1.2. Pathology and regeneration

There are numerous conditions that affect and damage bone tissue, such as traumas, cancer, infections, degenerative and inflammatory diseases. Even though bone self-repair process is possible, there are often lasting effects and a prolonged healing process. A wide range of diseases result from irregularities in either skeletal or dental system. Osteoporosis also negatively affects bone tissue, which, through the process of bone demineralization, becomes less dense and more fragile, which further complicates the healing process in case of trauma [26]. Bone defects caused by tumor extraction, inflammation or complicated fractures are prone to heal incorrectly, thus, the healing process must be assisted to avoid further complications and loss of mobility [37].

Depending on the type and severity of damage done to the bone there are two types of healing processes. If the damage is relatively small and bone fragments are close to each other – direct bone healing occurs [38]. In this case, osteoblasts and osteoclasts build new bone directly onto the damaged site and connect broken structures [39]. If damage is severe or bone fragments are further away from each other – indirect bone healing takes place. During this process, cartilaginous patches of tissue are formed first before they can be connected, and new bone tissue can be reformed. Mechanical stability of the fracture site increases as the cartilage mineralizes until the new bone is able to support the appropriate mechanical load [38]. The stages of bone fracture repair are presented in Fig. 3. However, this process is slow, so the establishment of normal bone integrity can take several months to complete. Successful fracture healing is dependent on a variety of factors and can be impaired by underlying pathological conditions and factors like aging, obesity, and smoking.

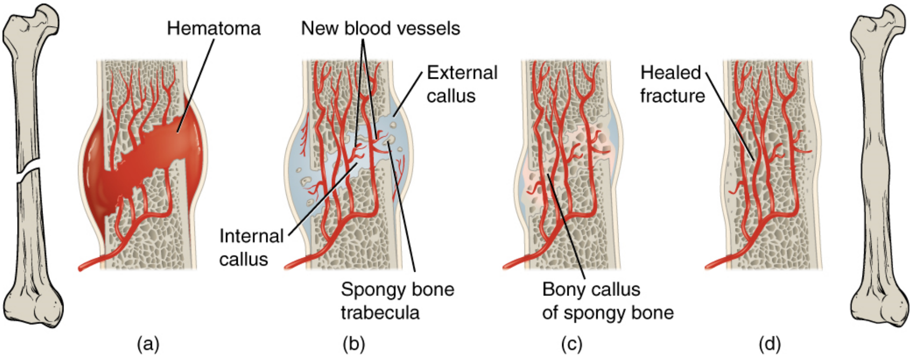

Fig. 3. Stages of bone fracture repair. The healing of a bone fracture follows a series of progressive steps: A fracture hematoma forms (a). Internal and external calli form (b). The cartilage of the calli is replaced by trabecular bone (c). Remodeling occurs (d) [31].

Bone regeneration is closely related to a variety of complex physiological processes. Therefore, there are numerous strategies to enhance natural bone tissue healing. These strategies involve stem cell and hormonal therapies, tissue transplantation, the use of materials for bone tissue regeneration, etc. Controlled delivery of bioactive molecules such as growth factors, nucleic acids, proteins, hormones, and vitamins to the damaged site can have beneficial therapeutical effects and promote healing [32, 38, 40]. Independent of their origin, bone substitute materials have to fit certain requirements. Ideal substitutes must be biocompatible and not cause any adverse immune effects [41]. They also should be biodegradable with a biodegradation rate comparable to the formation of bone tissue or integrate seamlessly into natural bone tissue [42, 43]. These materials should also be porous with a pore size suitable to permit ingrowth of bone cells or have surface properties that promote cell adhesion [26]. Mechanical stability is also an important factor since one of the major functions of bone tissue is load bearing.

To this day, autogenous bone is still most commonly used bone graft material, which is often described as the gold standard for bone tissue regeneration. Autogenous bone grafting is defined as the transplantation of bone tissue obtained from a donor site into a bone defect, non-union, or arthrodesis [44]. Since donor bone belongs to the patient themselves, there are no biocompatibility and immune intolerance – paramount issues, when any other material is used. Due to being natural bone tissue, it has perfect biocompatibility, enabling osteoinduction and osteoconduction with no toxicity [12]. However, donor tissue in the harvesting site is usually not available in sufficient quantities [26]. Also, the need for additional sampling sites for tissue extraction is a known disadvantage that adds complications associated with the surgical procedure itself [45, 46]. Allografts (human-derived) as well as xenografts (animal-derived) are viable solutions but they present risks of immune intolerance in the recipient patient, and the osteogenic properties might not always be retained, depending on the conservation methods that were used for the tissue [12, 47]. Due to these drawbacks, the use of synthetic bone substitutes is necessary.

Bone tissue engineering is a biomaterial-driven approach to bone regeneration that creates and utilizes materials which can integrate into the bone tissue and promote healing as well as provide a framework for the growth of new bone. These materials are usually solid support structures that possess certain biological, chemical, and physical properties required for their specific field of use. Synthetic bone graft substitutes may consist of metals, polymers, ceramics, and composites (Fig. 4) [47]. The broad range of materials used for this purpose can be explained by the fact that none of the currently used materials unite all essential criteria for ideal bone substituent material: mechanical strength, biocompatibility, biodegradability, osteogenesis, osteoinduction, osteoconduction as well as physical and chemical surface properties necessary for cell integration and new tissue formation [32]. This tissue regeneration approach requires a complex matrix that is yet to be discovered and implemented.

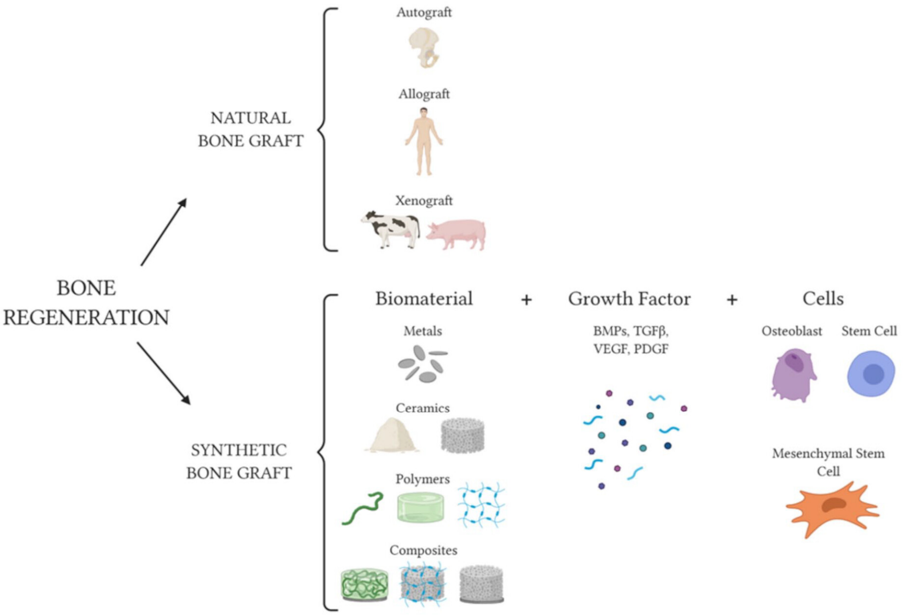

Fig. 4. Scheme of available biomaterials for bone tissue regeneration [48].

Inorganic biomaterials are an attractive option for regenerative medicine due to their tunable properties. Mineral-based particles can be easily ingested by cells and their ionic dissolution products can act as bioactive cues to direct cell behavior and overall osteogenesis process [49]. Synthetic CPs are especially attractive in this area because of their chemical and structural similarities to natural bone [1]. These materials are already widely used in the fields of bone regeneration and dentistry. Currently, the most commonly used CPs containing only Ca^{2+} cations are HAP, β-TCP, and ACP [3, 50-52]. Because of their similarities to natural bone, it is easier for a living bone tissue to attach itself to the material and therefore a more permanent fixation of the implant in the bone takes place [53]. Also, cationic and anionic substitution in CPs by biologically active ions is an effective way to further improve their biological properties [42]. Inorganic biomaterials have been shown to regulate cellular response, they can also play a vital role in defining cell identity, as well as driving tissue-specific functions [41, 49]. Growth factors, nucleic acids, other organic molecules and even cells can also be embedded into the CPs to further improve their biological properties [38].

Depending on the specific purpose in regenerative medicine, CPs can be used in different forms – powders, granules, coatings, cements, ceramics, and others. CPs are often used as coatings on metal implants. Since metal cannot form a stable bond between the implant and bone tissue, CP coatings can greatly improve their biointegration. The coating increases the surface roughness of the implant and creates a suitable environment for cells to adhere [26]. Cements are paste-like materials that can be injected through the syringe and harden inside a bone defect [40]. Their major advantage is their ability to adapt to the specific defect's geometry, which is limited for materials implanted as solids. Ceramics can be produced in a variety of shapes depending on the specific purpose. This solid implant prevents soft tissue ingrowth and speeds up the defect fill-in process. Porous ceramics also promote cell adhesion and vascularization [54, 55].

Composite scaffolds are increasingly used to keep specific advantages and overcome the disadvantages of specific types of biomaterial [38]. Composite ceramics and coatings show improved osteoinductivity, vascularization, and bonding properties compared to their phase-pure counterparts [56, 57]. Micro- and nanoparticles can be combined with various polymers to fabricate scaffolds, including fibrous scaffolds, microporous structures, bioactive glasses, and hydrogels [49]. An emerging approach for the fabrication of various forms of scaffolds is three-dimensional (3D) printing. [49] This additive manufacturing technique allows for the manufacture of artificial scaffolds in a precise and reproducible way. These techniques also allow for osteogenic cells, as well as variety of osteogenic compounds to be seeded into the scaffolds, further improving their biological properties. This also allows controlled drug delivery and gradient release of target molecules. Every material has its own advantages and disadvantages; however, there remains no clear consensus about which biomaterials, their combinations, designs or manufacturing techniques are optimal for bone regeneration and clinical use.

1.2. Metal ion role in bone tissue

1.2.1. Magnesium

Mg is a macroelement that is important to a wide variety of metabolic, structural, and regulatory functions in human body: it is essential for normal function of skeletal, muscular, and nervous systems [58]. Mg^{2+} also functions as a cofactor in a vast range of enzymes that are responsible for lipid metabolism, deoxyribonucleic acid (DNA) and ribonucleic acid (RNA) synthesis, and normal function of adenosine triphosphate (ATP).

More than half of all Mg in the human body is located in the bone tissue [59]. The majority of it exists as a part of WH structure. The rest is a constituent of HAP structure as well as a part of organic bone tissue matrix. This ion affects all stages of bone formation and is closely related to biological CPs [27]. Mg ions upregulate osteogenesis-related gene expression and enhance bone matrix mineralization [49].

Mg deficiency, or hypomagnesemia, affects the process of bone tissue crystallization and induces the development of various bone degenerative diseases such as osteoporosis. Due to lack a of Mg, certain compensation processes can start, where Mg ions are released from the surface layer of bone tissue. Because of Mg shortage during bone mineralization, larger and more crystalline HAP species are formed [59]. In this case, mechanical properties of the bone are negatively affected – they become less dense and more fragile [60]. Hypomagnesemia also affects the formation of other adjacent tissues such as cartilage. It also induces inflammatory processes by increasing concentrations of inflammatory cytokines such as tumor necrosis factor-α, interleukin-6, and interleukin-1 consequently causing oxidative stress. Mg deficiency is also known as a risk factor for a wide range of diseases, such as preeclampsia, stroke, heart disease, diabetes, atherosclerosis, asthma, osteoporosis, and many other pathological conditions [49].

The case of Mg excess is less studied but its effect on bone mineralization is undeniable. Hypermagnesemia causes a wide range of bone tissue crystallization defects and osteopenia. Such conditions also reduce the activity of osteoblasts, slowing down the overall bone mineralization process [61].

In biological organisms Ca and Mg metabolism is closely connected, therefore fluctuations of Mg content in the body can also cause Ca disbalance, which can significantly affect cell function and overall homeostasis. An increase in Mg content causes a decrease in Ca content. Lack of Mg also affects two major compounds responsible for Ca homeostasis, parathormone and 1,25$(OH)_2$-vitamin D [62].

1.2.2. Zinc

Zn is the second most common microelement in the human body, where most of it is stored in bone and muscle tissues. This element can be found in most types of cells and partakes in more than 200 enzyme systems as a cofactor. Zinc is important to cell differentiation, normal function of immune system, formation and maturation of reproductive cells, wound healing, cell apoptosis, etc. [63].

Approximately 30% of all Zn in the human body is stored in bone tissue. It accounts for 0.012–0.025% of overall bone mass [64]. The majority of it is stored in osteoid – part of the organic bone matrix that forms before the start of tissue mineralization process. Some of the bone Zn is also contained in the HAP structure [65]. Zn has a positive effect on bone formation *in vivo*.

Zn inhibits mesenchymal stem cell differentiation to osteoclasts by blocking specific receptors. This element also induces already existing osteoclast apoptosis by intracellular signaling regulation, therefore effectively slowing down osteoclastic bone tissue deterioration. This process also induces osteoblast activity and subsequently speeds up the bone tissue mineralization [66]. Zn is also essential for vascular endothelial growth factor production in osteoblasts. This factor induces the formation of blood vessel endothelial tissue, which is crucial for bone tissue regeneration when new blood vessels are formed [67]. Zinc has a known role in enzymes associated with cellular filamentous structures, such as collagenase, proteoglycans, and keratins [49].

Low Zn levels negatively affect the bone tissue formation process, which is considered to be one of the factors in development of osteoporosis. Additionally, zinc deficiency has been shown to decrease the proliferation of neural stem cells and enhance apoptosis of such cells partially due to increased reactive oxygen species (ROS) production [49]. Zn is also important for normal immune system function, as a large number of compounds that function as signal transmitters between immune cells have Zn^{2+} ions as their structural elements. Deficiency of this element significantly increases the risk of infection and slows down the healing process [68].

On the other hand, Zn excess can cause toxicity and cell death. However, such cases are rare, and the majority of them can be attributed to Cu deficiency, which develops due to the excess of Zn inhibiting the absorption of this element. Both Zn deficiency and overabundance promote inflammatory cytokine production. This can cause oxidative stress and other health issues attributed to prolonged inflammation [69].

1.2.3. Copper

Being an essential trace element in the human body, Cu is involved in a numerous physiological functions such as tissue formation, neuromodulation, and respiratory function and acts as an enzyme cofactor [12]. This element is important for the normal function of cardiovascular and immune systems [70]. Cu is the third most prevalent microelement in the human body, of which two-thirds are located in skeletal and muscular tissue. Other organs with heightened Cu concentrations are the liver, brain, kidneys, and heart [71].

Cu ions are known to bind with several growth factors involved in angiogenesis [72]. Angiogenesis is the process of formation and growth of new blood vessels, and it is crucial for both bone formation and overall wound healing process because it supplies all the necessary nutrition, oxygen, hormones, and growth factors to the damaged area of the body. Cu also promotes the expression of proteins such as collagen, elastin, fibroblast growth factor, and nerve growth factor [12]. This element also significantly increases the deposition of collagen fibers [73]. Cu also aids in the proliferation and migration of endothelial cells as well as fibroblast cells, which are important processes for the blood vessel formation. In addition, Cu-peptide complexes are known to have anti-inflammatory properties with the suppression of free radicals in order to prevent oxidative stress [74]. Cu appears essential for bone mineralization and osteoblast functions by stimulating the differentiation of bone marrow mesenchymal stem cells toward osteoblast cells, enhancing osteoblast activity and proliferation [70, 75].

Cu deficiency is harmful to human health and leads to several disorders such as anemia, leucopenia, myeloneuropathy, coronary heart disease, and Menke’s disease [76]. Menke’s disease is a genetic disorder that develops due to mutations of the copper transport protein ATP7A that normally facilitates Cu export from enterocytes to the blood, resulting in an intestinal accumulation of Cu [12]. With this condition individuals exhibit neurodegeneration, seizures, hypothermia, connective tissue and hair abnormalities and bone fragility, which, depending on the severity, can result in death. This, in part, is due to inhibition of important functions, such as catecholamine production, peptide amidation, and mitochondrial respiration [77]. Skeletal abnormalities such as a decrease in bone strength are overall a common symptom of other Cu deficiency related disorders [78].

In relatively high local concentrations, Cu is considered to be toxic. An excess of Cu is a result of Wilson's disease, which is a genetic disease linked to an accumulation of Cu in the body due to ATP7B protein mutation. It causes damage to the liver and nervous system – tissues that already have naturally heightened Cu levels. Progression of Alzheimer's disease, diabetes, and cancers are diseases that can be impacted by excess amounts of Cu due to a failure in Cu regulation and homeostasis mechanisms [71]. It can also result in an obstruction to the synthesis of collagen, which can damage blood vessels and other connective tissues [70]. Higher concentrations of Cu may also cause oxidative stress because of their ability to generate ROS [53].

1.2.4. Manganese

Manganese is an essential human dietary microelement, which is a critical component in dozens of proteins and enzymes [49]. This element is necessary for normal function of nervous, immune, and reproductive systems and also aids in defense mechanisms against ROS [49, 79]. The human body contains about 10–20 mg of Mn, of which 25% to 40% is found in bones [80].

Mn is a key trace element that contributes to overall body growth and development, and is also required for protein synthesis, nucleic acid synthesis, and carbohydrate, protein, and lipid metabolism [81] [82]. This element is a cofactor in several enzymes, such as manganese-superoxide dismutase that are essential for normal function of the brain and nervous system [49]. Even though the exact mechanisms of Mn effect on bone mineralization are not well understood yet, it is known that this element plays a role in bone homeostasis [83] and increases the production of osteogenic compounds [84]. Mn also promotes the differentiation of human bone marrow mesenchymal stem cells, therefore increasing osteoblast proliferation [85, 86]. The increase of ligand-binding affinity of integrins due to the existence of Mn ions promotes cellular adhesion, which is crucial for new tissue formation [81]. Supplementation of manganese can increase the serum osteocalcin and bone mass.

Mn deficiency can lead to poor bone formation and skeletal defects, including reduction of bone thickness and length, and growth impairment [79, 87, 88]. It also results in altered lipid and carbohydrate metabolism as well as

Mn affects the presence of a variety of glycoproteins, which are necessary for cell-adhesion abilities, growth, and differentiation [49].

At high dosages Mn^{2+} intake can be neurotoxic, causing symptoms ranging from increased irritability to dementia [49, 89]. Oxidative stress is one of many factors implicated in Mn-induced neurotoxicity. Since Mn preferentially accumulates in dopamine-rich brain regions, it is able to induce oxidation of this important neurotransmitter. Excess of this element might also interfere with proper respiration, thereby leading to excessive production of ROS, lipid peroxidation, and ensuing cell death [79]. Elevated whole-blood Mn levels are also associated with dystonia, a symptom closely related to Parkinson's disease [82].

1.3. Calcium phosphates

Ca and P are common chemical elements that account for 3.4% and 0.1% of the Earth's crust, respectively [35]. Together, these elements can form a variety of compounds with a wide range of properties. In geology, these compounds are found as minerals, sedimentary rocks (phosphorite) and, in rare cases, in volcanic rocks (fluorapatite). In biological systems, these compounds usually appear as either normal (bone tissue, teeth) or pathological (dental and urinary calculus, atherosclerosis-affected tissue) calcinations [26].

CPs differ severely in chemical composition, crystalline structure, chemical and physical properties. Which CP phase will be obtained through the synthesis process highly depends on reaction conditions such as temperature, pH, and additional ions in the reaction mixture. Table 1 shows major CP phases and their properties.

Table 1. Phases of common calcium phosphates [90].

Compound	**Chemical formula**	**Ca/P molar ratio**	**Solubility at 25 °C, -log(K_S)**	**Density, g/cm^3**
MCP	$Ca(H_2PO_4)_2$	0.5	1.14	2.58
DCPD	$CaHPO_4 \cdot 2H_2O$	1.0	6.59	2.32
DCPA	$CaHPO_4$	1.0	6.90	2.89
ACP	$Ca_x(PO_4)_y \cdot nH_2O$	1.2–2.2	–	–
WH	$Ca_{18}Mg_2(HPO_4)_2(PO_4)_{12}$	1.29	113.8	3.12
OCP	$Ca_8(HPO_4)_2(PO_4)_4 \cdot 5H_2O$	1.33	96.6	2.61
α-TCP	$Ca_3(PO_4)_2$	1.5	25.5	2.86
β-TCP	$Ca_3(PO_4)_2$	1.5	28.9	3.07
CDHA	$Ca_{10-x}(HPO_4)_x(PO_4)_{6-x}(OH)_{2-x}$ $(0<x<1)$	1.5–1.67	85.1	–
HAP	$Ca_{10}(PO_4)_6(OH)_2$	1.67	116.8	3.16
TTCP	$Ca_4(PO_4)_2O$	2.0	38–44	3.05

One of the major describing factors of CPs is their Ca/P molar ratio, which determines the acidity or basicity of the compound as well as its solubility. This parameter usually varies from 0.5 to 2.2. As a rule, CPs with lower Ca/P ratios are more acidic and have a higher solubility in water [26].

1.3.1. Metal ion substituted calcium phosphates

CPs that occur in both living and non-living nature can be substituted by a wide range of ions. Most commonly, Ca^{2+} ions in the crystalline lattice of naturally occurring CPs are substituted by Sr^{2+}, Ba^{2+}, Mg^{2+}, K^+, Na^+, and Fe^{2+} ions, while phosphate ions can be replaced by AsO_4^{3-}, CO_3^{2-}, and VO_4^{3-} ions. In fluorapatites F^- ions are commonly substituted by OH^-, Cl^-, Br^-, CO_3^{2-}, and O^{2-} ions. Partial ionic substitution can provide synthetic CPs with improved biological performance or specific properties as well as new fields of application [91, 92]. It can also simplify the synthesis process and make the control of structural parameters of the material easier [42].

Synthetic non-substituted CPs cannot replicate the complex matrix of natural bone tissue effectively, therefore showing subpar biological performance compared to natural material [64, 88]. For this reason, the incorporation of foreign ions into the structure of CPs is one of the factors that determines biocompatibility and biointegration of the material [63]. A huge number of studies were dedicated to the investigation of ion-substitution in various synthetic CP matrices on their structural, biological, mechanical, antibacterial, and other properties. For instance, Zn, Mg, Mn, and Si are elements naturally occurring in bone tissue; therefore, the addition of these elements into the structure of CPs has a positive effect on their osteointegration [27]. Partial substitution with Zn, Mg, Y, or Na enhances the osteoblast adhesion on the surface, improving the integration of the implant into the natural bone tissue [93]. Mn, Zn, Sr, and Fe ion-containing CPs have improved biological activity and induce osteogenic processes [81, 94]. Mn-doped CPs have been shown to promote osteoblast proliferation and differentiation [87].

Ionic substitution has a significant impact on density, microstructure, and mechanical properties of the material. Osteoinductivity in biological systems is highly affected by grain size and porosity. Si or Zn ions can significantly improve mechanical properties of CP ceramics, such as density and microhardness [64]. Zn also affects grain growth [67]. On the other hand, Mn, Mg, and Co, due to an increase in microporosity and smaller grain size, weakens HAP durability, microhardness, and resistance to mechanical stress [81].

Bioresorption is one of the important properties of CPs used for bone tissue regeneration. This parameter directly depends on the solubility of the material under physiological conditions, which is strongly affected by ionic substitution. Substitution with Mg^{2+} ions significantly decreases β-TCP solubility in the acidic environment [95], while HAP solubility under the same conditions increases [91]. Due to better solubility, Mg-substituted HAP has improved resorption and integrates more smoothly into the natural bone tissue. The same trend is seen in HAP partially substituted with Na^{+} [88]. Zn, however, has been shown to decrease solubility and overall resorption of the CPs [96].

Ionic substitution also can provide biomaterials with antibacterial properties. This is extremely important in the field of bone implants as infections are one of the most common side effects of this medical procedure. Cu^{2+}, Zn^{2+}, Ag^{+}, and Fe^{3+} ions greatly improve the antibacterial properties of β-TCP [42]. Zn-containing HAP stops the growth and reproduction of fungi and bacteria such as *E. coli*, *S. aureus*, *C. Albicans*, and *Streptococcus mutans* [97]. It also impedes the formation of dental calculus and bacterial growth on the surface of the enamel [53]. HAP powders doped with Ag and Cu have strong antibacterial properties against a wide range of microorganisms and are not cytotoxic [98]. Cu-containing CPs such as HAP, TCP, and dicalcium phosphate dihydrate (DCPD) demonstrated an antimicrobial effect as well as angiogenic and osteogenic properties [12, 99-101]. Antibacterial properties are also present in Mn-substituted CPs [15, 81], which also demonstrate a positive effect on osteogenic processes [16].

Functionalized materials can also be used as contrast agents in various diagnostic tools. Eu- and Tb-codoped Mg-WH nanoparticles possessed fluorescent properties that were successfully applied for bioimaging [102]. Various Mn-substituted CPs, such as HAP [13], ACP [14] and others can be used for MRI due to their magnetic properties [82, 103]. Fe, being a biologically active ion, is also very attractive element in terms of its magnetic properties that makes it suitable for bioimaging as well as potential application of Fe-doped CPs in hyperthermia for cancer treatment [37, 104].

1.4. Whitlockite

Mg-WH is a phosphate group mineral that can be found in a variety of different environments. It can form in aquatic environments as well as in various rock formations, when other CP deposits are nearby. For example, Mg-WH was found in the Palermo pegmatite quarry near North Groton, New Hampshire [105]. It was also found to be a major component of elephant shark hypermineralized tooth plates [106].

This material is most commonly found in vertebrates as a major component of the endoskeleton. It is the second most abundant mineral in the human body that accounts for 25–35% of bone and tooth tissue. WH can also be found in dentine [107], tooth enamel, and cartilage [108]. Higher concentrations of this mineral were observed in bone tissue of younger individuals as well as in areas, where intense osteogenic processes can be observed [3], for example, in a place of a fracture. That implies that WH is an important part of the human tissue formation process. It is speculated that this material could function as a framework on which further tissue mineralization can occur. With age, the amount of WH in skeletal tissue decreases. This might be determined by degenerative processes of bone tissue that intensify as the body ages [29].

Slightly acidic conditions are characteristic to body areas of intense osteogenic activity. This promotes integration of organic matrix into the bone tissue as well as bone tissue mineralization [109]. WH is more stable under acidic conditions than HAP. When WH dissolves, it increases local ion concentration and promotes protein adsorption, which are both known to be important aspects of the bone tissue formation process. Furthermore, the amount of Mg^{2+} and PO_4^{3-} ions is an important regulatory factor in monocyte differentiation, which controls both bone tissue regeneration and degeneration

[29]. As bone tissue ages, WH slowly undergoes phase transformation to HAP – most abundant component of bone tissue inorganic matrix, which gives bone structure rigidity [2].

WH deposits in the human body can also occur as a variety of pathological calcifications. These calcifications can be kidney and salivary gland stones, calculus, also it can be a consequence of a variety of diseases such as tuberculosis, arthritis, and atherosclerosis [110]. These deposits are usually a mixture of biological CPs, including ACP, HAP, WH, and others. These pathological deposits occur due to certain proteolipids forming centers of crystallization, where in favorable conditions ACP can be formed [111]. In further stages of crystallization ACP will transform to WH or HAP depending on local Mg^{2+} ion concentration [112]. This process can also occur due to a bacterial infection. HAP deposits in bacterial walls as well as some bacterial waste can serve as crystallization points [113].

It should be mentioned that there are some contradictions in the literature regarding the presence of Mg-WH in the human body. A recent literature analysis by Shah [114] did not confirm the claims of Mg-WH constituting a significant part of human hard tissues, concluding that Mg-WH is exclusively a pathological biomineral. According to Shah, Mg-WH has never been reported to be in bone extracellular matrix; therefore, Mg-WH does not constitute a biomimetic strategy for bone repair. Nevertheless, such contradictions do not deny the fact that Mg-WH is osteoconductive and bioresorbable material suitable for application as a bone graft substitute. Synthetic Mg-WH demonstrated superior biological performance in both *in vitro* and *in vivo* studies [3, 22, 115, 116]. Moreover, Mg-WH demonstrated piezoelectric properties, which allows to use it as a self-powered electrical stimulator for osteogenic, neurogenic, and angiogenic differentiation [117, 118].

1.4.1. Crystal structure

Mg-WH crystallizes in the rhombohedral crystal structure with a space group R3c (#161) and equivalent hexagonal unit cell (Fig. 5a) parameters a = b = 10.350(5) Å, c = 37.085(12) Å [119]. The crystal structure of Mg-WH is composed of two types of columns (A and B) that are periodically arrayed along the *c*-axis. Column A consists of Mg^{2+} and HPO_4^{2-} units alternating with empty spaces. More densely packed column B has a form of Ca(1) – P(3)O4 – P(2)O4 – Ca(2) – Ca(3) [19, 95]. Both A and B columns come in three different subtypes each (Fig. 5b). These subtypes are identical in atomic arrangement but are shifted relative to each other along the *c*-axis. Each A column is surrounded by six B columns of two different subtypes, while each B column is surrounded by two A columns of different subtypes on opposite sides and four B columns of two different subtypes (Fig. 5c-d). The unit cell of Mg-WH is composed of 3 A columns and 9 B columns. There are 3 inequivalent sites for calcium and 3 for phosphorus in the crystal structure of WH. Whereas Ca(1) (Fig. 5e) and Ca(2) (Fig. 5f) ions are both directly bonded with five PO_4^{3-} groups and one HPO_4^{2-} group, the Ca(3) (Fig. 5g) site has 4 neighboring PO_4^{3-} groups. In column A, all the x and y atomic coordinates of Mg and P(1) have the value of zero, showing that these atoms are located on a straight line. Meanwhile, in column B, the *x* and *y* atomic coordinates of Ca(1), Ca(2), Ca(3), P(2) and P(3) have different values, indicating that column B is distorted compared to the column A.

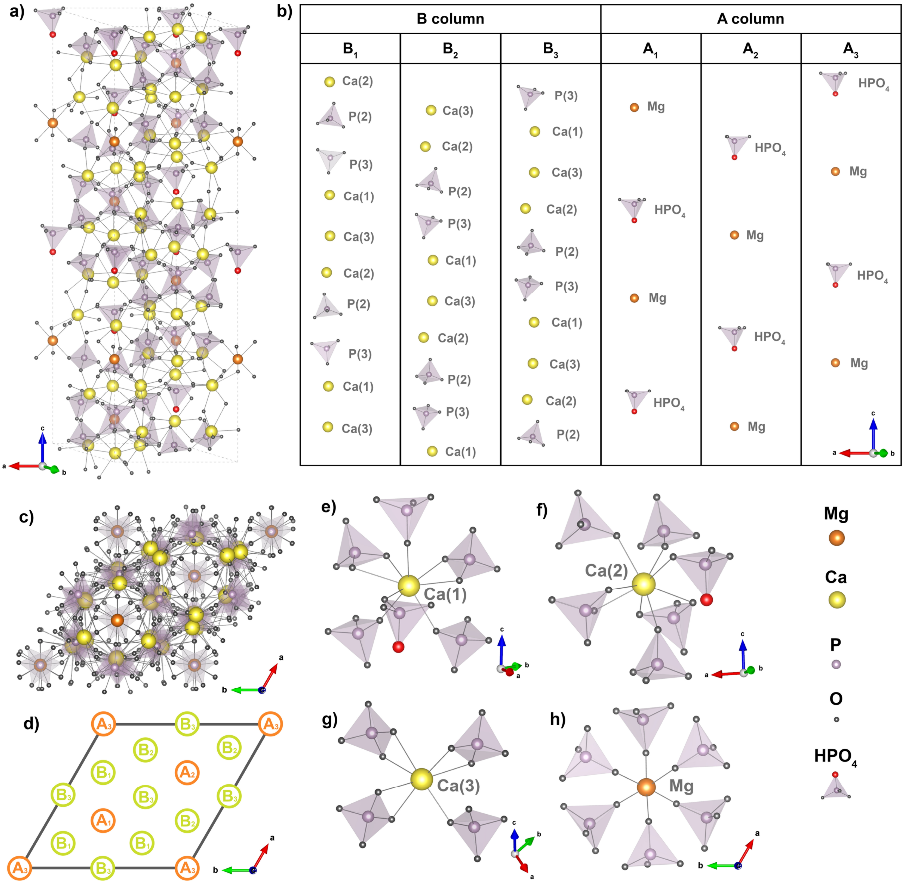

Fig. 5. Unit cell of Mg-WH (a, c); Arrangement of atoms in structural columns (b); Arrangement of columns in the unit cell (d); Different cationic crystallographic sites in WH structure with surrounding phosphate groups (e-h).

Due to the similarity of the crystal structure of WH and β-TCP, these two names are often used interchangeably and synonymously. These materials have the same rhombohedral structure and space group and have essentially similar values of the lattice parameters [119, 120]. However, these two materials cannot be classified as isostructural even though X-ray diffraction (XRD) data of these two compounds are identical. The difference between β-TCP and Mg-WH originates from the presence of HPO_4^{2-}, Ca^{2+}/Mg^{2+} substitution and cation vacancies in the latter. In β-TCP, the crystal lattice is composed of two periodically arrayed columns (A and B) along the *c*-axis. Column B is identical to Mg-WH, while in A columns Ca(5) and Ca(4) positions in β-TCP are occupied by Ca ions, whereas in WH structure Ca is substituted by Mg and H from HPO_4^{2-}, respectively [95, 121].

1.4.2. Synthesis

Even though WH is a perspective material for medical applications, this compound is not widely studied or described. The main reason for this is a tricky synthesis process, a large number of possible phase transitions, and the low thermal stability of WH itself [21]. In the human body WH is formed by phase transition from other CPs, when part of Ca^{2+} ions are substituted by Mg^{2+} ions [122]. However, WH can be formed with the help of other secondary cations, such as Co^{2+}, Mn^{2+}, Fe^{2+} or Zn^{2+}. These ions destabilize the structure of other CPs, such as anhydrous dicalcium phosphate (DCPA), octacalcium phosphate (OCP), and HAP, making WH the most energetically favorable structure [19]. These properties can also be used as an advantage, allowing WH to be synthesized in a variety of ways using a large pool of different starting materials.

One of the first known ways to synthesize WH was hydrothermal synthesis from an amorphous phosphatic gel. This gel was obtained by increasing the pH of the solution containing $Ca(NO_3)_2$, $Mg(NO_3)_2$, and $NH_4H_2PO_4$ by adding a certain amount of ammonia solution. This gel was then transferred to a stainless-steel autoclave, where the reaction took place [119].

A common way to obtain WH is through the precipitation synthesis method when $Ca(OH)_2$ and $Mg(OH)_2$ are used as starting materials. These compounds are dissolved, then a certain amount of H_3PO_4 is added to achieve the needed pH value. This type of reaction can be performed under both hydrothermal and atmospheric conditions. Other synthesis conditions vary between different sources [3, 19, 29, 123].

WH can also be obtained using other calcium salts as starting materials, such as DCPD, gypsum, and others. In the case of DCPD, the starting powder was sealed in a bottle with a $MgCl_2$ solution. Bottles were put in an oven where reactions of varied duration and temperature took place [108]. Gypsum can also be used as a starting material for dissolution-precipitation synthesis of WH. For this, the required amount of $CaSO_4$, $Mg(CH_3COO)_2$, Na_2HPO_4, and NaH_2PO_4 were dissolved in water and sealed in a bottle. The container was then placed in an oven at 80 °C for a varied period of time [124, 125].

The solvothermal synthesis *via* the solid-liquid-solid process can also be used for WH production [58]. A tri-solvent system was obtained by mixing the required amounts of oleic acid, ethanol, and NaOH solution. Then the starting materials $CaCl_2$, $MgCl_2$, and Na_2HPO_4 were added to the mixture and dissolved. The obtained solution was transferred into a stainless-steel autoclave and heated at 200 °C for 12 h. The optimized process allowed to generate particles with controlled size, morphology, and surface properties.

WH can also be synthesized in the form of coatings on other CPs, for example, β-TCP [21]. For this purpose, WH coatings were grown on the β-TCP ceramics using hydrothermal method. Ceramic pellets were sealed in a stainless-steel autoclave with saline solution. By varying synthesis conditions, a phase-pure WH was obtained.

Another way to synthesize WH is using microwave-assisted rapid synthesis. Using this method the solution of $CaCl_2$, $MgCl_2$, and either creatine phosphate disodium salt [126] or fructose 1,6-biphosphate trisodium salt [107] or adenosine 5-triphosphate disodium salt [127] was adjusted to a suitable pH. Then the solution was sealed in microwave reactor vessel for varied range of time, and the reaction was performed at different temperatures. Using this method, single-phase WH was obtained in the form of hollow microspheres. An analogous way to obtain hollow microspheres is by using hydrothermal synthesis instead [107].

WH can also form as a side product of HAP synthesis if Mg^{2+} ions are present in the reaction mixture. When sepia (*Sepia Officinalis L.*) bones were used as a starting material, the pretreated bones were put in a stainless-steel autoclave with $NH_4H_2PO_4$ and $MgCl_2 \cdot 6H_2O$ aqueous solution. In all samples an additional Mg-WH phase was formed [128]. Using the hydrothermal synthesis method, WH was also obtained as a secondary phase while synthesizing HAP form eggshells [129].

Although the ionic substitutions were widely investigated in conventionally used CPs [91], the works on ion-substituted Mg-WH are almost absent with a few rare exceptions, of which most appeared in recent years. One of the first sources that mention WH from 1976 describes Mn-WH that was synthesized by accident under hydrothermal conditions at 425 °C [8].

Just recently, Heng et al. reported a purposeful synthesis of Mn-WH nanoparticles using the solvothermal method [130]. The same group also synthesized Nd- [86] and Eu- [131] codoped Mn-WH nanoparticles using similar synthesis techniques. Belik et al. [7] prepared $Ca_9FeD(PO_4)_7$ (D being deuterium) by treating $Ca_9Fe(PO_4)_7$ with D_2 at elevated temperatures. In this case Fe ion possessed an oxidative state of 2+. Ce-doped Mg-WH was prepared by precipitation method using $Ca(OH)_2$, $Mg(OH)_2$, $Ce(OH)_3$, and H_3PO_4 [132]. Eu^{3+}/Tb^{3+}-doped Mg-WH nanocrystals were prepared using a tri-solvent system of oleic acid, ethanol, and aqueous solution of precursors and hydrothermal synthesis method [102]. A similar process was also used for the synthesis of Zn-WH [133]. Recently, Zn- and Co-WH [134], as well as Cu-WH [135] were also obtained using the hydrothermal synthesis method.

1.4.3. Application

Despite the presence of high content of Mg-WH in the human body, it is not yet used in clinics due to the challenges in the preparation of this material. Only in recent years, Mg-WH attracted significantly more attention as a number of studies reported various synthetic approaches and characterization of the material, resulting in the first medical research and usage potential [86, 136-138].

A major goal of WH-related research is to use this material in the medical field for bone tissue regeneration. Mg-WH has shown excellent biocompatibility and osteogenic capacity *in vivo* [20]. It was also found that Mg-WH stimulates bone neural activity and promotes development of neural cells [115]. Several comparative studies demonstrated that Mg-WH possesses superior properties compared to those of frequently used biomaterials such as HAP or TCP. Several comparative studies suggest that Mg-WH has improved biocompatibility as well as induces osteogenic cell differentiation and osteogenesis more effectively in comparison with HAP and β-TCP [3, 95, 139]. According to Kim et al. [116], under physiological conditions, Mg-WH nanoparticles can recapitulate the early stage of bone regeneration by stimulating osteogenic differentiation, prohibiting osteoclastic activity, and transforming into HAP – the main inorganic bone tissue component.

Research shows that WH can also be used as a component in a variety of composite materials. HAP/Mg-WH composite scaffolds were shown to have superior mechanical strength and osteogenic properties compared to pure HAP scaffolds [140]. Mg-WH containing scaffolds were shown to promote cell migration, differentiation, angiogenesis, and osteogenesis [22, 122, 137, 141].

Mg-WH was also used in clinical research in a variety of forms. For instance, Mg-WH was used in bone cements, where it showed enhanced bone formation and osteointegration properties *in vivo* as well as other suitable properties for clinical use [142]. Mg-WH containing borosilicate bioactive glass bone cements were shown to have great osteogenic properties in biological systems and significantly improved anti-collapse performance of the material [143]. Mg-WH containing hydrogels have also shown excellent osteogenic qualities [139]. Zhang et al. proposed to use Mg-WH as a component in nanocomposite fiber membranes to achieve better angiogenesis and osteogenic differentiation in periosteal tissue [23]. HAP/Mg-WH composite coatings showed enhanced osteoconductive effect and mechanical strength [144]. Coating on TCP ceramics exhibited an enhanced ability for osteogenesis and mineralization [21]. Bone screws consisting of poly(lactic-co-glycolic) acid and Mg-WH microspheres performed well in areas of osteogenic activity, cell proliferation, and vitality [109].

WH shows great potential as a material for drug delivery. Mg-WH nanoparticles containing ampicillin showed promise in localized antibiotic delivery [145]. Materials were also nontoxic and osteogenic. Mg-WH hollow microspheres exhibited sustainable drug release and high drug loading capacity, making them favorable for application in anticancer treatment [126]. Synthetic Mg-WH was also shown to have inhibitory properties on the proliferation of breast cancer cells, suggesting a possible use in cancer therapy [136].

WH can also act as a hemostatic agent in the form of chitosan hydrogel with incorporated Mg-WH nanoparticles. Ca^{2+}, Mg^{2+}, and phosphate ions can act as coagulation factor activators so their release can improve coagulation time and prevent blood loss during an injury. Developed hydrogels were shown to be suitable for injection into the injury site as well as decreased blood clotting time and decreased blood loss compared to unmodified chitosan gel as well as commercial hemostatic agents [123].

Mg-WH can also be used for adsorption of proteins [107] and heavy metals. Lin et al. [127] prepared Mg-WH microspheres to be used for the adsorption of Pb^{2+} from contaminated water. The material exhibited an excellent ability to adsorb heavy metal from contaminated water. Therefore, it could potentially be used for environmental remediation applications. Mg-WH powder was also used as lead adsorbent from solutions, where it performed significantly better than HAP [146].

There are also a few examples of WH synthesized with ions other than Mg. There is one instance of Zn-WH nanoparticles being used in nanocomposite scaffolds [133]. Zn-WH regulated expression of osteogenic genes, promoted bone growth, and inhibited growth of bacteria. Mn-WH nanoparticles showed high drug loading ability, outstanding photothermal properties, and stable MRI imaging ability – properties that could be applied for an effective chemo-photothermal synergistic treatment of tumors [130]. Nd- [86] and Eu- [131] codoped Mn-WH nanoparticles showed potential for osteosarcoma treatment and MRI bioimaging, respectively. Eu- and Tb-codoped Mg-WH nanoparticles possessed fluorescent properties that were successfully applied for bioimaging [102]. Nd-doped Mg-WH synthesized by dissolution-precipitation process exhibited rapid near-infrared (NIR) response for light and heat energy conversion, as well as fluorescence [138].

2. EXPERIMENTAL

2.1. Materials and reagents

Following chemicals were used for the synthesis of WH:

- Calcium hydrogen phosphate dihydrate (DCPD, $CaHPO_4 \cdot 2H_2O$, 99.1%, Eurochemicals);
- Zinc acetate dihydrate ($Zn(CH_3COO)_2 \cdot 2H_2O$, ≥ 99.5%, Roth);
- Magnesium acetate tetrahydrate ($Mg(CH_3COO)_2 \cdot 4H_2O$, ≥98%, Roth);
- Manganese acetate tetrahydrate ($Mn(CH_3COO)_2 \cdot 4H_2O$, ≥99%, Roth);
- Copper nitrate trihydrate ($Cu(NO_3)_2 \cdot 3H_2O$, ≥98%, Roth);
- Phosphoric acid (H_3PO_4, 75%, Roth);
- Concentrated ammonia solution (NH_4OH, 25%, Roth).

2.2. Synthesis of Mg-WH

Mg-WH powders were synthesized *via* a dissolution-precipitation process under hydrothermal conditions. For the synthesis, certain amounts of $CaHPO_4 \cdot 2H_2O$ and $Mg(CH_3COO)_2 \cdot 4H_2O$ corresponding to the Ca/Mg molar ratio of 9 were dissolved in a mixture of 50 mL of deionized water and 5.6 mL of 1 M H_3PO_4 in a 90 mL polytetrafluoroethylene (PTFE) liner to obtain a solution with a total metal ions concentration of 0.06 M. The above mixture was stirred with a magnetic stirrer at room temperature until the precursors were fully dissolved. Next, under continuous mixing, concentrated NH_4OH solution was added until the pH of the reaction medium raised to 6.4. Then, the reaction mixture was sealed in a Teflon-lined stainless-steel container and transferred into an oven preheated to 160 °C for 3 h. Afterward, the container was allowed to cool down to room temperature, and the resulting product was vacuum filtered, washed with deionized water, and dried at 50 °C in the oven overnight. The synthesis procedure is schematically illustrated in Fig. 6. Obtained powders were further annealed in air for 5 h at temperatures from 400 to 1300 °C with a step of 100 °C.

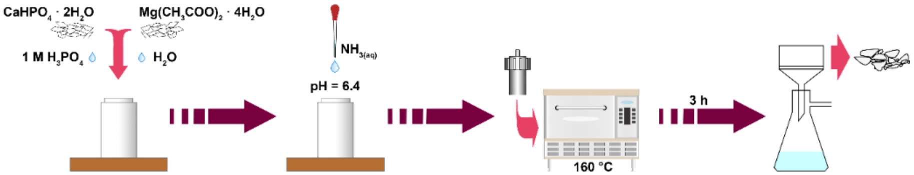

Fig. 6. Schematic representation of the synthesis of Mg-WH powders.

2.3. Synthesis of Zn-WH at ambient pressure

Zn-WH powders were synthesized *via* a dissolution-precipitation process at ambient pressure. For the synthesis of Zn-WH powders, certain amounts of $CaHPO_4 \cdot 2H_2O$ and $Zn(CH_3COO)_2 \cdot 2H_2O$ were mixed in various proportions to achieve Ca/Zn molar ratios of 9, 10, 12, 15, 20, 30. These mixtures were then dissolved in a mixture of 100 mL of distilled water and 13 mL of 1 M H_3PO_4. The total concentration of metal ions in the reaction mixture was 0.065 M. The obtained solution was mixed with a magnetic stirrer at 75 °C for 1 h. Next, under constant mixing, concentrated NH_4OH solution was added in order to adjust the pH to 5.6. The increase in the pH value of the reaction medium resulted in an instantaneous formation of white precipitates. The resulting mixture was stirred for another 3 h at 75 °C. Afterward, the precipitates were vacuum filtered, washed with distilled water, and dried at 60 °C in the oven overnight. Obtained powders were annealed in air at temperatures of 500, 600, 900 °C.

2.4. Synthesis of Zn-WH under hydrothermal conditions

Zn-WH powders were synthesized *via* a dissolution-precipitation process under hydrothermal conditions. In a typical procedure, certain amounts of $CaHPO_4 \cdot 2H_2O$ and $Zn(CH_3COO)_2 \cdot 2H_2O$ corresponding to Ca/Zn molar ratios of 6, 8, 9, 10, 12, 30 were dissolved in a mixture of 50 mL of deionized water and 6.5 mL of 1 M H_3PO_4 to obtain the solution with total metal ion concentration of 0.06 M. The obtained clear solution was stirred on a magnetic stirrer for 30 min at room temperature. Next, under constant mixing, concentrated NH_4OH solution was added in order to adjust the pH value to 5.8. The resulting mixture was transferred to a 90 mL PTFE liner and sealed in a stainless-steel reactor, which was transferred to a pre-heated oven and maintained at different temperatures (110–230 °C) for different periods of time (1–3 h). Duration of the reaction was calculated starting from the moment the reactor was placed in an oven until it was removed from it. After the reaction, the precipitates were vacuum filtered, washed with deionized water, and dried at 60 °C in an oven overnight.

2.5. Synthesis of Cu-WH

Cu-WH powders were synthesized *via* a dissolution-precipitation process under hydrothermal conditions. For the synthesis, certain amounts of $CaHPO_4 \cdot 2H_2O$ and $Cu(NO_3)_2 \cdot 3H_2O$ were transferred into 90 mL PTFE liners and dissolved at room temperature in a mixture of 50 mL of deionized water and 10 mL of 1 M H_3PO_4. The final metal ion concentration in the solution was 0.08 M. After the complete dissolution of precursors under constant mixing on a magnetic stirrer, a clear blue solution was obtained. Next, concentrated NH_4OH solution was added to the reaction mixture in order to adjust the pH to 6.4. The PTFE liners were transferred into a stainless-steel reactor, sealed and placed into a preheated oven, and heated at different temperatures (110–230 °C) for different periods of time (1–24 h). After the synthesis, the reactors were cooled down, and the resulting blue powders were separated from the solution by vacuum filtering. Afterward, the powders were washed with deionized water and dried in the oven at 70 °C. Obtained powders were annealed in air at temperatures of 500–1000 °C with a step of 100 °C.

2.6. Synthesis of Mn-WH

Mn-WH powder was synthesized by a dissolution-precipitation method by mixing required amounts of $CaHPO_4 \cdot 2H_2O$ and $Mn(CH_3COO)_2 \cdot 4H_2O$ corresponding to Ca/Mn molar ratio of 9 were dissolved in a mixture of 100 mL of deionized water and 13 mL of 1 M H_3PO_4. The total metal ion concentration of the obtained solution was 0.06 M. Next, a concentrated NH_4OH solution was added to the reaction mixture under constant stirring, and the pH of the reaction medium was raised to 5.6. The increased pH value resulted in the formation of white precipitates with a slight pink hue. The reaction mixture was sealed in a 250 mL glass bottle with a screw cap and placed in a shaker incubator (Biosan ES-20/80) for 3 h at 75 °C with a rotating speed of 220 rpm. At the end of the synthesis, the precipitates were vacuum-filtered, washed with deionized water, and dried at 60 °C in an oven overnight.

2.7. Characterization

Powder XRD study of the obtained Mg-WH samples was performed using a PANalytical X’Pert Powder diffractometer (Ni-filtered Cu-Kα radiation, $\lambda = 1.5419$ Å, PIXcel 1D detector). The data were collected in Bragg-Brentano geometry (θ/θ) geometry, and the exposition corresponded to 1 s per step of 0.02° over the angular range of 10–90° at room temperature. XRD data of all other samples was obtained using Rigaku MiniFlex II diffractometer (Cu-Kα, $\lambda = 1.5419$ Å) working in Bragg-Brentano (θ/2θ) geometry. The data were collected within 10–60° 2θ angle range with a speed of 1°/min. Additional data were collected in 10–100° 2θ angle range for the Rietveld refinement.

Structural refinement was performed using Match! (software version 3.10.2.173) and FullProf Suite (software version September-2020) programs. Data was fitted using ICSD 143481 as a reference [147].

Fourier transform infrared spectra (FTIR) were obtained in the range of 4000–400 cm^{-1} and resolution of 4 cm^{-1} with Bruker ALPHA-FTIR spectrometer.

For Mg-WH samples Raman spectra were recorded using a Reinshaw inVia Raman spectrometer equipped with a thermoelectrically cooled CCD camera and microscope. The spectra were excited with a 325 nm beam, while the high-resolution Raman spectra were observed with a 532 nm excitation wavelength. Position of the Raman bands on the wavenumber axis was calibrated by the polystyrene film (532 nm excitation) and Teflon (325 nm excitation) Raman spectrum. For all other samples, Raman spectra were recorded using combined Raman and scanning near field optical microscope WiTec Alpha 300 R equipped with a 532 nm excitation laser source. Position of the Raman bands on the wavenumber axis was calibrated by the polystyrene Raman spectrum.

The morphology of Zn-WH powder synthesized under hydrothermal conditions was analyzed by scanning electron microscopy (SEM) using a Hitachi SU-70 microscope. The morphology of all other samples was studied by field emission scanning electron microscopy using a Hitachi SU 9000 microscope equipped with energy dispersive X-ray spectrometer (EDX).

Transmission electron microscopy (TEM) analysis was performed on a JEOL JEM-2100F FEG TEM instrument.

The X-ray photoelectron spectroscopy (XPS) analysis was carried out with a Kratos Axis Supra spectrometer using a monochromatic Al-Kα source (25 mA, 15 kV). The instrument work function was calibrated to give a binding energy (BE) of 83.96 eV for the Au 4f7/2 line for metallic gold, and the spectrometer dispersion was adjusted to give a BE of 932.62 eV for the Cu 2p3/2 line of metallic copper. The Kratos charge neutralizer system was used on all specimens. Survey scan analyses were carried out with an analysis area of 300 x 700 microns and a pass energy of 160 eV. High-resolution analysis was carried out with an analysis area of 300 x 700 microns and a pass energy of 20 eV. Spectra have been charge corrected to the main line of the carbon 1s spectrum (adventitious carbon) set to 284.8 eV. Spectra were analyzed using CasaXPS software (version 2.3.23rev1.1R). Since Mn is sensitive to ion sputtering and the sample might be damaged by the cleaning process, the Mn-WH samples were not cleaned before the analysis.

Solid-state nuclear magnetic resonance (NMR) experiments were carried out at 14.1 T on a Bruker Avance Neo 600 NMR spectrometer operating at 600.3 and 243.0 MHz for ^{1}H and ^{31}P, respectively, using a 2.5 mm Trigamma magic angle spinning (MAS) probe and 2.5 mm zirconia rotors. Temperature was stabilized at 298 K and MAS rate was set to 10 kHz for Mg-WH samples and 20 kHz for Cu-WH samples. For ^{1}H MAS experiments a pulse sequence employing two π refocusing pulses with a delay of 2 μs was employed to eliminate the signal from the probe background. The ^{1}H 90° excitation pulse was 2.1 μs and 16 scans were accumulated using a repetition delay of 10 s. For ^{31}P MAS measurements, a saturation recovery pulse sequence was used. Saturation pulse train consisted of 20 $\pi/2$ for Mg-WH samples and 10 $\pi/2$ for Cu-WH samples pulses followed by 100 s delay. The $\pi/2$ excitation pulse was equal to 3.6 μs, 256 and 1024 scans were accumulated for Mg-WH and Cu-WH samples accordingly. $^1\text{H}\rightarrow^{31}\text{P}$ cross polarization magic angle spinning (CP MAS) measurements were performed with 4 ms for Mg-WH and 2 ms for Cu-WH samples CP contact time employing a 100 – 50% ramp on the ^{1}H channel, 1024 and 4096 scans were accumulated for Mg-WH and Cu-WH samples, respectively, using a repetition delay of 10 s. For ^{31}P – ^{31}P 1Q – 2Q experiments a standard pulse sequence was used, which employs a BABA (back-to-back) 2 rotor periods recoupling scheme [148]. The ^{31}P $\pi/2$ excitation pulse was equal to 3.57 μs, repetition delay was set to 250 s and 32 scans per 32 increments were accumulated. ^{1}H and ^{31}P spectra were referenced respectively to tetramethylsilane using adamantane (δ (^{1}H) = 1.85 ppm) and 85% H_3PO_4 using ADP (ammonium dihydrogen phosphate, $NH_4H_2PO_4$, δ (^{31}P) = 0.8 ppm). For Zn-WH samples, solid-state NMR experiments were carried out at 9.4 T on a Bruker Avance III HD 400 NMR spectrometer operating at 400.2 and 162.0 MHz for ^{1}H and ^{31}P, respectively, using a 4 mm double resonance CP MAS probe and 4 mm zirconia rotors.

Magnetic susceptibility data was obtained using a Quantum Design MPMS3 SQUID magnetometer. The data collection involved a temperature sweep ranging from 5 K to 300 K at a magnetic field strength of 100 Oe (0.01 T). Measurements were conducted in both zero-field cooled (ZFC) and field-cooled (FC) conditions. For ZFC data, the sample was initially cooled to 5 K in a 0 Oe field, and the moment was measured as the sample warmed to 300 K. Data collection was performed either in vibrating sample magnetometry mode with 5 mm scan lengths and 2 s averaging or in direct current (DC) scan mode with 30 mm scan lengths and 5 s averaging. All data were corrected for diamagnetic contributions using Pascal's Constants [149], and for sample shape and radial offset effects using the MPMS3 Sample Geometry Simulator [150].

The N_2 adsorption and desorption isotherms of samples were obtained at −196 °C by using Brunauer–Emmett–Teller (BET) analyzer TriStar II 3020, Micromeritics. Prior to the gas sorption measurements, all the samples were outgassed in N_2 atmosphere at 100 °C for 2 h.

For the ion release experiment, 0.6 g of WH powders were soaked in 30 mL of simulated body fluid (SBF), and the samples were prepared in triplicate. SBF solution was prepared according to the procedure reported by Kokubo et al. [151]. Samples were kept in closed containers in a shaker-incubator (BioSan ES-20/80) at 37 °C for 14 days under constant mixing at 250 rpm. Every day 1 mL of solution was taken from the sample for elemental analysis and was replaced with the same amount of fresh SBF solution to maintain constant volume.

The elemental composition of synthesized compounds, as well as ion release experiment samples, was determined using inductively coupled plasma optical emission spectrometry (ICP-OES) with a Perkin-Elmer Optima 7000 DV spectrometer.

The cell viability of Cu-WH and Mn-WH samples was assessed using an indirect method by collecting extract solutions, following the ISO 10993-5:2009 guidelines. *In Vitro* cytotoxicity studies on WH powders were carried out using the MC3T3-E1 cell line (preosteoblasts). In the extract test, 4,500 cells per well were seeded in a 96-well plate with 100 μL cell medium, composed of 89% Alpha Modified Eagle Medium (α-MEM), 10% fetal bovine serum (FBS) and 1% penicillin/streptomycin (P/S). The plates with the cells were incubated overnight at 37 °C, with 5% CO_2 (New Brunswick™ S41i CO2 Incubator Shaker, Eppendorf). Cu-WH powder sample was suspended in a fresh 5 mL of cell medium resulting in a concentration of 10 mg/mL. After 24 and 48 hours all of the solution was collected from samples and replaced with an additional 5 mL of fresh cell medium. The collected solution was then filtrated and subsequently used for dilution with fresh medium - extract to cell medium 1:10 and 1:100. Tested concentrations were 0.1 mg/mL and 0.01 mg/mL. Extract dilutions were immediately put onto the preincubated cells (100 μL for each well). Untreated cells were used as a positive control, and 5% dimethylsulfoxide (DMSO) solution in the medium was applied to cells as a negative control. There were six replicates for each sample and controls. Cell Counting Kit-8 (CCK-8) assay was used to assess the cytotoxicity of Cu-WH extracts. For both time points, samples were incubated for 24 h, and then 10 μL of CCK-8 solution was added to the cultivation media to each well and incubated for 1 h at 37 °C, with 5% CO_2. Absorption at 450 nm was measured using an Infinite M Nano microplate reader Tecan.

3. RESULTS AND DISCUSSION

3.1. Synthesis and thermal stability of Mg-WH

The XRD analysis confirmed the successful synthesis of single-phase Mg-WH (Fig. 7a). Rietveld refinement was used for further structural analysis. The calculated lattice parameters (a = 10.348 Å; c = 37.153 Å) were close to those reported in the literature for both synthetic and natural WH [119, 147], though the a parameter was slightly smaller while the c parameter was larger.

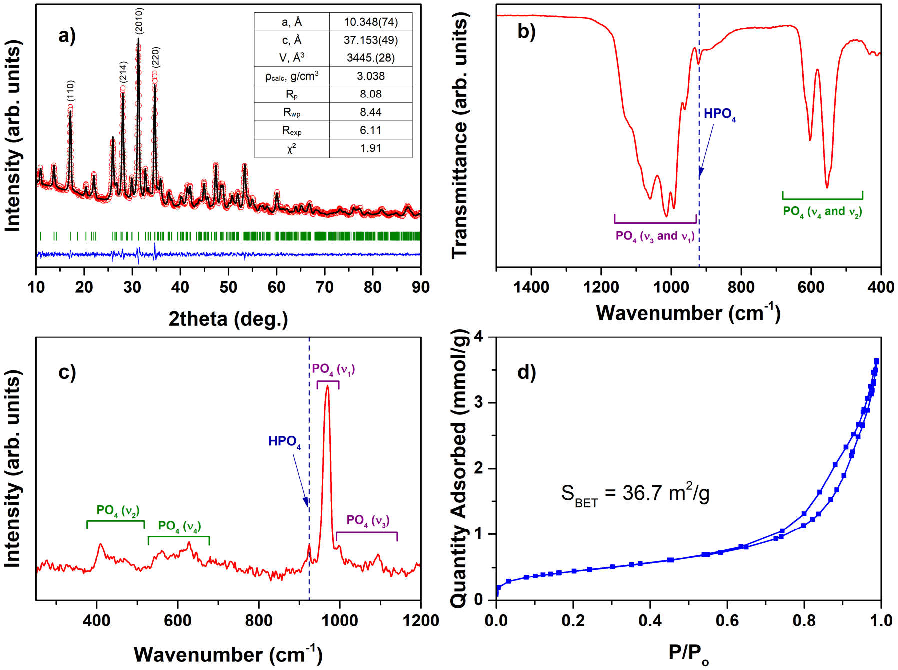

Fig. 7. Results of Rietveld refinement (a); FTIR spectrum (b); Raman spectrum (c); and N_2 absorption-desorption isotherm (d) of the as-prepared Mg-WH powder.

Vibrational spectroscopy is crucial for the reliable identification of WH structure as both Mg-WH and β-TCP are characterized by an identical powder XRD pattern. The most prominent difference between FTIR and Raman spectra of these two compounds is the band assigned to the HPO_4^{2-} group (920 cm^{-1}), which is present only in Mg-WH and absent in β-TCP [95]. Therefore, it can be assumed as a spectral marker for distinguishing these materials. The above-mentioned signal is clearly visible in both FTIR

(Fig. 7b) and Raman (Fig. 7c) spectra of our synthesized material, which confirms the formation of Mg-WH. Other observed bands are ascribed to different phosphate vibration modes; their positions are in good agreement with the data reported for WH in the literature [17, 152].

BET method was used to measure the surface area of as-prepared Mg-WH powder. The N_2 adsorption-desorption isotherm (Fig. 7d) was assigned to type IV with a type H3 hysteresis loop. The type H3 hysteresis loop is usually indicative to plate-like particle aggregates, which result in slit-shape pores [153]. The specific surface area (S_{BET}) was calculated to be 36.7 m^2/g.

SEM and TEM images (Fig. 8a-b) show that synthesized powder consists of agglomerated irregularly shaped plate-like particles of nanoscale dimensions. The size of the particles varies in the range of approximately 30–80 nm. Although it is known that Mg-WH is prone to form particles of distinctive polygonal shape [19, 21, 152], in our case, only a closer look allows us to see some well-defined hexagonally shaped particles. The EDX mapping (Fig. 8c-f) shows that all the elements are uniformly distributed in the sample. The Ca/Mg ratio was determined as 9:0.97, which is close to the theoretical chemical composition of Mg-WH.

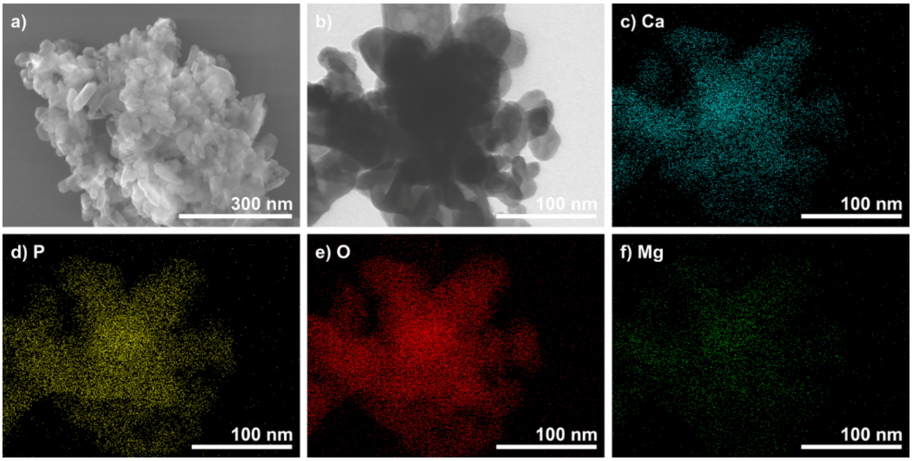

Fig. 8. SEM micrograph (a); TEM image (b); and EDX mapping (c-f) of the as-prepared Mg-WH powder.

Fig. 9 demonstrates the representative XRD patterns of Mg-WH samples annealed at different temperatures. There were no significant changes in the XRD patterns in terms of arising or disappearing of the reflection peaks up to 600 °C, the only observed trend was associated with the sharpening of the peaks. Evident changes were observed after annealing at 700 °C as two additional phases appeared. Both phases were identified as calcium pyrophosphate (CPP: $Ca_2P_2O_7$) polymorphs, namely, α-CPP and β-CPP. Although α-CPP is assumed to be a high-temperature polymorph [154], the simultaneous formation of both species could be explained by the Ostwald step rule [155]. After annealing at 800 °C the diffraction peaks of α-CPP disappeared, all newly observed reflections corresponded to β-CPP. This polymorph was observed in the range from 800 to 1100 °C along with the main WH and/or β-TCP phase. As the annealing temperature reached 1200 °C, β-CPP was replaced by α-CPP, which agrees well with the phase transition temperature between two polymorphs [154]. Surprisingly, after annealing at 1300 °C, the secondary phase was β-CPP again. It is worth noting that after annealing at 1300 °C the sample was partially melted and completely melted at 1400 °C. The observed melting point was lower as compared to the value of 1600 °C reported by Jang et al [95].

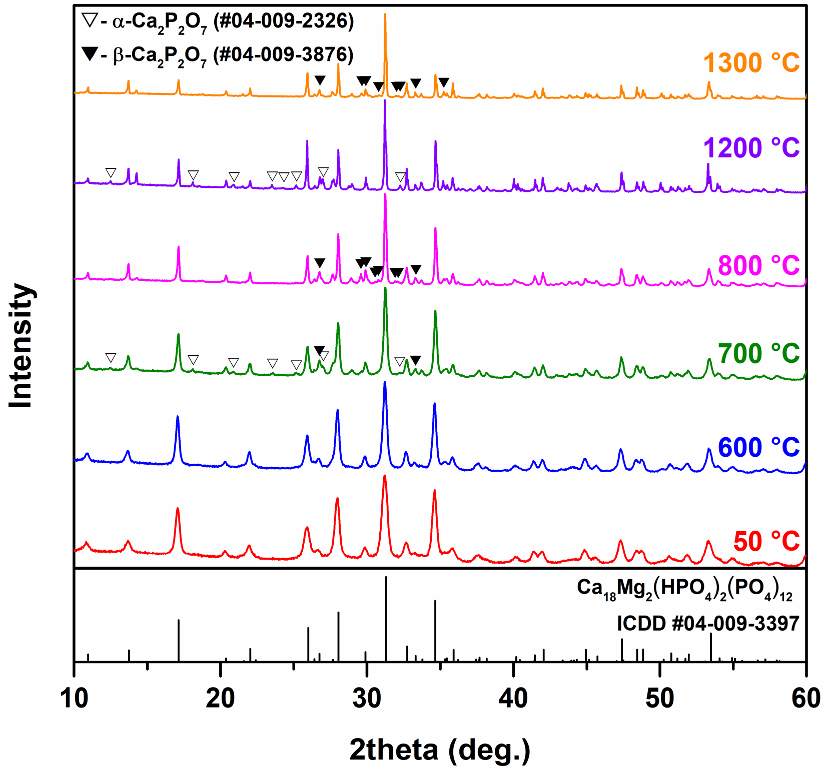

Fig. 9. XRD patterns of Mg-WH powders annealed at different temperatures.

Fig. 10 shows the FTIR and Raman spectra of Mg-WH powders annealed at representative temperatures. The FTIR spectra of β-TCP and Mg-WH are quite similar and show the same band multiplicity due to their very similar phosphate framework [147]; therefore, the phase transition from Mg-WH to β-TCP or co-existence of two materials cannot be clearly observed from the PO_4-related bands. However, the intensity of 920 cm^{-1} representing HPO_4^{2-} band increased with an increase of annealing temperature up to 600 °C because of the increased crystallinity of the material. After annealing at 700 °C the intensity started decreasing and the presence of this signal was indistinguishable after the treatment above 900 °C. The absorption bands corresponding to CPP can be observed after annealing above 700 °C. The most straightforward way to detect this material is to monitor the presence of absorption bands located at 726 and 754 cm^{-1}, which correspond to the P–O–P bond in β- and α-CPP, respectively [156].

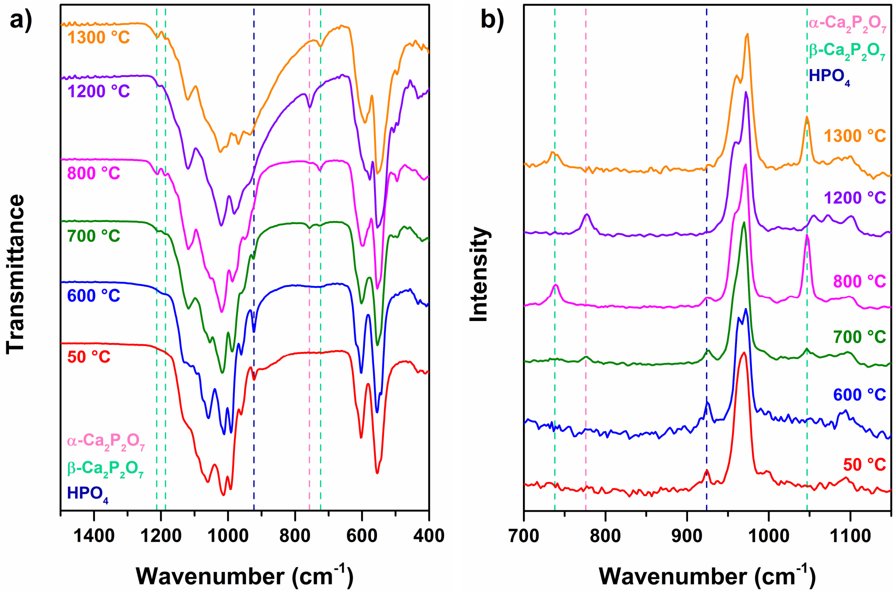

Fig. 10. FTIR (a) and Raman (excitation wavelength is 325 nm) (b) spectra of Mg-WH powders annealed at different temperatures.

In the Raman spectra of Mg-WH, the signal corresponding to HPO_4^{2-} group (926 cm^{-1}) does not overlap with the most intense peak of Mg-WH or β-TCP [157]. Raman spectroscopy data demonstrated the same trend as that shown by FTIR data (Fig. 10b). However, as compared to FTIR, HPO_4^{2-} band can be easily detected in a broader temperature range. Using a 532 nm excitation source, a very weak signal ascribed to HPO_4^{2-} is observed even in the sample annealed at 1200 °C (not shown) indicating the co-existence of Mg-WH and β-TCP in a wide temperature range. The signal completely vanishes only at 1300 °C.

^{1}H, ^{13}P MAS, and ^{1}H–^{31}P CP MAS spectra of Mg-WH samples are shown in Fig. 11. The spectra of as-prepared Mg-WH powder look similar to the previously reported for magnesium [158]. The ^{1}H spectrum consists mainly of a spectral line at 9.8 ppm, which is attributed to HPO_4^{2-} moiety in Mg-WH crystal structure. The ^{31}P MAS spectrum consists of the lines at 1.98, 1.14, and −0.50 ppm attributed to P(2), $HP(1)O_4^{2-}$ and P(3) moieties, respectively. In addition, a broad line at 0.47 ppm is observed, which is attributed to distorted phosphate moieties previously also detected for Zn-WH [159]. The line attributed to distorted phosphates decreases in intensity significantly upon annealing, thus the ^{31}P MAS spectrum looks more resolved. The line attributed to HPO_4^{2-} moiety in the ^{1}H MAS spectrum drops in intensity significantly at 700 °C, which shows that Mg-WH structure is disrupted. This line gradually vanishes upon increasing the annealing temperature to 1300 °C. In the ^{31}P MAS and ^{1}H–^{31}P CP MAS spectra corresponding to an annealing temperature of 700 °C, the spectral lines attributed to β-TCP and α-CPP (−8.01 and −10.32 ppm) start to emerge (Fig. 11). It is worth to note that CPP polymorphs have no signals in the range from 8 to −4 ppm, therefore all spectral changes in this region are attributed to the transformation of Mg-WH to Mg-substituted β-TCP [154].

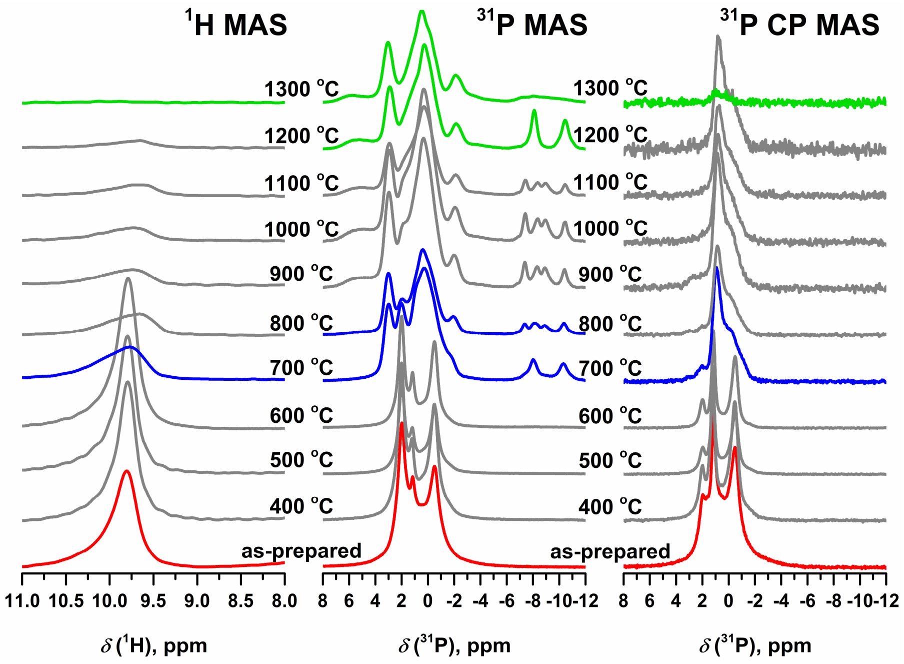

Fig. 11. ^{1}H MAS, ^{31}P MAS, and ^{1}H–^{31}P CP MAS spectra obtained for Mg-WH samples annealed at different temperatures. The spectra corresponding to the detected changes in crystal structures are colored.

3.2. Synthesis and characterization of Zn-WH prepared at ambient pressure

The XRD patterns of Zn-WH synthesized with different Ca/Zn ratios in the reaction mixture are illustrated in Fig. 12. Evidently, single-phase Zn-WH powders without a trace of crystalline byproducts were successfully synthesized when the Ca/Zn ratio in the reaction medium was in the range from 9 to 30. With higher Zn amounts, a secondary phase, scholzite [$CaZn_2(PO_4)_2 \cdot 2H_2O$] was formed, whereas with lower amounts of Zn, a mixture of WH and CDHA was obtained. These results demonstrate that a WH structure can be formed when the initial ratio of metal ions is different compared to stoichiometric.

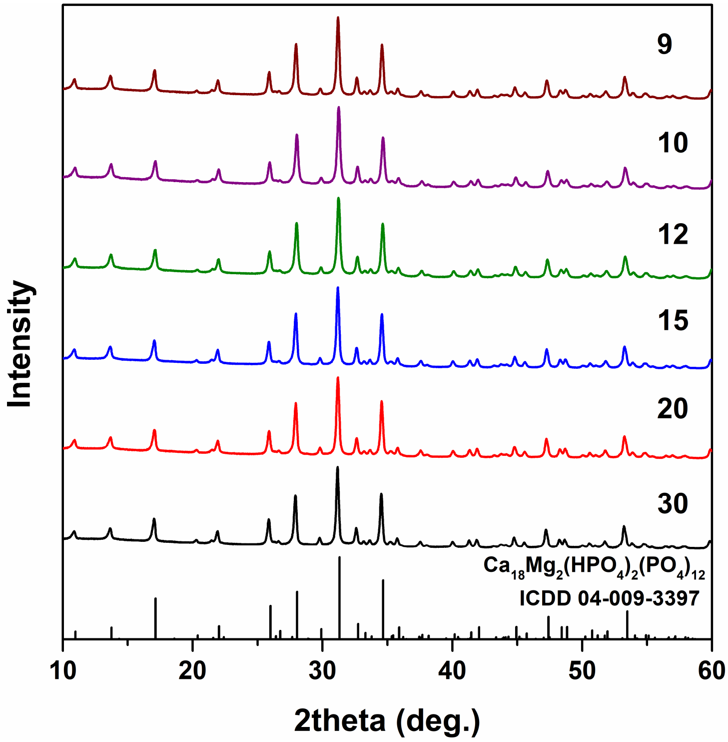

Fig. 12. XRD patterns of Zn-WH powders synthesized with different Ca/Zn ratios.

The FTIR spectra of Zn-WH are demonstrated in Fig. 13a. The band at 918 cm^{-1} representing the HPO_4^{2-} group is an indication of successful WH synthesis. The same band is also clearly visible in Raman spectra (Fig. 13b), confirming a successful Zn-WH synthesis. In both FTIR and Raman spectra there is no significant difference in the relative intensity of observed bands depending on the chemical composition of the samples.

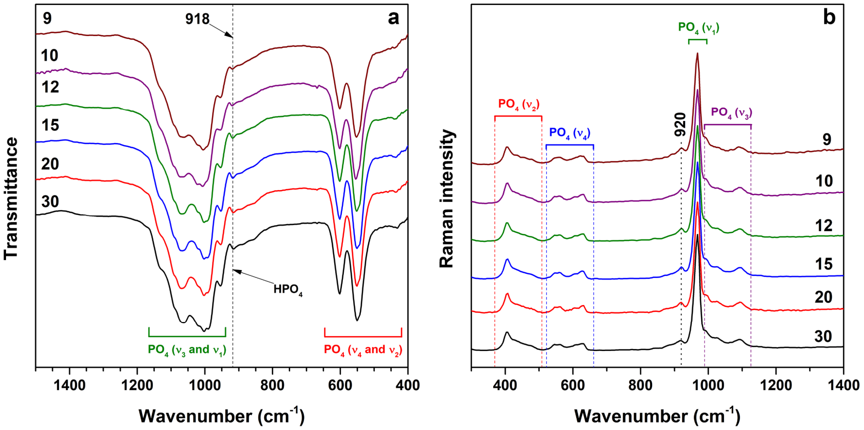

Fig. 13. FTIR (a) and Raman (b) spectra of Zn-WH powders synthesized with different Ca/Zn ratios.

The results of elemental analysis are summarized in Table 2. It is evident that with an increase of Zn concentration in the reaction mixture, Zn content in synthesized powders increased as well. The determined Ca/Zn ratio in the products is very close to the initial ratio of metals introduced in the reaction mixture. At the same time, the total metal ions to P ratio, regardless of starting ratios of metal ions, was maintained close to 1.428, which is the ratio in the ideal WH with the formula $Ca_{18}Zn_2(HPO_4)_2(PO_4)_{12}$.

Table 2. The results of ICP-OES analysis of Zn-WH powders.

Initial Ca/Zn molar ratio	Actual Ca/Zn molar ratio	Actual M/P molar ratio
30	29.7	1.41
20	18.5	1.41
15	14.5	1.40
12	12.2	1.41
10	9.85	1.40
9	8.94	1.41

The representative SEM micrographs of Zn-WH powders synthesized with Ca/Zn ratios of 20 and 10 are shown in Fig. 14. It is seen that powders synthesized with a Ca/Zn ratio of 20 (Fig. 14a) consist of mostly uniform and agglomerated particles. The size of individual particles varies in the range of approximately 60–80 nm. Despite the fact that synthesized powders were highly agglomerated, some particles have a very distinctive hexagonal shape (inset of Fig. 14a). An even higher degree of agglomeration was observed for the Zn-WH sample synthesized with a higher Zn amount (Fig. 14b) as the obtained particles were closely stacked on each other. It is interesting to note that the shape of the particles was found to be dependent on the chemical composition of the powders. With an increase in Zn content, the shape evolution of Zn-WH crystals from hexagonal to rhombohedral was observed.

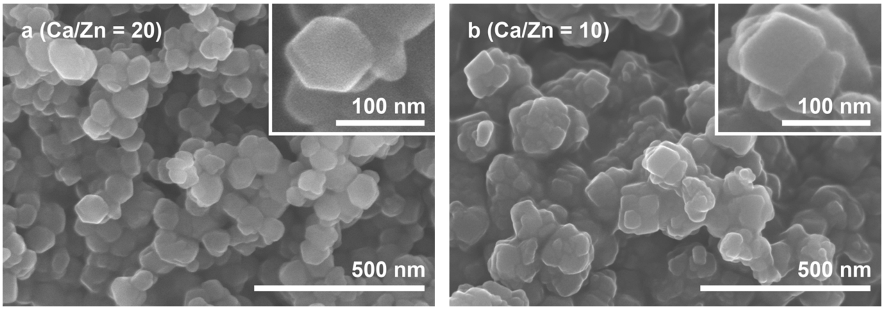

Fig. 14. SEM micrographs of Zn-WH powders synthesized with Ca/Zn ratios of 20 (a) and 10 (b).

In order to check the thermal stability of the synthesized Zn-WH powders, the samples were annealed at different temperatures. The XRD patterns and FTIR spectra of annealed Zn-WH powders are depicted in Fig. 15. No visible changes were noticed in neither XRD nor FTIR data after annealing at 500 °C. However, after heat treatment at higher temperatures, the appearance of additional peaks of CPP was observed. In FTIR spectra (Fig. 15b), 918 cm^{-1} band gradually disappeared, while at the same time, new absorption signals arose at 495, 726, 1187, and 1211 cm^{-1}. These bands confirm the formation of CPP [160].

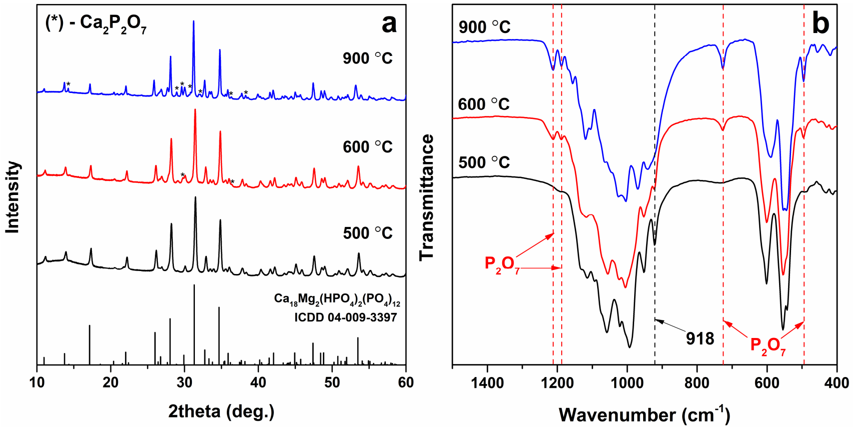

Fig. 15. XRD patterns (a) and FTIR spectra (b) of Zn-WH powders annealed at different temperatures (Ca/Zn ratio is 10).

3.3. Synthesis and characterization of Zn-WH prepared under hydrothermal conditions

The formation of Zn-WH *via* a dissolution–precipitation process under hydrothermal conditions was investigated in detail. The influence of medium pH, reaction time, temperature, and concentration of precursors on the formation of the single-phase material was studied. A series of powders were synthesized using different Ca/Zn ratios in the range from 6 to 30 (Fig. 16). In this case, phase-pure Zn-WH without noticeable neighboring crystalline phases was obtained when Ca/Zn ratio in the initial reaction mixture varied from 8 to 9. When Ca/Zn ratio was set as 10, a negligible amount of neighboring DCPA was obtained along with a major Zn-WH phase. With lower Zn content, the presence of this secondary phase can be clearly seen. FTIR and Raman spectra were also used for identification and clearly show an absorption band centered at 920 cm^{-1} attributed to the HPO_4^{2-} group.

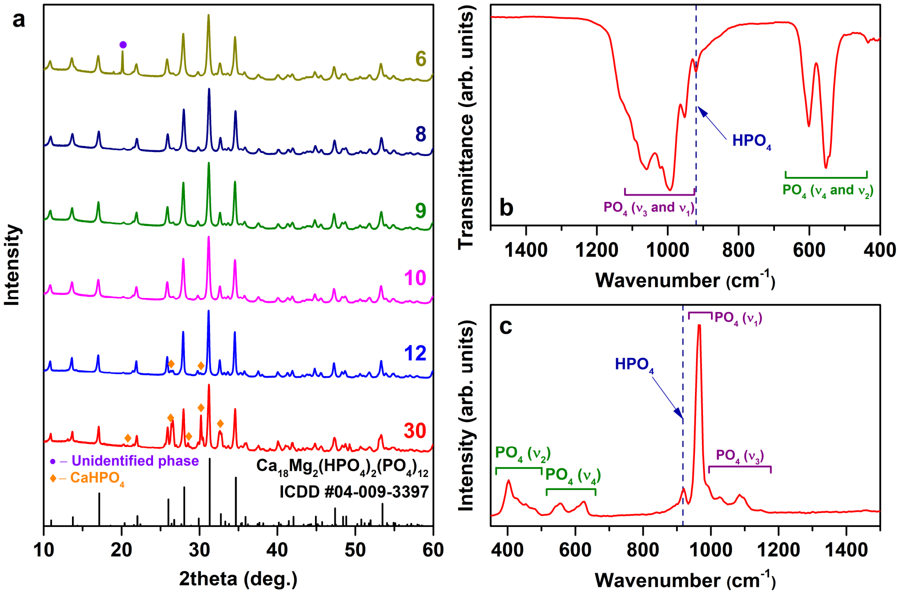

Fig. 16. XRD patterns of Zn-WH powders synthesized with different Ca/Zn initial ratios (a); FTIR spectrum (b) and Raman spectrum (c) of Zn-WH powder (Ca/Zn = 9).

Rietveld refinement was employed to calculate lattice parameters of synthesized Zn-WH. The values of lattice parameters were close to those reported for Mg-WH, particularly, parameter *a* was determined to be slightly smaller (10.342 Å) and parameter *c* slightly larger (37.114 Å) [119].

^{1}H MAS spectra of dried and wet Zn-WH samples are shown in Fig. 17. Wet sample stands for Zn-WH sample with adsorbed water from the atmosphere. There is a clear line at 9.8 ppm, which is attributed to protons from the HPO_4^{2-} moiety in the WH crystal structure. A similar assignment was found in the literature for Mg-WH [158, 161]. This observation agrees well with the results of vibrational spectroscopy and confirms the presence of the HPO_4^{2-} group in the structure of synthesized material. In addition, broad lines at 7 and 12 ppm show the presence of protonated low-crystalline or amorphous phosphates in the bulk and on the surface [162]. Lines at 5 and 1 ppm are attributed to bulk and surface water, respectively. The intensity of these lines increases for the wet sample, which corroborates the assignment. The width of the line attributed to the surface water reduces for the wet sample, which is due to the increased mobility.

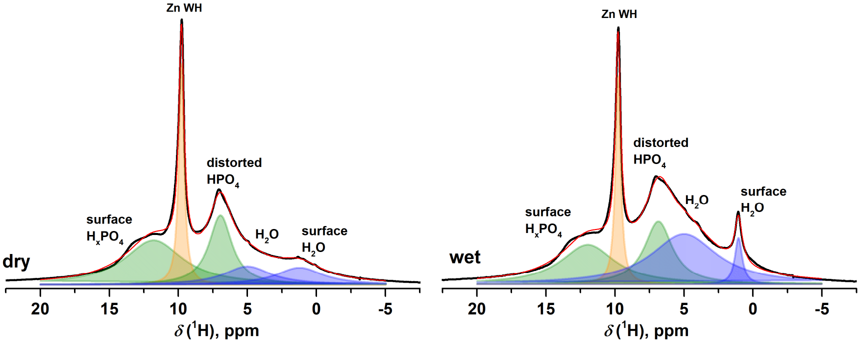

Fig. 17. ^{1}H MAS spectra and spectral assignment obtained for dried and wet Zn-WH samples. Lines attributed to Zn-WH are in orange, to other protonated phosphates in green and to water in blue, red line indicates the cumulative fit.

^{31}P MAS and ^{31}P CP MAS spectra obtained for Zn-WH sample are shown in Fig. 18. The ^{31}P MAS spectrum differs significantly compared to that of β-TCP [163], which is a clear evidence of the formation of WH structure. In the ^{31}P MAS spectrum there are three lines at 2, 1.4, and –0.5 ppm attributed to the P(2), $HP(1)O_4^{2-}$, and P(3) moieties in the Zn-WH crystal structure, respectively. Signal assignment was based on the comparison of crystal structures and assignments previously made for whitlockite-type β-TCP and $Ca_{10}Na(PO_4)_7$ [164, 165]. In the ^{31}P CP MAS spectrum, lines at 2, 1.4, and –0.5 ppm, which are attributed to Zn-WH are also present. The line at 1.4 ppm corresponding to the $HP(1)O_4^{2-}$ moiety is more enhanced in comparison to P(2) and P(3) due to the presence of proton in close vicinity. Lines observed at 4.5, 0.83, 0.3, and –1.4 ppm are attributed to protonated surface phosphates, amorphous phosphate phase, distorted HPO_4^{2-}, and phosphate in the hydrated layer, which are present as impurities [162, 166].

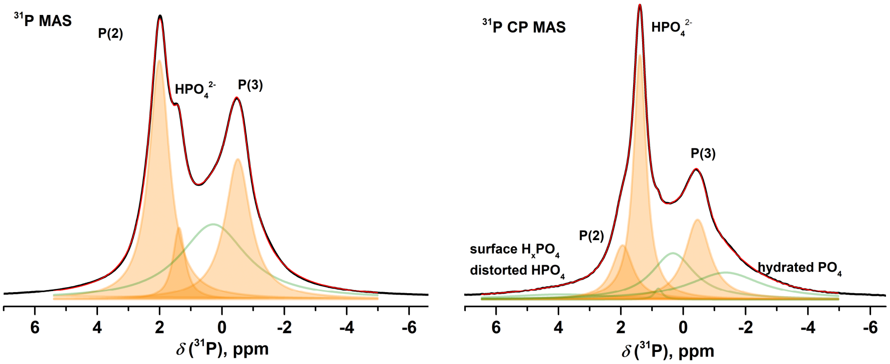

Fig. 18. ^{31}P MAS (left) and ^{1}H → ^{31}P MAS (right) spectra obtained for Zn-WH sample. Lines attributed to Zn-WH are in orange, to other phosphates in green and the cumulative fit is in red.

SEM micrographs of Zn-WH powders synthesized with different Ca/Zn ratios are given in Fig. 19a-c. When Ca/Zn ratio was 9, the powders consisted of rhombohedral plate-like particles of approximately 30–50 nm. However, some particles of undefined shape and comparable size were also present. The increase of Ca/Zn ratio to 12 and 30 preserved the shape of the particles but increased the size significantly up to 70–110 and 100–230 nm, respectively.

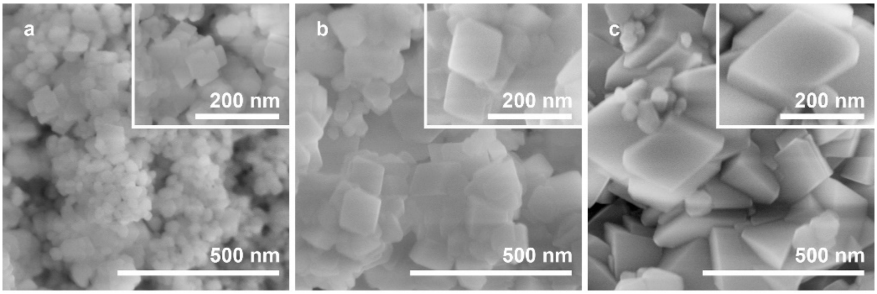

Fig. 19. SEM micrographs of Zn-WH synthesized with Ca/Zn molar ratio of 9 (a), 12 (b), and 30 (c).

The surface area of Zn-WH samples obtained with different total metal ion concentrations was measured. The N_2 adsorption-desorption isotherms of two representative samples can be classified as type IV with a hysteresis loop type H3 (not shown). The specific surface area calculated by the BET method (S_{BET}) was determined to be 24.6 and 35.0 m^2/g for the samples prepared with initial concentrations of 0.03 M and 0.12 M, respectively.

Ion release of Zn-WH was investigated and it was observed that concentration of Zn ions gradually increases with an increase of soaking time. The maximal concentration of Zn was determined to be 0.97 mg/L after 14 days.

3.4. Synthesis and characterization of Cu-WH

For the hydrothermal synthesis of Cu-WH, the pH of the reaction mixture, reaction time, temperature, and overall concentration of starting materials were the parameters investigated. We were also interested if the variable ratio of metal cations in the initial reaction mixture could lead to the formation of Cu-WH with a variable metal content. Fig. 20a shows the XRD patterns of the products obtained using different initial Ca/Cu ratios. The results showed 2 different trends. The Cu-rich reaction mixture (Ca/Cu < 9) resulted in the formation of the secondary $Ca_3Cu_3(PO_4)_4$ phase. In the case of Cu-lean reactions (Ca/Cu > 9), the formation of HAP along with the Cu-WH was observed. Therefore, the synthesis of Cu-WH with variable metal content is impossible under selected conditions. FTIR (Fig. 20b) and Raman (Fig. 20c) spectroscopy were employed in parallel and confirmed the successful synthesis of Cu-WH when the Ca/Cu = 9.

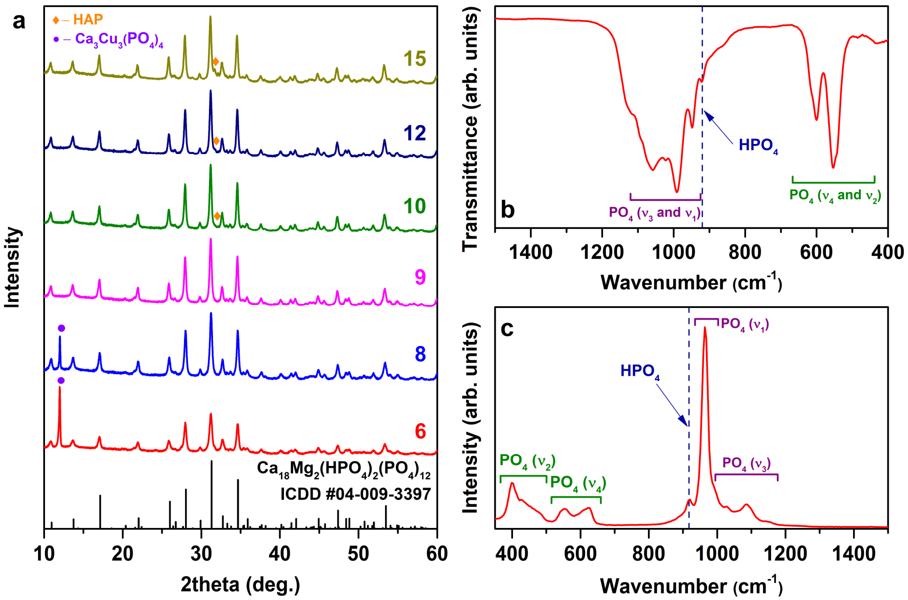

Fig. 20. XRD patterns of Cu-WH powders synthesized with different Ca/Cu ratios (a); FTIR spectrum (b) and Raman spectrum (c) of Cu-WH powder (Ca/Cu = 9).

Rietveld refinement was used to calculate cell parameters of the synthesized Cu-WH. The *a* parameter was calculated as 10.330 Å, while the *c* parameter was 37.077 Å. These values are slightly lower compared to those previously reported for Mg-WH [158, 167], Zn-WH [159], and Cu-WH [135].

The ^{1}H MAS spectra obtained for Cu-WH sample before and after annealing at 500 °C are shown in Fig. 21. The ^{1}H spectrum clearly contains a major spectral line at 9.9 ppm, which is attributed to the HPO_4^{2-} moiety in the Cu-WH crystal structure. Additional lines attributed to surface H_xPO_4 and distorted HPO_4 moieties are seen at 12.3 ppm and 6.2 ppm, respectively [162]. Water in the form of bulk and surface species is detected at 4.5–1.5 ppm.

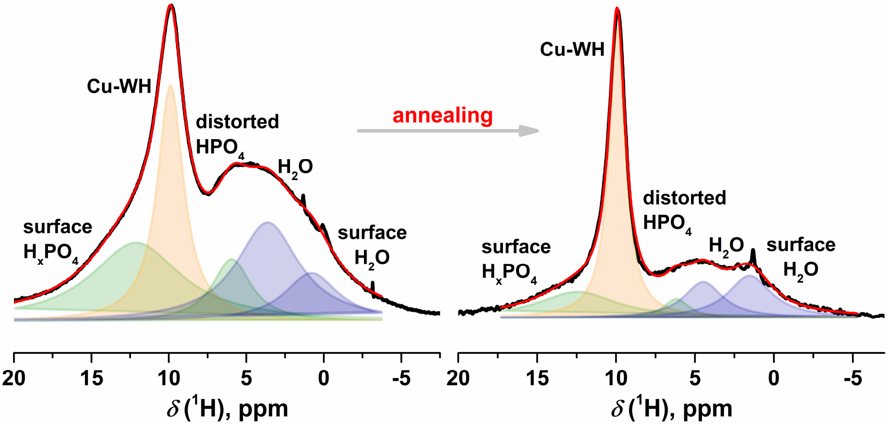

Fig. 21. ^{1}H MAS spectra of Cu-WH prior to and after annealing at 500 °C. Spectral components attributed to Cu-WH are shown in orange, water – blue, additional phosphate species in green.

Fig. 22 depicts the ^{31}P MAS and ^{1}H–^{31}P CP MAS spectra of Cu-WH before and after annealing. Similarly to ^{1}H data, the lines in ^{31}P data after annealing feature narrower linewidths, indicating the formation of Cu-WH phase of higher crystallinity. The ^{31}P MAS spectrum after annealing consists of the lines at 2.2, 1.3, and −0.5 attributed to P(2), $HP(1)O_4^{2-}$, and P(3) moieties, which are typical in the WH structure [159, 167], and the line at 0.4 ppm, which is an impurity phosphate phase. One more remark has to be made that in comparison to Zn- and Mg-WH, Cu-WH possesses significantly broader lines due to the paramagnetic nature of the Cu^{2+} environment. In the ^{1}H–^{31}P CP MAS spectra, the line assigned to HPO_4^{2-} is significantly more enhanced, which corroborates our assignment as the proton is in close vicinity. The line at −2.8 ppm is assigned to a side phase of the hydrated PO_4, which vanishes after annealing.

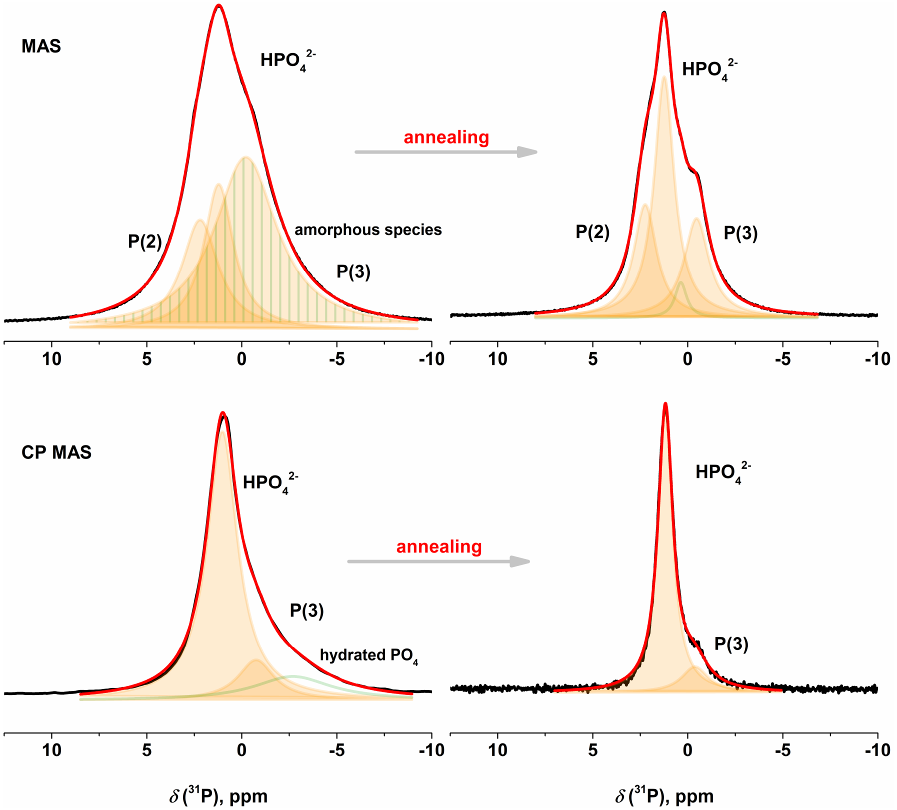

Fig. 22. ^{31}P MAS (upper) and ^{1}H–^{31}P CP MAS spectra of Cu-WH prior to and after annealing. Spectral components attributed to Cu-WH are shown in orange, additional phosphate phases in green.

The results of elemental analysis are summarized in Table 3. It is evident that experimentally obtained values agree well with the theoretical ones. The Ca/Cu and (Ca+Cu)/P molar ratios were determined to be very close to the theoretical values with the former being only slightly lower.

Table 3. The results of ICP-OES analysis of Cu-WH (pH = 6.4, T = 200 °C, t = 3 h, Ca/Cu = 9).

Sample	Determined Ca/Cu molar ratio	Determined (Ca+Cu)/P molar ratio	Theoretical Ca/Cu molar ratio	Theoretical (Ca+Cu)/P molar ratio
Cu-WH	8.79	1.39	9.00	1.43

Morphological features of Cu-WH were investigated by SEM and TEM. SEM images of Cu-WH powders synthesized using different concentrations of starting materials are shown in Fig. 23a,b. It is seen that the variation of the concentration had only a limited effect on the morphology of the material. The sample synthesized using a 3-fold higher concentration consisted of slightly smaller particles (Fig. 23b) compared to those observed using standard synthetic conditions (Fig. 23a). Both samples were composed of agglomerated particles of nanoscale dimensions. While most of the particles possessed an irregular shape, some of the particles were well-defined rhombohedral and hexagonal plate-like shape. The energy dispersive X-ray spectroscopy (EDX) mapping (Fig. 23e-h) indicated a homogeneous distribution of the constituting elements.

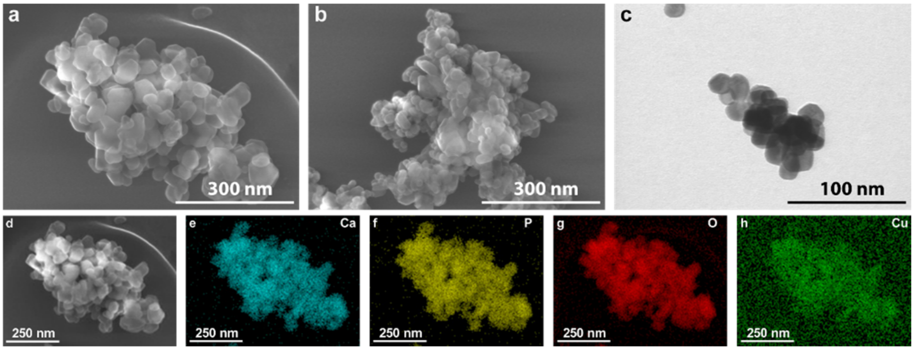

Fig. 23. SEM images of Cu-WH powder synthesized when initial concentration of metal ions was 0.08 M (a) and 0.24 M (b); TEM image of Cu-WH synthesized at concentration of 0.08 M (c); SEM image (d) and EDX mapping (e-h) of Cu-WH (pH = 6.4, T = 200 °C, t = 3 h, Ca/Cu = 9).

In order to investigate the structural changes and the phase evolution upon annealing, the as-prepared Cu-WH powders were annealed at different temperatures in the 500–1000 °C range with a step of 100 °C and XRD patterns of obtained samples are presented in Fig. 24a. The appearance of the secondary crystalline phase starts after annealing at 600 °C. The start of the thermal decomposition of Cu-WH was found to be around 100 °C lower compared to that of Mg-WH [167], but in good agreement with that of Zn-WH [152]. The thermal treatment at 800 °C resulted in the formation of both α- and β-CPP, while only β-CPP was detected in the samples annealed at 900 °C and 1000 °C. FTIR spectroscopy (Fig. 24b) was employed in parallel to the XRD analysis and confirms the observed structural changes.

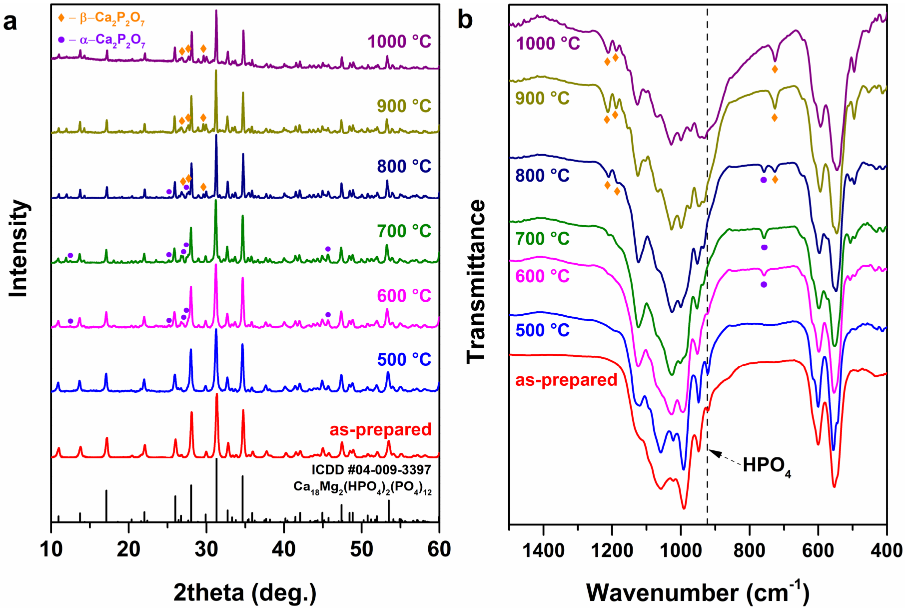

Fig. 24. XRD patterns (a) and FTIR spectra (b) of Cu-WH powders annealed at different temperatures.

During the ion release experiment, the concentration of Cu^{2+} ions linearly increased during the soaking. It should be underlined that a drastic release of Cu^{2+} was observed just after 1 day. The possible reason for such a behavior is the release of soluble trapped Cu-containing species. The maximal concentration of Cu^{2+} ions after 14 days was determined as 25.8 mg/L. Compared to Zn-WH prepared and treated under similar conditions, the amount of Cu^{2+} ions was observed to be around 25 times higher than that of Zn^{2+} [159].

The cell viability study revealed that none of the tested Cu-WH extract dilutions demonstrated cytotoxic effects after 48 h sample incubation, as these experiments showed cell viability exceeding 70% (Fig. 25). Lower cell viability (73.64 ± 9.48%) was noted for Cu-WH extracts with a concentration of 0.1 mg/mL after 24 h incubation period with a slight increase at 48-hour incubation timepoint. A similar trend of viability increase after 48 h was observed for the extract dilution with a lower concentration of 0.01 mg/mL. Decreased cell viability in the first 24 hours could be explained by the rapid Cu^{2+} ion release in the medium.

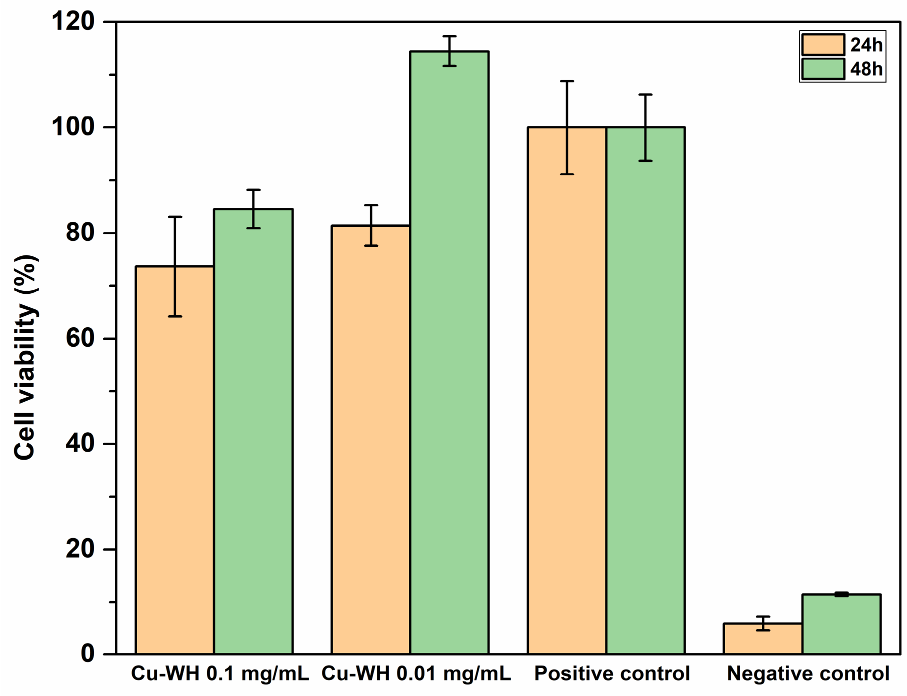

Fig. 25. Cu-WH extract effect on MC3T3-E1 cell proliferation.

3.5. Synthesis and characterization of Mn-WH

The XRD data showed a successful synthesis of single-phase Mn-WH (Fig. 26a). Further structural analysis was performed employing Rietveld refinement. The calculated lattice parameters were $a = 10.358(4)$ Å and $c = 37.077(7)$ Å. These values are similar to those previously reported in the literature for both Mn-WH [8] and Mg-WH [119, 147, 167], though both parameters are slightly smaller. The distinctive HPO_4^{2-} band is clearly visible in both FTIR (Fig. 26b) and Raman (Fig. 26c) spectra of the obtained material at 920 cm^{-1}. Therefore, a successful synthesis of Mn-WH can be confirmed. The positions of other absorption bands can be attributed to the vibrational modes of phosphates characteristic of WH compounds [167, 168].

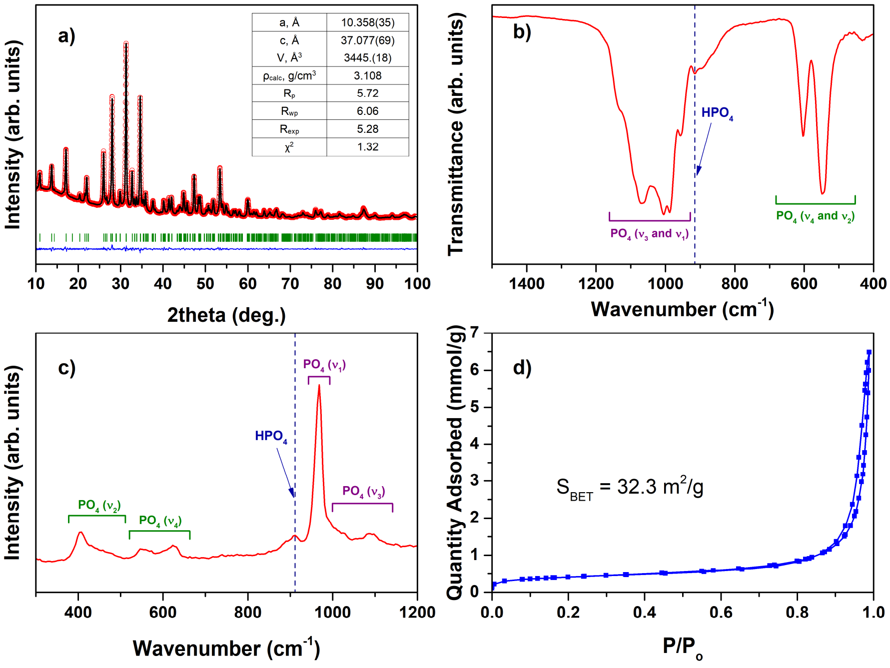

Fig. 26. Results of Rietveld refinement (a); FTIR spectrum (b); Raman spectrum (c); and N_2 absorption-desorption isotherm (d) of the as-prepared Mn-WH powder.

The BET method was used to measure the surface area of the as-prepared Mn-WH powder. The N_2 adsorption-desorption isotherm (Fig. 26d) was assigned to type IV with a type H3 hysteresis loop. The specific surface area (S_{BET}) was calculated to be 32.3 m^2/g.

To determine the chemical composition of the synthesized Mn-WH powder, the elemental analysis was performed by means of ICP-OES (Table 4). Experimentally determined Ca/Mn and (Ca+Mn)/P molar ratios were in good agreement with theoretical values, which reflects the reliability of the proposed synthetic approach.

Table 4. The results of ICP-OES analysis of Mn-WH powder.

Determined Ca/Mn molar ratio	**Determined (Ca+Mn)/P molar ratio**	**Theoretical Ca/Mn molar ratio**	**Theoretical (Ca+Mn)/P molar ratio**
8.84	1.40	9.00	1.43

The SEM image taken under lower magnification (Fig. 27a) demonstrates the homogeneity and uniformity of the obtained powder. A closer look

(Fig. 27b) reveals that synthesized powder is composed of agglomerated irregularly shaped particles. The individual particles are nanoscale, with sizes varying in the range of approximately 30–60 nm. Hexagonal or rhombohedral particle shape usually associated with materials having WH structure [19, 21, 152] was barely visible in the investigated sample, with only a few particles with a visibly expressed hexagonal shape.

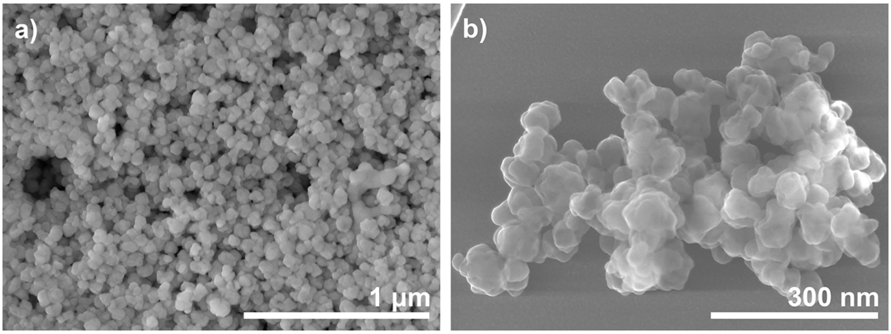

Fig. 27. SEM micrographs (a, b) of the as-prepared Mn-WH powder.

The obtained Mn-WH sample was further investigated by XPS analysis, acquiring the low-resolution survey and high-resolution spectra (Fig. 28). Survey spectra (Fig. 28a) revealed that powder was composed of C, Mn, Ca, O, P, and traces of Si (measurement contamination). Manganese oxidation state was investigated by measuring and modeling Mn $2p_{3/2}$ (Fig. 28b) and Mn 3s (Fig. 28c) spectra. It is known that Mn 2p spectra modeling might be very inaccurate due to small differences in chemical shifts between different manganese oxidation states. However, distinctive Mn^{2+} state satellite peaks were observed in the analyzed powder; therefore, the $Mn^{2+/3+}$ model was most likely. Using this model, it was determined that Mn^{2+} amounted to 89%, and the rest of Mn ions were in the Mn^{3+} oxidation state. The observed Mn 3s spectra peak multiplet splitting values (ΔBE) were approximately 5.8 eV. The Mn 3s peak energy difference usually correlates with the oxidation state of manganese, having a ΔBE of approximately 6.1 eV for Mn^{2+} and 5.5 eV for Mn^{3+} [169]. The measured Mn 3s and Mn 2p values in this work suggested that Mn was a mix of Mn^{2+}/Mn^{3+} with a dominant Mn^{2+} state. To the best of our knowledge, there are no reports on the ability of trivalent ions to stabilize WH; therefore, it can be concluded that Mn^{3+} species observed by XPS analysis are associated with surface defects.

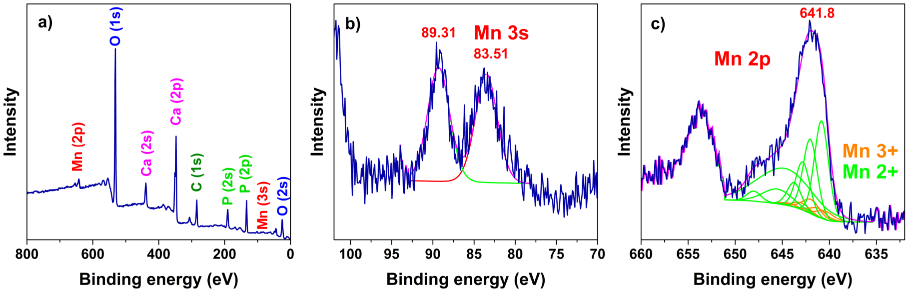

Fig. 28. Survey XPS spectra of Mn-WH (a), high-resolution XPS spectra and fitting results of Mn 3s (b) and Mn 2p (c) peaks.

The magnetic measurement data obtained for Mn-WH are given in Fig. 29. The magnetic data demonstrates an expected paramagnetic behavior as shown by the $1/\chi$-vs-T graph (Fig. 29a). The data shows an intercept at the origin, which is typical for paramagnetic materials, and a linear relationship between $1/\chi$ and T over the measured temperature range, demonstrating that this material follows Curie's Law. There was no difference depending on the measurement mode (FC or ZFC). The effective magnetic moment, $\mu_{\mathrm{eff}} = (8C)^{1/2}$, was calculated as 6.00 μ_B (μ_B, Bohr magneton) per Mn^{2+} ion. This value is close to the theoretical one, 5.92 μ_B, expected for the free Mn^{2+} ion. These data confirm that Mn ions in the synthesized material are in a +2 oxidation state. The M vs H curves at 5 K and 300 K also show an expected paramagnetic behavior (Fig. 29b).

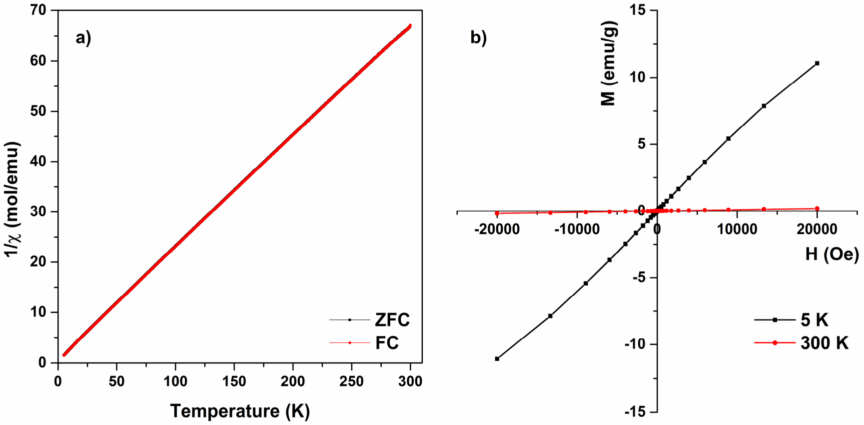

Fig. 29. Inverse magnetic susceptibility of Mn-WH vs T (a); M vs H curves of Mn-WH at 5 K and 300 K (b).

The results of cell viability revealed that none of the tested Mn-WH extract dilutions demonstrated cytotoxic effects after 24 h incubation; in all cases the observed cell viability was above 70% (Fig. 31). The lowest cell viability was determined for the highest Mn-WH concentration (1 mg/mL). The observed trend indicates that the cell viability decreases for all samples after the incubation for 48 h. However, the value does not drop below 70% with an exception for the dilution with 1 mg/mL of Mn-WH.

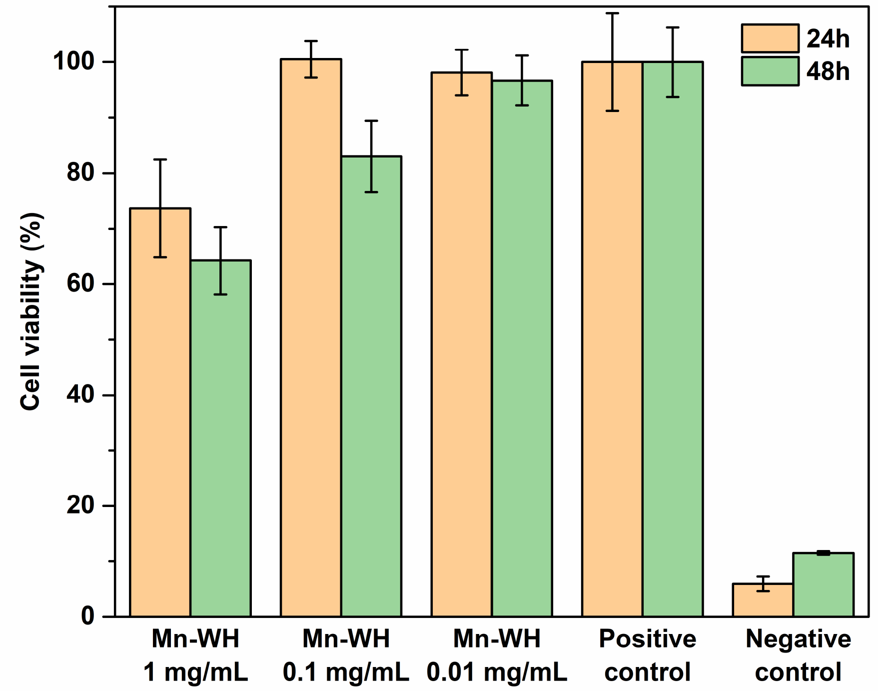

Fig. 30. Mn-WH extract effect on MC3T3-E1 cell proliferation.

CONCLUSIONS

1. While investigating thermally-induced decomposition of Mg-WH it was found that the degradation of Mg-WH upon annealing and its conversion to Mg-substituted β-TCP and CPP starts at 700 °C and occurs gradually with an increase in annealing temperature. The presence of negligible amount of HPO_4^{2-}, which belongs exclusively to the Mg-WH structure, was observed up to 1200 °C suggesting the co-existence of both Mg-WH and Mg-substituted β-TCP phases in a wide temperature range. Whereas all techniques were found to be suitable for the observation of the appearance of CPP phase, the ^{31}P NMR was found to be the most straightforward technique for the detection of Mg-WH to Mg-substituted β-TCP structural transformation.
2. Zn-WH powders with variable metal content have been synthesized by the low-temperature dissolution–precipitation process for the first time. Controllable chemical composition of the synthesis products was achieved by changing the initial Ca/Zn molar ratio in the reaction mixture. Regardless of the final Ca/Zn ratio in the obtained products, the total metal ions to phosphorus ratio was determined to be nearly constant, indicating the formation of a whitlockite structure with stoichiometric and Zn-lean composition. The morphology of the powders can be controlled by varying the metal-ion ratio in the reaction mixture. All synthesized compounds were determined to be thermally unstable at 600 °C and decomposed upon heat treatment with the formation of β-TCP and CPP.
3. Zn-WH was successfully synthesized *via* the dissolution-precipitation process under hydrothermal conditions. It was demonstrated that single-phase Zn-WH can be obtained in a very short period of time – 1 h. Variation of chemical composition in terms of Ca/Zn ratio was determined to be possible only within a narrow range. FTIR, Raman and ^{1}H solid-state NMR confirmed the presence of HPO_4^{2-} group in the crystal structure. ^{31}P NMR study confirmed the presence of three inequivalent phosphorus atoms, whereas only one PO_4 tetrahedron was determined to be protonated. The size and shape of the particles can be controlled by concentration of precursors as well as by initial Ca/Zn ratio in the reaction mixture.
4. Cu-WH powders were successfully synthesized by the dissolution-precipitation method under hydrothermal conditions. The optimal pH range was found to be very narrow, being from 6.4 to 6.5. Variation of the chemical composition in terms of Ca/Cu ratio was impossible under

selected synthesis conditions, and the initial Ca/Cu ratio of 9 was determined as optimal. Whereas XRD and vibrational spectroscopy did not indicate the presence of any impurity phase in the as-prepared Cu-WH powders, the NMR studies revealed the co-existence of amorphous/distorted phosphate species. The Cu^{2+} release from Cu-WH powder monitored for 14 days showed a gradually growing trend with a drastic release during the first day of soaking. The study on thermal stability revealed that Cu-WH is thermally unstable and gradually decomposes to Cu-substituted β-TCP and CPP upon annealing above 600 °C. The cell viability study revealed that none of the tested Cu-WH extract dilutions demonstrated cytotoxic effects, as all experiments demonstrated cell viability exceeding 70%.

5. Mn-WH was synthesized employing the dissolution-precipitation process at low temperature and ambient pressure. The results of Rietveld refinement indicated that the synthesized material is a single-phase Mn-WH. The combination of XRD, XPS and magnetic studies confirmed the presence of Mn ions in the +2 oxidation state, while temperature-dependent magnetic measurements revealed a paramagnetic behavior of Mn-WH down to 5 K temperature. The material did not exhibit a toxic effect on MC3T3-E1 cells after the incubation period of 24 h for the concentration range of 0.01–1 mg/L; however, the cell viability decreased after a longer incubation.

REFERENCES

[1] W. Habraken, P. Habibovic, M. Epple, M. Bohner, Calcium phosphates in biomedical applications: materials for the future?, *Materials Today*, 19(2), 2016, 69-87,
(https://doi.org/10.1016/j.mattod.2015.10.008).

[2] H. Cheng, R. Chabok, X. Guan, A. Chawla, Y. Li, A. Khademhosseini, H.L. Jang, Synergistic interplay between the two major bone minerals, hydroxyapatite and whitlockite nanoparticles, for osteogenic differentiation of mesenchymal stem cells, *Acta Biomaterialia*, 69(1), 2018, 342-351,
(https://doi.org/10.1016/j.actbio.2018.01.016).

[3] H.L. Jang, G. Bin Zheng, J. Park, H. Kim, H.-R. Baek, H. Kyoung Lee, K. Lee, H. Nam Han, C.-K. Lee, N. S Hwang, J.H. Lee, K.T. Nam, In Vitro and In Vivo Evaluation of Whitlockite Biocompatibility: Comparative Study with Hydroxyapatite and β-Tricalcium Phosphate, *Advanced healthcare materials*, 5(1), 2015, 128-136,
(https://doi.org/10.1002/adhm.201400824).

[4] N.V. Bulina, O.B. Vinokurova, I.Y. Prosanov, A.M. Vorobyev, K.B. Gerasimov, I.A. Borodulina, A. Pryadko, V.V. Botvin, M.A. Surmeneva, R.A. Surmenev, Mechanochemical synthesis of strontium- and magnesium-substituted and cosubstituted hydroxyapatite powders for a variety of biomedical applications, *Ceramics International*, 48(23, Part A), 2022, 35217-35226,
(https://doi.org/10.1016/j.ceramint.2022.08.123).

[5] V.H.M. Doan, D.D. Vu, S. Mondal, T.M.T. Vo, C.D. Ly, V.T. Nguyen, S. Park, J. Choi, T.P. Nguyen, B. Lee, J. Oh, Yb-Gd Codoped Hydroxyapatite as a Potential Contrast Agent for Tumor-Targeted Biomedical Applications, *ACS Biomater Sci Eng*, 9(8), 2023, 4607-4618,
(https://doi.org/10.1021/acsbiomaterials.3c00383).

[6] R.D. Shannon, Revised effective ionic radii and systematic studies of interatomic distances in halides and chalcogenides, *Acta Crystallographica Section A*, 32(5), 1976, 751-767,
(https://doi.org/10.1107/S0567739476001551).

[7] A.A. Belik, F. Izumi, S.Y. Stefanovich, B.I. Lazoryak, K. Oikawa, Chemical and Structural Properties of a Whitlockite-like Phosphate, $Ca_9FeD(PO_4)_7$, *Chemistry of Materials*, 14(9), 2002, 3937-3945,
(https://doi.org/10.1021/cm020411+).

[8] E. Kostiner, J.R. Rea, The crystal structure of manganese-whitlockite, $Ca_{18}Mn_2H_2(PO_4)_{14}$, *Acta Crystallographica Section B*, 32(1), 1976, 250-253,
(https://doi.org/10.1107/S0567740876002690).

[9] P. Habibovic, J.E. Barralet, Bioinorganics and biomaterials: Bone repair, *Acta Biomaterialia*, 7(8), 2011, 3013-3026,
(https://doi.org/10.1016/j.actbio.2011.03.027).

[10] S. Sprio, L. Preti, M. Montesi, S. Panseri, A. Adamiano, A. Vandini, N.M. Pugno, A. Tampieri, Surface Phenomena Enhancing the Antibacterial and Osteogenic Ability of Nanocrystalline Hydroxyapatite, Activated by Multiple-Ion Doping, *ACS Biomater Sci Eng*, 5(11), 2019, 5947-5959,
(https://doi.org/10.1021/acsbiomaterials.9b00893).

[11] Y. Su, K. Wang, J. Gao, Y. Yang, Y.-X. Qin, Y. Zheng, D. Zhu, Enhanced cytocompatibility and antibacterial property of zinc phosphate coating on biodegradable zinc materials, *Acta Biomaterialia*, 98, 2019, 174-185,

(https://doi.org/10.1016/j.actbio.2019.03.055).

[12] A. Jacobs, G. Renaudin, C. Forestier, J.-M. Nedelec, S. Descamps, Biological properties of copper-doped biomaterials for orthopedic applications: A review of antibacterial, angiogenic and osteogenic aspects, *Acta Biomaterialia*, 117, 2020, 21-39,
(https://doi.org/10.1016/j.actbio.2020.09.044).

[13] S.S. Syamchand, G. Sony, Multifunctional hydroxyapatite nanoparticles for drug delivery and multimodal molecular imaging, *Microchimica Acta*, 182(9), 2015, 1567-1589,
(https://doi.org/10.1007/s00604-015-1504-x).

[14] L.-H. Fu, Y.-R. Hu, C. Qi, T. He, S. Jiang, C. Jiang, J. He, J. Qu, J. Lin, P. Huang, Biodegradable Manganese-Doped Calcium Phosphate Nanotheranostics for Traceable Cascade Reaction-Enhanced Anti-Tumor Therapy, *ACS Nano*, 13(12), 2019, 13985-13994,
(https://doi.org/10.1021/acsnano.9b05836).

[15] Q. Nawaz, M.A.U. Rehman, A. Burkovski, J. Schmidt, A.M. Beltrán, A. Shahid, N.K. Alber, W. Peukert, A.R. Boccaccini, Synthesis and characterization of manganese containing mesoporous bioactive glass nanoparticles for biomedical applications, *Journal of Materials Science: Materials in Medicine*, 29(5), 2018, 64,
(https://doi.org/10.1007/s10856-018-6070-4).

[16] M.B. Pabbruwe, O.C. Standard, C.C. Sorrell, C.R. Howlett, Bone formation within alumina tubes: effect of calcium, manganese, and chromium dopants, *Biomaterials*, 25(20), 2004, 4901-4910,
(https://doi.org/10.1016/j.biomaterials.2004.01.005).

[17] C. Wang, K.-J. Jeong, H.J. Park, M. Lee, S.-C. Ryu, D.Y. Hwang, K.H. Nam, I.H. Han, J. Lee, Synthesis and formation mechanism of bone mineral, whitlockite nanocrystals in tri-solvent system, *J. Colloid Interface Sci.*, 569, 2020, 1-11,
(https://doi.org/10.1016/j.jcis.2020.02.072).

[18] A. Afonina, A. Kizalaite, A. Zarkov, A. Drabavicius, T. Goto, T. Sekino, A. Kareiva, I. Grigoraviciute-Puroniene, Synthesis of whitlockite nanopowders with different magnesium content, *Ceramics International*, 48(21), 2022, 32125-32130,
(https://doi.org/10.1016/j.ceramint.2022.07.152).

[19] H.L. Jang, H.K. Lee, K. Jin, H.-Y. Ahn, H.-E. Lee, K.T. Nam, Phase transformation from hydroxyapatite to the secondary bone mineral, whitlockite, *Journal of Materials Chemistry B*, 3(7), 2015, 1342-1349,
(https://doi.org/10.1039/C4TB01793E).

[20] W.-B. Lee, C. Wang, J.-H. Lee, K.-J. Jeong, Y.-S. Jang, J.-Y. Park, M.H. Ryu, U.-K. Kim, J. Lee, D.-S. Hwang, Whitlockite Granules on Bone Regeneration in Defect of Rat Calvaria, *ACS Applied Bio Materials*, 3(11), 2020, 7762-7768,
(https://doi.org/10.1021/acsabm.0c00960).

[21] X. Guo, X. Liu, H. Gao, X. Shi, N. Zhao, Y. Wang, Hydrothermal growth of whitlockite coating on β-tricalcium phosphate surfaces for enhancing bone repair potential, *Journal of Materials Science & Technology*, 34(6), 2018, 1054-1059,
(https://doi.org/10.1016/j.jmst.2017.07.009).

[22] J. Jeong, J.H. Shim, B.M. Koo, Y.B. Choy, C.Y. Heo, Synergistic Effect of Whitlockite Scaffolds Combined with Alendronate to Promote Bone Regeneration, *Tissue Engineering and Regenerative Medicine*, 19(1), 2022, 83-92,
(https://doi.org/10.1007/s13770-021-00416-2).

[23] X. Zhang, W. Liu, J. Liu, Y. Hu, H. Dai, Poly-ε-caprolactone/Whitlockite Electrospun Bionic Membrane with an Osteogenic–Angiogenic Coupling Effect for Periosteal Regeneration, *ACS Biomaterials Science & Engineering*, 7(7), 2021, 3321-3331,
(https://doi.org/10.1021/acsbiomaterials.1c00426).

[24] S. Amirthalingam, S.S. Lee, M. Pandian, J. Ramu, S. Iyer, N.S. Hwang, R. Jayakumar, Combinatorial effect of nano whitlockite/nano bioglass with FGF-18 in an injectable hydrogel for craniofacial bone regeneration, *Biomaterials Science*, 9(7), 2021, 2439-2453,
(https://doi.org/10.1039/D0BM01496F).

[25] R.A.M. Horowitz, Ziv.; Foitzik, Christian; Prasad, Hari; Rohrer, Michael; Palti, Ady, β-tricalcium phosphate as bone substitute material: properties and clinical applications, *Journal of Osseointegration*, 2(2), 2010, 61-68,
(https://doi.org/10.23805/jo.2010.02.02.04.).

[26] S.V. Dorozhkin, M. Epple, Biological and Medical Significance of Calcium Phosphates, *Angewandte Chemie International Edition*, 41(17), 2002, 3130-3146,
(https://doi.org/10.1002/1521-3773(20020902)41:17<3130::AID-ANIE3130>3.0.CO;2-1).

[27] A. Bandyopadhyay, S. Bernard, W. Xue, S. Bose, Calcium Phosphate-Based Resorbable Ceramics: Influence of MgO, ZnO, and SiO_2 Dopants, *Journal of the American Ceramic Society*, 89(9), 2006, 2675-2688,
(https://doi.org/10.1111/j.1551-2916.2006.01207.x).

[28] G. Usgu, S. Usgu, The Bone and Joint Structure, in: Functional Exercise Anatomy and Physiology for Physiotherapists, Cham, Springer International Publishing, 2023, pp. 53-75,
(https://doi.org/10.1007/978-3-031-27184-7_3).

[29] H.D. Kim, H.L. Jang, H.-Y. Ahn, H.K. Lee, J. Park, E.-s. Lee, E.A. Lee, Y.-H. Jeong, D.-G. Kim, K.T. Nam, N.S. Hwang, Biomimetic whitlockite inorganic nanoparticles-mediated in situ remodeling and rapid bone regeneration, *Biomaterials*, 112(1), 2017, 31-43,
(https://doi.org/10.1016/j.biomaterials.2016.10.009).

[30] R. Florencio-Silva, G.R. Sasso, E. Sasso-Cerri, M.J. Simões, P.S. Cerri, Biology of Bone Tissue: Structure, Function, and Factors That Influence Bone Cells, *Biomed Res Int*, 2015, 2015, 421746,
(http://dx.doi.org/10.1155/2015/421746).

[31] J. Betts, P. Desaix, E. Johnson, J. Johnson, O. Korol, D. Kruse, B. Poe, J. Wise, M. Wromble, K. Young, Bone tissue and the skeletal system, 2013.

[32] A. Oryan, S. Alidadi, A. Moshiri, N. Maffulli, Bone regenerative medicine: classic options, novel strategies, and future directions, *Journal of Orthopaedic Surgery and Research*, 9(1), 2014, 18,
(https://doi.org/10.1186/1749-799X-9-18).

[33] S. Weiner, H.D. Wagner, THE MATERIAL BONE: Structure-Mechanical Function Relations, *Annual Review of Materials Research*, 28(Volume 28, 1998), 1998, 271-298,
(https://doi.org/10.1146/annurev.matsci.28.1.271).

[34] K. Ishikawa, Bone Substitute Fabrication Based on Dissolution-Precipitation Reactions, *Materials*, 3(2), 2010, 1138-1155,
(https://doi.org/10.3390/ma3021138).

[35] S.V. Dorozhkin, Calcium Phosphates and Human Beings, *Journal of Chemical Education*, 83(5), 2006, 713,
(https://doi.org/10.4161/biom.21340).

[36] T. Sakae, H. Nakada, P.L. John, Historical Review of Biological Apatite Crystallography, *Journal of Hard Tissue Biology*, 24(2), 2015, 111-122,
(https://doi.org/10.2485/jhtb.24.111).

[37] R.K. Singh, M. Srivastava, N.K. Prasad, S. Awasthi, A. Dhayalan, S. Kannan, Iron doped β-Tricalcium phosphate: Synthesis, characterization, hyperthermia effect, biocompatibility and mechanical evaluation, *Materials Science and Engineering: C*, 78, 2017, 715-726,
(https://doi.org/10.1016/j.msec.2017.04.130).

[38] J.M. Kanczler, J.A. Wells, D.M.R. Gibbs, K.M. Marshall, D.K.O. Tang, R.O.C. Oreffo, Chapter 50 - Bone tissue engineering and bone regeneration, in: Principles of Tissue Engineering (Fifth Edition), Academic Press, 2020, pp. 917-935,
(https://doi.org/10.1016/B978-0-12-818422-6.00052-6).

[39] A. Salhotra, H.N. Shah, B. Levi, M.T. Longaker, Mechanisms of bone development and repair, *Nature Reviews Molecular Cell Biology*, 21(11), 2020, 696-711,
(https://doi.org/10.1038/s41580-020-00279-w).

[40] E. Verron, I. Khairoun, J. Guicheux, J.-M. Bouler, Calcium phosphate biomaterials as bone drug delivery systems: a review, *Drug Discovery Today*, 15(13), 2010, 547-552,
(https://doi.org/10.1016/j.drudis.2010.05.003).

[41] A. Tripathi, S. Saravanan, S. Pattnaik, A. Moorthi, N.C. Partridge, N. Selvamurugan, Bio-composite scaffolds containing chitosan/nano-hydroxyapatite/nano-copper–zinc for bone tissue engineering, *International Journal of Biological Macromolecules*, 50(1), 2012, 294-299,
(https://doi.org/10.1016/j.ijbiomac.2011.11.013).

[42] I.V. Fadeeva, M.R. Gafurov, I.A. Kiiaeva, S.B. Orlinskii, L.M. Kuznetsova, Y.Y. Filippov, A.S. Fomin, G.A. Davydova, I.I. Selezneva, S.M. Barinov, Tricalcium Phosphate Ceramics Doped with Silver, Copper, Zinc, and Iron (III) Ions in Concentrations of Less Than 0.5 wt.% for Bone Tissue Regeneration, *BioNanoScience*, 7(2), 2017, 434-438,
(https://doi.org/10.1007/s12668-016-0386-7).

[43] M. Gallo, B. Le Gars Santoni, T. Douillard, F. Zhang, L. Gremillard, S. Dolder, W. Hofstetter, S. Meille, M. Bohner, J. Chevalier, S. Tadier, Effect of grain orientation and magnesium doping on β-tricalcium phosphate resorption behavior, *Acta Biomaterialia*, 89, 2019, 391-402,
(https://doi.org/10.1016/j.actbio.2019.02.045).

[44] J. Zhang, S. Li, H. He, L. Han, S. Zhang, L. Yang, W. Han, X. Wang, J. Gao, J. Zhao, W. Shi, Z. Wu, H. Wang, Z. Zhang, L. Zhang, W. Chen, Q. Zhu, T. Sun, P. Tang, Y. Zhang, Clinical guidelines for indications, techniques, and complications of autogenous bone grafting, *Chin Med J (Engl)*, 137(1), 2024, 5-7,
(https://doi.org/10.1097%2FCM9.0000000000002691).

[45] J. Zhao, Y. Liu, W.-b. Sun, H. Zhang, Amorphous calcium phosphate and its application in dentistry, *Chemistry Central Journal*, 5(1), 2011, 40,
(https://doi.org/10.1186/1752-153X-5-40).

[46] A.H. Schmidt, Autologous bone graft: Is it still the gold standard?, *Injury*, 52, 2021, S18-S22,

(https://doi.org/10.1016/j.injury.2021.01.043).

[47] M. Bohner, L. Galea, N. Doebelin, Calcium phosphate bone graft substitutes: Failures and hopes, *Journal of the European Ceramic Society*, 32(11), 2012, 2663-2671,
(https://doi.org/10.1016/j.jeurceramsoc.2012.02.028).

[48] G. Battafarano, M. Rossi, V. De Martino, F. Marampon, L. Borro, A. Secinaro, A. Del Fattore, Strategies for Bone Regeneration: From Graft to Tissue Engineering, *Int J Mol Sci*, 22(3), 2021, 1128,
(https://doi.org/10.3390/ijms22031128).

[49] A.M. Brokesh, A.K. Gaharwar, Inorganic Biomaterials for Regenerative Medicine, *ACS Applied Materials & Interfaces*, 12(5), 2020, 5319-5344,
(https://doi.org/10.1021/acsami.9b17801).

[50] Y. Pang, D. Li, J. Zhou, X. Liu, M. Li, Y. Zhang, D. Zhang, X. Zhang, Q. Cai, In vitro and in vivo evaluation of biomimetic hydroxyapatite/whitlockite inorganic scaffolds for bone tissue regeneration, *Biomedical Materials*, 17(6), 2022, 065020,
(https://dx.doi.org/10.1088/1748-605X/ac95e9).

[51] I. Manjubala, M. Sivakumar, R.V. Sureshkumar, T.P. Sastry, Bioactivity and osseointegration study of calcium phosphate ceramic of different chemical composition, *Journal of Biomedical Materials Research*, 63(2), 2002, 200-208,
(https://doi.org/10.1002/jbm.10128).

[52] R.A. Surmenev, I.Y. Grubova, E. Neyts, A.D. Teresov, N.N. Koval, M. Epple, A.I. Tyurin, V.F. Pichugin, M.V. Chaikina, M.A. Surmeneva, Ab initio calculations and a scratch test study of RF-magnetron sputter deposited hydroxyapatite and silicon-containing hydroxyapatite coatings, *Surfaces and Interfaces*, 21, 2020, 100727,
(https://doi.org/10.1016/j.surfin.2020.100727).

[53] J. Kolmas, E. Groszyk, D. Kwiatkowska-Różycka, Substituted hydroxyapatites with antibacterial properties, *Biomed Res Int*, 1(1), 2014, 178123-178123,
(https://doi.org/10.1155/2014/178123).

[54] J. Jeong, J.H. Kim, J.H. Shim, N.S. Hwang, C.Y. Heo, Bioactive calcium phosphate materials and applications in bone regeneration, *Biomaterials Research*, 23(1), 2019, 4,
(https://doi.org/10.1186/s40824-018-0149-3).

[55] J. Lu, H. Yu, C. Chen, Biological properties of calcium phosphate biomaterials for bone repair: a review, *RSC Advances*, 8(4), 2018, 2015-2033,
(https://doi.org/10.1039/C7RA11278E).

[56] W. Zhang, Q. Chang, L. Xu, G. Li, G. Yang, X. Ding, X. Wang, D. Cui, X. Jiang, Graphene Oxide-Copper Nanocomposite-Coated Porous CaP Scaffold for Vascularized Bone Regeneration via Activation of Hif-1α, *Advanced healthcare materials*, 5(11), 2016, 1299-1309,
(https://doi.org/10.1002/adhm.201500824).

[57] H. Oliveira, S. Catros, O. Castano, S. Rey, R. Siadous, D. Clift, J. Marti-Munoz, M. Batista, R. Bareille, J. Planell, E. Engel, J. Amédée, The proangiogenic potential of a novel calcium releasing composite biomaterial: Orthotopic in vivo evaluation, *Acta Biomaterialia*, 54, 2017, 377-385,
(https://doi.org/10.1016/j.actbio.2017.02.039).

[58] C. Wang, K.-J. Jeong, H.J. Park, M. Lee, S.-C. Ryu, D.Y. Hwang, K.H. Nam, I.H. Han, J. Lee, Synthesis and formation mechanism of bone mineral, whitlockite nanocrystals in tri-solvent system, *Journal of Colloid and Interface Science*, 569(1), 2020, 1-11,

(https://doi.org/10.1016/j.jcis.2020.02.072).

[59] S. Castiglioni, A. Cazzaniga, W. Albisetti, J.A.M. Maier, Magnesium and osteoporosis: Current state of knowledge and future research directions, *Nutrients*, 5(8), 2013, 3022-3033,
(https://doi.org/10.3390/nu5083022).

[60] T.A. Grünewald, H. Rennhofer, B. Hesse, M. Burghammer, S.E. Stanzl-Tschegg, M. Cotte, J.F. Löffler, A.M. Weinberg, H.C. Lichtenegger, Magnesium from bioresorbable implants: Distribution and impact on the nano- and mineral structure of bone, *Biomaterials*, 76, 2016, 250-260,
(https://doi.org/10.1016/j.biomaterials.2015.10.054).

[61] L. Zhang, C. Yang, J. Li, Y. Zhu, X. Zhang, High extracellular magnesium inhibits mineralized matrix deposition and modulates intracellular calcium signaling in human bone marrow-derived mesenchymal stem cells, *Biochemical and Biophysical Research Communications*, 450(4), 2014, 1390-1395,
(https://doi.org/10.1016/j.bbrc.2014.07.004).

[62] Y. Yaegashi, T. Onoda, K. Tanno, T. Kuribayashi, K. Sakata, H. Orimo, Association of hip fracture incidence and intake of calcium, magnesium, vitamin D, and vitamin K, *European Journal of Epidemiology*, 23(3), 2008, 219-225,
(https://doi.org/10.1007/s10654-008-9225-7).

[63] S. Hesaraki, S. Farhangdoust, M.H. Barounian, Phase transformation and structural characteristics of zinc-incorporated β-tricalcium phosphate, *Materials Science-Poland*, 31(2), 2013, 281-287,
(https://doi.org/10.2478/s13536-013-0103-y).

[64] A. Bandyopadhyay, E.A. Withey, J. Moore, S. Bose, Influence of ZnO doping in calcium phosphate ceramics, *Materials Science and Engineering: C*, 27(1), 2007, 14-17,
(https://doi.org/10.1016/j.msec.2005.11.004).

[65] M. Yamaguchi, Role of nutritional zinc in the prevention of osteoporosis, *Molecular and Cellular Biochemistry*, 338(1), 2010, 241-254,
(https://doi.org/10.1007/s11010-009-0358-0).

[66] B. Li, H. Liu, S. Jia, Zinc Enhances Bone Metabolism in Ovariectomized Rats and Exerts Anabolic Osteoblastic/Adipocytic Marrow Effects Ex Vivo, *Biological Trace Element Research*, 163(1), 2015, 202-207,
(https://doi.org/10.1007/s12011-014-0185-3).

[67] G.A. Fielding, A. Bandyopadhyay, S. Bose, Effects of silica and zinc oxide doping on mechanical and biological properties of 3D printed tricalcium phosphate tissue engineering scaffolds, *Dental Materials*, 28(2), 2012, 113-122,
(https://doi.org/10.1016/j.dental.2011.09.010).

[68] A.B.G. Lansdown, U. Mirastschijski, N. Stubbs, E. Scanlon, M.S. Ågren, Zinc in wound healing: Theoretical, experimental, and clinical aspects, *Wound Repair and Regeneration*, 15(1), 2007, 2-16,
(https://doi.org/10.1111/j.1524-475X.2006.00179.x).

[69] L.M. Plum, L. Rink, H. Haase, The essential toxin: impact of zinc on human health, *International Journal of Environmental Research and Public Health*, 7(4), 2010, 1342-1365,
(https://doi.org/10.3390/ijerph7041342).

[70] S. Jin, L. Ren, K. Yang, Bio-Functional Cu Containing Biomaterials: a New Way to Enhance Bio-Adaption of Biomaterials, *Journal of Materials Science & Technology*, 32(9), 2016, 835-839,

(https://doi.org/10.1016/j.jmst.2016.06.022).

[71] A.P. Ingle, P. Paralikar, S. Shende, I. Gupta, J.K. Biswas, L.H. da Silva Martins, M. Rai, Copper in Medicine: Perspectives and Toxicity, in: Biomedical Applications of Metals, Cham, Springer International Publishing, 2018, pp. 95-112, (https://doi.org/10.1007/978-3-319-74814-6_4).

[72] A.P. Kornblatt, V.G. Nicoletti, A. Travaglia, The neglected role of copper ions in wound healing, *Journal of Inorganic Biochemistry*, 161, 2016, 1-8, (https://doi.org/10.1016/j.jinorgbio.2016.02.012).

[73] C. Gérard, L.-J. Bordeleau, J. Barralet, C.J. Doillon, The stimulation of angiogenesis and collagen deposition by copper, *Biomaterials*, 31(5), 2010, 824-831, (https://doi.org/10.1016/j.biomaterials.2009.10.009).

[74] L. Pickart, J.M. Vasquez-Soltero, A. Margolina, The Human Tripeptide GHK-Cu in Prevention of Oxidative Stress and Degenerative Conditions of Aging: Implications for Cognitive Health, *Oxidative Medicine and Cellular Longevity*, 2012(1), 2012, 324832, (https://doi.org/10.1155/2012/324832).

[75] N.M. Lowe, W.D. Fraser, M.J. Jackson, Is there a potential therapeutic value of copper and zinc for osteoporosis?, *Proceedings of the Nutrition Society*, 61(2), 2002, 181-185, (https://doi.org/10.1079/PNS2002154).

[76] S.M. Wazir, I. Ghobrial, Copper deficiency, a new triad: anemia, leucopenia, and myeloneuropathy, *Journal of Community Hospital Internal Medicine Perspectives*, 7(4), 2017, 265-268, (https://doi.org/10.1080/20009666.2017.1351289).

[77] P. de Bie, P. Muller, C. Wijmenga, L.W.J. Klomp, Molecular pathogenesis of Wilson and Menkes disease: correlation of mutations with molecular defects and disease phenotypes, *Journal of Medical Genetics*, 44(11), 2007, 673-688, (https://doi.org/10.1136/jmg.2007.052746).

[78] J.P. Rodríguez, S. Ríos, M. González, Modulation of the proliferation and differentiation of human mesenchymal stem cells by copper, *Journal of Cellular Biochemistry*, 85(1), 2002, 92-100, (https://doi.org/10.1002/jcb.10111).

[79] J.L. Aschner, M. Aschner, Nutritional aspects of manganese homeostasis, *Molecular Aspects of Medicine*, 26(4), 2005, 353-362, (https://doi.org/10.1016/j.mam.2005.07.003).

[80] A.C. Ross, B. Caballero, R.J. Cousins, K.L. Tucker, Modern Nutrition in Health and Disease, 11th ed., Burlington, Jones & Bartlett Learning, 2020.

[81] M.E. Zilm, L. Yu, W.A. Hines, M. Wei, Magnetic properties and cytocompatibility of transition-metal-incorporated hydroxyapatite, *Materials Science and Engineering: C*, 87, 2018, 112-119, (https://doi.org/10.1016/j.msec.2018.02.018).

[82] L. García-Hevia, M. Bañobre-López, J. Gallo, Recent Progress on Manganese-Based Nanostructures as Responsive MRI Contrast Agents, *Chemistry – A European Journal*, 25(2), 2019, 431-441, (https://doi.org/10.1002/chem.201802851).

[83] Y.-J. Bae, M.-H. Kim, Manganese Supplementation Improves Mineral Density of the Spine and Femur and Serum Osteocalcin in Rats, *Biological Trace Element Research*, 124(1), 2008, 28-34, (https://doi.org/10.1007/s12011-008-8119-6).

[84] B. Bracci, P. Torricelli, S. Panzavolta, E. Boanini, R. Giardino, A. Bigi, Effect of Mg^{2+}, Sr^{2+}, and Mn^{2+} on the chemico-physical and in vitro biological properties of calcium phosphate biomimetic coatings, *Journal of Inorganic Biochemistry*, 103(12), 2009, 1666-1674,
(https://doi.org/10.1016/j.jinorgbio.2009.09.009).
[85] S. Bose, G. Fielding, S. Tarafder, A. Bandyopadhyay, Understanding of dopant-induced osteogenesis and angiogenesis in calcium phosphate ceramics, *Trends Biotechnol*, 31(10), 2013, 594-605,
(https://doi.org/10.1016/j.tibtech.2013.06.005).
[86] C. Heng, X. Zheng, J. Hui, X. Ma, D. Fan, Neodymium and manganese ions co-doped whitlockite for temperature monitoring, photothermal therapy, and bone tissue repair in osteosarcoma, *Journal of Colloid and Interface Science*, 653, 2024, 1488-1503,
(https://doi.org/10.1016/j.jcis.2023.09.186).
[87] E. Boanini, F. Silingardi, M. Gazzano, A. Bigi, Synthesis and Hydrolysis of Brushite (DCPD): The Role of Ionic Substitution, *Crystal Growth & Design*, 21(3), 2021, 1689–1697,
(https://doi.org/10.1021/acs.cgd.0c01569).
[88] E. Boanini, M. Gazzano, A. Bigi, Ionic substitutions in calcium phosphates synthesized at low temperature, *Acta Biomaterialia*, 6(6), 2010, 1882-1894,
(https://doi.org/10.1016/j.actbio.2009.12.041).
[89] D. Hamai, S.C. Bondy, Oxidative Basis of Manganese Neurotoxicity, *Annals of the New York Academy of Sciences*, 1012(1), 2004, 129-141,
(https://doi.org/10.1196/annals.1306.010).
[90] S.M. Barinov, Calcium phosphate-based ceramic and composite materials for medicine, *Russian Chemical Reviews*, 79(1), 2010, 13-29,
(https://dx.doi.org/10.1070/RC2010v079n01ABEH004098).
[91] M. Šupová, Substituted hydroxyapatites for biomedical applications: A review, *Ceramics International*, 41(8), 2015, 9203-9231,
(https://doi.org/10.1016/j.ceramint.2015.03.316).
[92] K. Hurle, J.M. Oliveira, R.L. Reis, S. Pina, F. Goetz-Neunhoeffer, Ion-doped Brushite Cements for Bone Regeneration, *Acta Biomaterialia*, 2021,
(https://doi.org/10.1016/j.actbio.2021.01.004).
[93] T.J. Webster, E.A. Massa-Schlueter, J.L. Smith, E.B. Slamovich, Osteoblast response to hydroxyapatite doped with divalent and trivalent cations, *Biomaterials*, 25(11), 2004, 2111-2121,
(https://doi.org/10.1016/j.biomaterials.2003.09.001).
[94] P.M.C. Torres, A. Marote, A.R. Cerqueira, A.J. Calado, J.C.C. Abrantes, S. Olhero, O.A.B. da Cruz e Silva, S.I. Vieira, J.M.F. Ferreira, Injectable MnSr-doped brushite bone cements with improved biological performance, *Journal of Materials Chemistry B*, 5(15), 2017, 2775-2787,
(https://doi.org/10.1039/C6TB03119F).
[95] H.L. Jang, K. Jin, J. Lee, Y. Kim, S.H. Nahm, K.S. Hong, K.T. Nam, Revisiting Whitlockite, the Second Most Abundant Biomineral in Bone: Nanocrystal Synthesis in Physiologically Relevant Conditions and Biocompatibility Evaluation, *ACS Nano*, 8(1), 2014, 634-641,
(https://doi.org/10.1021/nn405246h).
[96] R. Cruz, J. Calasans-Maia, S. Sartoretto, V. Moraschini, A.M. Rossi, R.S. Louro, J.M. Granjeiro, M.D. Calasans-Maia, Does the incorporation of zinc into calcium

phosphate improve bone repair? A systematic review, *Ceramics International*, 44(2), 2018, 1240-1249,
(https://doi.org/10.1016/j.ceramint.2017.10.157).

[97] E. Thian, T. Konishi, Y. Kawanobe, P.N. Lim, C. Choong, B. Ho, M. Aizawa, Zinc-substituted hydroxyapatite: A biomaterial with enhanced bioactivity and antibacterial properties, *Journal of materials science. Materials in medicine*, 24(2), 2012, 437-445,
(https://doi.org/10.1007/s10856-012-4817-x).

[98] J. Raphel, M. Holodniy, S.B. Goodman, S.C. Heilshorn, Multifunctional coatings to simultaneously promote osseointegration and prevent infection of orthopaedic implants, *Biomaterials*, 84, 2016, 301-314,
(https://doi.org/10.1016/j.biomaterials.2016.01.016).

[99] V. Stanić, S. Dimitrijević, J. Antić-Stanković, M. Mitrić, B. Jokić, I.B. Plećaš, S. Raičević, Synthesis, characterization and antimicrobial activity of copper and zinc-doped hydroxyapatite nanopowders, *Applied Surface Science*, 256(20), 2010, 6083-6089,
(https://doi.org/10.1016/j.apsusc.2010.03.124).

[100] D.V. Deyneko, Y.F. Zheng, K. Barbaro, V.N. Lebedev, S.M. Aksenov, E.Y. Borovikova, M.R. Gafurov, I.V. Fadeeva, B.I. Lazoryak, G. Di Giacomo, C. Cicione, V. Tilotta, F. Russo, G. Vadala, J.V. Rau, Dependence of antimicrobial properties on site-selective arrangement and concentration of bioactive Cu^{2+} ions in tricalcium phosphate, *Ceramics International*, 49(13), 2023, 21308-21323,
(https://doi.org/10.1016/j.ceramint.2023.03.260).

[101] X. Li, G. Li, K. Zhang, Z. Pei, S. Zhao, J. Li, Cu-loaded Brushite bone cements with good antibacterial activity and operability, *Journal of Biomedical Materials Research Part B: Applied Biomaterials*, 109(6), 2021, 877-889,
(https://doi.org/10.1002/jbm.b.34752).

[102] Z. Yang, T. Yao, X. Zheng, J. Hui, D. Fan, Eu^{3+}/Tb^{3+}-doped whitlockite nanocrystals: Controllable synthesis, cell imaging, and the degradation process in the bone reconstruction, *Nano Research*, 2021,
(https://doi.org/10.1007/s12274-021-3654-y).

[103] J. Lu, S. Ma, J. Sun, C. Xia, C. Liu, Z. Wang, X. Zhao, F. Gao, Q. Gong, B. Song, X. Shuai, H. Ai, Z. Gu, Manganese ferrite nanoparticle micellar nanocomposites as MRI contrast agent for liver imaging, *Biomaterials*, 30(15), 2009, 2919-2928,
(https://doi.org/10.1016/j.biomaterials.2009.02.001).

[104] B. Srinivasan, E. Kolanthai, N. Eluppai Asthagiri Kumaraswamy, R.R. Jayapalan, D.S. Vavilapalli, L.H. Catalani, G.S. Ningombam, N.S. Khundrakpam, N.R. Singh, S.N. Kalkura, Thermally Modified Iron-Inserted Calcium Phosphate for Magnetic Hyperthermia in an Acceptable Alternating Magnetic Field, *The Journal of Physical Chemistry B*, 123(26), 2019, 5506-5513,
(https://doi.org/10.1021/acs.jpcb.9b03015).

[105] C. Calvo, R. Gopal, The Crystal Structure of Whitlockite from the Palermo Quarry, *American Mineralogist*, 60(1-2), 1975, 120-133.

[106] M. Iijima, K. Komatsu, H. Kagi, Y. Maekawa, T. Sasaki, S. Hyodo, R. Kimura, T. Futami, M. Suzuki, Hydroxyapatite in Whitlockite-Based Hypermineralized Hard Tissue of Elephant Shark (Callorhinchus milii) Tooth Plate, *Crystal Growth & Design*, 23(4), 2023, 2031-2041,
(https://doi.org/10.1021/acs.cgd.2c00820).

[107] C. Qi, F. Chen, J. Wu, Y.-J. Zhu, C.-N. Hao, J.-L. Duan, Magnesium whitlockite hollow microspheres: a comparison of microwave-hydrothermal and conventional hydrothermal syntheses using fructose 1,6-bisphosphate, and application in protein adsorption, *RSC Advances*, 6(40), 2016, 33393-33402, (https://doi.org/10.1039/C6RA00775A).

[108] A.C. Tas, Transformation of Brushite ($CaHPO_4 \cdot 2H_2O$) to Whitlockite ($Ca_9Mg(HPO_4)(PO_4)_6$) or Other CaPs in Physiologically Relevant Solutions, *Journal of the American Ceramic Society*, 99(4), 2016, 1200-1206, (https://doi.org/10.1111/jace.14069).

[109] G. Jose, K.T. Shalumon, H.-T. Liao, C.-Y. Kuo, J.-P. Chen, Preparation and Characterization of Surface Heat Sintered Nanohydroxyapatite and Nanowhitlockite Embedded Poly (Lactic-co-glycolic Acid) Microsphere Bone Graft Scaffolds: In Vitro and in Vivo Studies, *Int J Mol Sci*, 21(2), 2020, 528, (https://doi.org/10.3390/ijms21020528).

[110] T. Debroise, E. Colombo, G. Belletti, J. Vekeman, Y. Su, R. Papoular, N.S. Hwang, D. Bazin, M. Daudon, P. Quaino, F. Tielens, One Step Further in the Elucidation of the Crystallographic Structure of Whitlockite, *Crystal Growth & Design*, 20(4), 2020, 2553-2561, (https://doi.org/10.1021/acs.cgd.9b01679).

[111] R. Lagier, C.A. Baud, Magnesium Whitlockite, a Calcium Phosphate Crystal of Special Interest in Pathology, *Pathology - Research and Practice*, 199(5), 2003, 329-335, (https://doi.org/10.1078/0344-0338-00425).

[112] I. Perrotta, E. Perri, Ultrastructural, Elemental and Mineralogical Analysis of Vascular Calcification in Atherosclerosis, *Microscopy and Microanalysis*, 23(5), 2017, 1030-1039, (https://doi.org/10.1017/S1431927617012533).

[113] F.A. Shiekh, M. Khullar, S.K. Singh, Lithogenesis: induction of renal calcifications by nanobacteria, *Urological Research*, 34(1), 2006, 53-57, (https://doi.org/10.1007/s00240-005-0034-0).

[114] F.A. Shah, Magnesium whitlockite – omnipresent in pathological mineralisation of soft tissues but not a significant inorganic constituent of bone, *Acta Biomaterialia*, 125, 2021, 72-82, (https://doi.org/10.1016/j.actbio.2021.02.021).

[115] Y. Yang, H. Wang, H. Yang, Y. Zhao, J. Guo, X. Yin, T. Ma, X. Liu, L. Li, Magnesium-Based Whitlockite Bone Mineral Promotes Neural and Osteogenic Activities, *ACS Biomaterials Science & Engineering*, 6(10), 2020, 5785-5796, (https://doi.org/10.1021/acsbiomaterials.0c00852).

[116] H.D. Kim, H.L. Jang, H.-Y. Ahn, H.K. Lee, J. Park, E.-s. Lee, E.A. Lee, Y.-H. Jeong, D.-G. Kim, K.T. Nam, N.S. Hwang, Biomimetic whitlockite inorganic nanoparticles-mediated in situ remodeling and rapid bone regeneration, *Biomaterials*, 112, 2017, 31-43, (https://doi.org/10.1016/j.biomaterials.2016.10.009).

[117] V.K. Kaliannagounder, N.P.M.J. Raj, A.R. Unnithan, J. Park, S.S. Park, S.-J. Kim, C.H. Park, C.S. Kim, A.R.K. Sasikala, Remotely controlled self-powering electrical stimulators for osteogenic differentiation using bone inspired bioactive piezoelectric whitlockite nanoparticles, *Nano Energy*, 85, 2021, 105901, (https://doi.org/10.1016/j.nanoen.2021.105901).

[118] L. Wang, Y. Pang, Y. Tang, X. Wang, D. Zhang, X. Zhang, Y. Yu, X. Yang, Q. Cai, A biomimetic piezoelectric scaffold with sustained Mg^{2+} release promotes neurogenic and angiogenic differentiation for enhanced bone regeneration, *Bioact Mater*, 25, 2023, 399-414,
(https://doi.org/10.1016/j.bioactmat.2022.11.004).

[119] R. Gopal, C. Calvo, J. Ito, W.K. Sabine, Crystal Structure of Synthetic Mg-Whitlockite, $Ca_{18}Mg_2H_2(PO_4)_{14}$, *Canadian Journal of Chemistry*, 52(7), 1974, 1155-1164,
(https://doi.org/10.1139/v74-181).

[120] M. Yashima, A. Sakai, T. Kamiyama, A. Hoshikawa, Crystal structure analysis of β-tricalcium phosphate $Ca_3(PO_4)_2$ by neutron powder diffraction, *Journal of Solid State Chemistry*, 175(2), 2003, 272-277,
(https://doi.org/10.1016/S0022-4596(03)00279-2).

[121] T. Konishi, S. Watanabe, Amorphous-precursor mediated formation of magnesium-free whitlockite, *Phosphorus Research Bulletin*, 37, 2021, 1-10,
(https://doi.org/10.3363/prb.37.1).

[122] D. Zhou, C. Qi, Y.-X. Chen, Y.-J. Zhu, T.-W. Sun, F. Chen, C.-Q. Zhang, Comparative study of porous hydroxyapatite/chitosan and whitlockite/chitosan scaffolds for bone regeneration in calvarial defects, *Int J Nanomedicine*, 12(1), 2017, 2673-2687,
(https://doi.org/10.2147/IJN.S131251).

[123] N.S. Muthiah Pillai, K. Eswar, S. Amirthalingam, U. Mony, P. Kerala Varma, R. Jayakumar, Injectable Nano Whitlockite Incorporated Chitosan Hydrogel for Effective Hemostasis, *ACS Applied Bio Materials*, 2(2), 2019, 865-873,
(https://doi.org/10.1021/acsabm.8b00710).

[124] R. Raiseliene, G. Linkaite, A. Zarkov, A. Kareiva, I. Grigoraviciute, Large-Scale Green Synthesis of Magnesium Whitlockite from Environmentally Benign Precursor, *Materials*, 17(4), 2024, 788,
(https://doi.org/10.3390/ma17040788).

[125] A. Afonina, A. Dubauskas, V. Klimavicius, A. Zarkov, A. Kareiva, I. Grigoraviciute, Phase transformations during the dissolution-precipitation synthesis of magnesium whitlockite nanopowders from gypsum, *Ceramics International*, 49(23, Part A), 2023, 38157-38164,
(https://doi.org/10.1016/j.ceramint.2023.09.146).

[126] C. Qi, Y.-J. Zhu, F. Chen, J. Wu, Porous microspheres of magnesium whitlockite and amorphous calcium magnesium phosphate: microwave-assisted rapid synthesis using creatine phosphate, and application in drug delivery, *Journal of Materials Chemistry B*, 3(39), 2015, 7775-7786,
(http://dx.doi.org/10.1039/C5TB01106J).

[127] C. Lin, Y. Wang, Y. Zhou, Y. Zeng, A rapid way to synthesize magnesium whitlockite microspheres for high efficiency removing heavy metals, *Desalination and Water Treatment*, 162(1), 2019, 220-227,
(https://doi.org/10.5004/dwt.2019.24290).

[128] L. Bauer, M. Ivanković, H. Ivanković, Magnesium substituted hydroxyapatite scaffolds hydrothermally synthesized from cuttlefish bone, in: MATRIB 2018, Vele Luka, Croatia, 2018.

[129] F. Nigar, A.-L. Johnston, J. Smith, W. Oakley, M.T. Islam, R. Felfel, D. Grant, E. Lester, I. Ahmed, Production of Nano Hydroxyapatite and Mg-Whitlockite from

Biowaste-Derived products via Continuous Flow Hydrothermal Synthesis: A Step towards Circular Economy, *Materials*, 16(6), 2023, 2138, (https://doi.org/10.3390/ma16062138).

[130] C. Heng, W. Liu, X. Zheng, X. Ma, J. Hui, D. Fan, Dopamine and DNA functionalized manganese whitlockite nanocrystals for magnetic resonance imaging and chemo-photothermal therapy of tumors, *Colloids and Surfaces B: Biointerfaces*, 222, 2023, 113120, (https://doi.org/10.1016/j.colsurfb.2022.113120).

[131] C. Heng, X. Zheng, J. Hui, X. Ma, D. Fan, DNA aptamer functionalized monodisperse Eu/Mn-WH nanoparticle for in vivo magnetic resonance and fluorescence imaging, *Ceramics International*, 2023, (https://doi.org/10.1016/j.ceramint.2023.11.046).

[132] M. Hu, F. Xiao, Q.-F. Ke, Y. Li, X.-D. Chen, Y.-P. Guo, Cerium-doped whitlockite nanohybrid scaffolds promote new bone regeneration via SMAD signaling pathway, *Chemical Engineering Journal*, 359, 2019, 1-12, (https://doi.org/10.1016/j.cej.2018.11.116).

[133] M. Wang, J. Yao, S. Shen, C. Heng, Y. Zhang, T. Yang, X. Zheng, A scaffold with zinc-whitlockite nanoparticles accelerates bone reconstruction by promoting bone differentiation and angiogenesis, *Nano Research*, 16(1), 2023, 757-770, (https://doi.org/10.1007/s12274-022-4644-4).

[134] S.Y. Stefanovich, B.I. Lazoryak, A.M. Antipin, A.S. Volkov, A.I. Evdokimov, O.A. Gurbanova, O.V. Dimitrova, D.V. Deyneko, Crystal structures of biocompatible Mg-, Zn-, and Co-whitlockites synthesized via one-step hydrothermal reaction, *Zeitschrift für Kristallographie - Crystalline Materials*, 238(9-10), 2023, 301-309, (https://doi.org/10.1515/zkri-2023-0016).

[135] T. Konishi, S. Watanabe, Copper whitlockite synthesized via hydrothermal transformation of calcium hydrogen phosphate dihydrate, *Phosphorus Research Bulletin*, 38, 2022, 18-24, (https://doi.org/10.3363/prb.38.18).

[136] L.V. Maximiano, L.B. Correa, N.C. Gomes-da-Silva, L.S. da Costa, M.G.P. Da Silva, A.V. Chaves, M.L. Franco, P.B.A. Fechine, A.S. de Menezes, R. Santos-Oliveira, D.M. Andrade Neto, Magnesium whitlockite nanoparticles: Hydrothermal synthesis, anti-inflammatory and anti-cancer potential, *Colloids and Surfaces B: Biointerfaces*, 239, 2024, 113931, (https://doi.org/10.1016/j.colsurfb.2024.113931).

[137] X. Lin, Y. Wang, L. Liu, X. Du, W. Wang, S. Guo, J. Zhang, K. Ge, G. Zhou, Enhanced bone regeneration by osteoinductive and angiogenic zein/whitlockite composite scaffolds loaded with levofloxacin, *RSC Advances*, 14(21), 2024, 14470-14479, (http://dx.doi.org/10.1039/D4RA00772G).

[138] W. Hou, J. Liu, W. Wei, Y. Zhao, X. Wu, H. Dai, All-in-one strategy to develop a near-infrared triggered multifunctional bioactive magnesium phosphate bone cement for bone repair, *Acta Biomaterialia*, 182, 2024, 111-125, (https://doi.org/10.1016/j.actbio.2024.05.028).

[139] S. Pouraghaei Sevari, J.K. Kim, C. Chen, A. Nasajpour, C.-Y. Wang, P.H. Krebsbach, A. Khademhosseini, S. Ansari, P.S. Weiss, A. Moshaverinia, Whitlockite-Enabled Hydrogel for Craniofacial Bone Regeneration, *ACS Applied Materials & Interfaces*, 13(30), 2021, 35342-35355, (https://doi.org/10.1021/acsami.1c07453).

[140] L. Bauer, M. Antunović, A. Rogina, M. Ivanković, H. Ivanković, Bone-mimetic porous hydroxyapatite/whitlockite scaffolds: preparation, characterization and interactions with human mesenchymal stem cells, *Journal of Materials Science*, 56(5), 2021, 3947-3969,
(https://doi.org/10.1007/s10853-020-05489-3).
[141] Y.-Z. Jin, G.-B. Zheng, H.L. Jang, K.M. Lee, J.H. Lee, Whitlockite Promotes Bone Healing in Rabbit Ilium Defect Model, *Journal of Medical and Biological Engineering*, 39(6), 2019, 944-951,
(https://doi.org/10.1007/s40846-019-00471-0).
[142] Q. Liu, J.H. Kim, M. Cho, S.H. Kim, B. Xu, S. Amirthalingam, N.S. Hwang, J.H. Lee, Bioactive magnesium-based whitlockite ceramic as bone cement additives for enhancing osseointegration and bone regeneration, *Materials & Design*, 229, 2023, 111914,
(https://doi.org/10.1016/j.matdes.2023.111914).
[143] Y. Chang, R. Zhao, H. Wang, L. Pang, J. Ding, Y. Shen, Y. Guo, D. Wang, A novel injectable whitlockite-containing borosilicate bioactive glass cement for bone repair, *Journal of Non-Crystalline Solids*, 547, 2020, 120291,
(https://doi.org/10.1016/j.jnoncrysol.2020.120291).
[144] J. Li, K. Li, Y. Ding, S. Zhang, T. Hu, S. Wang, X. Zheng, Hydroxyapatite-whitlockite composite coating as a biomimetic material for bone integration, *Surface and Coatings Technology*, 487, 2024, 131019,
(https://doi.org/10.1016/j.surfcoat.2024.131019).
[145] J. Nazurudeen, S. Palati, S. Sekaran, D. Ganapathy, Biocompatibility Evaluation of Ampicillin-Loaded Whitlockite for Bone Regeneration, *Cureus*, 16(5), 2024, e61461,
(https://doi.org/10.7759/cureus.61461).
[146] J.S. Hong, H.J. Kim, C.H. Sohn, O.Y. Gong, J.H. Choi, K.H. Cho, G.S. Han, K.T. Nam, H.S. Jung, High-Throughput Pb Recycling for Perovskite Solar Cells Using Biomimetic Whitlockite, *Energy & Environmental Materials*, 6(3), 2023, e12374,
(https://doi.org/10.1002/eem2.12374).
[147] F. Capitelli, F. Bosi, S.C. Capelli, F. Radica, G. Della Ventura, Neutron and XRD Single-Crystal Diffraction Study and Vibrational Properties of Whitlockite, the Natural Counterpart of Synthetic Tricalcium Phosphate, *Crystals*, 11(3), 2021, 225,
(https://doi.org/10.3390/cryst11030225).
[148] M. Feike, D.E. Demco, R. Graf, J. Gottwald, S. Hafner, H.W. Spiess, Broadband Multiple-Quantum NMR Spectroscopy, *Journal of Magnetic Resonance, Series A*, 122(2), 1996, 214-221,
(https://doi.org/10.1006/jmra.1996.0197).
[149] G.A. Bain, J.F. Berry, Diamagnetic Corrections and Pascal's Constants, *Journal of Chemical Education*, 85(4), 2008, 532,
(https://doi.org/10.1021/ed085p532).
[150] G. Morrison, H.-C. zur Loye, Simple correction for the sample shape and radial offset effects on SQUID magnetometers: Magnetic measurements on Ln_2O_3 (Ln=Gd, Dy, Er) standards, *Journal of Solid State Chemistry*, 221, 2015, 334-337,
(https://doi.org/10.1016/j.jssc.2014.10.026).
[151] T. Kokubo, H. Takadama, How useful is SBF in predicting in vivo bone bioactivity?, *Biomaterials*, 27(15), 2006, 2907-2915,
(https://doi.org/10.1016/j.biomaterials.2006.01.017).

[152] A. Kizalaite, I. Grigoraviciute-Puroniene, D.R.C. Asuigui, S.L. Stoll, S.H. Cho, T. Sekino, A. Kareiva, A. Zarkov, Dissolution–Precipitation Synthesis and Characterization of Zinc Whitlockite with Variable Metal Content, *ACS Biomaterials Science & Engineering*, 7(8), 2021, 3586-3593, (https://doi.org/10.1021/acsbiomaterials.1c00335).

[153] K.S.W. Sing, Reporting physisorption data for gas/solid systems with special reference to the determination of surface area and porosity (Recommendations 1984), *Pure and Applied Chemistry*, 57(4), 1985, 603-619, (https://doi.org/10.1351/pac198557040603).

[154] D. Griesiute, E. Garskaite, A. Antuzevics, V. Klimavicius, V. Balevicius, A. Zarkov, A. Katelnikovas, D. Sandberg, A. Kareiva, Synthesis, structural and luminescent properties of Mn-doped calcium pyrophosphate ($Ca_2P_2O_7$) polymorphs, *Scientific Reports*, 12(1), 2022, 7116, (https://doi.org/10.1038/s41598-022-11337-y).

[155] R.A. Van Santen, The Ostwald step rule, *The Journal of Physical Chemistry*, 88(24), 1984, 5768-5769, (https://doi.org/10.1021/j150668a002).

[156] D. Griesiute, E. Raudonyte-Svirbutaviciene, A. Kareiva, A. Zarkov, The influence of annealing conditions on the Ca/P ratio and phase transformations in bulk calcium phosphates, *CrystEngComm*, 24(6), 2022, 1166-1170, (https://doi.org/10.1039/D1CE01625C).

[157] L. Sinusaite, A. Popov, A. Antuzevics, K. Mazeika, D. Baltrunas, J.-C. Yang, J.L. Horng, S. Shi, T. Sekino, K. Ishikawa, A. Kareiva, A. Zarkov, Fe and Zn co-substituted beta-tricalcium phosphate (β-TCP): Synthesis, structural, magnetic, mechanical and biological properties, *Materials Science and Engineering: C*, 112, 2020, 110918, (https://doi.org/10.1016/j.msec.2020.110918).

[158] T. Konishi, S. Watanabe, Hydrothermal transformation of calcium hydrogen phosphate dihydrate into magnesium whitlockite, *Phosphorus Research Bulletin*, 37, 2021, 21-25, (http://dx.doi.org/10.3363/prb.37.21).

[159] A. Kizalaite, V. Klimavicius, J. Versockiene, E. Lastauskiene, T. Murauskas, R. Skaudzius, T. Yokoi, M. Kawashita, T. Goto, T. Sekino, A. Zarkov, Peculiarities of the formation, structural and morphological properties of zinc whitlockite ($Ca_{18}Zn_2(HPO_4)_2(PO_4)_{12}$) synthesized via a phase transformation process under hydrothermal conditions, *CrystEngComm*, 24(28), 2022, 5068-5079, (http://dx.doi.org/10.1039/D2CE00497F).

[160] B.O. Fowler, E.C. Moreno, W.E. Brown, Infra-red spectra of hydroxyapatite, octacalcium phosphate and pyrolysed octacalcium phosphate, *Archives of Oral Biology*, 11(5), 1966, 477-492, (https://doi.org/10.1016/0003-9969(66)90154-3).

[161] F.M. McCubbin, B.L. Phillips, C.T. Adcock, K.T. Tait, A. Steele, J.S. Vaughn, M.D. Fries, V. Atudorei, K.E.V. Kaaden, E.M. Hausrath, Discreditation of bobdownsite and the establishment of criteria for the identification of minerals with essential monofluorophosphate (PO_3F^{2-}), *American Mineralogist*, 103(8), 2018, 1319-1328, (https://doi.org/10.2138/am-2018-6440).

[162] M. Ben Osman, S. Diallo-Garcia, V. Herledan, D. Brouri, T. Yoshioka, J. Kubo, Y. Millot, G. Costentin, Discrimination of Surface and Bulk Structure of Crystalline

Hydroxyapatite Nanoparticles by NMR, *The Journal of Physical Chemistry C*, 119(40), 2015, 23008-23020,
(https://doi.org/10.1021/acs.jpcc.5b08732).

[163] R.G. Carrodeguas, S. De Aza, α-Tricalcium phosphate: Synthesis, properties and biomedical applications, *Acta Biomaterialia*, 7(10), 2011, 3536-3546,
(https://doi.org/10.1016/j.actbio.2011.06.019).

[164] L. Obadia, P. Deniard, B. Alonso, T. Rouillon, S. Jobic, J. Guicheux, M. Julien, D. Massiot, B. Bujoli, J.-M. Bouler, Effect of Sodium Doping in β-Tricalcium Phosphate on Its Structure and Properties, *Chemistry of Materials*, 18(6), 2006, 1425-1433,
(https://doi.org/10.1021/cm052135f).

[165] A.T. Grigg, M. Mee, P.M. Mallinson, S.K. Fong, Z. Gan, R. Dupree, D. Holland, Cation substitution in β-tricalcium phosphate investigated using multi-nuclear, solid-state NMR, *Journal of Solid State Chemistry*, 212, 2014, 227-236,
(https://doi.org/10.1016/j.jssc.2013.10.026).

[166] E. Davies, M.J. Duer, S.E. Ashbrook, J.M. Griffin, Applications of NMR Crystallography to Problems in Biomineralization: Refinement of the Crystal Structure and ^{31}P Solid-State NMR Spectral Assignment of Octacalcium Phosphate, *Journal of the American Chemical Society*, 134(30), 2012, 12508-12515,
(https://doi.org/10.1021/ja3017544).

[167] A. Kizalaite, V. Klimavicius, V. Balevicius, G. Niaura, A.N. Salak, J.C. Yang, S.H. Cho, T. Goto, T. Sekino, A. Zarkov, Dissolution-precipitation synthesis and thermal stability of magnesium whitlockite, *Crystengcomm*, 25(30), 2023, 4370-4379,
(https://doi.org/10.1039/D3CE00602F).

[168] D. Griesiute, A. Kizalaite, A. Dubnika, V. Klimavicius, V. Kalendra, V. Tyrpekl, S.H. Cho, T. Goto, T. Sekino, A. Zarkov, A copper-containing analog of the biomineral whitlockite: dissolution–precipitation synthesis, structural and biological properties, *Dalton Transactions*, 53(4), 2024, 1722-1734,
(http://dx.doi.org/10.1039/D3DT03756H).

[169] A.J. Nelson, J.G. Reynolds, J.W. Roos, Core-level satellites and outer core-level multiplet splitting in Mn model compounds, *Journal of Vacuum Science & Technology A*, 18(4), 2000, 1072-1076,
(https://doi.org/10.1116/1.582302).

SANTRAUKA

ĮVADAS

Kaulinį audinį gali pažeisti traumos, uždegiminiai procesai, vėžys ir daugybė ligų, tokių kaip osteoporozė. Kasmet šie susirgimai paliečia vis daugiau žmonių. Ši problema ypač opi vyresnio amžiaus žmonėms dėl dažnesnių kaulinio audinio ligų bei didesnės sužalojimų rizikos, siejamos su mažėjančia kaulų mase bei tankiu. Nors kaulinis audinys gali gyti savaime, šiam procesui didelę įtaką daro pažeidimo mastas bei pobūdis. Kaulai taip pat pasižymi ilga gijimo trukme ir gali sugyti netinkamai. Dėl šių priežasčių moksliniai tyrimai, kuriantys naujas medžiagas kaulinio audinio pakeitimui bei gydymui, yra itin svarbūs šiuolaikinėje medicinoje.

Pagrindiniai neorganinės kaulinio audinio matricos komponentai yra kalcio fosfatai (CPs). Būtent šie junginiai yra daugiausia potencialo turintys ir plačiausiai naudojami kaulų regeneracinės medicinos srityje dėl savo cheminių ir struktūrinių panašumų į natūralų kaulinį audinį [1]. Vienas iš CP šeimai priklausančių junginių yra magnio vitlokitas (Mg-WH: $Ca_{18}Mg_2H_2(PO_4)_{14}$), kurį galime laikyti Mg jonais pakeistu CP, aptinkamu ir natūraliame kauliniame audinyje. Tai antras pagal paplitimą mineralas žmogaus organizme, sudarantis 20–35 % viso kaulinio audinio [2]. Deja, šis junginys dar nėra plačiai ištirtas, todėl mažai žinoma apie šio junginio reikšmę ir formavimosi procesus žmogaus organizme. Nepaisant to, sintetinis Mg-WH yra žinomas dėl savo biologinio aktyvumo ir biologinio suderinamumo bei osteogeninių savybių, nebūdingų daugumai kitų CPs [3]. Palyginamasis *in vitro* ir *in vivo* tyrimas, kuriame buvo tiriamas Mg-WH, hidroksiapatito (HAP: $Ca_{10}(PO_4)_6(OH)_2$) ir β-trikalcio fosfato (β-TCP) biologinis suderinamumas, atskleidė, kad karkasai, į kurių struktūrą buvo įterpta Mg-WH, darė teigiamą įtaką kaulinio audinio ląstelių specializacijai lyginant su kitais nagrinėtais CPs [3].

Vienas iš būdų pagerinti kalcio fosfatinių medžiagų savybes yra dalinis Ca jonų pakeitimas kitais jonais [4]. Ši strategija leidžia išlaikyti reikiamas CPs savybes, suteikiant junginiui naujų – antibakterinių, optinių, magnetinių ir t. t. Taikant joninio pakeitimo metodą sukuriami nauji biologiniu suderinamumu pasižymintys daugiafunkciniai junginiai, turintys plačias panaudojimo galimybes [5].

Nors pirmos eilės pereinamųjų metalų jonų dydis yra panašus į Mg^{2+} jonų [6], yra vos keletas literatūros šaltinių, kuriuose minimi kitų metalų jonais pakeisti WH struktūros tipo junginiai. Zn yra vienas iš žmogaus organizmui būtinų jonų, dalyvaujantis daugybėje biologinių procesų, kurio trūkumas gali lemti įvairius skeleto pakitimus [9]. Zn savo stuktūroje turintiems CPs yra būdingas aukštas biologinis aktyvumas ir antibakterinės savybės [10, 11]. Cu legiruoti CPs pasižymi angiogeninėmis ir antibakterinėmis savybėmis bei teigiamai veikia kaulinio audinio formavimosi procesus [12]. Įvairūs Mn turintys CPs, tokie kaip HAP [13], amorfinis kalcio fosfatas (ACP) [14] ir kt., yra naudojami magnetinio rezonanso vaizdinime (MRI) dėl savo magnetinių savybių. Daliai Cu, Zn, Mn savo sudėtyje turinčių junginių būdingos antibakterinės savybės [15] bei osteogeniškumas [16].

Palyginus su kitais CPs, WH nėra plačiai ištirtas nei biologinio aktyvumo, nei kristalinės struktūros, nei terminio stabilumo aspektais. Ilgą laiką buvo manoma, kad šio junginio sintezė yra sudėtinga dėl pašalinių CPs fazių susidarymo. Tačiau šiais laikais tai nebėra problema ir jau yra žinoma nemažai skirtingų sėkmingo faziškai gryno WH gavimo būdų [17-19]. Priklausomai nuo panaudojimo srities, CPs medicinoje gali būti naudojami įvairiais pavidalais. Literatūros šaltiniuose Mg-WH yra minimas miltelių [18], granulių [20], dangų ant TCP keramikos [21] ir įvairių kompozitų [22-24] formoje. Tačiau duomenų apie Mg-WH keramikos gamybą nėra. Įprastai keramikos gamybos metu naudojamas sukepinimas aukštoje temperatūroje, būtinas medžiagos sutankinimui. Šiam procesui didelę įtaką daro junginio terminis stabilumas, todėl bazinės žinios apie medžiagos terminį skilimą yra būtinos siekiant tinkamai pasiruošti keramikos gamybos procesui. Mg- WH yra laikomas termiškai nestabiliu junginiu, tačiau šios medžiagos terminio skilimo procesas ir faziniai virsmai iki šiol nebuvo nuodugniai išnagrinėti.

Šio darbo tikslas buvo susintetinti ir nuodugniai ištirti Mg ir pereinamųjų metalų WH savybes bei šių junginių potencialą regeneracinėje medicinoje.

Darbo uždaviniai:

- Sukurti patikimą tirpinimo-nusodinimo sintezės metodą Mg-, Zn- ir Cu-WH milteliams hidroterminėmis sąlygomis.
- Susintetinti Zn- ir Mn-WH miltelius vandeniniuose tirpaluose, atmosferos slėgyje, tirpinimo-nusodinimo metodu.
- Ištirti, aprašyti susintetintų produktų struktūrines, fizikines, morfologines ir biologines savybes bei terminį stabilumą.

Mg-WH sintezė

Mg-WH miltelių sintezė buvo atliekama hidroterminėmis sąlygomis tirpinimo-nusodinimo metodu. Vykdant sintezę reikiami $CaHPO_4 \cdot 2H_2O$ ir $Mg(CH_3COO)_2 \cdot 4H_2O$ kiekiai, atitinkantys Ca/Mg molinį santykį 9, buvo ištirpinami dejonizuoto vandens ir H_3PO_4 mišinyje, PTFE inde. Gautame tirpale bendra metalų jonų koncentracija buvo 0,06 M. Tuomet pH buvo pakeltas iki 6,4, į tirpalą įlašinus nedidelį kiekį koncentruoto NH_4OH tirpalo. Gautas reakcijos mišinys buvo užsandarinamas nerūdijančio plieno reaktoriuje ir kaitinamas krosnyje 160 °C temperatūroje 3 val.

Zn-WH sintezė atmosferos slėgyje

Vykdant sintezę reikiami $CaHPO_4 \cdot 2H_2O$ ir $Zn(CH_3COO)_2 \cdot 2H_2O$ kiekiai, atitinkantys Ca/Zn molinius santykius 9; 10; 12; 15; 20; 30, buvo ištirpinti 100 mL dejonizuoto vandens ir 13 mL 1 M H_3PO_4 tirpalo. Mišiniai buvo maišomi ir šildomi naudojant magnetinę maišyklę 75 °C temperatūroje 1 val. Tuomet tirpalo pH buvo pakeliamas iki 5,6 naudojant NH_4OH tirpalą. Gautas reakcijos mišinys buvo toliau maišomas 75 °C temperatūroje 3 val.

Zn-WH sintezė hidroterminėmis sąlygomis

Atliekant šią sintezę reikiami $CaHPO_4 \cdot 2H_2O$ ir $Zn(CH_3COO)_2 \cdot 2H_2O$ kiekiai, atitinkantys Ca/Zn molinius santykius 6; 8; 9; 10; 12; 30, buvo ištirpinti 50 mL dejonizuoto vandens ir 6,5 mL 1 M H_3PO_4 tirpalo. Mišiniai buvo maišomi naudojant magnetinę maišyklę 30 min. Tuomet tirpalo pH buvo pakeliamas iki 5,8 naudojant NH_4OH tirpalą. Gautas reakcijos mišinys buvo užsandarinamas nerūdijančio plieno reaktoriuje ir kaitinamas krosnyje keičiant reakcijos laiką ir temperatūrą.

Cu-WH sintezė

Atliekant šią sintezę reikiami $CaHPO_4 \cdot 2H_2O$ ir $Cu(NO_3)_2 \cdot 3H_2O$ kiekiai, buvo ištirpinti 50 mL dejonizuoto vandens ir 10 mL 1 M H_3PO_4 tirpalo. Mišinys buvo maišomas naudojant magnetinę maišyklę kol medžiagos ištirpo ir pašarmintas naudojant NH_4OH tirpalą. Gautas reakcijos mišinys buvo užsandarinamas nerūdijančio plieno reaktoriuje ir kaitinamas krosnyje keičiant reakcijos laiką ir temperatūrą.

Mn-WH sintezė

Vykdant sintezę reikiami $CaHPO_4 \cdot 2H_2O$ ir $Mn(CH_3COO)_2 \cdot 4H_2O$ kiekiai, atitinkantys Ca/Mg molinį santykį 9, buvo ištirpinami dejonizuoto vandens ir H_3PO_4 mišinyje. Tuomet tirpalo pH buvo pakeliamas iki 5,6 naudojant NH_4OH tirpalą. Tuomet mišiniai buvo patalpinti į 250 mL užsukamą stiklinį butelį ir maišomi inkubatoriuje (Biosan ES-20/80) 3 val. 75 °C temperatūroje.

Tyrimo metodai

Rentgeno spindulių difrakcinė (XRD) analizė buvo atlikta naudojant rentgeno spindulių difraktometrą Rigaku MiniFlex II (rentgeno spindulių šaltinis Cu-Kα, λ = 1,5419 Å). Matavimai buvo atliekami 2θ intervale 10–100 °, 1 °/min greičiu. Mg-WH bandiniams ši analizė buvo atlikta naudojant PANalytical X’Pert Powder difraktometrą (rentgeno spindulių šaltinis Cu-Kα, λ = 1,5419 Å). Gauti duomenys buvo panaudoti kristalinės gardelės parametrų, sudėties ir struktūros tikslinimui Rietveld metodu. Šiam tikslui buvo naudojamos Match! (versija 3.10.2.173) ir FullProf Suite (versija September-2020) programos, etalonu naudojant ICSD 143481. Tiriant junginius Furjė transformacijos infraraudonųjų spindulių spektroskopijos (FTIR) metodu, spektrams užrašyti buvo naudojamas Bruker ALPHA-FTIR spektrometras. Spektrai buvo rašomi 4000–400 cm^{-1} intervale. Raman analizė buvo atlikta naudojant WiTec Alpha 300 R su 532 nm lazeriu. Mg-WH Raman spektrams nustatyti buvo naudojamas Reinshaw inVia Raman spektrometras su 325 nm ir 532 nm bangos ilgio lazeriais. Susintetintų junginių morfologija buvo tiriama naudojant skenuojantį elektroninį mikroskopą (SEM) Hitachi SU 9000. Zn-WH mėginių analizei naudotas SEM Hitachi SU-70. Peršviečiamosios elektroninės mikroskopijos (TEM) tyrimai buvo atlikti naudojant JEOL JEM-2100F FEG TEM prietaisą. Rentgeno fotoelektronų spektrometrijos (XPS) tyrimams buvo naudojamas Kratos Axis Supra spektrometras su Al-Kα spinduliuotės šaltinius (25 mA, 15 kV). Kieto kūno branduolių magnetinio rezonanso tyrimams buvo pasiteltas Bruker Avance Neo 600 NMR spektrometras naudojant 600,3 MHz dažnį ^{1}H ir 243,0 MHz – ^{31}P spektrams gauti. Susintetintų junginių elementinė sudėtis buvo tiriama induktyviai susietos plazmos optinės emisijos spektrometrijos (ICP-OES) metodu, naudojant Perkin-Elmer Optima 7000 DV spektrometrą. Magnetinio jautrio tyrimai buvo atlikti naudojant Quantum Design MPMS3 SQUID magnetometrą. N_2 adsorbcijos ir desorbcijos izotermoms gauti buvo pasitektas TriStar II 3020 analizatorius. Ląstelių gyvybingumo tyrimai buvo atlikti taikant ISO 10993-5:2009 standarte pateikiamas rekomendacijas, naudojant MC3T3-E1 preosteoblastų ląsteles.

REZULTATŲ APTARIMAS

Pirmasis šiame darbe nagrinėjamas kalcio fosfatas yra Mg-WH, kurio sėkminga sintezė esant hidroterminėms sąlygoms buvo patvirtinta XRD (1a pav.), FTIR (1b pav.) bei Raman (1c pav.) analizės metodais. Vibracinė spektroskopija yra būtina siekiant patikimai nustatyti WH struktūros tipo junginius, nes Mg-WH ir β-TCP yra būdingos identiškos rentgeno spindulių difraktogramos. Žymiausias šių junginių struktūrinis skirtumas pastebimas FTIR ir Raman spektruose. Čia matoma HPO_4^{2-} grupei būdinga smailė ties 920 cm^{-1}, egzistuojanti tik Mg-WH struktūroje. β-TCP struktūrose šios smailės nėra. Rietveld tikslinimo metodu nustatyti gardelės parametrai $a = 10{,}348$ Å; $c = 37{,}153$ Å savo vertėmis buvo artimi literatūroje minimoms vertėms. Gautai N_2 absorbcijos-desorbcijos izotermai (1d pav.) buvo priskirtas IV tipas su H3 histerezės kilpos tipu. Šiam tipui būdingi plokštelių pavidalo dalelių agregatai, su plyšių formos poromis. Tokia dalelių morfologija taip pat buvo patvirtinta SEM bei TEM matavimais ir yra būdinga visiems šiame darbe nagrinėjamiems WH junginiams.

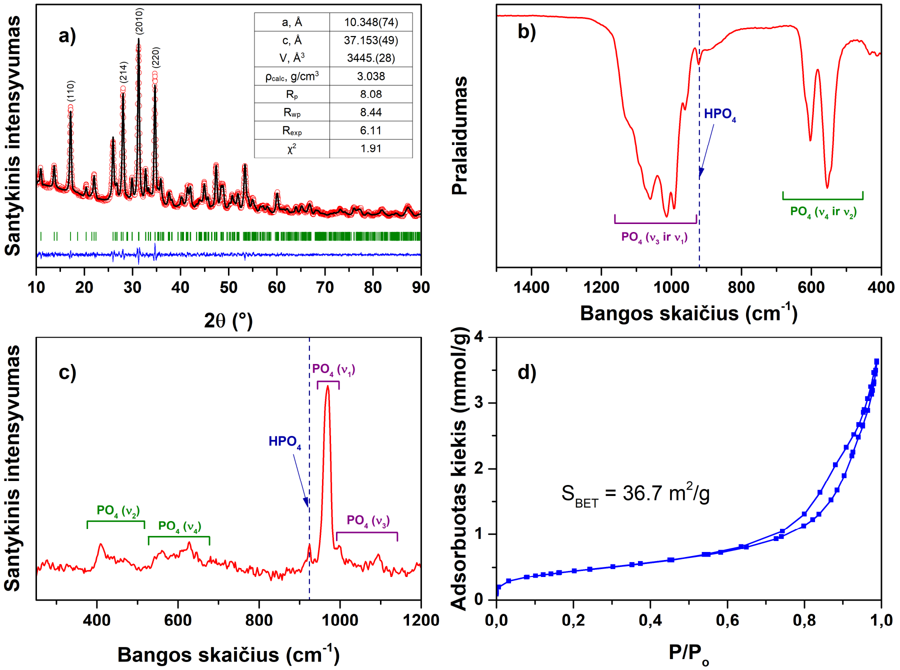

1 pav. Mg-WH miltelių Rietveld tikslinimo rezultatai (a); FTIR spektras (b); Raman spektras (c); ir N_2 absorbcijos-desorbcijos izoterma (d).

Atlikus išsamią šio junginio terminio stabilumo analizę pastebėta, jog Mg-WH yra stabilus žemesnėje nei 700 °C temperatūroje. Pasiekus 700 °C stebimas CPP polimorfams būdingų smailių atsiradimas rentgeno spindulių difraktogramose (2 pav.). 800–1100 °C temperatūrų ruože stebimas tik β-CPP bei β-TCP būdingos smailės. 1200 °C temperatūroje β-CPP transformuojasi į α-CPP fazės junginį, o 1300 °C – vėl grįžta į β-CPP fazę. Šie rezultatai buvo patvirtinti FTIR, Raman ir NMR analizės metodais.

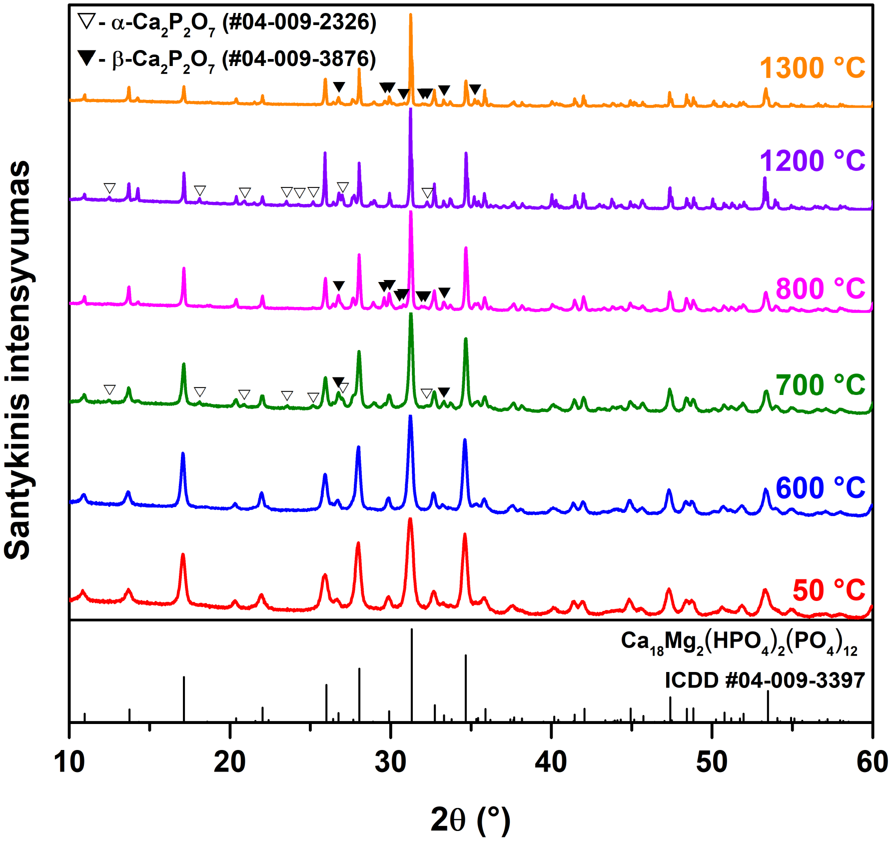

2 pav. Skirtingose temperatūrose iškaitintų Mg-WH miltelių rentgeno spindulių difraktogramos.

Atmosferos slėgio sąlygose gauta Zn-WH junginių serija su kintamu Zn kiekiu struktūroje. Ca/Zn santykiui pradiniame reakcijos mišinyje esant intervale tarp 9 ir 30 gauti faziškai gryni junginiai. Esant didesniam Zn kiekiui, buvo gaunama papildoma šiolzito fazė, o Zn kiekį sumažinus, gaunamas WH ir CDHA mišinys. Ištyrus elementinę gautų miltelių sudėtį, nustatyta, kad keičiant Ca/Zn santykį pradiniame mišinyje, šis santykis gaunamų sintezės produktų struktūroje taip pat kinta (1 lentelė). Tuo tarpu, bendras metalo jonų ir P santykis išlieka pastovus ir artimas teoriniam WH būdingam santykiui. Susidariusių dalelių dydis bei forma gali būti kontroliuojamas keičiant bendrą pradinių medžiagų koncentraciją pradiniame mišinyje bei Ca/Zn molinį santykį.

1 lentelė. Zn-WH miltelių elementinės analizės ICP-OES metodu rezultatai.

Pradinis Ca/Zn molinis santykis	**Produktų Ca/Zn molinis santykis**	**Produktų M/P molinis santykis**
30	29,7	1,41
20	18,5	1,41
15	14,5	1,40
12	12,2	1,41
10	9,85	1,40
9	8,94	1,41

Sintetinant Zn-WH hidroterminėmis sąlygomis, faziškai gryni junginiai buvo gaunami tik siaurame pradinio mišinio sudėties intervale, kai Ca/Zn molinis santykis buvo tarp 8 ir 9. WH struktūros tipo junginio susidarymas buvo patvirtintas FTIR, Raman ir NMR spektroskopijos pagalba. Susidariusiems junginiams būdingos romboedro formos plokštelių pavidalo dalelės, kurių dydis bei forma gali būti kontroliuojami keičiant bendrą pradinių medžiagų koncentraciją pradiniame mišinyje.

Cu-WH atveju faziškai gryni junginiai gauti tik pradiniam Ca/Cu santykiui esant 9. Atlikus Rietveld tikslinimą nustatyta, kad gautam junginiui būdingi gardelės parametrai a = 10,330 Å ir c =37,077 Å. Cu-WH terminio stabilumo analizė parodė, kad šio junginio terminio skilimo produktui α-CPP būdingos smailės XRD matomos jau 600 °C temperatūroje, t. y. 100 °C žemesnėje nei Mg-WH atveju (3 pav.). Temperatūrai kylant toliau, ties 800 °C matomas α- ir β-CPP būdingos smailės, o nuo 900 °C tik β-CPP būdingos smailės. Ląstelių gyvybingumo tyrimas parodė, kad Cu-WH nebūdingas citotoksiškumas, visuose mėginiuose ląstelių gyvybingumas viršijo 70 %.

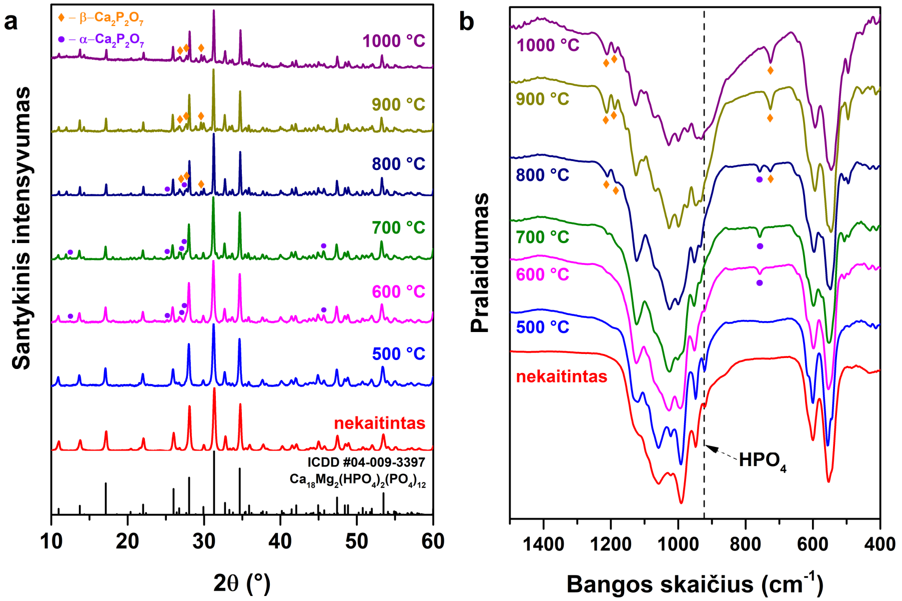

3 pav. Skirtingose temperatūrose iškaitintų Cu-WH miltelių rentgeno spindulių difraktogramos (a) ir FTIR spektrai (b).

Mn-WH buvo sėkmingai susintetintas, kai Ca/Mn molinis santykis reakcijos mišinyje yra 9. Sėkminga junginio sintezė buvo patvirtinta FTIR bei Raman analizės metodais. Rietveld analizės rezultatai rodo, kad šiam junginiui būdingi gardelės parametrai yra a = 10,358(4) Å ir c = 37,077(7) Å. XPS analizė parodė, kad junginio struktūroje dominuojanti Mn jonų oksidacinė būsena yra +2. Magnetinių savybių tyrimai parodė, kad šis junginys pasižymi paramagnetinėmis savybėmis. Atlikus ląstelių gyvybingumo tyrimus buvo nustatyta, kad visoms tirtoms koncentracijoms būdingas gyvybingumo sumažėjimas po 48 val. inkubavimo.

IŠVADOS

1. Tiriant Mg-WH terminį skilimą, buvo pastebėta, kad Mg-WH skilimas kaitinant ir virsmas į Mg-pakeistą β-TCP ir CPP prasideda nuo 700 °C ir vyksta palaipsniui, kylant temperatūrai. Nedidelis kiekis HPO_4^{2-}, būdingas tik Mg-WH struktūrai, buvo stebimas iki 1200 °C. Tai leidžia daryti prielaidą, jog Mg-WH ir Mg pakeisto β-TCP fazės plačiame temperatūrų ruože egzistuoja kartu. Nors visos naudotos tyrimo metodikos buvo tinkamos CPP fazei mėginiuose aptikti, ^{31}P BMR metodas buvo tinkamiausias Mg-WH virsmui į β-TCP stebėti.
2. Zn-WH milteliai su kintamu metalo kiekiu buvo susintetinti pirmą kartą, žemoje temperatūroje, pasitelkiant tirpinimo-nusodinimo metodą. Sintezės produktų sudėties kontrolė buvo pasiekta keičiant Ca/Zn molinį santykį pradiniame reakcijos mišinyje. Nustatyta, kad bendras metalo jonų ir fosforo santykis buvo pastovus ir nepriklausė nuo Ca/Zn molinio santykio galutiniame junginyje. Miltelių morfologija gali būti keičiama, keičiant metalo jonų santykį pradiniame mišinyje. Pastebėta, kad visi susintetinti junginiai buvo termiškai nestabilūs 600 °C temperatūroje ir kaitinant skilo į β-TCP ir CPP.
3. Zn-WH buvo sėkmingai susintetintas tirpinimo-nusodinimo metodu, hidroterminėmis sąlygomis. Faziškai grynas Zn-WH buvo gautas reakciją vykdant trumpą laiką – 1 val. Pastebėta, kad Ca/Zn molinis santykis reakcijos produktuose gali būti keičiamas siaurame sudėties intervale. FTIR, Raman ir ^{1}H kieto kūno BMR patvirtino HPO_4^{2-} grupės buvimą kristalinėje gardelėje. ^{31}P BMR patvirtino trijų ekvivalenčių fosforo atomų egzistavimą junginyje, kur tik vienas iš PO_4 tetraedrų savo struktūroje turi vandenilį. Reakcijos metu gaunamų dalelių dydis bei forma gali būti kontroliuojami keičiant pradinių medžiagų koncentraciją ir Ca/Zn santykį reakcijos mišinyje.
4. Cu-WH buvo sėkmingai susintetintas tirpinimo-nusodinimo metodu, naudojant hidrotermines sąlygas. Pastebėta, kad reakcijai tinkamas pH intervalas buvo labai siauras – nuo 6,4 iki 6,5. Esant parinktoms sintezės sąlygoms, produktų sudėties keitimas nebuvo įmanomas, todėl Ca/Cu molinis santykis 9 buvo parinktas kaip tinkamiausias. Nors XRD ir vibracinės spektroskopijos tyrimų rezultatuose nebuvo įžvelgta pašalinių fazių Cu-WH milteliuose, tačiau BMR tyrimai atskleidė pašalinės amorfinio fosfato fazės buvimą. Cu^{2+} atpalaidavimo biologinėje terpėje tyrimas parodė tolygų koncentracijos didėjimą viso 14 dienų stebėjimo laikotarpio metu, su didžiausiu koncentracijos šuoliu pirmąją dieną po eksperimento pradžios. Terminio stabilumo tyrimai parodė, kad Cu-WH

yra termiškai nestabilus ir skyla į Cu pakeistą β-TCP ir CPP aukštesnėje nei 600 °C temperatūroje. Ląstelių gyvybingumo tyrimai parodė, kad nei vienas iš bandinių nepasižymėjo citotoksiniu poveikiu – visų bandymų metu ląstelių gyvybingumas viršijo 70 %.

5. Mn-WH buvo sėkmingai susintetintas tirpinimo-nusodinimo metodu žemoje temperatūroje atmosferos slėgyje. Rietveld tikslinimo metodas parodė, kad susintetinta medžiaga buvo fazėškai grynas Mn-WH. XRD, XPS ir magnetiniai tyrimai patvirtino Mn jonų egzistavimą +2 oksidacinėje būsenoje, tuo tarpu magnetiniai tyrimai skirtingose temperatūrose patvirtino, kad medžiagai būdingos paramagnetinės savybės temperatūrose iki 5 K. Medžiaga nepasižymėjo toksiškomis savybėmis MC3T3-E1 ląstelėms 24 val. laiko intervale esant koncentracijų intervalui nuo 0,01 iki 1 mg/L. Inkubuojant ląsteles ilgesnį laiką jų gyvybingumas mažėjo.

CURRICULUM VITAE

PERSONAL INFORMATION

Name, Surname:	Agnė Kizalaitė
E-mail:	agne.kizalaite@chgf.vu.lt

EDUCATION

2014 – 2018	Bachelor of Chemistry, Vilnius University.
2018 – 2020	Master of Chemistry, Vilnius University.
2020 – 2024	PhD in Chemistry, Vilnius University.

WORK EXPERIENCE

2018-09 – 2019-05	Vilnius University, Faculty of Chemistry and Geosciences, Senior Specialist.
2021-02 – 2022-04	Vilnius University, Faculty of Chemistry and Geosciences, Junior Researcher.
2022-04 – 2022-12	Vilnius University, Faculty of Chemistry and Geosciences, Junior Researcher.
2022-09 – 2023-09	Vilnius University, Faculty of Chemistry and Geosciences, Project Expert.
2019-06 – 2024-02	Vilnius University, Faculty of Chemistry and Geosciences, Laboratory Technician.
2023-12 – 2024-11	Vilnius University, Methodological STEAM Education Centre, Methodologist.
2023-10 – now	Vilnius University, Faculty of Chemistry and Geosciences, Specialist.
2024-09 – now	Vilnius University, Methodological STEAM Education Centre, Laboratory curator.
2024-12 – now	Vilnius University, Faculty of Chemistry and Geosciences, Junior Assistant.

NOTEWORTHY AWARDS

2021-09-08	Award for best oral presentation at Membrane Materials – Modification and Separation (M3-S) Conference, Torun, Poland.
2022-10-08	Award for best oral presentation at Functional Inorganic Materials (FIM 2022), Vilnius, Lithuania.
2023	Scholarship for scientific achievements from Research Council of Lithuania.

OTHER ACTIVITIES

2021-02 – 2022-04	Participant of the project “Novel bulk and nano composite materials – a way towards superior multiferroic properties” (BUNACOMP) (No. S-MIP-19-9), financed by Research Council of Lithuania.
2022-04 – 2022-12	Participant of the project “New calcium phosphates with whitlockite structure for regenerative medicine purposes: advanced synthesis and fabrication of ceramics” (WHITCERAM) (P-LJB-22-1).
2022-06	Scientific internship at University of Aveiro, Aveiro, Portugal (2022, 1 month).
2023-02-22 – 23	Participant in winter school “Emerging Antimicrobial Biomaterials for Orthopedic Applications”, Zagreb, Croatia.

LIST OF PUBLICATIONS INCLUDED IN THE DISSERTATION

Articles in journals indexed in Claritive Analytics Web of Science database:

1. **A. Kizalaitė**, I. Grigoravičiūtė-Puronienė, D. R. C. Asuigui, S. L. Stoll, S. H. Cho, T. Sekino, A. Kareiva, A. Žarkov, Dissolution–precipitation synthesis and characterization of zinc whitlockite with variable metal content, *ACS Biomaterials Science & Engineering*, 7(8), 2021, 3586-3593, (https://doi.org/10.1021/acsbiomaterials.1c00335).
2. **A. Kizalaitė**, V. Klimavičius, J. Versockienė, E. Lastauskienė, T. Murauskas, R. Skaudžius, T. Yokoi, M. Kawashita, T. Goto, T. Sekino, A. Žarkov, Peculiarities of the formation, structural and morphological properties of zinc whitlockite ($Ca_{18}Zn_2(HPO_4)_2(PO_4)_{12}$) synthesized via a phase transformation process under hydrothermal conditions, *CrystEngComm*, 24(28), 2022, 5068-5079, (http://dx.doi.org/10.1039/D2CE00497F).
3. **A. Kizalaitė**, V. Klimavičius, V. Balevičius, G. Niaura, A. N. Salak, J.-C. Yang, S. H. Cho, T. Goto, T. Sekino, A. Žarkov, Dissolution–precipitation synthesis and thermal stability of magnesium whitlockite, *CrystEngComm*, 25(30), 2023, 4370-4379, (https://doi.org/10.1039/D3CE00602F).
4. D. Griesiūtė, **A. Kizalaitė**, A. Dubnika, V. Klimavičius, V. Kalendra, V. Tyrpekl, S. H. Cho, T. Goto, T. Sekino, A. Žarkov, A copper-containing analog of the biomineral whitlockite: dissolution–precipitation synthesis, structural and biological properties, *Dalton Transactions*, 53(4), 2024, 1722-1734, (https://doi.org/10.1039/D3DT03756H).
5. **A. Kizalaitė**, A. Dubnika, A. Antuzevičs, T. Murauskas, O. Stewart, S. L. Stoll, T. Goto, T. Sekino, A. Žarkov, Low-temperature aqueous synthesis and biocompatibility of manganese whitlockite, *Ceramics International*, 50(16), 2024, 28490-28497, (https://doi.org/10.1016/j.ceramint.2024.05.157).

CO-AUTHORED PUBLICATIONS

The list of co-authored publications that are not part of this dissertation:

1. D. Coglitore, N. Giamblanco, **A. Kizalaitė**, P. E. Coulon, B. Charlot, J.-M. Janot, S. Balme, Unexpected Hard Protein Behavior of BSA on Gold Nanoparticle Caused by Resveratrol, *Langmuir*, 34(30), 2018, 8866-8874, (https://doi.org/10.1021/acs.langmuir.8b01365).
2. **A. Kizalaitė**, V. Brimienė, G. Brimas, J. Kiuberis, S. Tautkus, A. Žarkov, A. Kareiva, Determination of Trace Elements in Adipose Tissue of Obese People by Microwave-Assisted Digestion and Inductively Coupled Plasma Optical Emission Spectrometry, *Biological Trace Element Research*, 189(1), 2019, 10-17, (https://doi.org/10.1007/s12011-018-1450-7).
3. D. Griesiūtė, L. Sinušaitė, **A. Kizalaitė**, A. Antuzevičs, K. Mažeika, D. Baltrūnas, T. Goto, T. Sekino, A. Kareiva, A. Žarkov, The influence of Fe^{3+} doping on thermally induced crystallization and phase evolution of amorphous calcium phosphate, *CrystEngComm*, 23(26), 2021, 4627-4637, (https://doi.org/10.1039/D1CE00371B).
4. V. Klimavičius, A. Maršalka, **A. Kizalaitė**, A. Žarkov, A. Kareiva, K. Aidas, J. Hirschinger, V. Balevičius, Step-by-step from amorphous phosphate to nano-structured calcium hydroxyapatite: monitoring by solid-state 1H and 31P NMR and spin dynamics, *Physical Chemistry Chemical Physics*, 24(31), 2022, 18952-18965, (https://doi.org/10.1039/D2CP02108K).
5. A. Afonina, **A. Kizalaitė**, A. Žarkov, A. Drabavičius, T. Goto, T. Sekino, A. Kareiva, I. Grigoravičiūtė-Puronienė, Synthesis of whitlockite nanopowders with different magnesium content, *Ceramics International,* 48(21), 2022, 32125-32130, (https://doi.org/10.1016/j.ceramint.2022.07.152).
6. D. Karoblis, O. C. Stewart, Jr., P. Glaser, S. E. El Jamal, **A. Kizalaitė**, T. Murauskas, A. Žarkov, A. Kareiva, S. L. Stoll, Low-Temperature Synthesis of Magnetic Pyrochlores ($R_2Mn_2O_7$, R = Y, Ho–Lu) at Ambient Pressure and Potential for High-Entropy Oxide Synthesis, *Inorganic Chemistry*, 62(27), 2023, 10635-10644, (https://doi.org/10.1021/acs.inorgchem.3c00913).
7. G. Inkrataitė, J.-N. Keil, **A. Kizalaitė**, T. Jüstel, R. Skaudžius, Synthesis of praseodymium doped lutetium and gadolinium aluminum garnets modified by scandium and boron to improve luminescence properties, *Ceramics International*, 50(21), 2024, 41879-41891, (https://doi.org/10.1016/j.ceramint.2024.08.041).

PARTICIPATION IN CONFERENCES

1. **A. Kizalaitė**, A. Žarkov. Determination of Magnesium Whitlockite Structural Properties: Rietveld Modeling. Open Readings 2023, Vilnius, Lithuania, 18-21 March 2023, *Poster presentation.*
2. **A. Kizalaitė**, D. Griesiūtė, A. Žarkov. Novel whitlockite compounds: structure and properties. Functional Inorganic Materials (FIM 2022), Vilnius, Lithuania, 6-8 October 2022, *Oral presentation.*
3. **A. Kizalaitė**, H. Klipan, V. Klimavičius, G. Niaura, A. Žarkov. Synthesis, Structural Properties and Thermal Stability of Nanoscale Magnesium Whitlockite. Nanomaterials: Applications & Properties (IEEE NAP-2022), Krakow, Poland, 11-16 September 2022, *Oral presentation.*
4. A. Žarkov; **A. Kizalaitė**; V. Klimavičius; A. Kareiva. Zinc Whitlockite ($Ca_{18}Zn_2(HPO_4)_2(PO_4)_{12}$): Dissolution-Precipitation Synthesis, Structural and Morphological Features. Junior Euromat 2022, Coimbra, Portugal, 19-22 July 2022, *Poster presentation.*
5. **A. Kizalaitė**, H. Klipan, T. Murauskas, A. Žarkov. Synthesis of Manganese Whitlockite via Dissolution-Precipitation Process. Multiscale Phenomena in Condensed Matter (Multis 2022), Kraków, Poland, 27-30 June 2022, *Poster presentation.*
6. **A. Kizalaitė**, E. Kabašinskas, D. Griesiūtė, H. Klipan, G. Klydžiūtė, A. Žarkov. Synthesis of Novel Calcium Phosphates with Whitlockite Structure via Dissolution-Precipitation Process. Open Readings 2022, Vilnius, Lithuania, 15-18 March 2022, *Poster presentation.*
7. **A. Kizalaitė**, T. Murauskas, A. Žarkov, Insight into the Formation of Zinc Whitlockite: Synthesis, Structure and Characterisation, EcoBalt 2021, Riga, Latvia, 21-23 October, 2021, *Oral presentation.*
8. A. Žarkov, **A. Kizalaitė**, D. Griesiūtė, L. Sinušaitė, I. Grigoravičiūtė-Puronienė, A. Kareiva. Dissolution-Precipitation Synthesis of Nanoscale Ion-Substituted Calcium Phosphates with Whitlockite Structure. Nanomaterials: Applications & Properties" (IEEE NAP-2021), Odesa, Ukraine, 5-11 September 2021, *Poster presentation.*
9. **A. Kizalaitė**, A. Kareiva, A. Žarkov. Calcium Phospates for Bone Graft Membranes with Enhanced Biological Properties. Membrane Materials – Modification and Separation (M3-S) Conference, Torun, Poland, 6-8 September 2021, *Oral presentation.*
10. **A. Kizalaitė**, A. Žarkov. Comparative Study of Zinc Whitlockite Synthesized by Different Methods. Advanced Materials and Technologies 2021, Palanga, Lithuania, 23-27 August, 2021, *Poster presentation.*

11. **A. Kizalaitė**, A. Žarkov. Hydrothermal Synthesis of Zinc Whitlockite. Open Readings 2021, Vilnius, Lithuania, 16-19 March 2021, *Poster presentation*.
12. D. Griesiūtė, **A. Kizalaitė**, H. Klipan, A. Žarkov. Synthesis of Cu-Containing Calcium Phosphate with Whitlockite Structure through the Low-Temperature Dissolution-Precipitation Process. Open Readings 2021, Vilnius, Lithuania, 16-19 March 2021, *Poster presentation*.
13. **A. Kizalaitė**, H. Klipan, I. Grigoravičiūtė-Puronienė, A. Kareiva, A. Žarkov. Synthesis of Zinc Whitlockite by Dissolution-Precipitation Process. Nanostructures Bioceramic Materials 2020, Vilnius, Lithuania, 1-3 December 2020, *Poster presentation*.

PUBLICATION REPRINTS

1st publication

Dissolution–precipitation synthesis and thermal stability of magnesium whitlockite

A. Kizalaitė, V. Klimavičius, V. Balevičius, G. Niaura, A. N. Salak,
J. -C. Yang, S. H. Cho, T. Goto, T. Sekino, A. Žarkov

CrystEngComm, 25(30), 2023, 4370-4379
(https://doi.org/10.1039/D3CE00602F)

CrystEngComm

ROYAL SOCIETY OF CHEMISTRY

PAPER

View Article Online
View Journal | View Issue

Check for updates

Cite this: *CrystEngComm*, 2023, **25**, 4370

Dissolution–precipitation synthesis and thermal stability of magnesium whitlockite†

Agne Kizalaite,[a] Vytautas Klimavicius,[b] Vytautas Balevicius,[b] Gediminas Niaura,[b] Andrei N. Salak,[c] Jen-Chang Yang,[d] Sung Hun Cho,[e] Tomoyo Goto,[ef] Tohru Sekino[e] and Aleksej Zarkov*[a]

Received 15th June 2023,
Accepted 5th July 2023

DOI: 10.1039/d3ce00602f

rsc.li/crystengcomm

Magnesium whitlockite (Mg-WH, $Ca_{18}Mg_2(HPO_4)_2(PO_4)_{12}$) is a promising candidate for biomedical application in bone regeneration; however, the fabrication of Mg-WH bioceramics by conventional methods is limited. Mg-WH is known to be thermally unstable and decomposes upon heating. The mechanism of thermal decomposition and phase evolution has not comprehensively been investigated so far. In the present work, Mg-WH was synthesized by a dissolution–precipitation process under hydrothermal conditions. Thermally induced degradation of the synthesized powders was investigated in detail by combining X-ray diffraction (XRD) analysis, infrared spectroscopy (FTIR), Raman spectroscopy as well as ^1H and ^{31}P solid-state nuclear magnetic resonance (NMR). The as-prepared Mg-WH powders were annealed at different temperatures in the range from 400 to 1300 °C. It was found that thermal decomposition starts at around 700 °C with the formation of beta-tricalcium phosphate (β-TCP, $Ca_3(PO_4)_2$) and a mixture of two $Ca_2P_2O_7$ polymorphs. Thermal decomposition occurs gradually and the co-existence of both Mg-WH and Mg-substituted β-TCP phases was observed in a wide temperature range up to 1200 °C. Complete disappearance of the HPO_4^{2-} structural unit was confirmed only after annealing at 1300 °C followed by melting at 1400 °C.

1. Introduction

Calcium phosphates (CPs) are major inorganic constituents of human hard tissues.[1] This reason makes synthetic CPs widely used in the fields of bone regeneration and dentistry due to their chemical and structural similarities to natural bone.[2] While calcium hydroxyapatite (HA, $Ca_{10}(PO_4)_6(OH)_2$) and beta-tricalcium phosphate (β-TCP, $Ca_3(PO_4)_2$) are currently the most commonly used CPs; these materials still have some drawbacks.[3–6] In recent years, another member of the CP family, namely magnesium whitlockite (Mg-WH, $Ca_{18}Mg_2(HPO_4)_2(PO_4)_{12}$) gained a lot of attention from the scientific community. Although in the literature Mg-WH is often mentioned as the second most abundant biomineral in the human body,[7,8] a very recent literature analysis by Shah[9] did not confirm this claim, concluding that Mg-WH is exclusively a pathological biomineral. According to Shah, Mg-WH has never been reported to be in the bone extracellular matrix; therefore, Mg-WH does not constitute a biomimetic strategy for bone repair. Nevertheless, such contradictions do not deny the fact that Mg-WH is an osteoconductive and bioresorbable material suitable for the application as a bone graft substitute. Synthetic Mg-WH demonstrated superior biological performance in both *in vitro* and *in vivo* studies.[4,10–12] Moreover, Mg-WH demonstrated piezoelectric properties, which allows it to be used as a self-powered electrical stimulator for osteogenic, neurogenic and angiogenic differentiation.[13,14]

It was assumed for a long time that synthesis of phase-pure Mg-WH is a challenging task due to the formation of other CPs; however, in recent years this issue was overcame and different successful synthetic approaches were demonstrated.[15–17] Depending on the specific purpose in regenerative medicine, CPs can be used in different forms. To the best of our knowledge, to date Mg-WH has already been prepared in the form of powders,[16] granules,[18] coating

---

[a] *Institute of Chemistry, Vilnius University, Naugarduko 24, LT-03225 Vilnius, Lithuania. E-mail: aleksej.zarkov@chf.vu.lt*
[b] *Institute of Chemical Physics, Vilnius University, Sauletekio 3, LT-10257 Vilnius, Lithuania*
[c] *Department of Materials and Ceramics Engineering/CICECO-Aveiro Institute of Materials, University of Aveiro, 3810-193 Aveiro, Portugal*
[d] *Graduate Institute of Nanomedicine and Medical Engineering, College of Biomedical Engineering, Taipei Medical University, 250 Wu-Hsing St., Taipei 11052, Taiwan*
[e] *SANKEN (The Institute of Scientific and Industrial Research), Osaka University, 8-1 Mihogaoka, Ibaraki, Osaka 567–0047, Japan*
[f] *Institute for Advanced Co-Creation Studies, Osaka University, 1-1 Yamadaoka, Suita, Osaka 565-0871, Japan*

† Electronic supplementary information (ESI) available. See DOI: **https://doi.org/10.1039/d3ce00602f**

This journal is © The Royal Society of Chemistry 2023

on TCP ceramics[19] and different composites;[10,20,21] however, there are no data on the fabrication of ceramics. Conventional ceramic routes consider sintering at high temperature, which is needed for the densification of materials. It is obvious that such an approach is limited by thermal stability of materials; therefore, the basic knowledge on the thermal degradation of the material is crucial as preparation work for the fabrication of ceramics.

Mg-WH is assumed to be thermally unstable; however, the mechanism of thermal decomposition and phase evolution was not comprehensively investigated so far. Moreover, some contradictions can be found in the literature regarding the thermal stability of WH. For instance, Gopal *et al.*[22] reported that Mg-WH decomposes in two steps by releasing water and transforming into β-TCP. Around 20% of water is released at *ca.* 780 °C and the remaining amount at around 1035 °C. These results were partially confirmed by Kaliannagounder *et al.*,[13] who concluded that Mg-WH powders retain the WH structure after annealing at 750 °C; however, the powders transform into β-TCP and $Ca_2P_2O_7$ at 1000 °C. On the other hand, Jang *et al.*[7] did not observe any secondary phase after the heat treatment of Mg-WH even at 1450 °C.

The difference between polycrystalline WH and β-TCP (or Mg-substituted β-TCP) is not distinguishable by means of laboratory XRD, since both these materials have a rhombohedral structure with the *R*3*c* space group (#161) and essentially similar values of the lattice parameters.[22] This is also the reason why these two names are often used in the literature interchangeably and synonymously. The crystal lattice is composed of two periodically arrayed columns (A and B) along the *c*-axis. Column B is identical in both β-TCP and Mg-WH structures consisting of Ca^{2+} and PO_4^{3-} ions arranged in a pattern: Ca(1)–P(3)O_4–P(2)O_4–Ca(2)–Ca(3). Compositional differences occur in column A: Ca(5) and Ca(4) positions in β-TCP are occupied by Ca ions, whereas in the WH structure Ca is substituted by Mg and H from HPO_4^{2-}, respectively.[7,23] These structural similarities lead to both materials sharing an almost identical XRD pattern.[23,24]

Upon heating, Mg-WH releases H_2O, which is accompanied by the disappearance of the HPO_4^{2-} group and the formation of $P_2O_7^{4-}$; therefore, the HPO_4^{2-} unit could serve as a specific structural marker to monitor thermally induced degradation. The detection of this species is feasible, employing spectroscopic techniques such as infrared or Raman spectroscopy and solid-state nuclear magnetic resonance (NMR). Despite the fact that both ^1H and ^{31}P nuclei are perfect probes for NMR, this technique is very rarely used for the structural characterization of WH. To the best of our knowledge, there are only few studies reporting the use of NMR for the characterization of materials with a WH structure.[25–27] At the same time, it is widely used for the investigation of other CPs.[28,29]

In this work, we present a time-effective and low-cost way to synthesize Mg-WH by a dissolution–precipitation process. The obtained product was evaluated by a full range of characterization techniques to give a comprehensive view on the material. The detailed analysis of the thermal degradation of Mg-WH was performed by annealing the as-prepared material at different temperatures followed by characterization of the obtained products by means of XRD, FTIR and Raman spectroscopy as well as ^1H and ^{31}P NMR.

2. Materials and methods

2.1. Synthesis

Mg-WH powders were synthesized *via* a dissolution–precipitation process under hydrothermal conditions by modifying the previously reported procedure.[25] Calcium hydrogen phosphate dihydrate ($CaHPO_4·2H_2O$, 99.1%, Eurochemicals) and magnesium acetate tetrahydrate ($Mg(CH_3COO)_2·4H_2O$, ≥98%, Roth) were used as starting materials. For the synthesis, certain amounts of $CaHPO_4·2H_2O$ and $Mg(CH_3COO)_2·4H_2O$ corresponding to the Ca-to-Mg molar ratio of 9 were dissolved in a 90 cm^3 Teflon liner in a mixture of 50 mL of deionized water and 5.6 mL of 1 M phosphoric acid (H_3PO_4, 75%, Roth) to obtain a solution with a total metal ion concentration of 0.06 M. The above mixture was stirred with a magnetic stirrer at room temperature until the precursors were fully dissolved. Next, under continuous mixing, concentrated ammonia solution (NH_4OH, 25%, Roth) was added until the pH of the reaction medium raised to 6.4. The increase of pH resulted in the instantaneous formation of white precipitates. Then, the reaction mixture was sealed in a Teflon-lined stainless-steel container and transferred into an oven preheated to 160 °C for 3 h. Afterwards, the container was allowed to cool down to room temperature; the resulting product was vacuum filtered, washed with deionized water, and dried at 50 °C in the oven overnight. The synthesis procedure is schematically illustrated in Fig. 1. The obtained powders were further annealed in air for 5 h at temperatures from 400 to 1300 °C with a step of 100 °C.

2.2. Characterization

Powder X-ray diffraction (XRD) study of the obtained samples was performed using a PANalytical X'Pert Powder diffractometer (Ni-filtered Cu-K_α radiation, λ = 1.5419 Å, PIXcel 1D detector, and the exposition corresponded to about 1 s per step of 0.02° over the angular range of 10–90°) at room temperature. Structural refinement was performed using Match! (software version 3.10.2.173) and FullProf Suite (software version September-2020) programs. Data were fitted using CSD 2046688 as a reference.[30] Fourier transform infrared (FTIR) spectra were obtained in the range of 4000–400 cm^{-1} with a Bruker ALPHA-FTIR spectrometer. Raman spectra were recorded using an inVia Raman (Renishaw, United Kingdom) spectrometer equipped with a thermoelectrically cooled (−70 °C) CCD camera and microscope. The spectra were excited with a 325 nm beam from a continuous wave helium–cadmium (He–Cd) gas laser. The laser power at the sample was restricted to 0.2 mW. A 15×/0.32 NA objective was used during the measurements. The Raman spectra were dispersed by 3600 lines per mm

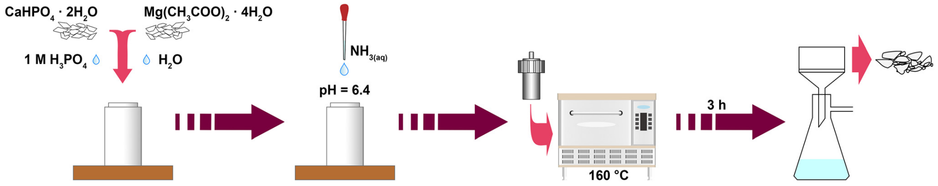

Fig. 1 Schematic representation of the synthesis of Mg-WH powders.

grating. The high-resolution Raman spectra were observed with a 532 nm excitation wavelength, 3000 lines per mm grating, and 20×/0.40 NA objective. The laser power at the sample was 0.5 mW. The spectral slit width determined as the full width at half maximum of the Ne line near 811 cm^{-1} was found to be 2.4 cm^{-1}. The overall integration time for both 325 and 532 nm excitation wavelengths was 400 s. The position of the Raman bands on the wavenumber axis was calibrated using the polystyrene film (532 nm excitation) or Teflon (325 nm excitation) Raman spectrum. The spectra were background corrected by using a 6 order baseline function fit. Parameters of the bands were determined by fitting the experimental spectra with the Gaussian–Lorentzian shape components using GRAMS/A1 8.0 (Thermo Scientific, USA) software. The morphology of the samples was studied by field emission scanning electron microscopy (FE-SEM, SU9000, Hitachi) and transmission electron microscopy (TEM, JEM-ARM 200F, JEOL Ltd.).

Solid-state NMR experiments were carried out at 14.1 T on a Bruker Avance Neo 600 NMR spectrometer operating at 600.3 and 243.0 MHz for ^{1}H and ^{31}P, respectively, using a 2.5 mm Trigamma MAS probe and 2.5 mm zirconia rotors. The temperature was stabilized at 298 K and the MAS rate was set to 10 kHz. For ^{1}H MAS experiments, a pulse sequence employing two π refocusing pulses with a delay of 2 μs was employed to eliminate the signal from the probe background. The ^{1}H 90° excitation pulse was 2.1 μs and 16 scans were accumulated using a repetition delay of 10 s. For ^{31}P MAS measurements, a saturation recovery pulse sequence was used. The saturation pulse train consisted of 20 $\pi/2$ pulses followed by 100 s delay. The $\pi/2$ excitation pulse was equal to 3.6 μs, and 256 scans were accumulated. $^{1}H \rightarrow {}^{31}P$ CP MAS measurements were performed with 4 ms CP contact time employing a 100–50% ramp on the ^{1}H channel, and 1024 scans were accumulated using a repetition delay of 10 s. For ^{31}P–^{31}P 1Q–2Q experiments, a standard pulse sequence was used which employs a BABA (back-to-back) 2 rotor period recoupling scheme.[31] The ^{31}P $\pi/2$ excitation pulse was equal to 3.57 μs, the repetition delay was set to 250 s and 32 scans per 32 increments were accumulated. ^{1}H and ^{31}P spectra were referenced respectively to TMS using adamantane (δ (^{1}H) = 1.85 ppm) and 85% H_3PO_4 using ADP (ammonium dihydrogen phosphate, $NH_4H_2PO_4$, δ (^{31}P) = 0.8 ppm).

The N_2 adsorption and desorption isotherms of the samples were obtained at −196 °C by using a Brunauer–Emmett–Teller (BET) analyzer TriStar II 3020 (Micromeritics). Prior to the gas sorption measurements, all the samples were outgassed in a N_2 atmosphere at 100 °C for 2 h.

Thermogravimetric (TG-DTG) analysis was performed using a Perkin Elmer STA 6000 simultaneous thermal analyzer. A sample of 10 mg was heated from 25 to 900 °C at a heating rate of 10 °C min^{-1} in a dry flowing air (20 mL min^{-1}).

3. Results and discussion

The XRD analysis confirmed the successful synthesis of single-phase Mg-WH; no diffraction peaks attributed to other crystalline phases were observed in the XRD pattern (Fig. 2a). Rietveld refinement was used for further structural analysis; the refinement was successful with adequate description of all the observed diffraction peaks. The calculated lattice parameters (a = 10.348 Å; c = 37.153 Å) were close to those reported in the literature for both synthetic and natural WH,[22,30] though the a parameter was slightly smaller while the c parameter was slightly larger. Besides, the experimental data indicated slightly more intense reflections from the (110), (214) and (220) planes and less intense reflection from the (2010) plane as compared to the calculated data.

Vibrational spectroscopy is crucial for the reliable identification of the WH structure as both Mg-WH and β-TCP are characterized by an identical powder XRD pattern. The most prominent difference between the FTIR and Raman spectra of these two compounds is the band assigned to the HPO_4^{2-} group (*ca.* 920 cm^{-1}), which is present only in Mg-WH and absent in β-TCP;[7] therefore, it can be assumed as a spectral marker for distinguishing these materials. The above-mentioned signal is clearly visible in both FTIR (Fig. 2b) and Raman (Fig. 2c) spectra of our synthesized material, which confirms the formation of Mg-WH. Other observed bands are ascribed to different phosphate vibration modes; their positions are in good agreement with the data reported for WH in the literature.[15,32] It is worth noting that no visible bands associated with other CPs were observed, which agrees well with the XRD data and confirms the purity of the synthesized material.

The BET method was used to measure the surface area of the as-prepared Mg-WH powder. The N_2 adsorption–desorption isotherm (Fig. 2d) was assigned to type IV with a type H3 hysteresis loop. The type H3 hysteresis loop is usually indicative to plate-like particle aggregates which

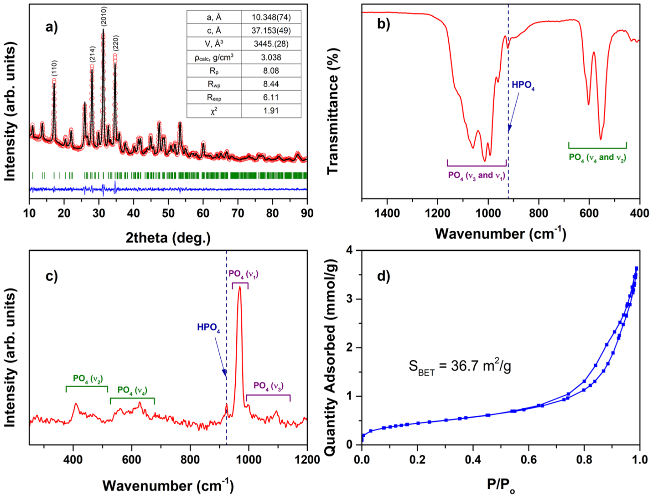

Fig. 2 Results of Rietveld refinement (a), the red circle symbols and the black solid line represent the experimental and calculated intensities, respectively, and the blue line below is the difference between them. The green tick marks indicate the positions of the Bragg peaks; FTIR spectrum (b); 532 nm excited Raman spectrum (c); N_2 absorption–desorption isotherm (d) of the as-prepared Mg-WH powder.

result in slit-shape pores.[33] The specific surface area (S_{BET}) was calculated to be 36.7 m^2 g^{-1}.

SEM and TEM images (Fig. 3) show that the synthesized powder consists of agglomerated irregularly shaped plate-like particles of nanoscale dimensions. The size of the particles varies in the range of approximately 30–80 nm. Although it is known that Mg-WH is prone to form particles with a distinctive polygonal shape,[17,19,32] in our case only a closer look allows us to see some well-defined hexagonally shaped particles. The observed morphology of the synthesized powder correlates well with the results of BET analysis. The EDX mapping (Fig. 3c–f) shows that all the elements are uniformly distributed in the sample. The Ca-to-Mg ratio was determined as 9 : 0.97, which is close to the theoretical chemical composition of Mg-WH.

As mentioned above, Mg-WH is known to be thermally unstable and degradable upon annealing. Thermal degradation of ideally stoichiometric and defect-free Mg-WH is expected to occur according to eqn (1) with a total weight loss of around 0.8 wt%.

$$Ca_{18}Mg_2(HPO_4)_2(PO_4)_{12} \rightarrow 6Ca_{2.67}Mg_{0.33}(PO_4)_2 + Ca_2P_2O_7 + H_2O \quad (1)$$

The results of thermogravimetric analysis showed a total weight loss of 4.3 wt% in the range from 30 to 900 °C (Fig. S1†), which assumes the presence of adsorbed or trapped

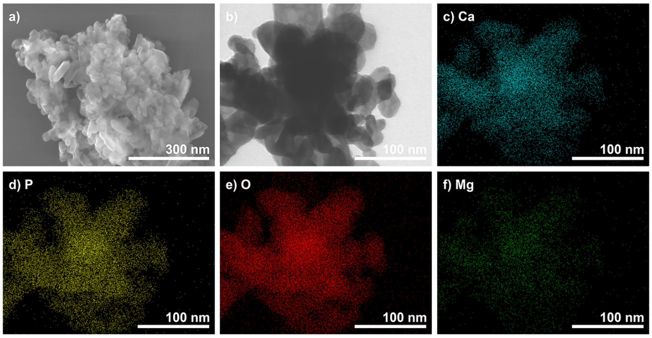

Fig. 3 SEM micrograph (a); TEM image (b); EDX mapping images (c–f) of the as-prepared Mg-WH powder.

moisture and/or other relatively volatile species. More than half of this loss (2.2 wt%) occurs below 200 °C, which can be ascribed to the removal of adsorbed water. It can be seen from the DTG curve that the next significant weight loss occurs in the range of 300–450 °C and the last significant weight loss was observed at 790 °C, which is in a good agreement with the previously reported results.[13,22]

Fig. 4 demonstrates the representative XRD patterns of the Mg-WH samples annealed at different temperatures. The XRD patterns of the Mg-WH samples annealed in the whole range of temperatures from 400 to 1300 °C with a step of 100 °C are given in Fig. S2.†

There were no significant changes in the XRD patterns in terms of arising or disappearing reflection peaks up to 600 °C; the only observed trend was associated with the sharpening of the peaks, which reflects the increase of the grain size and crystallinity of the material. The FWHM values calculated for the (2010) diffraction peak decreased from 0.441° to 0.095° in the transition from as-prepared material to annealed at 1300 °C. The most drastic change reflecting in a 2-fold decrease of FWHM was observed in the range from 600 to 800 °C. The dependence of FWHM on annealing temperature is depicted in Fig. S3.† Evident changes were observed after annealing at 700 °C as two additional phases appeared. Both phases were identified as $Ca_2P_2O_7$ polymorphs, namely α-$Ca_2P_2O_7$ and β-$Ca_2P_2O_7$, which agrees well with the literature data.[13,32] Although α-$Ca_2P_2O_7$ is assumed to be a high-temperature polymorph,[34] the simultaneous formation of both species could be explained by the Ostwald step rule.[35] After annealing at 800 °C, the diffraction peaks of α-$Ca_2P_2O_7$ disappeared, and all newly observed reflections corresponded to β-$Ca_2P_2O_7$. This polymorph was observed in the range from 800 to 1100 °C along with the main WH and/or β-TCP phase. As the annealing temperature reached 1200 °C, β-$Ca_2P_2O_7$ was replaced by α-$Ca_2P_2O_7$, which agrees well with the phase transition temperature between the two polymorphs.[34] Surprisingly, after the annealing at 1300 °C, the secondary phase was β-$Ca_2P_2O_7$ again. Since its formation was unexpected, the annealing procedure was repeated three times with different portions of the as-prepared material; however, the results were reproducible. It is worth noting that after annealing at 1300 °C, the sample was partially melted and completely melted at *ca.* 1400 °C. The observed melting point was lower as compared to the value of 1600 °C reported by Jang *et al.*[7] Summarizing the results of the XRD analysis, it can be concluded that Mg-WH/β-TCP was the dominant product throughout the whole degradation process; however, from the XRD data alone it is impossible to distinguish the co-existence or full replacement of the WH phase by β-TCP.

Rietveld analysis was employed to calculate the lattice parameters and to estimate the structural changes during the Mg-WH decomposition. The obtained data suggest that after the start of the thermal degradation of Mg-WH at 700 °C, Mg^{2+} ions were transferred to the β-TCP structure occupying Ca(5) and Ca(4) crystallographic positions. It is reasonable considering the structural similarities between these two compounds and the ability of β-TCP to adopt small cations.[36,37] According to the literature, the β-TCP structure can adopt around 14 mol% of Mg^{2+} ions, which preferably occupy 6-fold coordinated Ca(5) sites.[38,39] The calculations did not confirm the presence of Mg^{2+} ions in the $Ca_2P_2O_7$ structure; however, due to the fact that only a small amount of $Ca_2P_2O_7$ is visible in the XRD patterns, precise calculations of its Mg content could not be performed. Since the relative Mg content increases during the transformation from WH to β-TCP (from 10 to 11 mol% in Mg-WH and β-TCP, respectively), it was concluded that the Ca(5) position is fully occupied by Mg, while Ca(4) is occupied only partially, which agrees well with previous reports.[38,39] The variation of the lattice parameters of Mg-WH/β-TCP in the range of 600–1300 °C is illustrated in Fig. 5; the numerical values and refinement parameters are provided in Table S1.† The dashed lines indicate the lattice parameters of the as-prepared

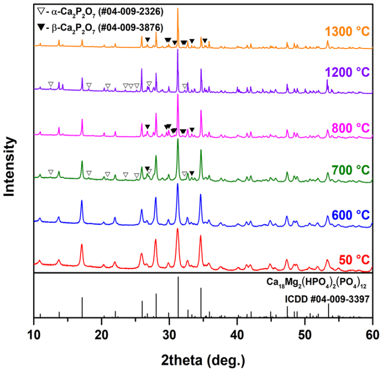

Fig. 4 XRD patterns of Mg-WH powders annealed at different temperatures.

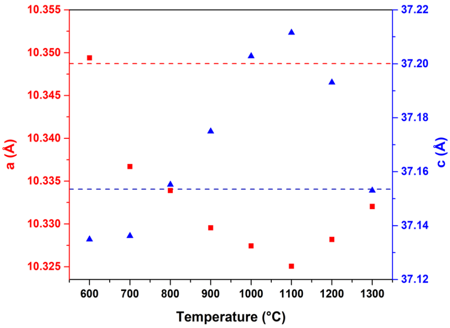

Fig. 5 Lattice parameters of Mg-WH/β-TCP annealed at different temperatures.

material. In the range from 600 to 700 °C, the *c* parameter was nearly constant, while the *a* parameter demonstrated a drastic decrease. A gradual decrease of the *a* parameter was observed in the range of 700–1100 °C, while the *c* parameter increased. The opposite trend was observed in the temperature range of 1100–1300 °C, where the *c* parameter decreased and the *a* parameter increased. This change of trend might be tied to the closeness to the melting point of the obtained β-TCP and $Ca_2P_2O_7$ mixture that should be around 1300 °C.[40] As was mentioned above, in our case the sample annealed at 1300 °C was partially melted.

Fig. 6 shows the FTIR and Raman spectra of the Mg-WH powders annealed at representative temperatures. The spectra of the samples annealed in the whole range of temperatures are given in Fig. S4 and S5.† As it could be expected, the FTIR spectra of β-TCP and Mg-WH are quite similar and show the same band multiplicity due to their very similar phosphate frameworks;[30] therefore, the phase transition from Mg-WH to β-TCP or the co-existence of the two materials cannot be clearly observed from the PO_4-related bands. Thus, attention should be paid on the band centered at 920 cm^{-1}, which is assigned to the HPO_4^{2-} group in the Mg-WH structure. First, the intensity of this band increased with an increase of annealing temperature up to 600 °C, which can be attributed to the increased crystallinity of the material. After annealing at higher temperatures, the trend was opposite: the intensity obviously decreased after the thermal treatment at 700 °C and the presence of this signal was indistinguishable after the treatment above 900 °C. This observation is in good agreement with eqn (1); however, it is worth noting that the temperature of the complete disappearance of the band cannot be detected precisely due to the overlapping with other bands. The absorption bands corresponding to $Ca_2P_2O_7$ can be observed after annealing above 700 °C. The most straightforward way to detect this material is to monitor the presence of absorption bands located at *ca.* 726 and 754 cm^{-1}, which correspond to the P–O–P bond in β- and α-$Ca_2P_2O_7$, respectively.[41] The temperature of the formation and the type of the $Ca_2P_2O_7$ polymorph are in good agreement with the XRD results (Fig. 4).

In the Raman spectra of Mg-WH, the signal corresponding to the HPO_4^{2-} group (*ca.* 926 cm^{-1}) does not overlap with the most intense peak of Mg-WH or β-TCP.[42] The Raman spectroscopy data demonstrated the same trend as the FTIR data (Fig. 6b). The intensity of the band ascribed to HPO_4^{2-} gradually decreased after annealing above 600 °C; however, as compared to FTIR, this band can be easily detected in a broader temperature range. We also tried to detect the Raman spectra with a 532 nm excitation source; however, it was impossible for the samples annealed below 700 °C due to the strong luminescence. High-resolution spectra taken with a 532 nm source are given in Fig. S6.† It is seen that a very weak signal ascribed to HPO_4^{2-} is observed even in the sample annealed at 1200 °C indicating the co-existence of Mg-WH and β-TCP in a wide temperature range. The signal completely vanishes only at 1300 °C. The Raman spectra also show the bands at 738 and 1047 cm^{-1} distinctive to β-$Ca_2P_2O_7$ (ref. 43 and 44) and 776 cm^{-1} ascribed to the α-$Ca_2P_2O_7$ structure.[44,45] Overall, it can be concluded that FTIR and Raman data correlate well with the XRD results.

The ^1H, ^{31}P MAS and ^1H–^{31}P CP MAS spectra of the Mg-WH samples are shown in Fig. 7. The spectra of the as-prepared Mg-WH powder look similar to those previously reported for magnesium and zinc whitlockites.[25,26] The ^1H spectrum consists mainly of a spectral line at 9.8 ppm, which is attributed to the HPO_4^{2-} moiety in the Mg-WH crystal structure. The ^{31}P MAS spectrum consists of the lines at 1.98,

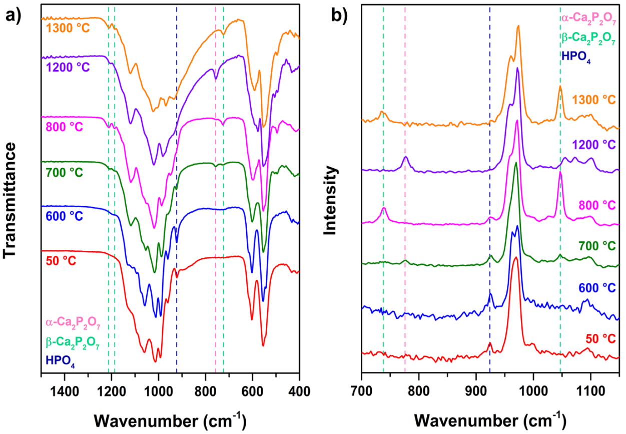

Fig. 6 FTIR (a) and Raman (excitation wavelength is 325 nm) (b) spectra of Mg-WH powders annealed at different temperatures.

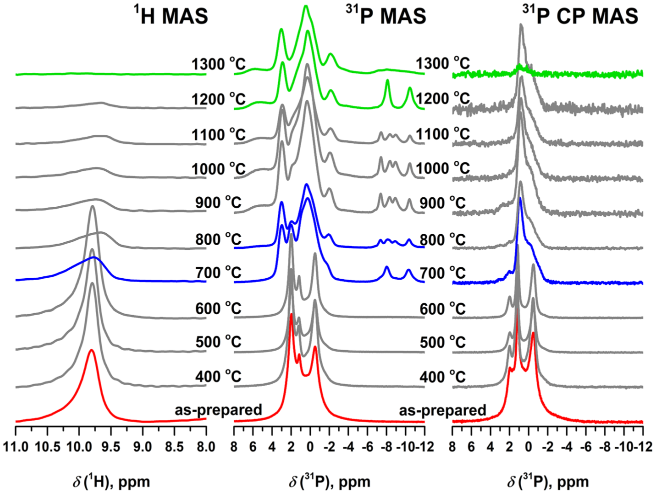

Fig. 7 ^{1}H MAS, ^{31}P MAS and ^{1}H–^{31}P CP MAS spectra obtained for Mg-WH samples annealed at different temperatures. The spectra corresponding to the detected changes in crystal structures are colored.

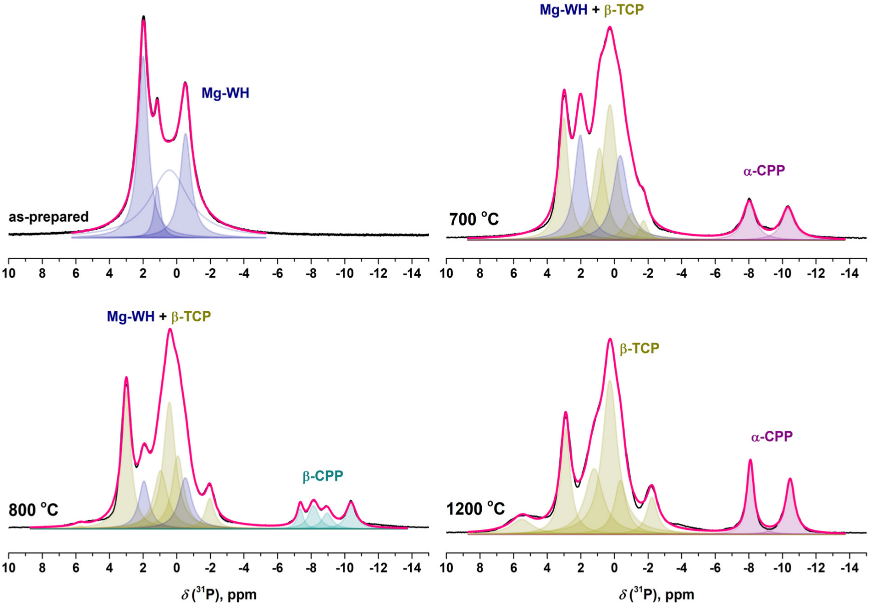

Fig. 8 Selected ^{31}P MAS spectra of the as-prepared and annealed Mg-WH samples; annealing temperatures are indicated in the figure. Signals referring to the Mg-WH phase are indicated in blue, to Mg-substituted β-TCP in dark yellow, to α-$Ca_2P_2O_7$ in purple and to β-$Ca_2P_2O_7$ in dark cyan. Cumulative fit is indicated in pink.

1.14 and −0.50 ppm attributed to P(2), HP(1)O_4^{2-} and P(3) moieties, respectively. In addition, a broad line at 0.47 ppm is observed, which is attributed to distorted phosphate moieties also previously detected for Zn-WH.[25] The line attributed to distorted phosphates decreases in intensity significantly upon annealing, and thus the ^{31}P MAS spectrum looks more resolved. The same lines are observed in the ^{1}H–^{31}P CP MAS spectrum; however, the line at 1.14 ppm is more intense due to the close proximity of phosphorous to ^{1}H in the HPO_4^{2-} moiety. The obvious changes in the NMR spectra upon annealing appear at 700 °C. The line attributed to the HPO_4^{2-} moiety in the ^{1}H MAS spectrum drops in intensity significantly, which shows that the Mg-WH structure is disrupted. This line gradually vanishes upon increasing the annealing temperature to 1300 °C.

In the ^{31}P MAS and ^{1}H–^{31}P CP MAS spectra corresponding to the annealing temperature of 700 °C, the spectral lines attributed to β-TCP and α-$Ca_2P_2O_7$ (−8.01 and −10.32 ppm) start to emerge (Fig. 7). It is worth noting that $Ca_2P_2O_7$ polymorphs have no signals in the range from 8 to −4 ppm; therefore, all spectral changes in this region are attributed to the transformation of Mg-WH to Mg-substituted β-TCP.[34] For better visibility, the ^{31}P MAS spectra, where the spectral changes were detected, are highlighted in Fig. 8. The lines attributed to Mg-WH completely vanished after annealing at 1200 °C and only the lines attributed to Mg-substituted β-TCP (5.56, 2.90, 1.19, 0.27, −0.37, −2.22 ppm) are seen in the spectral region between 8 and −4 ppm.[46] The α-$Ca_2P_2O_7$ polymorph is transformed into β-$Ca_2P_2O_7$ (−7.34, −8.15, −8.90, −10.34 ppm) at 800 °C, then back to α-$Ca_2P_2O_7$ at 1200 °C and ultimately only unresolved traces of $Ca_2P_2O_7$ are seen after the treatment at 1300 °C (Fig. 7 and 8). The observed trend is similar to those previously described for other techniques.

In order to justify the spectral fitting in Fig. 8, ^{31}P–^{31}P 1Q–2Q spectra were obtained for the samples annealed at various temperatures (Fig. 9) and typical correlations referring to Mg-WH and Mg-substituted β-TCP species were assigned.

The representative SEM micrographs of the Mg-WH samples annealed at different temperatures are given in Fig. 10. The size of the particles increased with increasing annealing temperature; however, agglomerated individual particles can still be seen after annealing at 500 °C. After annealing at 600 °C, the individual particles were hardly distinguishable due to the sintering. Finally, after the heat treatment at 700 °C the porous monoliths without visible grain boundaries were formed; however, as was mentioned above, this drastic change in the morphology is accompanied by the start of the thermal degradation of Mg-WH. The morphological changes correlate very well with the sharpening of diffraction peaks in the XRD patterns (Fig. S3†).

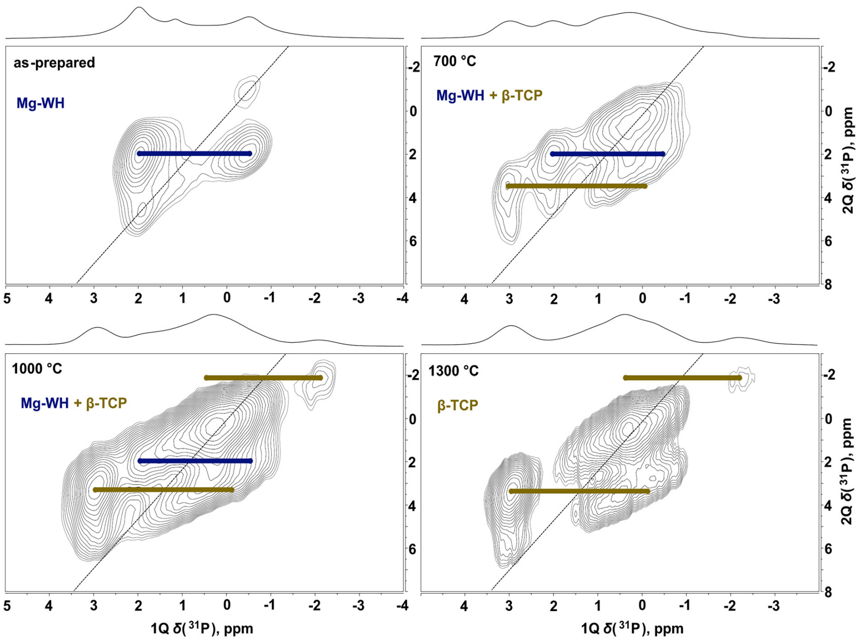

Fig. 9 Selected ^{31}P–^{31}P 1Q–2Q spectra of the as-prepared and annealed Mg-WH samples; annealing temperatures are indicated in the figure. Correlations referring to the Mg-WH phase are indicated in blue and to Mg-substituted β-TCP in dark yellow.

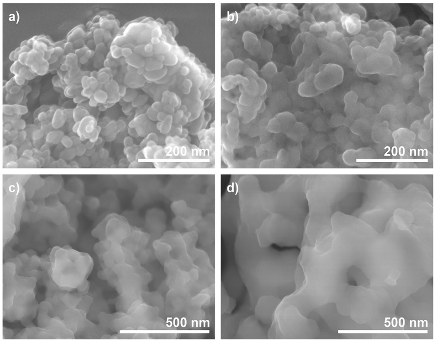

Fig. 10 SEM micrographs of Mg-WH powders annealed at 400 °C (a), 500 °C (b), 600 °C (c) and 700 °C (d).

Taking into account the limitations of employed methods, it can be concluded that the results of all characterization techniques on the thermal degradation of Mg-WH correlate very well. All methods indicated the partial decomposition of Mg-WH accompanied by the formation of the secondary phase at *ca.* 700 °C. The presence of a negligible amount of HPO_4^{2-} structural unit was observed up to 1200 °C suggesting the co-existence of both Mg-WH and Mg-substituted β-TCP phases in a wide temperature range. NMR was found to be the most suitable technique for the detection of Mg-WH to Mg-substituted β-TCP structural transformation.

4. Conclusions

In this study, single-phase Mg-WH nanoparticles were successfully synthesized through the dissolution–precipitation process under hydrothermal conditions. Thermally induced degradation and phase transformations of the synthesized powders were investigated in detail by combining XRD analysis, FTIR and Raman spectroscopy as well as ^1H and ^{31}P NMR. It was found that the degradation of Mg-WH upon annealing and its conversion to Mg-substituted β-TCP and $Ca_2P_2O_7$ occur gradually with an increase of annealing temperature. All employed methods indicated that the decomposition of Mg-WH starts at *ca.* 700 °C. The presence of a negligible amount of HPO_4^{2-}, which belongs exclusively to the Mg-WH structure, was observed up to 1200 °C suggesting the co-existence of both Mg-WH and Mg-substituted β-TCP phases in a wide temperature range. Although all the techniques were found to be suitable for the observation of the appearance of the $Ca_2P_2O_7$ phase, ^{31}P NMR was found to be the most straightforward technique for the detection of Mg-WH to Mg-substituted β-TCP structural transformation. The obtained results suggest that the fabrication of phase-pure Mg-WH bioceramics does not seem to be achievable by conventional high-temperature methods; however, the fabrication of Mg-WH-containing multi-phase ceramics could be possible.

Conflicts of interest

There are no conflicts to declare.

Acknowledgements

This research was funded by a grant WHITCERAM (No. S-LJB-22-1) from the Research Council of Lithuania and supported by the Joint Research Projects under the Bilateral Program (JSPS), RCL JSPS, No. 120224202. The research done in the University of Aveiro was supported by the project CICECO-Aveiro Institute of Materials, UIDB/50011/2020, UIDP/50011/2020 & LA/P/0006/2020, financed by national funds through the FCT/MEC (PIDDAC). V. K., V. B., and G. N. gratefully acknowledge the Center of Spectroscopic Characterization of Materials and Electronic/Molecular Processes (SPECTROVERSUM Infrastructure) for the use of Raman and NMR spectrometers. The authors sincerely acknowledge Dr. Justina Gaidukevic (Vilnius University) for technical assistance.

References

1 S. V. Dorozhkin, *Biomatter*, 2011, **1**, 121–164.
2 W. Habraken, P. Habibovic, M. Epple and M. Bohner, *Mater. Today*, 2016, **19**, 69–87.
3 Y. Pang, D. Li, J. Zhou, X. Liu, M. Li, Y. Zhang, D. Zhang, X. Zhang and Q. Cai, *Biomed. Mater.*, 2022, **17**, 065020.
4 H. L. Jang, G. B. Zheng, J. Park, H. D. Kim, H.-R. Baek, H. K. Lee, K. Lee, H. N. Han, C.-K. Lee, N. S. Hwang, J. H. Lee and K. T. Nam, *Adv. Healthcare Mater.*, 2016, **5**, 128–136.
5 I. Manjubala, M. Sivakumar, R. V. Sureshkumar and T. P. Sastry, *J. Biomed. Mater. Res.*, 2002, **63**, 200–208.
6 R. A. Surmenev, I. Y. Grubova, E. Neyts, A. D. Teresov, N. N. Koval, M. Epple, A. I. Tyurin, V. F. Pichugin, M. V. Chaikina and M. A. Surmeneva, *Surf. Interfaces*, 2020, **21**, 100727.
7 H. L. Jang, K. Jin, J. Lee, Y. Kim, S. H. Nahm, K. S. Hong and K. T. Nam, *ACS Nano*, 2014, **8**, 634–641.
8 H. Cheng, R. Chabok, X. Guan, A. Chawla, Y. Li, A. Khademhosseini and H. L. Jang, *Acta Biomater.*, 2018, **69**, 342–351.
9 F. A. Shah, *Acta Biomater.*, 2021, **125**, 72–82.
10 J. Jeong, J. H. Shim, B. M. Koo, Y. B. Choy and C. Y. Heo, *Tissue Eng. Regener. Med.*, 2022, **19**, 83–92.
11 Y. Yang, H. Wang, H. Yang, Y. Zhao, J. Guo, X. Yin, T. Ma, X. Liu and L. Li, *ACS Biomater. Sci. Eng.*, 2020, **6**, 5785–5796.
12 H. D. Kim, H. L. Jang, H.-Y. Ahn, H. K. Lee, J. Park, E.-s. Lee, E. A. Lee, Y.-H. Jeong, D.-G. Kim, K. T. Nam and N. S. Hwang, *Biomaterials*, 2017, **112**, 31–43.
13 V. K. Kaliannagounder, N. P. M. J. Raj, A. R. Unnithan, J. Park, S. S. Park, S.-J. Kim, C. H. Park, C. S. Kim and A. R. K. Sasikala, *Nano Energy*, 2021, **85**, 105901.
14 L. Wang, Y. Pang, Y. Tang, X. Wang, D. Zhang, X. Zhang, Y. Yu, X. Yang and Q. Cai, *Bioact. Mater.*, 2023, **25**, 399–414.
15 C. Wang, K.-J. Jeong, H. J. Park, M. Lee, S.-C. Ryu, D. Y. Hwang, K. H. Nam, I. H. Han and J. Lee, *J. Colloid Interface Sci.*, 2020, **569**, 1–11.

16 A. Afonina, A. Kizalaite, A. Zarkov, A. Drabavicius, T. Goto, T. Sekino, A. Kareiva and I. Grigoraviciute-Puroniene, *Ceram. Int.*, 2022, **48**, 32125–32130.

17 H. L. Jang, H. K. Lee, K. Jin, H.-Y. Ahn, H.-E. Lee and K. T. Nam, *J. Mater. Chem. B*, 2015, **3**, 1342–1349.

18 W.-B. Lee, C. Wang, J.-H. Lee, K.-J. Jeong, Y.-S. Jang, J.-Y. Park, M. H. Ryu, U.-K. Kim, J. Lee and D.-S. Hwang, *ACS Appl. Bio Mater.*, 2020, **3**, 7762–7768.

19 X. Guo, X. Liu, H. Gao, X. Shi, N. Zhao and Y. Wang, *J. Mater. Sci. Technol.*, 2018, **34**, 1054–1059.

20 X. Zhang, W. Liu, J. Liu, Y. Hu and H. Dai, *ACS Biomater. Sci. Eng.*, 2021, **7**, 3321–3331.

21 S. Amirthalingam, S. S. Lee, M. Pandian, J. Ramu, S. Iyer, N. S. Hwang and R. Jayakumar, *Biomater. Sci.*, 2021, **9**, 2439–2453.

22 R. Gopal, C. Calvo, J. Ito and W. K. Sabine, *Can. J. Chem.*, 1974, **52**, 1155–1164.

23 T. Konishi and S. Watanabe, *Phosphorus Res. Bull.*, 2021, **37**, 1–10.

24 R. Gopal and C. Calvo, *Nat. Phys. Sci.*, 1972, **237**, 30–32.

25 A. Kizalaite, V. Klimavicius, J. Versockiene, E. Lastauskiene, T. Murauskas, R. Skaudzius, T. Yokoi, M. Kawashita, T. Goto, T. Sekino and A. Zarkov, *CrystEngComm*, 2022, **24**, 5068–5079.

26 T. Konishi and S. Watanabe, *Phosphorus Res. Bull.*, 2021, **37**, 21–25.

27 T. Konishi and S. Watanabe, *Phosphorus Res. Bull.*, 2022, **38**, 18–24.

28 C. Gervais, C. Bonhomme and D. Laurencin, *Solid State Nucl. Magn. Reson.*, 2020, **107**, 101663.

29 V. Klimavicius, A. Maršalka, A. Kizalaite, A. Zarkov, A. Kareiva, K. Aidas, J. Hirschinger and V. Balevicius, *Phys. Chem. Chem. Phys.*, 2022, **24**, 18952–18965.

30 F. Capitelli, F. Bosi, S. C. Capelli, F. Radica and G. Della Ventura, *Crystals*, 2021, **11**, 225.

31 M. Feike, D. E. Demco, R. Graf, J. Gottwald, S. Hafner and H. W. Spiess, *J. Magn. Reson., Ser. A*, 1996, **122**, 214–221.

32 A. Kizalaite, I. Grigoraviciute-Puroniene, D. R. C. Asuigui, S. L. Stoll, S. H. Cho, T. Sekino, A. Kareiva and A. Zarkov, *ACS Biomater. Sci. Eng.*, 2021, **7**, 3586–3593.

33 K. S. W. Sing, *Pure Appl. Chem.*, 1985, **57**, 603–619.

34 D. Griesiute, E. Garskaite, A. Antuzevics, V. Klimavicius, V. Balevicius, A. Zarkov, A. Katelnikovas, D. Sandberg and A. Kareiva, *Sci. Rep.*, 2022, **12**, 7116.

35 R. A. Van Santen, *J. Phys. Chem.*, 1984, **88**, 5768–5769.

36 K. Matsunaga, T. Kubota, K. Toyoura and A. Nakamura, *Acta Biomater.*, 2015, **23**, 329–337.

37 L. Sinusaite, A. Kareiva and A. Zarkov, *Cryst. Growth Des.*, 2021, **21**, 1242–1248.

38 R. Enderle, F. Götz-Neunhoeffer, M. Göbbels, F. A. Müller and P. Greil, *Biomaterials*, 2005, **26**, 3379–3384.

39 J. C. Araújo, M. S. Sader, E. L. Moreira, V. C. A. Moraes, R. Z. LeGeros and G. A. Soares, *Mater. Chem. Phys.*, 2009, **118**, 337–340.

40 M. Maciejewski, T. J. Brunner, S. F. Loher, W. J. Stark and A. Baiker, *Thermochim. Acta*, 2008, **468**, 75–80.

41 D. Griesiute, E. Raudonyte-Svirbutaviciene, A. Kareiva and A. Zarkov, *CrystEngComm*, 2022, **24**, 1166–1170.

42 L. Sinusaite, A. Popov, A. Antuzevics, K. Mazeika, D. Baltrunas, J.-C. Yang, J. L. Horng, S. Shi, T. Sekino, K. Ishikawa, A. Kareiva and A. Zarkov, *Mater. Sci. Eng., C*, 2020, **112**, 110918.

43 V. C. Ghantani, M. K. Dongare and S. B. Umbarkar, *RSC Adv.*, 2014, **4**, 33319–33326.

44 P. Gras, C. Rey, O. Marsan, S. Sarda and C. Combes, *Eur. J. Inorg. Chem.*, 2013, **2013**, 5886–5895.

45 B. C. Cornilsen and R. A. Condrate, *J. Inorg. Nucl. Chem.*, 1979, **41**, 602–605.

46 E. Boanini, M. Gazzano, C. Nervi, M. R. Chierotti, K. Rubini, R. Gobetto and A. Bigi, *J. Funct. Biomater.*, 2019, **10**, 20.

Electronic Supplementary Material (ESI) for CrystEngComm.
This journal is © The Royal Society of Chemistry 2023

Supplementary information

Dissolution-Precipitation Synthesis and Thermal Stability of Magnesium Whitlockite

Agne Kizalaite[1], Vytautas Klimavicius[2], Vytautas Balevicius[2], Gediminas Niaura[2], Andrei N. Salak[3], Jen-Chang Yang[4], Sung Hun Cho[5], Tomoyo Goto[5,6], Tohru Sekino[5], Aleksej Zarkov[1,*]

[1]*Institute of Chemistry, Vilnius University, Naugarduko 24, LT-03225 Vilnius, Lithuania*

[2]*Institute of Chemical Physics, Vilnius University, Sauletekio 3, LT-10257 Vilnius, Lithuania*

[3]*Department of Materials and Ceramics Engineering/CICECO-Aveiro Institute of Materials, University of Aveiro, 3810-193 Aveiro, Portugal*

[4]*Graduate Institute of Nanomedicine and Medical Engineering, College of Biomedical Engineering, Taipei Medical University, 250 Wu-Hsing St., Taipei 11052, Taiwan*

[5]*SANKEN (The Institute of Scientific and Industrial Research), Osaka University, 8–1 Mihogaoka, Ibaraki, Osaka 567–0047, Japan*

[6]*Institute for Advanced Co-Creation Studies, Osaka University, 1-1 Yamadaoka, Suita, Osaka 565-0871, Japan*

*Author to whom correspondence should be addressed.

Aleksej Zarkov: e-mail: aleksej.zarkov@chf.vu.lt

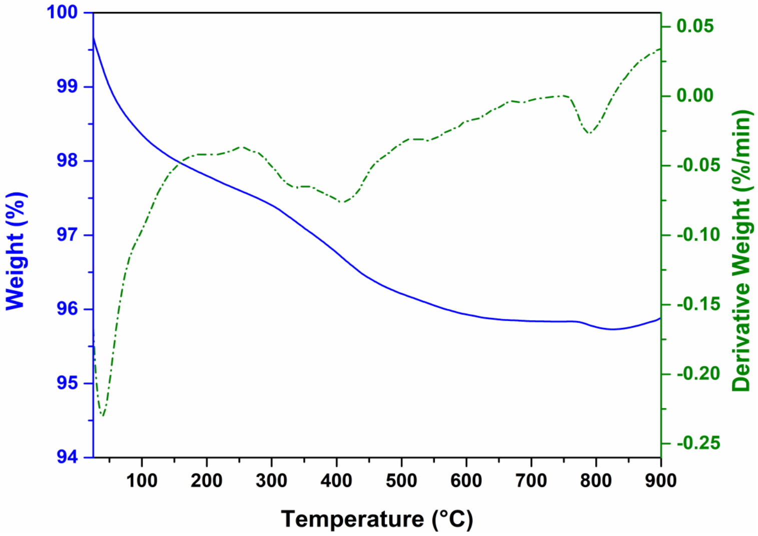

Figure S1. TG/DTG curves of as-prepared Mg-WH powder.

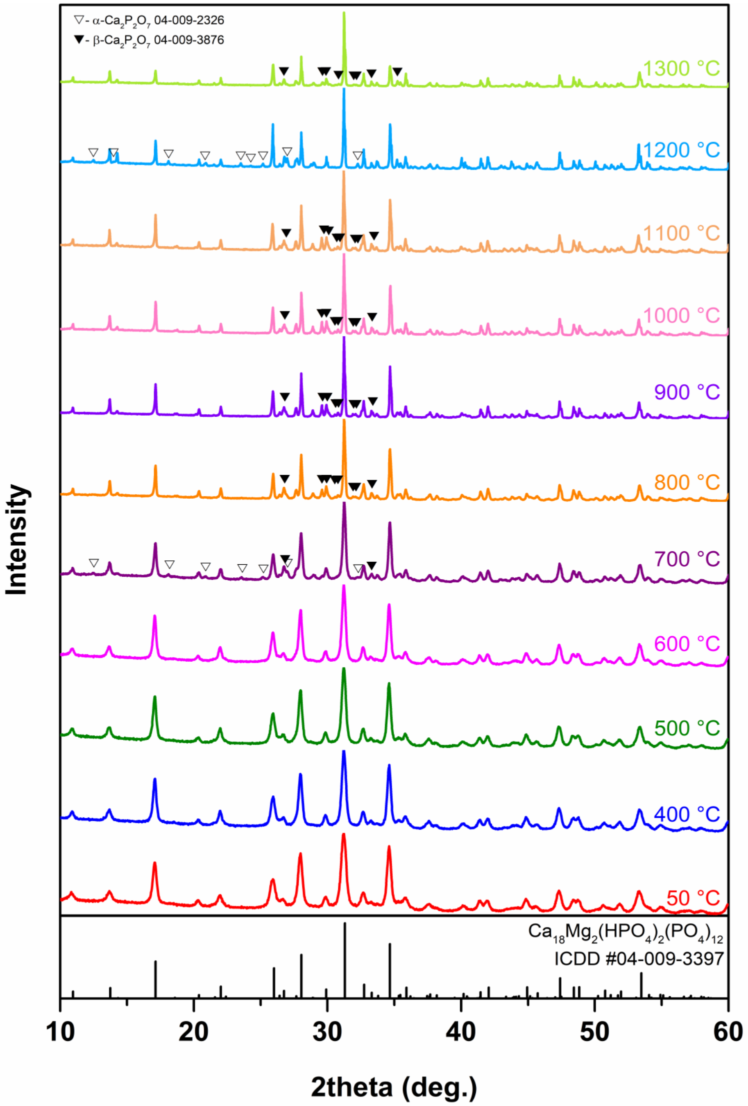

Figure S2. XRD patterns of Mg-WH powders annealed at different temperatures.

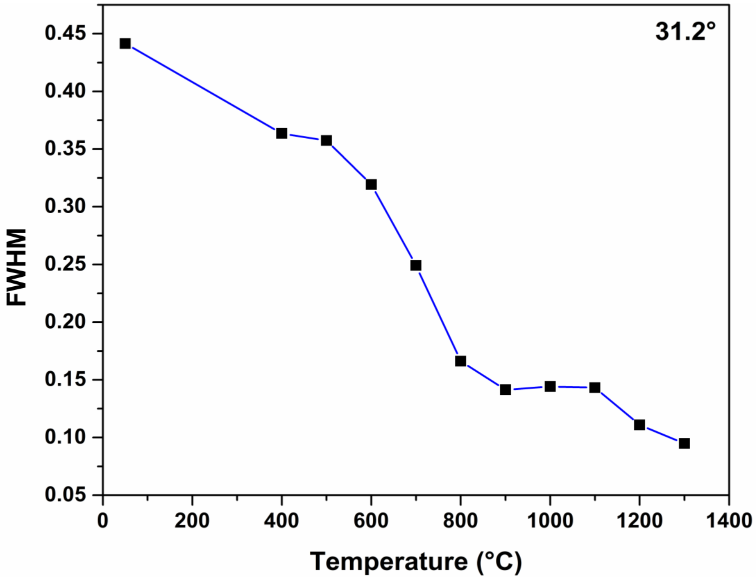

Figure S3. FWHM of (2010) peak of Mg-WH/β-TCP powders annealed at different temperatures.

Table S1. Results of Rietveld refinement of Mg-WH powders annealed at different temperatures.

Temperature, °C	*a*, Å	Standard deviation, Å	*c*, Å	Standard deviation, Å	χ^2
50	10.348(74)	0.00045	37.15(349)	0.00167	1.91
600	10.349(40)	0.00030	37.13(499)	0.00109	1.52
700	10.336(71)	0.00026	37.13(620)	0.00100	1.92
800	10.333(89)	0.00018	37.15(524)	0.00070	2.57
900	10.329(56)	0.00012	37.17(502)	0.00050	2.90
1000	10.327(44)	0.00015	37.20(289)	0.00062	3.12
1100	10.325(05)	0.00013	37.21(154)	0.00055	2.71
1200	10.328(19)	0.00016	37.19(312)	0.00057	6.60
1300	10.332(03)	0.00011	37.15(300)	0.00060	9.50

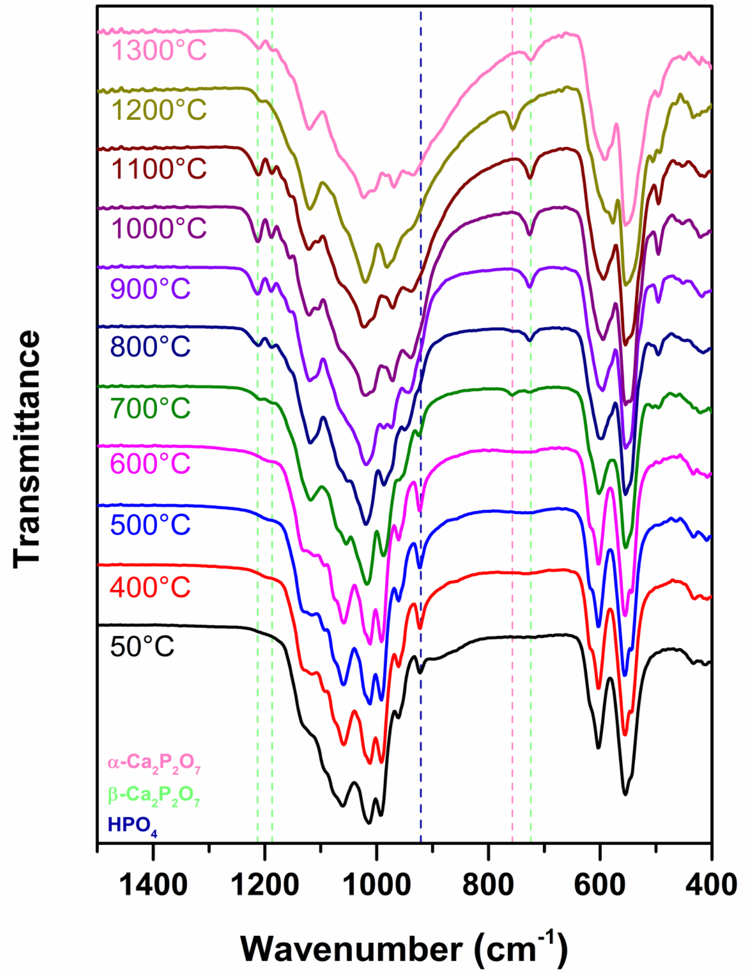

Figure S4. FTIR spectra of Mg-WH powders annealed at different temperatures.

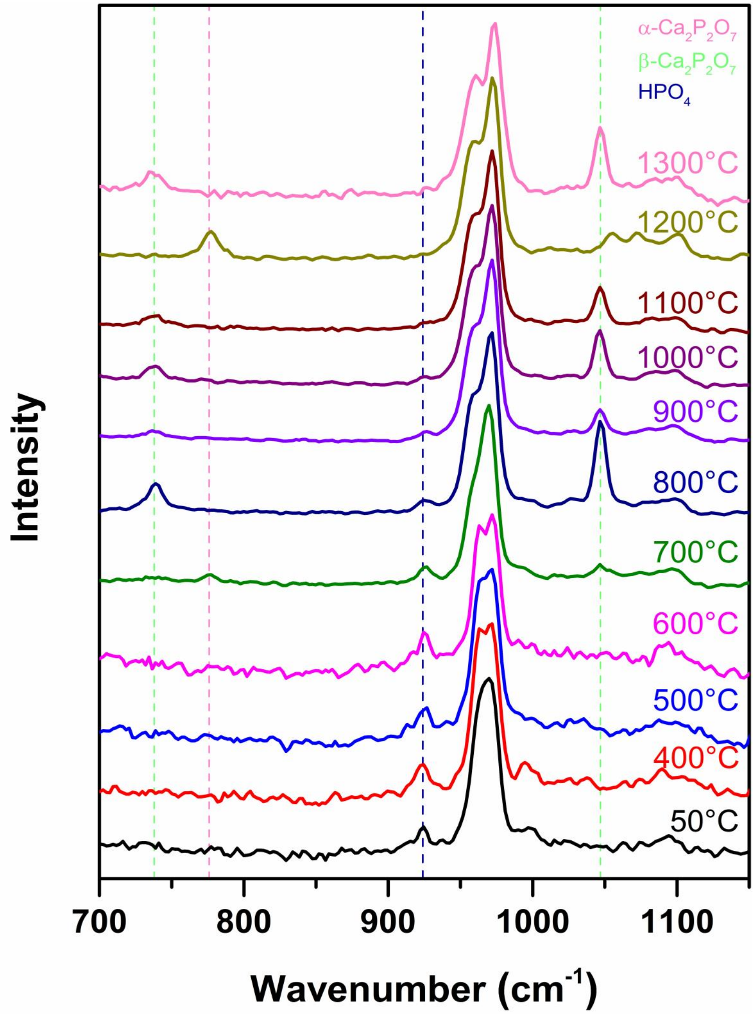

Figure S5. Raman spectra of Mg-WH powders annealed at different temperatures (excitation wavelength 325 nm).

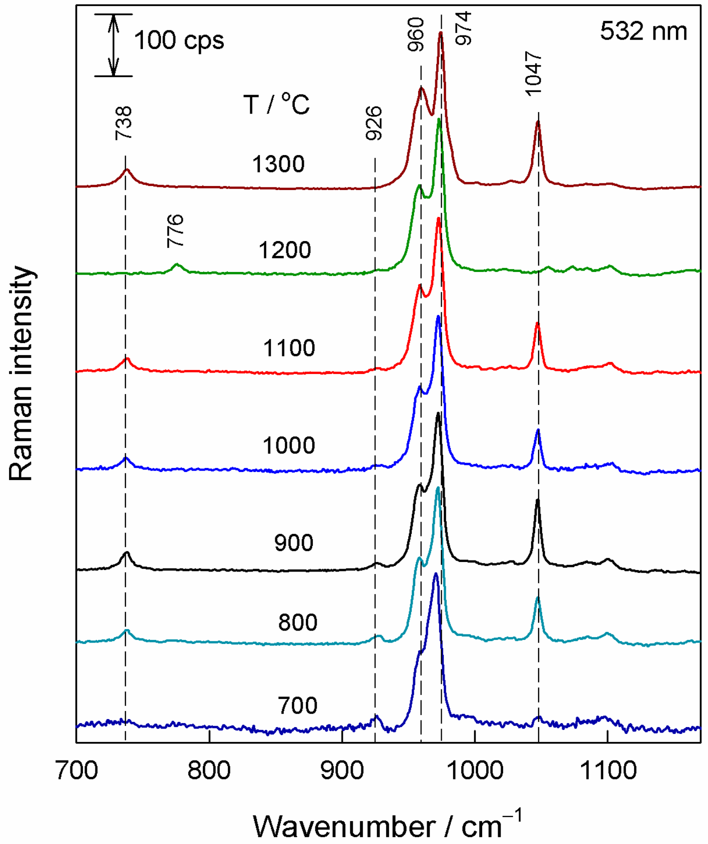

Figure S6. Raman spectra of Mg-WH powders annealed at different temperatures (excitation wavelength 532 nm).

2nd publication

Dissolution–precipitation synthesis and characterization of zinc whitlockite with variable metal content

A. Kizalaitė, I. Grigoravičiūtė-Puronienė, D. R. C. Asuigui, S. L. Stoll,
S. H. Cho, T. Sekino, A. Kareiva, A. Žarkov

ACS Biomaterials Science & Engineering, 7(8), 2021, 3586-3593
(https://doi.org/10.1021/acsbiomaterials.1c00335)

ACS Biomaterials SCIENCE & ENGINEERING

pubs.acs.org/journal/abseba Article

Dissolution–Precipitation Synthesis and Characterization of Zinc Whitlockite with Variable Metal Content

Agne Kizalaite, Inga Grigoraviciute-Puroniene, Dane Romar C. Asuigui, Sarah L. Stoll, Sung Hun Cho, Tohru Sekino, Aivaras Kareiva, and Aleksej Zarkov*

Cite This: *ACS Biomater. Sci. Eng.* 2021, 7, 3586–3593

Read Online

ACCESS | Metrics & More | Article Recommendations | Supporting Information

ABSTRACT: In the present work, a series of zinc whitlockite ($Ca_xZn_y(HPO_4)_2(PO_4)_{12}$) powders was synthesized by a low-temperature dissolution–precipitation process for the first time. The phase conversion from calcium hydroxyapatite to zinc whitlockite occurred in an acidic medium in the presence of Zn^{2+} ions. Variable chemical composition of the synthesis products was achieved by changing Ca-to-Zn molar ratio in the reaction mixture. Investigation of the phase evolution as a function of time demonstrated that phase-pure zinc whitlockite powders can be synthesized in just 3 h. It is also demonstrated that single-phase products can be obtained when the Ca-to-Zn ratio in the reaction medium is in the range from 9 to 30. With higher or lower ratios, neighboring crystal phases such as scholzite or calcium hydroxyapatite were obtained. The morphology of the synthesized powders was found to be dependent on the chemical composition, transforming from hexagonal to rhombohedral plates with the increase of Zn content. Thermal stability studies revealed that the synthesized compounds were thermally unstable and decomposed upon heat treatment.

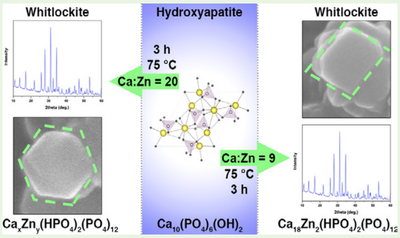

KEYWORDS: *zinc whitlockite, dissolution–precipitation, phase conversion, thermal stability*

1. INTRODUCTION

Calcium phosphates (CPs) represent the most widespread class of ceramic biomaterials used for bone regeneration purposes due to their excellent biological performance and similarity in chemical composition to the natural bone.[1] Despite the high biocompatibility of non-ion-substituted CPs, the partial substitution of calcium or phosphate ions is commonly employed for the preparation of CPs with improved biological properties. Synthetic CPs substituted with other biologically active ions can be considered as a sub-group of the CP family while possessing specific properties provided by incorporated foreign ions.[2,3] This approach appears especially reasonable due to the fact that biological CPs contain significant amounts of other ions.[4]

Magnesium whitlockite [Mg-WH, $Ca_{18}Mg_2(HPO_4)_2(PO_4)_{12}$] can be considered as a Mg-substituted CP, which naturally occurs in humans. This compound is known to be the second most abundant biomineral in human hard tissues constituting around 20–35 wt % of the total inorganic components of the bone.[5] The crystal structure of synthetic Mg-WH was described by Gopal et al.[6] It was determined that WH crystals have a space group of *R*3*c* (#161) with hexagonal parameters $a = 10.350(5)$ and $c = 37.085(12)$ Å. Although structural relationship between WH and β-tricalcium phosphate [β-TCP, $Ca_3(PO_4)_2$] has been resolved, these two names are often used interchangeably and synonymously. The reason is high similarity of the X-ray diffraction (XRD) patterns of both compounds, which makes it almost impossible to distinguish between these materials. Nevertheless, unlike WH, pristine β-TCP contains only Ca cations and neither β-TCP nor its Mg-substituted version contains HPO_4^{2-}.

Despite the presence of high content of Mg-WH in the human body, it is not so widely used in clinics, basically due to the challenges in the preparation of this material. Nevertheless, in recent years, Mg-WH attracted significantly more attention as a number of studies reported various synthetic approaches and characterization of Mg-WH.[7−13] It was demonstrated that Mg-WH possesses some superior properties compared to those of frequently used biomaterials such as calcium hydroxyapatite [HAp, $Ca_{10}(PO_4)_6(OH)_2$] or TCP. The comparative study on in vitro and in vivo biocompatibility of Mg-WH, HAp, and β-TCP revealed that Mg-WH-containing scaffolds facilitated

Received: March 10, 2021
Accepted: July 16, 2021
Published: July 28, 2021

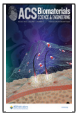

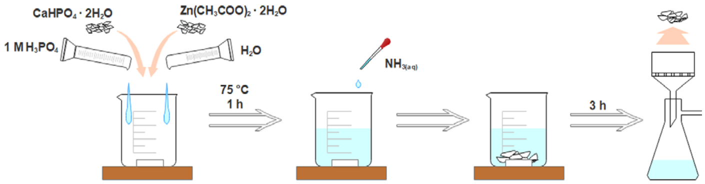

Figure 1. Schematic representation of the synthesis of Zn-WH powders by the dissolution−precipitation method.

bone-specific differentiation in comparison with HAP-reinforced composite scaffolds. Moreover, WH implants induced comparable or even better bone regeneration in calvarial defects in a rat model compared to HAP and β-TCP implants.[14] According to Kim et al.,[15] under physiological conditions, Mg-WH nanoparticles can recapitulate the early stage of bone regeneration through stimulating osteogenic differentiation, prohibiting osteoclastic activity, and transforming into HAp-neo bone tissues. It was shown that the phase transformation from Mg-WH into HAP is a key factor leading to the rapid bone regeneration with a denser hierarchical structure. Comparison of HAp/chitosan and Mg-WH/chitosan scaffolds revealed that the Mg-WH/chitosan composite possessed better biocompatibility, enhancing proliferation and osteogenic differentiation ability of human mesenchymal stem cells. In addition, Mg-WH-containing scaffolds significantly promoted bone regeneration in calvarial defects.[16]

Despite the fact that the ionic radius of Mg^{2+} is very similar to those of the first-row divalent transition-metal (TM) ions,[17] reports on the synthesis of TM-WH are almost absent. The rare example of TM-WH was published by Belik et al.,[18] who prepared $Ca_9FeD(PO_4)_7$ by treating $Ca_9Fe(PO_4)_7$ with D_2 at elevated temperatures. Earlier, Kostiner and Rea reported the crystal structure of accidently synthesized manganese WH (Mn-WH).[19] To the best of our knowledge, there are no reports in the literature regarding the zinc analogue−zinc whitlockite (Zn-WH). At the same time, Zn is known to be an essential and biologically active ion, which is involved in many biological processes in the human body, and its' deficiency leads to a number of skeletal anomalies.[20] The Zn content in the human bone varies from 0.012 to 0.025 wt %, which is relatively high compared to other tissues.[21] It should also be mentioned that Zn is a relatively harmless element; thus, many studies on synthetic Zn-substituted CPs report much higher levels of Zn doping with respect to physiological amounts.[22] Different Zn-substituted CPs such as HAp, β-TCP, and monetite demonstrated superior biological performance; moreover, Zn ions are known for their antibacterial properties.[23−28]

In the present work, we report the low-temperature synthesis of Zn-WH by a time- and cost-effective dissolution−precipitation process. We believe that this material has strong potential to be used in applications where Mg-WH has proven to be superior in biocompatibility and bone regeneration but has so far proven to be challenging synthetically. Further, in addition to the simplicity of the synthesis, we have demonstrated a wide range of composition stabilities by successfully synthesizing and characterizing a series of phase-pure Zn-WH powders containing different amounts of Ca and Zn ions. The composition of the products could be achieved by changing the Ca-to-Zn ratio in the reaction mixture, leading to remarkable phase stability.

2. MATERIALS AND METHODS

2.1. Synthesis. For the synthesis of Zn-WH powders, calcium hydrogen phosphate dihydrate ($CaHPO_4 \cdot 2H_2O$, 99.1%, Eurochemicals) and zinc acetate dihydrate [$Zn(CH_3COO)_2 \cdot 2H_2O$, ≥99.5%, Roth] were used as starting materials. All chemicals were used as received without additional purification. To achieve variable chemical compositions of the products, metal-ion precursors were mixed in various proportions. In a typical synthesis, certain amounts of $CaHPO_4 \cdot 2H_2O$ and $Zn(CH_3COO)_2$ corresponding to Ca-to-Zn molar ratios of 9, 10, 12, 15, 20, and 30 were dissolved in a mixture of 100 mL of distilled water and 13 mL of 1 M phosphoric acid (H_3PO_4, 75%, Roth). The total concentration of metal ions in the reaction mixture was 0.065 M. The temperature of the obtained solution was set to 75 °C, and the mixture was stirred for 1 h. Next, under constant mixing on a magnetic stirrer, concentrated ammonia solution (NH_4OH, 25%, Roth) was added in order to adjust the pH to 5.6. The increase of the pH value of the reaction medium resulted in instantaneous formation of white precipitates. The resulting mixture was stirred for 3 h at 75 °C; afterward the precipitates were vacuum-filtered, washed with distilled water, and dried at 60 °C in an oven overnight. Hereafter, the synthesized powders will be indicated in the text by initial Ca-to-Zn ratio in the reaction mixture. Schematic representation of the synthesis procedure is illustrated in Figure 1.

2.2. Characterization. Powder XRD data of synthesized specimens were obtained using a Rigaku MiniFlex II diffractometer (Cu Kα, $\lambda = 1.5419$ Å) working in the Bragg−Brentano ($\theta/2\theta$) geometry. The data were obtained within the 10−60° 2θ angle range with a speed of 1°/min. Fourier transform infrared spectra (FTIR) were recorded in the range of 4000−400 cm^{-1} with a Bruker ALPHA-FTIR spectrometer. Raman spectra were recorded using a combined Raman and scanning near-field optical microscope WiTec Alpha 300 R equipped with a 532 nm excitation laser source. Elemental composition of synthesized compounds was determined using inductively coupled plasma optical emission spectrometry (ICP−OES) with a PerkinElmer Optima 7000 DV spectrometer. The morphology of synthesized powders and elemental distribution were analyzed by scanning electron microscopy (SEM) using a Hitachi SU-9000 microscope equipped with an energy-dispersive X-ray spectrometer. Transmission electron microscopy (TEM) analysis was performed on a JEOL JEM-2100F FEG TEM instrument.

3. RESULTS AND DISCUSSION

The XRD patterns of the synthesis products as a function of reaction time are represented in Figure 2. It was observed that as-precipitated (0 h) powders possess a low-crystallinity calcium-deficient hydroxyapatite (CDHA) crystal structure (ICDD #00-046-0905); there were no diffraction peaks corresponding to WH, brushite ($CaHPO_4 \cdot 2H_2O$), or any other crystalline material. With an increase of reaction time, gradual transformation of CDHA to WH occurred. A mixture of two phases was obtained when the reaction time was 1 and 2

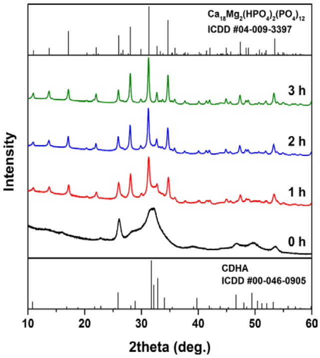

Figure 2. XRD patterns of synthesis products as a function of reaction time (the Ca-to-Zn ratio is 10).

h, while single-phase WH was observed after 3 h. As seen, all X-ray reflection peaks correspond to the WH crystal phase and peak positions match well with those of Mg-WH (ICDD #04-009-3397). The absence of reflections related to phases other than WH indicates high phase purity of the powders. Based on these results, the reaction time of 3 h was assumed to be optimal and all further syntheses were carried out for 3 h. Such a quick conversion of CDHA to WH was surprising when taking into account previous studies on the preparation of Mg-WH. Jang et al.[9] synthesized Mg-WH powders by the dissolution−precipitation method through the conversion of CDHA to Mg-WH in the presence of Mg ions. Phase-pure Mg-WH was obtained only after 12 h of reaction at 80 °C or 24 h at 65 °C, which is significantly longer compared to our results. Moreover, in our case, we did not observe any intermediate CP phase, such as brushite. Instead, phase conversion occurred directly from CDHA to WH. In a separate study by Wang et al.,[7] the preparation of Mg-WH required hydrothermal conditions at 200 °C for a 12 h treatment, which is also a considerably long time. In this light, our proposed method is time-efficient, which is a very beneficial synthetic feature.

The XRD patterns of Zn-WH synthesized with different Ca-to-Zn ratios in the reaction mixture are illustrated in Figure 3. Evidently, single-phase Zn-WH powders without a trace of crystalline byproducts were successfully synthesized when the Ca-to-Zn ratio in the reaction medium was in the range from 9 to 30. With higher Zn amounts, a secondary phase, scholzite [$CaZn_2(PO_4)_2 \cdot 2(H_2O)$] was formed, whereas with lower amounts of Zn, a mixture of WH and CDHA was obtained (see Figure S1). These results demonstrate that a WH structure can be formed when the initial ratio of metal ions is different compared to stoichiometric WH [$Ca_{18}M_2(HPO_4)_2(PO_4)_{12}$]. The obtained results supplement the data reported on the synthesis of Mg-WH.[9] Previously reported synthesis conditions and the suggested phase diagram deduced that the formation of Mg-WH occurred with an excess of Mg and phosphate ions. In our case, we also have an excess of phosphates; however, Zn-WH compounds were obtained with Zn amounts lower than those in the nominal WH formula. Moreover, as mentioned, we were not able to prepare single-phase Zn-WH from the Zn-rich reaction mixture, when the Ca-to-Zn ratio was lower than 9.

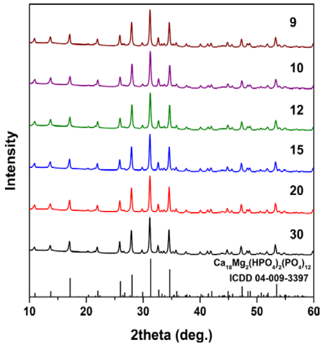

Figure 3. XRD patterns of Zn-WH powders synthesized with different Ca-to-Zn ratios.

As previously mentioned, it is hard to distinguish the XRD patterns of WH and β-TCP; therefore, the use of vibrational spectroscopy is crucial for the full characterization of WH powders and confirmation of the presence of distinct functional groups. Infrared and Raman spectroscopies use chemical functional group frequency analysis to identify the molecular components of the substances. These techniques are sensitive to the crystallographic site symmetry of the material, which allows distinction among crystallographically similar structures. The FTIR spectra of synthesized Zn-WH powders in the representative spectral range of 1500−400 cm^{-1} are demonstrated in Figure 4.

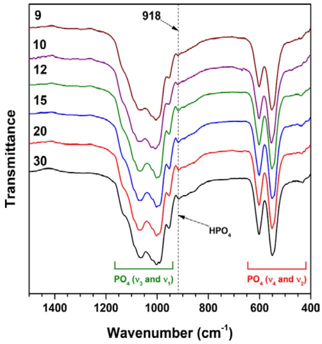

Figure 4. FTIR spectra of Zn-WH powders synthesized with different Ca-to-Zn ratios.

The most intense absorption bands correspond to the vibrations of phosphate functional groups. The absorption bands in the range from approximately 1200 to 930 cm^{-1} correspond to the phosphate ν_3 and ν_1 stretching modes. The bands in the 640−500 cm^{-1} region and at 436 cm^{-1} are also characteristic of phosphate groups and ascribed to the ν_4 and ν_2 bending modes, respectively.[29] The shape of these bands is nearly the same for all compounds regardless of the amounts of Ca and Zn precursors used for the synthesis. For the identification of WH, attention must be paid to the absorption bands located at 918 and 865 cm^{-1}, indicative of HPO_4^{2-}.[7,8,30] While the band at 865 cm^{-1} is not so pronounced, the band at 918 cm^{-1} is clearly visible in all presented spectra, suggesting a WH phase. Moreover, it should be noted that the relative intensity of this band is comparable for all compounds, which suggests that the number of HPO_4^{2-} groups does not depend significantly on the content of smaller Zn cations. Both cationic and anionic substitutions in phosphates can cause changes in the FTIR spectra such as broadening and shifting of the position of absorption bands.[31,32] For instance, Bigi et al.[33] demonstrated that partial substitution of Ca^{2+} with Zn^{2+} in β-TCP leads to the degeneracy of PO_4^{3-} absorption bands. In our case, we did not observe any drastic changes correlated to the amounts of Ca and Zn precursors used for the synthesis; however, some subtle changes could be observed. For example, with increasing Zn content, the signals ascribed to the ν_4 mode (640−500 cm^{-1}) became more overlapped. The enlarged view of the FTIR spectra (Figure S2) demonstrates a negligible difference in the position of bands ascribed to HPO_4^{2-} groups (ca. 918 cm^{-1}).

The room-temperature Raman spectra of synthesized Zn-WH specimens are given in Figure 5. Characteristic bands can be observed in the ranges of approximately 370−510 (ν_2), 530−645 (ν_4), and 990−1125 cm^{-1} (ν_3). The most intense band centered at 965 cm^{-1} is ascribed to the ν_1 symmetric-stretching vibrational mode. All these bands are also present in the Raman spectra of β-TCP and associated with internal vibrations of PO_4^{3-} ions.[34] The remarkable feature of all obtained Raman spectra is the clearly visible band at 920 cm^{-1}, which is the characteristic spectral marker for HPO_4^{2-}.[35,36] This band is absent in the Raman spectrum of β-TCP.[29,37] Another obvious difference compared to β-TCP is that the signal corresponding to the ν_1 mode in the Raman spectrum of β-TCP is usually observed as a doublet;[29,34] however, in our case, we can see only a single peak. Possibly, this spectral change can be caused by the low crystallinity of our prepared WH powders since the synthesis was performed at low temperature. A previously reported Raman spectrum of terrestrial WH exhibited a strong and well-resolved doublet of the ν_1 band.[35] On the other hand, in ion-substituted β-TCP, this band can also be observed as a singlet.[37] Similarly, like in the FTIR spectra, there is no significant difference in relative intensity of observed bands depending on the chemical composition of the samples; particularly, the relative intensity of the band at 920 cm^{-1} does not change depending on the Ca-to-Zn ratio. This observation suggests that the number of HPO_4^{2-} groups in all synthesized specimens is equal or very similar. A closer look (Figure S3) shows that the position of the ν_1 band does not change in the series. A very negligible difference in the position of the HPO_4^{2-}-related signal (ca. 920 cm^{-1}) can be observed as in the case of the FTIR spectra. Overall, it can be concluded that vibrational spectroscopy supported the results obtained by XRD analysis (Figure 2) and confirmed the WH structure of the compounds.

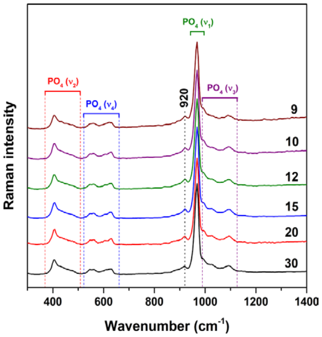

Figure 5. Raman spectra of Zn-WH powders synthesized with different Ca-to-Zn ratios.

In order to check the chemical composition of synthesized products, the elemental analysis by means of ICP−OES was performed. The results are summarized in Table 1. It is evident that with an increase of Zn concentration in the reaction mixture, Zn content in synthesized powders increased as well. The determined Ca-to-Zn ratio in the products is very close to the initial ratio of metals introduced in the reaction mixture. At the same time, the total metal ions to P ratio regardless of starting ratios of metal ions was maintained close to 1.428, which is the ratio in the ideal WH with the formula $Ca_{18}Zn_2(HPO_4)_2(PO_4)_{12}$. These results, together with the data of XRD, FTIR, and Raman spectroscopies, demonstrate that the crystal structure of WH can be formed with lower contents of smaller cations and when the Ca-to-Zn ratio exceeds the nominal value of 9. To our knowledge, the phenomenon of the formation of small-cation-lean WH (Zn-lean in our case) is a very new one, which was not described previously. While the only existing system for comparison is Mg-WH, it is not surprising that Mg-lean WH was not reported since it is not an expected product of the synthesis procedure in a Mg-rich medium.[7−9,13] These observations open new horizons for the structural investigations of WH-type materials.

Table 1. Results of the Elemental Analysis of Zn-WH Powders

initial Ca-to-Zn molar ratio	actual Ca-to-Zn molar ratio	actual M-to-P molar ratio
30	29.7	1.41
20	18.5	1.41
15	14.5	1.40
12	12.2	1.41
10	9.85	1.40
9	8.94	1.41

The representative SEM micrographs of Zn-WH powders synthesized with Ca-to-Zn ratios of 20 and 10 are shown in Figure 6. It is seen that powders synthesized with a Ca-to-Zn ratio of 20 (Figure 6a) consist of mostly uniform and agglomerated particles. The size of individual particles varies in the range of approximately 60−80 nm. Despite the fact that synthesized powders were highly agglomerated, a closer look shows that some particles have a very distinctive hexagonal shape (inset of Figure 6a). An even higher degree of agglomeration was observed for the Zn-WH sample synthesized with a higher Zn amount (Figure 6b) as the obtained particles were closely stacked on each other. It is interesting to note that the shape of the particles was found to be dependent on the chemical composition of the powders. With an increase

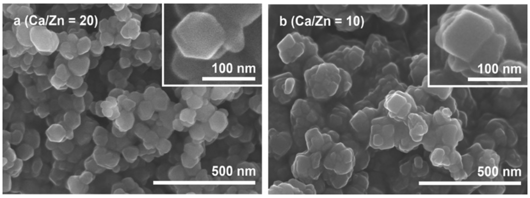

Figure 6. SEM micrographs of Zn-WH powders synthesized with Ca-to-Zn ratios of 20 (a) and 10 (b).

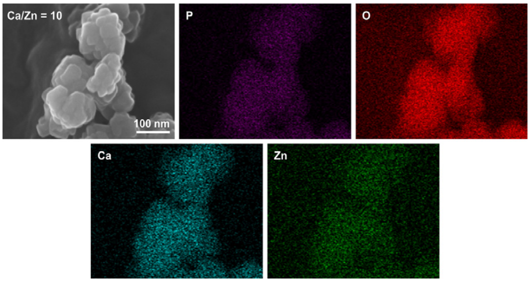

Figure 7. SEM micrograph and EDX mapping of Zn-WH powders synthesized with a Ca-to-Zn ratio of 10.

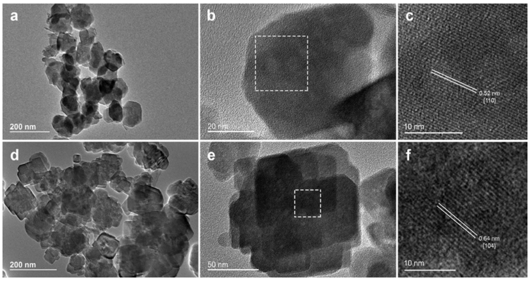

Figure 8. TEM images of Zn-WH synthesized with Ca-to-Zn ratios of 20 (a−c) and 10 (d−f).

of Zn content, the shape evolution of Zn-WH crystals from hexagonal to rhombohedral was observed. The hexagonal shape was previously achieved for Mg-WH and β-TCP powders synthesized by different methods.[7,10,38−42] Guo et al.[38] demonstrated that the shape of the grains of Mg-WH grown on the surface of β-TCP pellets under hydrothermal conditions can be varied by changing the reaction time. Wang et al.[7] achieved morphology control of Mg-WH powders by varying the ratio of Mg and Ca precursors. Mg-WH crystals with a rhombohedral shape were previously obtained by Jang et al.[9] The SEM micrographs of Zn-WH powders synthesized with other Ca-to-Zn ratios as well as images taken at lower magnification are given in Figures S4 and S5. It is shown that there are no crystals with obviously different morphologies, which can be considered as additional indirect evidence of the phase purity of the products.

Figure 7 demonstrates the SEM image and EDX mapping of Zn-WH samples. These results confirm uniform distribution of all elements in Zn-WH powders; there are no visible regions with high concentrations of some elements and complete absence of others. This indicates an absence of neighboring Zn-rich phases, which might not be detected by XRD or vibrational spectroscopy.

TEM images of Zn-WH powders are depicted in Figure 8. These images agree with the results obtained by SEM and confirm the presence of hexagonal plates with clearly defined sides in the Zn-WH sample synthesized with a Ca-to-Zn ratio of 20 (Figure 8a). High-resolution TEM of a single-crystalline hexagonal plate revealed a d-spacing of 0.52 nm, which is the characteristic of (110) lattice planes. The top/bottom surface of the plate was identical to (001) facets of WH, which is in good agreement with previous studies.[7,41,42] Well-defined rhombohedral particles of Zn-WH (a Ca-to-Zn ratio of 10) can be seen in Figures 8d,e. Fast Fourier transform of the top crystal revealed a d-spacing of 0.64 nm, which corresponds to the (104) lattice planes; in this case, the top/bottom surface of

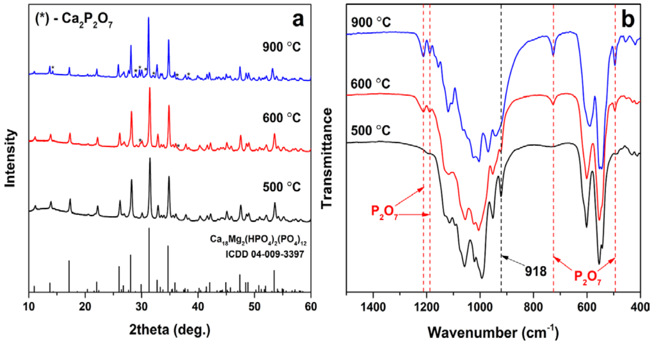

Figure 9. XRD patterns (a) and FTIR spectra (b) of Zn-WH powders annealed at different temperatures (the Ca-to-Zn ratio is 10).

the plate was assigned to (10−2) facets. This observed structural geometry also coincides well with that reported for Mg-WH.[15]

In order to check thermal stability and to estimate a potential use of the synthesized Zn-WH powders for the high-temperature fabrication of ceramics, the samples were annealed at different temperatures. The XRD patterns and FTIR spectra of Zn-WH powders annealed at different temperatures are depicted in Figure 9. No visible changes and newly aroused diffraction peaks were noticed in the XRD pattern after annealing at 500 °C; however, after the heat treatment at higher temperatures, the appearance of additional peaks was observed (Figure 9a). The newly formed crystalline phase was identified as $Ca_2P_2O_7$ (PDF #00-081-2257). A similar trend can be seen in the FTIR spectra (Figure 9b). It should be noted that the absorption band at 918 cm^{-1}, corresponding to HPO_4^{2-}, after annealing at 500 °C became more intense compared to the FTIR spectra of the as-synthesized powders (Figure 4). A possible explanation of this change could be found in the increase of degree of crystallinity after the heat treatment. After annealing at higher temperatures, this band gradually disappeared, while at the same time, new absorption signals arose at 495, 726, 1187, and 1211 cm^{-1}. These bands confirm the formation of $Ca_2P_2O_7$.[43] Making an assumption that all Zn ions are transferred to the β-TCP structure, the water release and degradation of Zn-WH can be described by the following reaction:

$$Ca_{18}Zn_2(HPO_4)_2(PO_4)_{12} \rightarrow 6Ca_{2.67}Zn_{0.33}(PO_4)_2 + Ca_2P_2O_7 + H_2O \quad (1)$$

The same behavior was observed for all Zn-WH powders synthesized with other Ca-to-Zn ratios; moreover, the relative intensity of the diffraction peaks corresponding to $Ca_2P_2O_7$ did not depend on the chemical composition of initial compounds (see Figure S6). According to Gopal and Calvo,[44] Mg-WH transforms to Mg-doped β-TCP at around 900 °C; however, the authors do not mention about the formation of a secondary crystalline phase. On the other hand, Jang et al.[8] did not observe any appearing crystal structure or changes in the XRD pattern of Mg-WH after heat treatment to temperatures of up to 1450 °C. In our case, it is evident that the intensity of both diffraction peaks and absorption bands corresponding to $Ca_2P_2O_7$ increases as annealing temperature increases, indicating the thermally unstable nature of the synthesized materials.

Summarizing the obtained results, it can be concluded that the new material for the potential use in regenerative medicine was synthesized. Further studies will be focused on the behavior of Zn-WH under physiological conditions and rigorous investigation of structural and biological properties.

4. CONCLUSIONS

Zinc whitlockite powders with variable metal content have been synthesized by a low-temperature dissolution−precipitation process. Complete phase transformation from CDHA to zinc whitlockite occurred in an acidic medium in the presence of Zn^{2+} ions. Controllable chemical composition of the synthesis products was achieved by changing the initial Ca-to-Zn molar ratio in the reaction mixture. Regardless of the final Ca-to-Zn ratio in the obtained products, the total metal ions to phosphorus ratio was determined to be nearly constant, indicating the formation of a whitlockite structure with stoichiometric and Zn-lean composition. The morphology of the powders can be controlled by varying the metal-ion ratio in the reaction mixture. All synthesized compounds were determined to be thermally unstable and decomposed upon heat treatment with the formation of β-TCP and $Ca_2P_2O_7$.

■ ASSOCIATED CONTENT

Supporting Information

The Supporting Information is available free of charge at https://pubs.acs.org/doi/10.1021/acsbiomaterials.1c00335.

XRD patterns of the products synthesized with other Ca-to-Zn ratios; enlarged view of FTIR and Raman spectra; additional SEM images of Zn-WH powders; and XRD patterns of annealed Zn-WH powders (PDF)

■ AUTHOR INFORMATION

Corresponding Author

Aleksej Zarkov − *Institute of Chemistry, Vilnius University, LT-03225 Vilnius, Lithuania;* orcid.org/0000-0002-3574-2296; Email: aleksej.zarkov@chf.vu.lt

Authors

Agne Kizalaite − *Institute of Chemistry, Vilnius University, LT-03225 Vilnius, Lithuania*
Inga Grigoraviciute-Puroniene − *Institute of Chemistry, Vilnius University, LT-03225 Vilnius, Lithuania*
Dane Romar C. Asuigui − *Department of Chemistry, Georgetown University, Washington, D.C. 20057, United States*
Sarah L. Stoll − *Department of Chemistry, Georgetown University, Washington, D.C. 20057, United States;* orcid.org/0000-0001-7184-8672
Sung Hun Cho − *SANKEN (The Institute of Scientific and Industrial Research), Osaka University, Osaka 567-0047, Japan;* orcid.org/0000-0002-6254-1094
Tohru Sekino − *SANKEN (The Institute of Scientific and Industrial Research), Osaka University, Osaka 567-0047, Japan;* orcid.org/0000-0002-6605-9166
Aivaras Kareiva − *Institute of Chemistry, Vilnius University, LT-03225 Vilnius, Lithuania*

Complete contact information is available at: https://pubs.acs.org/10.1021/acsbiomaterials.1c00335

Notes

The authors declare no competing financial interest.

■ ACKNOWLEDGMENTS

This project has received funding from the European Social Fund (project no. 09.3.3-LMT-K-712-19-0069) under grant agreement with the Research Council of Lithuania (LMTLT).

■ REFERENCES

(1) Habraken, W.; Habibovic, P.; Epple, M.; Bohner, M. Calcium phosphates in biomedical applications: materials for the future? *Mater. Today* **2016**, *19*, 69−87.

(2) Šupová, M. Substituted hydroxyapatites for biomedical applications: A review. *Ceram. Int.* **2015**, *41*, 9203−9231.

(3) Hurle, K.; Oliveira, J. M.; Reis, R. L.; Pina, S.; Goetz-Neunhoeffer, F. Ion-doped Brushite Cements for Bone Regeneration. *Acta Biomater.* **2021**, *123*, 51−71.

(4) Boanini, E.; Gazzano, M.; Bigi, A. Ionic substitutions in calcium phosphates synthesized at low temperature. *Acta Biomater.* **2010**, *6*, 1882−1894.

(5) Cheng, H.; Chabok, R.; Guan, X.; Chawla, A.; Li, Y.; Khademhosseini, A.; Jang, H. L. Synergistic interplay between the two major bone minerals, hydroxyapatite and whitlockite nanoparticles, for osteogenic differentiation of mesenchymal stem cells. *Acta Biomater.* **2018**, *69*, 342−351.

(6) Gopal, R.; Calvo, C.; Ito, J.; Sabine, W. K. Crystal Structure of Synthetic Mg-Whitlockite, $Ca_{18}Mg_2H_2(PO_4)_{14}$. *Can. J. Chem.* **1974**, *52*, 1155−1164.

(7) Wang, C.; Jeong, K.-J.; Park, H. J.; Lee, M.; Ryu, S.-C.; Hwang, D. Y.; Nam, K. H.; Han, I. H.; Lee, J. Synthesis and formation mechanism of bone mineral, whitlockite nanocrystals in tri-solvent system. *J. Colloid Interface Sci.* **2020**, *569*, 1−11.

(8) Jang, H. L.; Jin, K.; Lee, J.; Kim, Y.; Nahm, S. H.; Hong, K. S.; Nam, K. T. Revisiting Whitlockite, the Second Most Abundant Biomineral in Bone: Nanocrystal Synthesis in Physiologically Relevant Conditions and Biocompatibility Evaluation. *ACS Nano* **2014**, *8*, 634−641.

(9) Jang, H. L.; Lee, H. K.; Jin, K.; Ahn, H.-Y.; Lee, H.-E.; Nam, K. T. Phase transformation from hydroxyapatite to the secondary bone mineral, whitlockite. *J. Mater. Chem. B* **2015**, *3*, 1342−1349.

(10) Tas, A. C. Transformation of Brushite ($CaHPO_4{\cdot}2H_2O$) to Whitlockite ($Ca_9Mg(HPO_4)(PO_4)_6$) or Other CaPs in Physiologically Relevant Solutions. *J. Am. Ceram. Soc.* **2016**, *99*, 1200−1206.

(11) Qi, C.; Chen, F.; Wu, J.; Zhu, Y.-J.; Hao, C.-N.; Duan, J.-L. Magnesium whitlockite hollow microspheres: a comparison of microwave-hydrothermal and conventional hydrothermal syntheses using fructose 1,6-bisphosphate, and application in protein adsorption. *RSC Adv.* **2016**, *6*, 33393−33402.

(12) Lee, W.-B.; Wang, C.; Lee, J.-H.; Jeong, K.-J.; Jang, Y.-S.; Park, J.-Y.; Ryu, M. H.; Kim, U.-K.; Lee, J.; Hwang, D.-S. Whitlockite Granules on Bone Regeneration in Defect of Rat Calvaria. *ACS Appl. Bio Mater.* **2020**, *3*, 7762−7768.

(13) Qi, C.; Zhu, Y.-J.; Chen, F.; Wu, J. Porous microspheres of magnesium whitlockite and amorphous calcium magnesium phosphate: microwave-assisted rapid synthesis using creatine phosphate, and application in drug delivery. *J. Mater. Chem. B* **2015**, *3*, 7775−7786.

(14) Jang, H. L.; Zheng, G. B.; Park, J.; Kim, H. D.; Baek, H.-R.; Lee, H. K.; Lee, K.; Han, H. N.; Lee, C.-K.; Hwang, N. S.; Lee, J. H.; Nam, K. T. In Vitro and In Vivo Evaluation of Whitlockite Biocompatibility: Comparative Study with Hydroxyapatite andβ-Tricalcium Phosphate. *Adv. Healthcare Mater.* **2016**, *5*, 128−136.

(15) Kim, H. D.; Jang, H. L.; Ahn, H.-Y.; Lee, H. K.; Park, J.; Lee, E.-s.; Lee, E. A.; Jeong, Y.-H.; Kim, D.-G.; Nam, K. T.; Hwang, N. S. Biomimetic whitlockite inorganic nanoparticles-mediated in situ remodeling and rapid bone regeneration. *Biomaterials* **2017**, *112*, 31−43.

(16) Zhou, D.; Qi, C.; Chen, Y.-X.; Zhu, Y.-J.; Sun, T.-W.; Chen, F.; Zhang, C.-Q. Comparative study of porous hydroxyapatite/chitosan and whitlockite/chitosan scaffolds for bone regeneration in calvarial defects. *Int. J. Nanomed.* **2017**, *12*, 2673−2687.

(17) Shannon, R. D. Revised effective ionic radii and systematic studies of interatomic distances in halides and chalcogenides. *Acta Crystallogr., Sect. A: Cryst. Phys., Diffr., Theor. Gen. Crystallogr.* **1976**, *32*, 751−767.

(18) Belik, A. A.; Izumi, F.; Stefanovich, S. Y.; Lazoryak, B. I.; Oikawa, K. Chemical and Structural Properties of a Whitlockite-like Phosphate, $Ca_9FeD(PO_4)_7$. *Chem. Mater.* **2002**, *14*, 3937−3945.

(19) Kostiner, E.; Rea, J. R. The crystal structure of manganese-whitlockite, $Ca_{18}Mn_2H_2(PO_4)_{14}$. *Acta Crystallogr., Sect. B: Struct. Crystallogr. Cryst. Chem.* **1976**, *32*, 250−253.

(20) Habibovic, P.; Barralet, J. E. Bioinorganics and biomaterials: Bone repair. *Acta Biomater.* **2011**, *7*, 3013−3026.

(21) Ito, A.; Ojima, K.; Naito, H.; Ichinose, N.; Tateishi, T. Preparation, solubility, and cytocompatibility of zinc-releasing calcium phosphate ceramics. *J. Biomed. Mater. Res.* **2000**, *50*, 178−183.

(22) Sprio, S.; Preti, L.; Montesi, M.; Panseri, S.; Adamiano, A.; Vandini, A.; Pugno, N. M.; Tampieri, A. Surface Phenomena Enhancing the Antibacterial and Osteogenic Ability of Nanocrystalline Hydroxyapatite, Activated by Multiple-Ion Doping. *ACS Biomater. Sci. Eng.* **2019**, *5*, 5947−5959.

(23) Thian, E. S.; Konishi, T.; Kawanobe, Y.; Lim, P. N.; Choong, C.; Ho, B.; Aizawa, M. Zinc-substituted hydroxyapatite: a biomaterial with enhanced bioactivity and antibacterial properties. *J. Mater. Sci.: Mater. Med.* **2013**, *24*, 437−445.

(24) Raja, F. N. S.; Worthington, T.; Isaacs, M. A.; Rana, K. S.; Martin, R. A. The antimicrobial efficacy of zinc doped phosphate-based glass for treating catheter associated urinary tract infections. *Mater. Sci. Eng. C* **2019**, *103*, 109868.

(25) Ke, D.; Tarafder, S.; Vahabzadeh, S.; Bose, S. Effects of MgO, ZnO, SrO, and SiO_2 in tricalcium phosphate scaffolds on in vitro gene expression and in vivo osteogenesis. *Mater. Sci. Eng. C* **2019**, *96*, 10−19.

(26) Cama, G.; Nkhwa, S.; Gharibi, B.; Lagazzo, A.; Cabella, R.; Carbone, C.; Dubruel, P.; Haugen, H.; Di Silvio, L.; Deb, S. The role of new zinc incorporated monetite cements on osteogenic differentiation of human mesenchymal stem cells. *Mater. Sci. Eng. C* **2017**, *78*, 485−494.

(27) Su, Y.; Wang, K.; Gao, J.; Yang, Y.; Qin, Y.-X.; Zheng, Y.; Zhu, D. Enhanced cytocompatibility and antibacterial property of zinc phosphate coating on biodegradable zinc materials. *Acta Biomater.* **2019**, *98*, 174−185.

(28) Sergi, R.; Bellucci, D.; Candidato, R. T.; Lusvarghi, L.; Bolelli, G.; Pawlowski, L.; Candiani, G.; Altomare, L.; De Nardo, L.; Cannillo, V. Bioactive Zn-doped hydroxyapatite coatings and their antibacterial efficacy against Escherichia coli and Staphylococcus aureus. *Surf. Coat. Technol.* **2018**, *352*, 84−91.

(29) Carrodeguas, R. G.; De Aza, S. α-Tricalcium phosphate: Synthesis, properties and biomedical applications. *Acta Biomater.* **2011**, *7*, 3536−3546.

(30) Stähli, C.; Thüring, J.; Galea, L.; Tadier, S.; Bohner, M.; Döbelin, N. Hydrogen-substituted β-tricalcium phosphate synthesized in organic media. *Acta Crystallogr., Sect. B: Struct. Sci., Cryst. Eng. Mater.* **2016**, *72*, 875−884.

(31) Boanini, E.; Silingardi, F.; Gazzano, M.; Bigi, A. Synthesis and Hydrolysis of Brushite (DCPD): The Role of Ionic Substitution. *Cryst. Growth Des.* **2021**, *21*, 1689−1697.

(32) Bajda, T.; Mozgawa, W.; Manecki, M.; Flis, J. Vibrational spectroscopic study of mimetite-pyromorphite solid solutions. *Polyhedron* **2011**, *30*, 2479−2485.

(33) Bigi, A.; Foresti, E.; Gandolfi, M.; Gazzano, M.; Roveri, N. Isomorphous substitutions in β-tricalcium phosphate: The different effects of zinc and strontium. *J. Inorg. Biochem.* **1997**, *66*, 259−265.

(34) de Aza, P. N.; Santos, C.; Pazo, A.; de Aza, S.; Cuscó, R.; Artús, L. Vibrational Properties of Calcium Phosphate Compounds. 1. Raman Spectrum of β-Tricalcium Phosphate. *Chem. Mater.* **1997**, *9*, 912−915.

(35) Jolliff, B. L.; Hughes, J. M.; Freeman, J. J.; Zeigler, R. A. Crystal chemistry of lunar merrillite and comparison to other meteoritic and planetary suites of whitlockite and merrillite. *Am. Mineral.* **2006**, *91*, 1583−1595.

(36) Wopenka, B.; Pasteris, J. D. A mineralogical perspective on the apatite in bone. *Mater. Sci. Eng. C* **2005**, *25*, 131−143.

(37) Sinusaite, L.; Popov, A.; Antuzevics, A.; Mazeika, K.; Baltrunas, D.; Yang, J.-C.; Horng, J. L.; Shi, S.; Sekino, T.; Ishikawa, K.; Kareiva, A.; Zarkov, A. Fe and Zn co-substituted beta-tricalcium phosphate (β-TCP): Synthesis, structural, magnetic, mechanical and biological properties. *Mater. Sci. Eng. C* **2020**, *112*, 110918.

(38) Guo, X.; Liu, X.; Gao, H.; Shi, X.; Zhao, N.; Wang, Y. Hydrothermal growth of whitlockite coating on β-tricalcium phosphate surfaces for enhancing bone repair potential. *J. Mater. Sci. Technol.* **2018**, *34*, 1054−1059.

(39) Tao, J.; Jiang, W.; Zhai, H.; Pan, H.; Xu, X.; Tang, R. Structural Components and Anisotropic Dissolution Behaviors in One Hexagonal Single Crystal of β-Tricalcium Phosphate. *Cryst. Growth Des.* **2008**, *8*, 2227−2234.

(40) Galea, L.; Bohner, M.; Thuering, J.; Doebelin, N.; Ring, T. A.; Aneziris, C. G.; Graule, T. Growth kinetics of hexagonal sub-micrometric β-tricalcium phosphate particles in ethylene glycol. *Acta Biomater.* **2014**, *10*, 3922−3930.

(41) Tao, J.; Pan, H.; Zhai, H.; Wang, J.; Li, L.; Wu, J.; Jiang, W.; Xu, X.; Tang, R. Controls of Tricalcium Phosphate Single-Crystal Formation from Its Amorphous Precursor by Interfacial Energy. *Cryst. Growth Des.* **2009**, *9*, 3154−3160.

(42) Galea, L.; Bohner, M.; Thuering, J.; Doebelin, N.; Aneziris, C. G.; Graule, T. Control of the size, shape and composition of highly uniform, non-agglomerated, sub-micrometer β-tricalcium phosphate and dicalcium phosphate platelets. *Biomaterials* **2013**, *34*, 6388−6401.

(43) Fowler, B. O.; Moreno, E. C.; Brown, W. E. Infra-red spectra of hydroxyapatite, octacalcium phosphate and pyrolysed octacalcium phosphate. *Arch. Oral Biol.* **1966**, *11*, 477−492.

(44) Gopal, R.; Calvo, C. Structural Relationship of Whitlockite and β-$Ca_3(PO_4)_2$. *Nat. Phys. Sci.* **1972**, *237*, 30−32.

Supporting information

Dissolution-Precipitation Synthesis and Characterization of Zinc Whitlockite with Variable Metal Content

Agne Kizalaite[1], Inga Grigoraviciute-Puroniene[1], Dane Romar C. Asuigui[2], Sarah L. Stoll[2], Sung Hun Cho[3], Tohru Sekino[3], Aivaras Kareiva[1], Aleksej Zarkov[1,*]

[1]Institute of Chemistry, Vilnius University, Naugarduko 24, LT-03225 Vilnius, Lithuania

[2]Department of Chemistry, Georgetown University, 37th and O Streets NW, Washington, D.C. 20057, United States

[3]SANKEN (The Institute of Scientific and Industrial Research), Osaka University, 8–1 Mihogaoka, Ibaraki, Osaka 567–0047, Japan

**Corresponding author: E-mail: aleksej.zarkov@chf.vu.lt;*

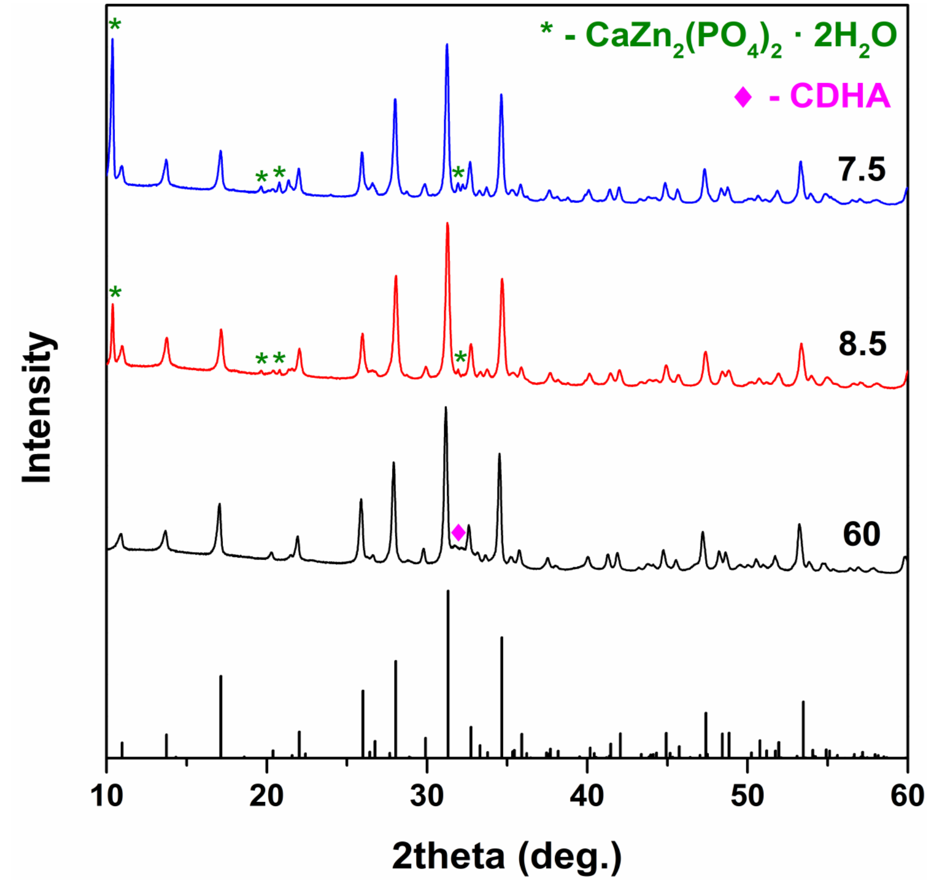

Figure S1. XRD patterns of Zn-WH synthesized with different Ca-to-Zn ratios (7.5, 8.5 and 60).

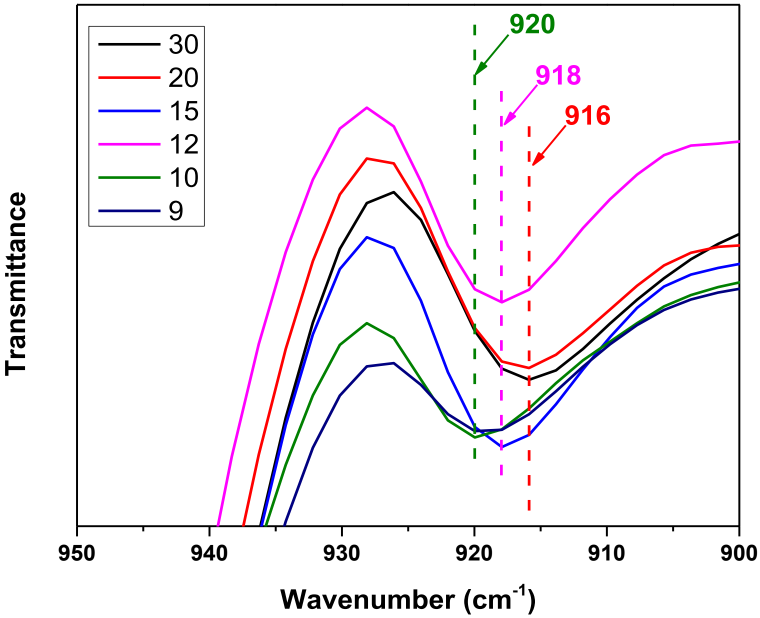

Figure S2. Enlarged view of the FTIR spectra of Zn-WH synthesized with different Ca-to-Zn ratios.

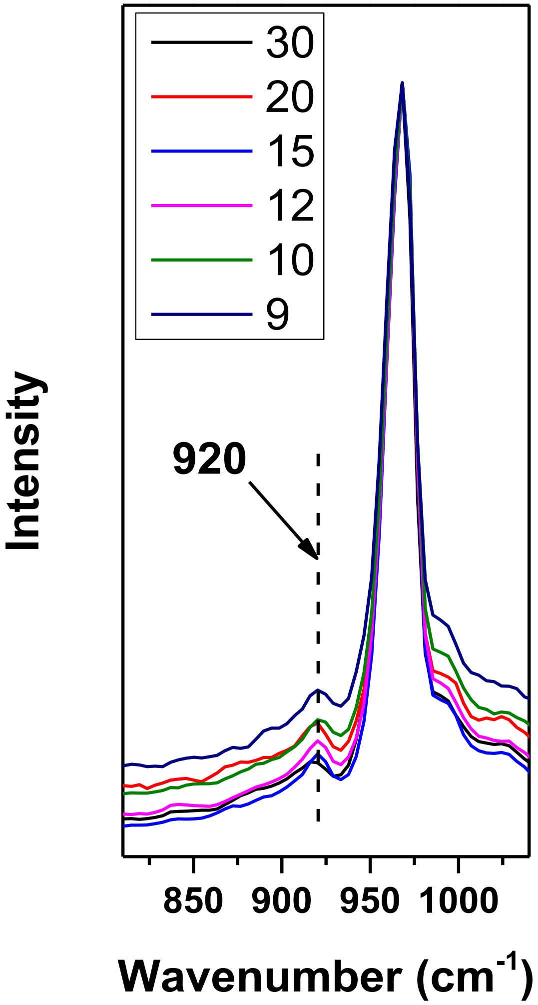

Figure S3. Enlarged view of the Raman spectra of Zn-WH synthesized with different Ca-to-Zn ratios.

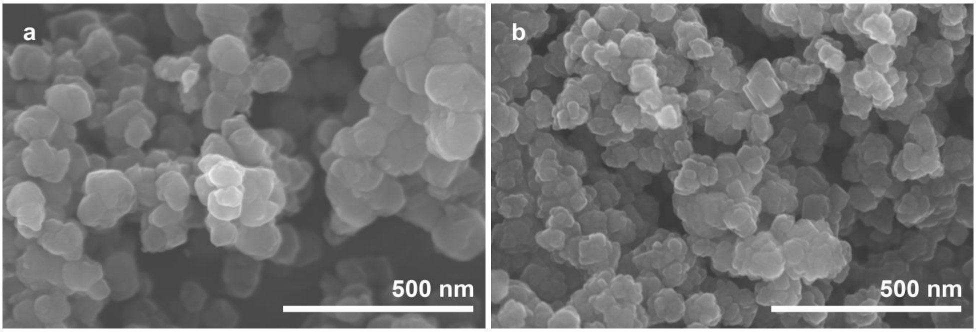

Figure S4. SEM micrographs of Zn-WH powders synthesized with Ca-to-Zn ratios 30 (a) and 9 (b).

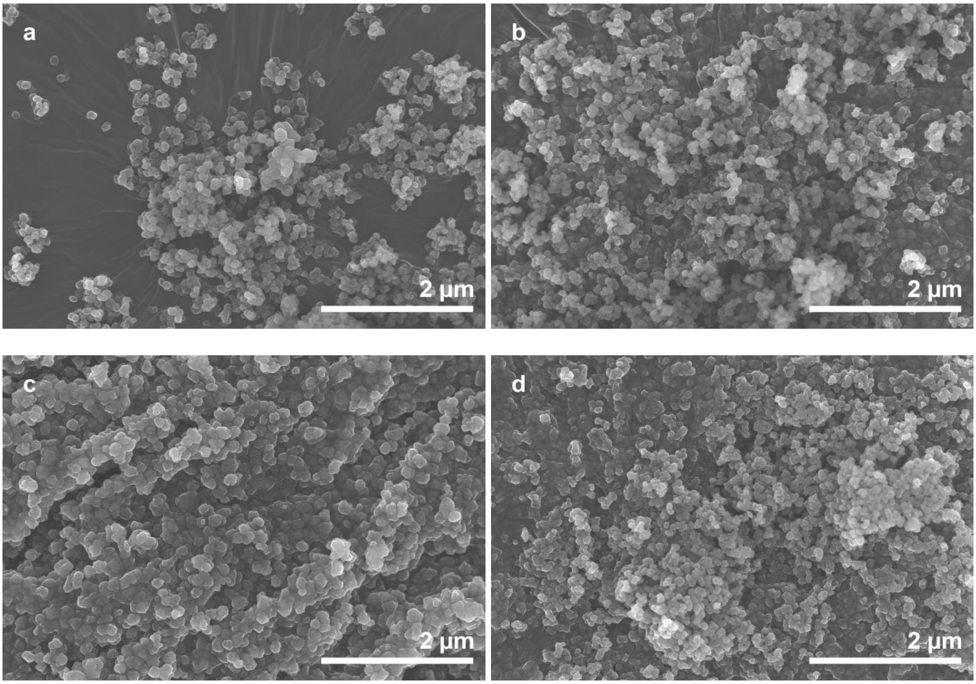

Figure S5. Low magnification SEM micrographs of Zn-WH powders synthesized with Ca-to-Zn ratios 30 (a), 20 (b), 10 (c) and 9 (d).

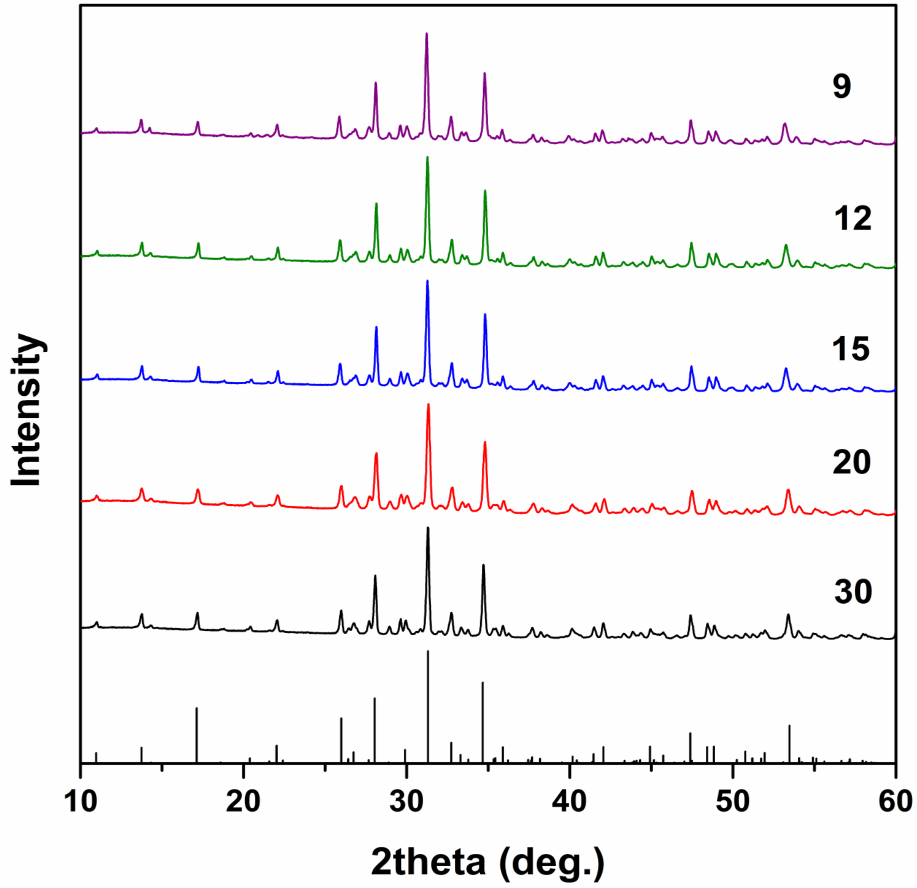

Figure S6. XRD patterns of Zn-WH powders synthesized with different Ca-to-Zn ratios and annealed at 900 ºC.

3rd publication

Peculiarities of the formation, structural and morphological properties of zinc whitlockite ($Ca_{18}Zn_2(HPO_4)_2(PO_4)_{12}$) synthesized via a phase transformation process under hydrothermal conditions

A. Kizalaitė, V. Klimavičius, J. Versockienė, E. Lastauskienė,
T. Murauskas, R. Skaudžius, T. Yokoi, M. Kawashita, T. Goto, T. Sekino,
A. Žarkov

CrystEngComm, 24(28), 2022, 5068-5079
(http://dx.doi.org/10.1039/D2CE00497F)

CrystEngComm

ROYAL SOCIETY OF CHEMISTRY

PAPER

View Article Online
View Journal | View Issue

Check for updates

Cite this: *CrystEngComm*, 2022, **24**, 5068

Peculiarities of the formation, structural and morphological properties of zinc whitlockite ($Ca_{18}Zn_2(HPO_4)_2(PO_4)_{12}$) synthesized *via* a phase transformation process under hydrothermal conditions†

Agne Kizalaite,[a] Vytautas Klimavicius,[b] Justina Versockiene,[c] Egle Lastauskiene,[c] Tomas Murauskas,[a] Ramunas Skaudzius,[a] Taishi Yokoi,[d] Masakazu Kawashita,[d] Tomoyo Goto,[ef] Tohru Sekino[e] and Aleksej Zarkov*[a]

Received 8th April 2022,
Accepted 2nd June 2022

DOI: 10.1039/d2ce00497f

rsc.li/crystengcomm

Zinc whitlockite (Zn-WH, $Ca_{18}Zn_2(HPO_4)_2(PO_4)_{12}$) is a new synthetic analog of the second most abundant biomineral – magnesium whitlockite (Mg-WH, $Ca_{18}Mg_2(HPO_4)_2(PO_4)_{12}$), which is considered as a potential material for bone regeneration. In the present work, the formation of Zn-WH *via* a dissolution–precipitation process under hydrothermal conditions was investigated in detail. The influence of medium pH, reaction time, temperature and concentration of precursors on the formation of the single-phase material was studied. It was demonstrated that the phase-pure material can be obtained in the pH range from 5.6 to 6.2 in a very short period of time – 1 h. Variation of chemical composition in terms of the Ca-to-Zn ratio was determined to be possible in a narrow range. The structural properties of the synthesized Zn-WH were investigated by powder X-ray diffraction analysis along with ^1H and ^{31}P solid-state NMR spectroscopy, FTIR spectroscopy, Raman spectroscopy and XPS. Rietveld refinement confirmed that the synthesized material has a rhombohedral structure with the *R*3*c* space group. The NMR study confirmed the presence of three inequivalent phosphorus atoms in the crystal structure, whereas only one PO_4^{3-} tetrahedron was determined to be protonated. The size and shape of the particles can be controlled by the concentration of the precursors as well as by the initial Ca-to-Zn ratio in the reaction mixture.

1. Introduction

Calcium phosphates (CPs) are widely used in medicine for the regeneration of hard tissues due to their structural and compositional similarity to natural bone.[1] The most commonly used materials are CPs containing only Ca^{2+} cations such as calcium hydroxyapatite (HA, $Ca_{10}(PO_4)_6(OH)_2$), tricalcium phosphate (TCP, $Ca_3(PO_4)_2$) or amorphous CP (ACP). In recent years, there has been rapidly increasing interest in another CP additionally containing Mg^{2+} ions – magnesium whitlockite (Mg-WH, $Ca_{18}Mg_2(HPO_4)_2(PO_4)_{12}$), which is believed to be a promising candidate in the context of bone repair biomaterials. Besides being a biomineral existing in the human body, Mg-WH can also be found in nature. The first studies on the structural properties of natural and synthetic Mg-WH were performed by Gopal *et al.*[2,3] in the early 1970s; however, just recently a neutron diffraction study of natural WH was reported by Capitelli *et al.*[4] It is noteworthy that due to the hardly distinguishable X-ray diffraction patterns of β-TCP and Mg-WH, these two names are often used in the literature interchangeably and synonymously. Nevertheless, the crystal structures of β-TCP and Mg-WH differ significantly.[2] Unlike WH, pristine β-TCP contains only Ca^{2+} cations and neither β-TCP nor its Mg-substituted version contains HPO_4^{2-}. Moreover, literature analysis revealed that despite the presence of ^1H and ^{31}P atoms in the WH structure, it was never studied in detail by

---

[a] *Institute of Chemistry, Vilnius University, Naugarduko 24, LT-03225 Vilnius, Lithuania. E-mail: aleksej.zarkov@chf.vu.lt*
[b] *Institute of Chemical Physics, Vilnius University, Sauletekio 3, LT-10257, Vilnius, Lithuania*
[c] *Institute of Biosciences, Life Sciences Center, Vilnius University, Sauletekio 7, LT-10257 Vilnius, Lithuania*
[d] *Institute of Biomaterials and Bioengineering, Tokyo Medical and Dental University, 2-3-10 Kanda-Surugadai, Chiyoda-ku, Tokyo 101-0062, Japan*
[e] *SANKEN (The Institute of Scientific and Industrial Research), Osaka University, 8-1 Mihogaoka, Ibaraki, Osaka 567-0047, Japan*
[f] *Institute for Advanced Co-Creation Studies, Osaka University, 1-1 Yamadaoka, Suita, Osaka 565-0871, Japan*

† Electronic supplementary information (ESI) available. See DOI: **https://doi.org/10.1039/d2ce00497f**

such a powerful technique for structural analysis as solid-state NMR. The rare exceptions of the use of solid-state NMR are two recent studies on Mg-WH.[5,6]

Overall, compared to HA or TCP, WH is a quite poorly investigated material in terms of both the biological performance and crystal structure. It was assumed for a long time that Mg-WH is a material very difficult to synthesize due to the formation of many neighboring CP phases. In recent years this issue was overcome and numerous papers reported the successful preparation of Mg-WH,[7–9] which led to further investigation of biological properties of this material.[10,11] The very recent comprehensive literature analysis by Shah[12] revealed that Mg-WH is not a significant inorganic constituent of bone, but exclusively a pathological biomineral, which has never been reported in the bone extracellular matrix, therefore, Mg-WH does not constitute a biomimetic strategy for bone repair. Nevertheless, such a conclusion does not deny the fact that synthetic Mg-WH is both osteoconductive and bioresorbable and in some aspects of bone regeneration it exhibits superior or at least equivalent biological performance compared to the most widely used CPs. Such conclusions were made in numerous studies, where Mg-WH was used in its pure form or in the form of composites.[10,11,13–20]

Although ionic substitutions have been widely investigated in conventionally used CPs,[21] studies on ion-substituted Mg-WH are almost absent, but the rare exception is a study by Yang *et al.*,[22] who prepared and applied Eu^{3+}/Tb^{3+}-doped Mg-WH nanocrystals for bone reconstruction and bioimaging. Despite the fact that the first row transition metal (TM) ions have comparable size with Mg^{2+} ions,[23] there are just a couple of studies on materials with a WH crystal structure, where Mg is replaced with other divalent cations. One of them from 1976 described structural properties of accidently synthesized Mn-WH.[24] At the same time TM ions can provide some very specific properties. For instance, currently, there is enormous interest in Cu-containing CPs due to the bio-functional advantages offered by Cu such as antibacterial, angiogenic and osteogenic properties.[25] Fe being a biologically active ion is also a very attractive element in terms of its magnetic properties and the potential application of Fe-doped CPs in hyperthermia for cancer treatment.[26] In our recent study we reported for the first time on the feasibility of the formation of zinc whitlockite (Zn-WH, $Ca_{18}Zn_2(HPO_4)_2(PO_4)_{12}$) – a Zn-containing analog of Mg-WH.[27]

The main goal of the present work is to investigate in detail the conditions of the phase formation and the structural and morphological properties of Zn-WH as a potential non-investigated CP for biomedical applications. Zinc was chosen as an element of interest to replace Mg^{2+} ions due to several reasons. Firstly, the ionic radius of Zn^{2+} in six-fold coordination (74 pm) is very similar to that of Mg^{2+} (72 pm).[23] Secondly, Zn is an essential element, which is involved in many biological processes; its highest content in the human body is observed in hard tissues.[28] Moreover, Zn is a relatively harmless element, which means that its content in bone substitutes can be relatively high.[29] Finally, other Zn-containing CPs are known for their superior biological performance and antibacterial properties.[29,30]

2. Materials and methods

2.1. Synthesis

Zn-WH powders were synthesized using calcium hydrogen phosphate dihydrate (DCPD, $CaHPO_4·2H_2O$, 99.1%, Eurochemicals) and zinc acetate dihydrate ($Zn(CH_3COO)_2·2H_2O$, ≥99.5%, Roth) as starting materials. All chemicals were used as received without additional purification. In a typical procedure certain amounts of $CaHPO_4·2H_2O$ and $Zn(CH_3COO)_2·2H_2O$ corresponding to a Ca-to-Zn molar ratio of 9 were dissolved in a mixture of 50 mL of deionized water and 6.5 mL of 1 M phosphoric acid (H_3PO_4, 75%, Roth) to obtain a solution with a total metal ion concentration of 0.06 M. To investigate the influence of the Ca-to-Zn molar ratio on the synthesis products, the metal-ion precursors were mixed in different proportions (6; 8; 9; 10; 12; 30). The obtained clear solution was stirred using a magnetic stirrer for 30 min at room temperature. Next, under constant mixing, concentrated ammonia solution (NH_4OH, 25%, Roth) was added in order to adjust the pH value to 5.8. The increase of the pH induced instantaneous formation of white precipitates. The resulting mixture was transferred to a 90 mL PTFE liner and sealed in a stainless steel reactor, which was transferred to a pre-heated oven and maintained at a certain temperature for different periods of time. The duration of the reaction was calculated starting from the moment the reactor was placed in the oven until it was removed to room temperature. After the reaction the precipitates were vacuum filtered, washed with deionized water and dried at 60 °C in an oven overnight. The schematic representation of the synthesis procedure is shown in Fig. S1.†

2.2. Characterization

The powder X-ray diffraction (XRD) data of the synthesized specimens were obtained using a Rigaku MiniFlex II diffractometer (Cu-K_α, λ = 1.5419 Å) working in the Bragg–Brentano ($\theta/2\theta$) geometry. The data were collected within the 10–60° 2θ angle range with a speed of 1° min^{-1}. Additional data were collected in the 10–100° 2θ angle range for the Rietveld refinement. The FullProf Suite was used for structural refinement (FullProf Suite software version September-2020). Fourier transform infrared (FTIR) spectra were obtained in the range of 4000–400 cm^{-1} with a Bruker ALPHA-FTIR spectrometer. Raman spectra were recorded using a combined Raman and scanning near field optical microscope WiTec Alpha 300 R equipped with a 532 nm excitation laser source. The morphology of synthesized powders was analyzed by scanning electron microscopy (SEM) using a Hitachi SU-70 microscope. The XPS analyses were carried out with a Kratos Axis Supra spectrometer using a monochromatic Al-K_α source (25 mA, 15 kV). The instrument work function was calibrated to give a binding energy (BE) of 83.96 eV for the Au $4f_{7/2}$ line for metallic gold and the spectrometer dispersion was adjusted to give a BE of 932.62 eV for the Cu $2p_{3/2}$ line of metallic copper. A Kratos charge neutralizer system was used on all specimens. Survey scan analyses were carried out with an analysis area of 300 × 700 microns and a pass energy of 160 eV. High resolution analyses were carried out with an analysis area of 300 × 700 microns and a pass energy of 20 eV. Spectra have been charge corrected to the main line of the carbon 1s spectrum (adventitious carbon) set to 284.8 eV. Spectra were analyzed using CasaXPS software (version 2.3.23rev1.1R). Solid-state NMR experiments were carried out at 9.4 T on a Bruker Avance III HD 400 NMR spectrometer operating at 400.2 and 162.0 MHz for ^1H and ^{31}P, respectively, using a 4 mm double resonance CP MAS probe and 4 mm zirconia rotors. The temperature was stabilized at 298 K and the MAS rate was set to 10 kHz. For ^1H MAS experiments a sequence employing two π refocusing pulses with a delay of 2 μs was employed to eliminate the signal from the probe background. The ^1H 90° excitation pulse was 2.4 μs and 64 scans were accumulated using a repetition delay of 10 s. For ^{31}P MAS measurements a saturation recovery pulse sequence was used. The saturation pulse train consisted of 20 $\pi/2$ pulses followed by a 60 s delay. The $\pi/2$ excitation pulse was equal to 2.5 μs, and 128 scans were accumulated. $^1H \rightarrow {}^{31}P$ CP MAS measurements were performed with a 2 ms CP contact time employing a 100–50% ramp on the ^1H channel, and 512 scans were accumulated using a repetition delay of 10 s. For ^{31}P–^{31}P 1Q–2Q experiments standard and CP based pulse sequences were used which employ a BABA (back-to-back) 2 rotor period recoupling scheme. The ^{31}P $\pi/2$ excitation pulse was equal to 2.5 μs, the repetition delay was set to 60 s and 16 scans per 128 increments were accumulated. For $^1H \rightarrow {}^{31}P$ CP MAS FSLG HETCOR experiments, 64 scans per 48 increments were accumulated using 50 μs or 2 ms contact pulses in the CP sequence, the repetition delay was 10 s and the homonuclear FSLG decoupling field was set to 100 kHz. ^1H and ^{31}P spectra were referenced respectively to TMS using adamantane (δ (^1H) = 1.85 ppm) and 85% H_3PO_4 using ADP (ammonium dihydrogen phosphate, $NH_4H_2PO_4$, δ (^{31}P) = 0.8 ppm).

The thermal decomposition of the synthesized powders was analyzed by thermogravimetric analysis using a Perkin Elmer STA 6000 simultaneous thermal analyzer. A dried sample of about 20 mg was heated from 25 to 900 °C with a heating rate of 10 °C min^{-1} in a dry flowing air (20 mL min^{-1}). The N_2 adsorption and desorption isotherms of the samples were obtained at −196 °C by using a Brunauer–Emmett–Teller (BET) analyzer TriStar II 3020, Micromeritics. Prior to the gas sorption measurements, all the samples were outgassed in a N_2 atmosphere at 100 °C for 2 h. For the ion release experiment 0.6 g of Zn-WH powders were soaked in 30 mL of simulated body fluid (SBF), and the samples were prepared in triplicate. The SBF solution was prepared according to the procedure reported by Kokubo *et al.*[31] The samples were kept in closed containers in a shaker-incubator (BioSan ES-20/80) at 37 °C for 14 days under constant mixing at 250 rpm. Every day 1 mL of solution was taken from the sample for elemental analysis and was replaced with the same amount of fresh SBF solution to maintain a constant volume. Quantitative determination of released Zn^{2+} ions was performed using a Perkin Elmer Optima 7000DV inductively coupled plasma optical emission spectrometer (ICP-OES).

3. Results and discussion

Due to the absence of crystallographic data for Zn-WH, the crystal structure of closely related and previously investigated Mg-WH will be discussed first (Fig. 1). Mg-WH crystallizes in a rhombohedral crystal structure with the space group *R3c* (#161) and equivalent hexagonal unit cell parameters $a = b = 10.350(5)$ Å and $c = 37.085(12)$ Å.[3] The crystal structure of Mg-WH is composed of two types of columns (A and B) that are periodically arrayed along the *c*-axis. Column A consists of Mg^{2+} and HPO_4^{2-} units alternating with empty spaces. More densely packed column B has a form of Ca(1)–P(3)O_4–P(2)O_4–Ca(2)–Ca(3).[7,8] Both A and B columns come in three different subtypes each (Fig. 1b). These subtypes are identical in atomic arrangement, but are shifted relative to each other along the *c*-axis. Each A column is surrounded by six B columns of two different subtypes, while each B column is surrounded by two A columns of different subtypes on opposite sides and four B columns of two different subtypes (Fig. 1d). The unit cell of Mg-WH is composed of 3 A columns and 9 B columns. There are 3 inequivalent sites for calcium and 3 for phosphorus in the crystal structure of WH. Whereas Ca(1) and Ca(2) ions are both directly bonded with five PO_4^{3-} groups and one HPO_4^{2-} group, the Ca(3) site has 4 neighboring PO_4^{3-} groups. In column A all the *x* and *y* atomic coordinates of Mg and P(1) have the value of zero, showing that these atoms are located on a straight line. Meanwhile, in column B the *x* and *y* atomic coordinates of Ca(1), Ca(2), Ca(3), P(2) and P(3) have different values, indicating that column B is distorted compared to column A. The crystal structure of WH is in close relationship with that of β-TCP, which crystallizes in the same space group.[32] This material has 5 inequivalent cationic crystallographic sites, which can be potentially substituted with other ions. The difference between β-TCP and Mg-WH originates from the presence of HPO_4^{2-}, Ca^{2+}/Mg^{2+} substitution and cation vacancies in the latter. With the notation reported for the isotypic β-TCP phase, the Mg^{2+} ions in the WH structure replace Ca^{2+} in the most energetically favorable octahedrally coordinated Ca(5) site, while Ca(4) is the most stable as a vacancy. The protons are known to be close to the Ca(4) sites.[33]

In order to determine the optimal conditions for the preparation of Zn-WH, the influence of the medium pH was investigated first. It is known that WH is more stable in acidic medium compared to HA,[34] therefore, the experiments were performed exactly in the acidic pH range. The XRD patterns of the synthesis products obtained at different pH

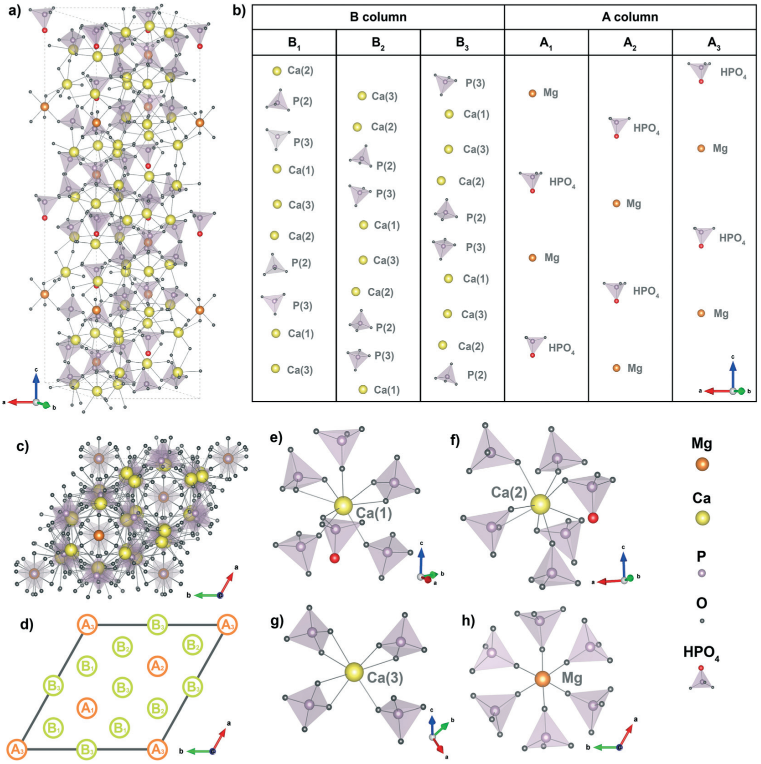

Fig. 1 Unit cell of Mg-WH (a and c); arrangement of atoms in structural columns (b); arrangement of columns in the unit cell (d); different cationic crystallographic sites in the WH structure with surrounding phosphate groups (e–h).

values are depicted in Fig. 2. Due to the absence of standard XRD data for Zn-WH, the obtained experimental patterns were compared to that of Mg-WH (ICDD #04-009-3397). It was observed that single-phase Zn-WH can be obtained in the pH range from 5.6 to 6.2. There were no additional diffraction peaks in the XRD patterns of the materials synthesized in this pH range. As expected, at higher pH values an additional HA phase was observed; there was a clear trend that the amount of HA gradually increased with an increase of pH. At low pH values (<5.6) a neighboring Zn-rich scholzite phase ($CaZn_2(PO_4)_2 \cdot 2H_2O$) was obtained. The dependence of the phase composition on pH in a broader range is depicted in Fig. S2.†

Fig. S3† shows the XRD patterns reflecting the phase composition dependence on reaction time. The as-precipitated material (0 h) was identified as DCPD (ICDD #96-231-0524), and there were no sharp diffraction peaks corresponding to other crystalline phases. At the same time, a very broad peak centered at around 30° was also observed, which is characteristic of amorphous calcium phosphate.[35] The FTIR spectrum of the as-precipitated powders (Fig. S4†) was completely different compared to that of DCPD[36] and contained only a few broad bands. All these bands are characteristic of ACP and the broadening demonstrates the absence of or very poor crystalline ordering.[37] Based on the combination of the XRD and FTIR results, it can be concluded that the as-precipitated material was mostly amorphous with the crystalline DCPD component. The formation of the amorphous material can be explained by the presence of a relatively high content of Zn^{2+} ions, which are significantly smaller compared to Ca^{2+} ions and inhibit the crystallization of CPs.[38] The transformation to Zn-WH occurred in just 1 h, which is significantly faster compared to the synthesis at ambient pressure.[27] Whereas faster formation of WH under hydrothermal conditions is not surprising, previous studies on the hydrothermal synthesis of Mg-WH also demonstrated the need for significantly longer reaction time.[9,22,39] The XRD patterns of the products obtained at different temperatures in the range from 110 to 230 °C are given in Fig. S5.† It is seen that single-phase Zn-

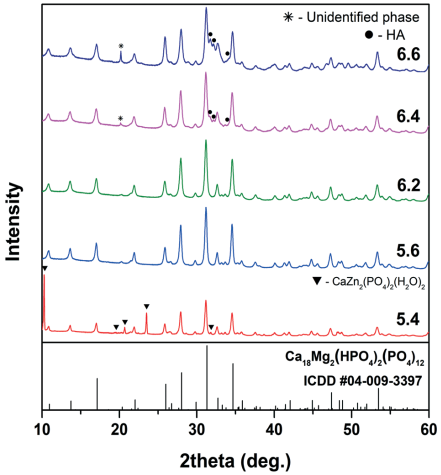

Fig. 2 XRD patterns of the synthesis products obtained at different pH values (t = 3 h; T = 200 °C).

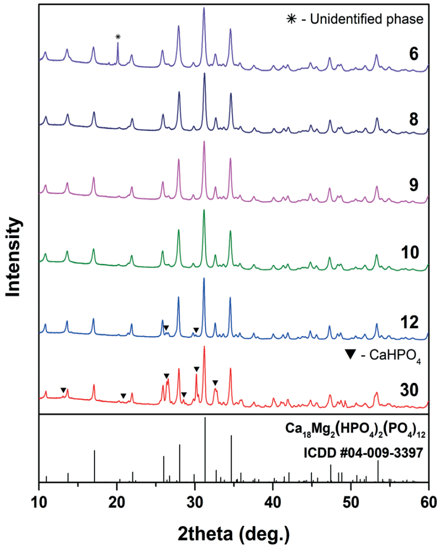

Fig. 3 XRD patterns of Zn-WH powders synthesized with different Ca-to-Zn initial ratios (pH = 5.8; T = 200 °C; t = 3 h).

WH is formed in all cases regardless of the reaction temperature.

To further investigate the synthesis conditions, a series of powders were synthesized using different Ca-to-Zn ratios in the range from 6 to 30 (Fig. 3). It was shown in previous studies that for the synthesis of high-purity Mg-WH the ratio of ions in the reaction mixture should be different compared to that in the Mg-WH formula. According to the suggested phase diagram,[8] Mg-WH can be synthesized with an excess of Mg and phosphate ions. In our case phase-pure Zn-WH without noticeable neighboring crystalline phases was obtained when the Ca-to-Zn ratio in the initial reaction mixture varied from 8 to 9. When the Ca-to-Zn ratio was set at 10, a negligible amount of neighboring monetite (CaHPO$_4$) was obtained along with a major Zn-WH phase. With a lower Zn content the presence of this secondary phase is obviously seen. Contrary to previous studies on Mg-WH, the excess of Zn ions in the reaction mixture resulted in the formation of a secondary unidentified phase. Thus, it can be concluded that in our suggested synthetic approach the stoichiometric Ca-to-Zn ratio is optimal for the preparation of single-phase Zn-WH.

Rietveld refinement was employed to calculate the lattice parameters of synthesized Zn-WH (Fig. S6†). The refinement was performed using a rhombohedral structure (space group $R3c$) adopted from Mg-WH. The results indicated good agreement between the calculated and experimental powder XRD patterns, and it can be concluded that Zn-WH possesses the same crystal structure as Mg-WH. The values of lattice parameters were close to those reported for Mg-WH, particularly, parameter a was determined to be slightly smaller (10.342 Å) and parameter c slightly larger (37.114 Å).[3] The Rietveld analysis also confirmed that there is no evidence of the presence of secondary crystalline phases.

Due to the identical XRD patterns of WH and β-TCP, the use of vibrational spectroscopy is crucial for the reliable identification and confirmation of the WH structure. The FTIR spectrum of Zn-WH is given in the representative wavenumber range of 1500–400 cm^{-1} in Fig. 4a. Few

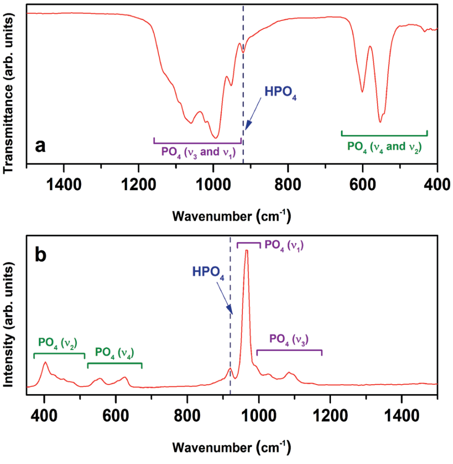

Fig. 4 FTIR (a) and Raman (b) spectra of Zn-WH powder (T = 200 °C; t = 3 h; pH = 5.8).

absorption bands associated with the vibrations of phosphate functional groups are clearly seen. The bands located in the range from approximately 1170 to 930 cm^{-1} correspond to v_3 and v_1 stretching modes of phosphates. The bands in a shorter wavenumber range (640–500 cm^{-1} and 436 cm^{-1}) are assigned to v_4 and v_2 bending modes, respectively. For the identification of WH special attention must be paid to the absorption band centered at *ca.* 920 cm^{-1}; this band is attributed to the HPO_4^{2-} group and can be assumed as a characteristic spectral marker of WH, which is absent in the FTIR spectrum of β-TCP.[40] In our case this absorption band is clearly seen and well-resolved.

The Raman spectrum of Zn-WH (Fig. 4b) exhibits several characteristic bands observed in the ranges of *ca.* 370–510 (v_2), 530–645 (v_4) and 990–1125 cm^{-1} (v_3). The most intense band centered at 965 cm^{-1} is attributed to the v_1 symmetric-stretching vibrational mode.[41] The characteristic band at 920 cm^{-1} confirms the presence of the HPO_4^{2-} group in the structure of the synthesized material.[42] Thus, the results of both spectroscopic techniques are in good agreement between themselves and confirm the formation of the WH structure. It is worth noting that though the DFT calculations performed by Debroise *et al.*[33] did not predict the presence of the band at 920 cm^{-1} in both the FTIR and Raman spectra of WH, it is commonly observed in the experimentally obtained spectra of natural and synthetic WH.[7,9,43,44]

The ^1H MAS spectra of dried and wet Zn-WH samples are shown in Fig. 5A and B. The wet sample stands for the Zn-WH sample with adsorbed water from the atmosphere. There is a clear line at 9.8 ppm, which is attributed to protons from the HPO_4^{2-} moiety in the WH crystal structure. A similar assignment was found in the literature for Mg-WH.[5,6] This observation agrees well with the results of vibrational spectroscopy and confirms the presence of the HPO_4^{2-} group in the structure of the synthesized material. In addition, broad lines at 7 and 12 ppm show the presence of protonated low-crystalline or amorphous phosphates in the bulk and on the surface.[45] Lines at 5 and 1 ppm are attributed to bulk and surface water, respectively. The intensity of these lines increases for the wet sample which corroborates the assignment. The width of the line attributed to the surface water is reduced for the wet sample which is due to the increased mobility.

^{31}P MAS and ^{31}P CP MAS spectra obtained for the Zn-WH sample are shown in Fig. 5C and D. The ^{31}P MAS spectrum differs significantly compared to that of β-TCP,[40] which is clear evidence of the formation of the WH structure. In the ^{31}P MAS spectrum there are three lines at 2, 1.4 and −0.5 ppm attributed to the P(2), $HP(1)O_4^{2-}$ and P(3) moieties in the Zn-WH crystal structure, respectively. Signal assignment was based on the comparison of the crystal structures and assignments previously made for whitlockite-type β-TCP and $Ca_{10}Na(PO_4)_7$.[46,47] In addition, the broad line at 0.3 ppm possibly originates due to the low crystallinity of the synthesized material and the presence of phosphate species in the amorphous state. The obtained spectrum is similar to

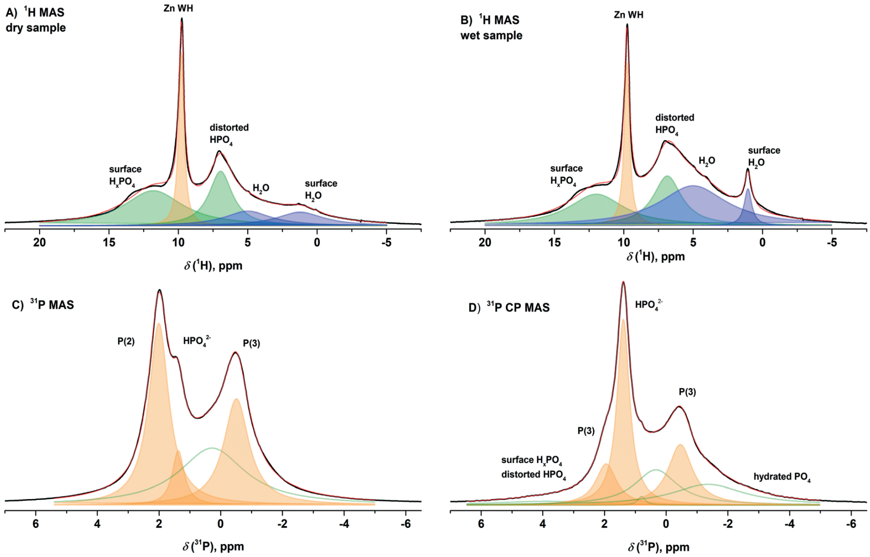

Fig. 5 ^1H MAS spectra and spectral assignment obtained for dried (A) and wet (B) Zn-WH samples. Lines attributed to Zn-WH are in orange, to other protonated phosphates in green and to water in blue, and the red line indicates the cumulative fit; ^{31}P MAS (C) and $^1H \rightarrow {}^{31}P$ MAS (D) spectra obtained for the Zn-WH sample. Lines attributed to Zn-WH are in orange, to other phosphates in green and the cumulative fit is in red.

that of Mg-WH recently reported by Konishi *et al.*;[6] however, in our case the obtained lines are less resolved, which can be associated with the lower crystallinity of obtained Zn-WH. In the ^{31}P CP MAS spectrum, lines at 2, 1.4 and −0.5 ppm which are attributed to Zn-WH are also present. The line at 1.4 ppm corresponding to the $HP(1)O_4^{2-}$ moiety is more enhanced in comparison to those of P(2) and P(3) due to the presence of protons in close vicinity. Lines observed at 4.5, 0.83, 0.3 and −1.4 ppm are attributed to protonated surface phosphates, the amorphous phosphate phase, distorted HPO_4 and phosphate in the hydrated layer which are present as impurities.[45,48]

The standard and CP based ^{31}P–^{31}P 1Q–2Q correlation spectra are shown in Fig. 6A and B. In both spectra correlations originating from the dipolar interactions of P(3)–P(3), $HP(1)O_4$–P(3), P(2)–P(3), P(2)–$HP(1)O_4$, and P(2)–P(2) moieties are seen. In the CP based spectrum correlations which include the $HP(1)O_4$ moiety are better resolved. These correlations are in accordance with the crystal structure of WH (Fig. 1). What is more, the presence of the correlations proves that the mentioned phosphorus moieties are in the same crystal lattice.

The ^{1}H–^{31}P FSLG CP MAS HETCOR spectra measured for the Zn-WH sample using 50 μs and 2 ms contact times are shown in Fig. 6C and D. In the HETCOR spectrum measured using 50 μs contact time $HP(1)O_4$ and P(3) phosphorus correlations with the HPO_4 proton are seen. In addition correlations between the hydrated PO_4 and protons from surface H_xPO_4 are seen. The presence of these correlations seems logical as a very short contact time was used, which means that the correlations from the P moieties close to protons are obtained. In the HETCOR spectrum measured using 2 ms contact time the correlation from the impurity phase is masked, though the correlation between the P(2) phosphorus and HPO_4 proton is now better seen. According to the neutron

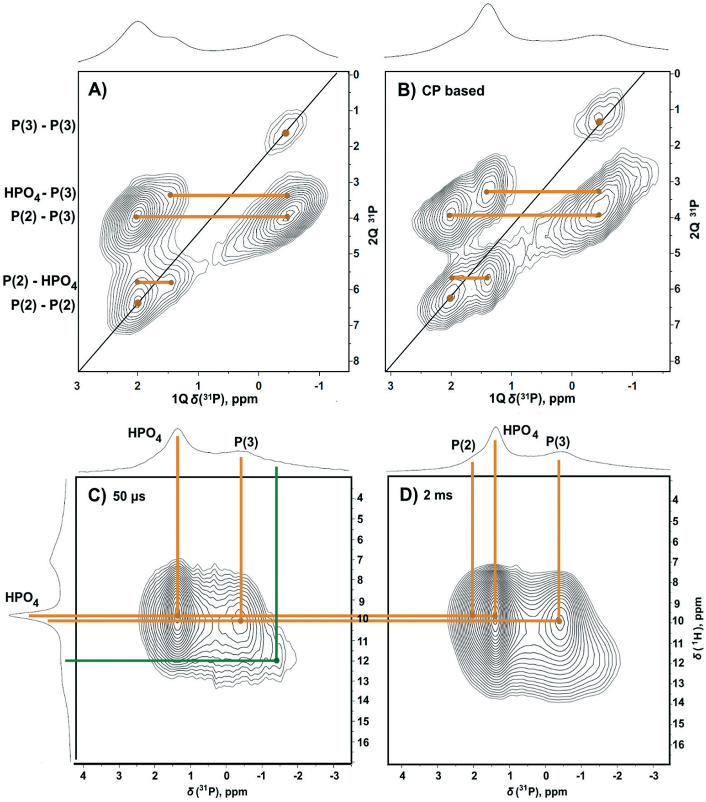

Fig. 6 Standard (A) and CP based (B) ^{31}P MAS 1Q–2Q correlation spectra; ^{1}H–^{31}P FSLG CP MAS HETCOR spectra obtained for the Zn-WH sample using 50 μs (C) and 2 ms (D) CP contact times.

diffraction data published very recently by Capitelli *et al.*[4] for natural WH, the HP(1)O_4 tetrahedron may flip 180° along the *c*-axis. This results in the displacement of P(1) along the *c* axis and two different positions of protons – downward (−*c*) and upward (+*c*). In natural WH this proportion was calculated to be 85% and 15%. The observed stronger correlation between P(3) and protons suggests that in our case the protons are most probably oriented upward (+*c*), otherwise we would observe a stronger correlation between P(2) and protons (Fig. 1). Overall, the HETCOR and CP MAS data obtained here are in good agreement with each other.

The additional broad signals in the ^{1}H MAS spectrum suggest the presence of hydrogen-containing species either adsorbed on the surface or trapped. It is known that Zn-WH is thermally unstable and decomposes upon heating.[27] Making an assumption that the ideally stoichiometric Zn-WH degrades according to eqn (1), the theoretical mass loss after annealing is expected to be only around 0.8 wt%. Based on the results of thermogravimetric analysis (Fig. S7†) the total mass loss was calculated to be 3.6 wt%. Around 1.3 wt% was lost at temperatures below 200 °C, which can be ascribed to the removal of adsorbed water. The residual part can be attributed to the removal of water molecules from the WH structure (eqn (1)) and adsorbed or trapped thermally unstable species.

$$\begin{aligned} &Ca_{18}Zn_2(HPO_4)_2(PO_4)_{12} \\ &\quad \rightarrow 6Ca_{2.67}Zn_{0.33}(PO_4)_2 + Ca_2P_2O_7 + H_2O \end{aligned} \tag{1}$$

It was shown in previous studies that the shape and size of WH particles can be dependent on the metal ion ratio in the initial reaction mixture.[9,27] SEM micrographs of Zn-WH powders synthesized with different Ca-to-Zn ratios are given in Fig. 7a–c. When the Ca-to-Zn ratio was 9, the powders consisted of rhombohedral plate-like particles of approximately 30–50 nm; however, some particles with undefined shape and comparable size were also present. The increase of the Ca-to-Zn ratio to 12 and 30 preserved the shape of the particles; however, it increased the size significantly up to 70–110 and 100–230 nm, respectively.

The initial concentration of metal ion precursors also resulted in the formation of the particles of different sizes, which is obviously seen from Fig. 7d–f. The size of the particles varied in the ranges of approximately 20–45, 30–60 and 50–100 nm for Zn-WH powders synthesized with initial concentrations of 0.12, 0.06 and 0.01 M, respectively. It is worth noting that the largest particles possessed different morphologies and had an octahedral shape. These observations are in good agreement with previously published results. According to the literature, a rhombohedral or hexagonal plate-like morphology is characteristic of nano- or microscale WH particles;[7–9,22]

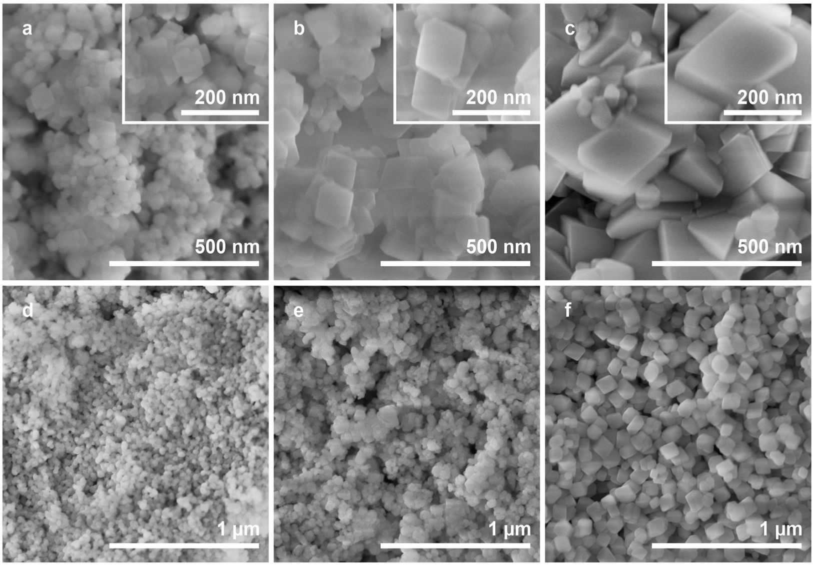

Fig. 7 SEM micrographs of Zn-WH synthesized with Ca-to-Zn molar ratios of 9 (a), 12 (b) and 30 (c), when the concentration of metal ion precursors was 0.06 M; Zn-WH powders synthesized with a Ca-to-Zn molar ratio of 9, when the initial concentration of metal ion precursors was 0.12 M (d), 0.06 M (e) and 0.01 M (f).

however, previously reported large sub-millimeter crystals of Mg-WH possessed an exactly octahedral shape.[49,50]

The surface areas of the Zn-WH samples obtained with different total metal ion concentrations were measured (Fig. S9†). The N_2 adsorption–desorption isotherms of two representative samples can be classified as type IV with a type H3 hysteresis loop.[51] The type IV isotherm indicates that mesopores are dominant in the samples. The type H3 loop is usually observed with aggregates of plate-like particles which give rise to slit-shape pores. The specific surface area calculated by the BET method (S_{BET}) was determined to be 24.6 and 35.0 m^2 g^{-1} for the samples prepared with initial concentrations of 0.03 M and 0.12 M, respectively. These data correlate well with the SEM micrographs of the samples.

The low-resolution XPS survey spectrum of the Zn-WH particles can be seen in Fig. 8a. Besides the expected Ca, P, O, and Zn, the sample contained only a small amount of C 1s. High-resolution Ca 2p, P 2p, O 1s, Zn 2p and Zn LMM

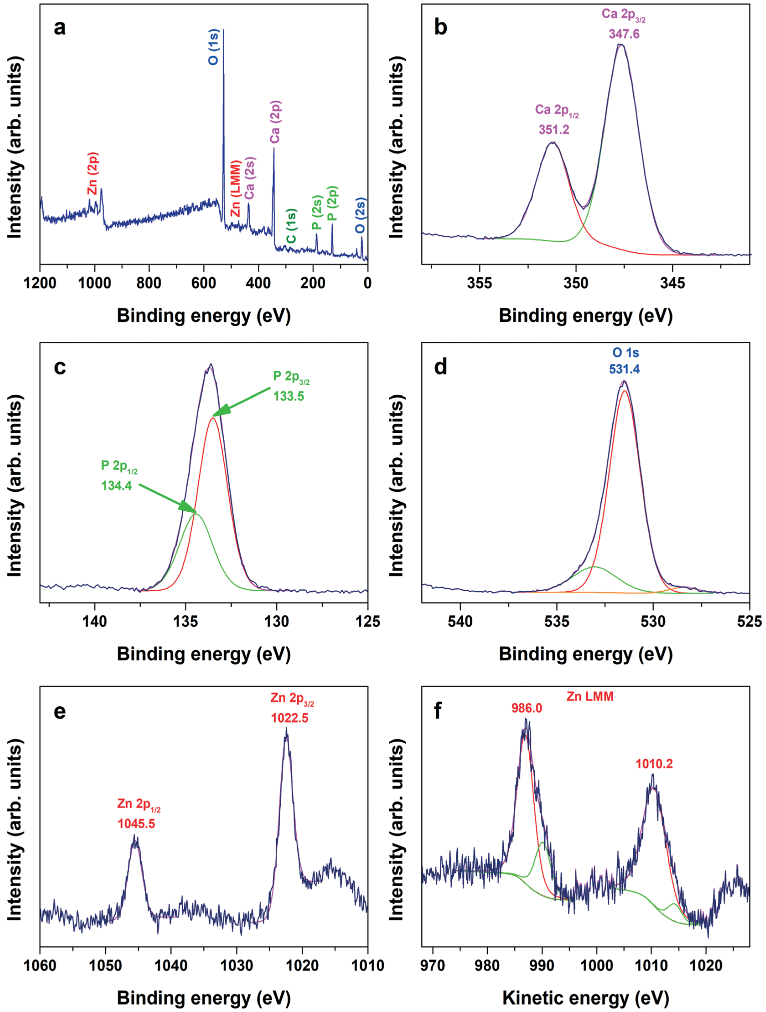

Fig. 8 Survey XPS spectrum of Zn-WH (a), high-resolution XPS spectra and fitting results of Ca 2p (b), P 2p (c), O 1s (d) and Zn 2p (e) peaks, and Auger Zn_{LMM} spectrum (f).

XPS spectra were collected to further reveal the chemical nature of the elements (Fig. 8). Curve fitting of the P core level lines was performed maintaining the 3/2 and 1/2 peak area ratio to 2 : 1. The Ca 2p band exhibited a well-resolved Ca $2p_{3/2}$ (347.6 ± 0.2 eV) and Ca $2p_{1/2}$ (351.2 ± 0.2 eV) doublet with a distinctive spin–orbit splitting δ of 3.6 eV (Fig. 8b). The BEs of the respective Ca 2p components were similar to the reported values of calcium ions that are bonded with PO_4^{3-} (ref. 52 and 53) as well as HPO_4^{2-} groups.[54] Due to the similar phosphorus chemical shifts of PO_4^{3-} and HPO_4^{2-} ions, adequate spectral fit was achieved using two P $2p_{3/2}$ and P $2p_{1/2}$ components at respective BEs of 133.5 eV and 134.4 eV.[53,54] The P 2p phosphate peak energies were similar to their reported values.[53] Due to spectral complexity and multiple possible contributions from carbonate, adsorbed water and other species at the sample surface, the O 1s spectrum was fitted using two major components (Fig. 8d). The peak at 531.4 eV was attributed to lattice oxygen, while the peak at 532.73 eV was attributed to other oxygen species such as carbonate, adsorbed water and hydrocarbon-related oxygen.[52,53,55] The high-resolution Zn 2p spectrum, unlike other common transition metals, does not exhibit multiplet splitting, and is seen as a pair of spin–orbit components.[56] However, zinc chemical state interpretation is difficult due to the minimal chemical shift in its compounds. To better discern different states of zinc a modified Auger parameter (m-AP) was calculated. This parameter was calculated by adding the most intense photoelectron peak BE to the kinetic energy of the most intense Auger peak – Zn $2p_{3/2}$ and Zn $L_3M_{45}M_{45}$. The Zn 2p spectrum consisted of two symmetric peaks located at 1045.5 (Zn $2p_{1/2}$) and 1022.5 eV (Zn $2p_{3/2}$). The Auger Zn $L_3M_{45}M_{45}$ peak positions are at kinetic energies of 986.0 and 1010.2 eV (Fig. 8f). The positions of these peaks, as well as the value of the modified Auger parameter of 2010 eV, correspond to the Zn^{2+} chemical state.[57,58] The (Ca + Zn)/P ratio in the analyzed material from the XPS data was calculated to be 1.39, which is slightly lower compared to the theoretical value of 1.43 in stoichiometric WH.

Fig. S10† shows the concentrations of Zn ions released into SBF solution from Zn-WH powders after soaking for different periods of time up to 14 days. It is evident that the concentration of Zn ions gradually increases with the increase of soaking time. The maximal concentration of Zn was determined to be 0.97 mg L^{-1} after 14 days. Unfortunately, we cannot compare the obtained results with other data on Zn-WH due to the absence of such studies. Overall, the comparison of the amount of released ions with other results is quite complicated due to the different experimental conditions such as the ion release medium, the powdered or pelletized form of the samples, different substitution levels, *etc.* Nevertheless, our obtained values are lower compared to those of previously analyzed β-TCP substituted with 5 mol% of Zn^{2+}.[59] On the other hand, the ion release experiment performed with 10 mol% Zn-substituted HA in Ca and Mg-free Hank's balanced salt solution did not reveal any Zn release even after soaking for 15 days.[29] At the same time, pelletized biphasic CPs composed of Zn-doped β-TCP and HA demonstrated considerably higher released amounts of Zn.[60] Further studies should be focused on the biological properties of Zn-WH *in vitro* and *in vivo*.

4. Conclusions

In the present study, zinc whitlockite (Zn-WH, $Ca_{18}Zn_2(HPO_4)_2(PO_4)_{12}$) was successfully synthesized *via* a dissolution–precipitation process under hydrothermal conditions for the first time. The influence of synthesis parameters such as medium pH, reaction time, temperature and concentration of precursors on the formation of the material was investigated in detail. It was demonstrated that Zn-WH without any crystalline impurities can be obtained in the pH range from 5.6 to 6.2 in a very short period of time – 1 h. Variation of chemical composition in terms of the Ca-to-Zn ratio was determined to be possible in a narrow range. Powder X-ray diffraction analysis and Rietveld refinement confirmed that the synthesized Zn-WH has a rhombohedral structure with the *R*3*c* space group. FTIR, Raman and ^1H solid-state NMR confirmed the presence of the HPO_4^{2-} group in the crystal structure. The ^{31}P NMR study confirmed the presence of three inequivalent phosphorus atoms, whereas only one PO_4 tetrahedron was determined to be protonated. The size and shape of the particles can be controlled by the concentration of the precursors as well as by the initial Ca-to-Zn ratio in the reaction mixture.

Conflicts of interest

There are no conflicts to declare.

Acknowledgements

This research was funded by a grant WHITCERAM (No. S-LJB-22-1) from the Research Council of Lithuania. Vilnius University is highly acknowledged for support from the Science Promotion Foundation (MSF-JM-5/2021). The center SPECTROVERSUM (**https://www.spectroversum.ff.vu.lt**) is acknowledged for use of solid-state NMR spectroscopic equipment. The authors sincerely acknowledge Dr. Justina Gaidukevic (Vilnius University) for technical assistance.

References

1 W. Habraken, P. Habibovic, M. Epple and M. Bohner, *Mater. Today*, 2016, **19**, 69–87.
2 R. Gopal and C. Calvo, *Nat. Phys. Sci.*, 1972, **237**, 30–32.
3 R. Gopal, C. Calvo, J. Ito and W. K. Sabine, *Can. J. Chem.*, 1974, **52**, 1155–1164.
4 F. Capitelli, F. Bosi, S. C. Capelli, F. Radica and G. Della Ventura, *Crystals*, 2021, **11**, 225.
5 F. M. McCubbin, B. L. Phillips, C. T. Adcock, K. T. Tait, A. Steele, J. S. Vaughn, M. D. Fries, V. Atudorei, K. E. V. Kaaden and E. M. Hausrath, *Am. Mineral.*, 2018, **103**, 1319–1328.

6 T. Konishi and S. Watanabe, *Phosphorus Res. Bull.*, 2021, **37**, 21–25.

7 H. L. Jang, K. Jin, J. Lee, Y. Kim, S. H. Nahm, K. S. Hong and K. T. Nam, *ACS Nano*, 2014, **8**, 634–641.

8 H. L. Jang, H. K. Lee, K. Jin, H.-Y. Ahn, H.-E. Lee and K. T. Nam, *J. Mater. Chem. B*, 2015, **3**, 1342–1349.

9 C. Wang, K.-J. Jeong, H. J. Park, M. Lee, S.-C. Ryu, D. Y. Hwang, K. H. Nam, I. H. Han and J. Lee, *J. Colloid Interface Sci.*, 2020, **569**, 1–11.

10 H. L. Jang, G. B. Zheng, J. Park, H. D. Kim, H.-R. Baek, H. K. Lee, K. Lee, H. N. Han, C.-K. Lee, N. S. Hwang, J. H. Lee and K. T. Nam, *Adv. Healthcare Mater.*, 2016, **5**, 128–136.

11 H. D. Kim, H. L. Jang, H.-Y. Ahn, H. K. Lee, J. Park, E.-S. Lee, E. A. Lee, Y.-H. Jeong, D.-G. Kim, K. T. Nam and N. S. Hwang, *Biomaterials*, 2017, **112**, 31–43.

12 F. A. Shah, *Acta Biomater.*, 2021, **125**, 72–82.

13 S. Amirthalingam, S. S. Lee, M. Pandian, J. Ramu, S. Iyer, N. S. Hwang and R. Jayakumar, *Biomater. Sci.*, 2021, **9**, 2439–2453.

14 X. Zhang, W. Liu, J. Liu, Y. Hu and H. Dai, *ACS Biomater. Sci. Eng.*, 2021, **7**, 3321–3331.

15 S. Pouraghaei Sevari, J. K. Kim, C. Chen, A. Nasajpour, C. Y. Wang, P. H. Krebsbach, A. Khademhosseini, S. Ansari, P. S. Weiss and A. Moshaverinia, *ACS Appl. Mater. Interfaces*, 2021, **13**, 35342–35355.

16 W.-B. Lee, C. Wang, J.-H. Lee, K.-J. Jeong, Y.-S. Jang, J.-Y. Park, M. H. Ryu, U.-K. Kim, J. Lee and D.-S. Hwang, *ACS Appl. Bio Mater.*, 2020, **3**, 7762–7768.

17 Y. Yang, H. Wang, H. Yang, Y. Zhao, J. Guo, X. Yin, T. Ma, X. Liu and L. Li, *ACS Biomater. Sci. Eng.*, 2020, **6**, 5785–5796.

18 J. Jeong, J. H. Shim, B. M. Koo, Y. B. Choy and C. Y. Heo, *Tissue Eng. Regener. Med.*, 2022, **19**, 83–92.

19 F. Nazir, L. Abbas and M. Iqbal, *Appl. Nanosci.*, 2022, **12**, 47–68.

20 D. Zhou, C. Qi, Y.-X. Chen, Y.-J. Zhu, T.-W. Sun, F. Chen and C.-Q. Zhang, *Int. J. Nanomed.*, 2017, **12**, 2673–2687.

21 M. Šupová, *Ceram. Int.*, 2015, **41**, 9203–9231.

22 Z. C. Yang, T. Y. Yao, X. Y. Zheng, J. F. Hui and D. D. Fan, *Nano Res.*, 2022, **15**, 1303–1309.

23 R. D. Shannon, *Acta Crystallogr., Sect. A: Cryst. Phys., Diffr., Theor. Gen. Crystallogr.*, 1976, **32**, 751–767.

24 E. Kostiner and J. R. Rea, *Acta Crystallogr., Sect. B: Struct. Crystallogr. Cryst. Chem.*, 1976, **32**, 250–253.

25 A. Jacobs, G. Renaudin, C. Forestier, J.-M. Nedelec and S. Descamps, *Acta Biomater.*, 2020, **117**, 21–39.

26 B. Srinivasan, E. Kolanthai, N. E. A. Kumaraswamy, R. R. Jayapalan, D. S. Vavilapalli, L. H. Catalani, G. S. Ningombam, N. S. Khundrakpam, N. R. Singh and S. N. Kalkura, *J. Phys. Chem. B*, 2019, **123**, 5506–5513.

27 A. Kizalaite, I. Grigoraviciute-Puroniene, D. R. C. Asuigui, S. L. Stoll, S. H. Cho, T. Sekino, A. Kareiva and A. Zarkov, *ACS Biomater. Sci. Eng.*, 2021, **7**, 3586–3593.

28 A. Ito, K. Ojima, H. Naito, N. Ichinose and T. Tateishi, *J. Biomed. Mater. Res.*, 2000, **50**, 178–183.

29 S. Sprio, L. Preti, M. Montesi, S. Panseri, A. Adamiano, A. Vandini, N. M. Pugno and A. Tampieri, *ACS Biomater. Sci. Eng.*, 2019, **5**, 5947–5959.

30 Y. Su, K. Wang, J. Gao, Y. Yang, Y.-X. Qin, Y. Zheng and D. Zhu, *Acta Biomater.*, 2019, **98**, 174–185.

31 T. Kokubo and H. Takadama, *Biomaterials*, 2006, **27**, 2907–2915.

32 M. Yashima, A. Sakai, T. Kamiyama and A. Hoshikawa, *J. Solid State Chem.*, 2003, **175**, 272–277.

33 T. Debroise, E. Colombo, G. Belletti, J. Vekeman, Y. Su, R. Papoular, N. S. Hwang, D. Bazin, M. Daudon, P. Quaino and F. Tielens, *Cryst. Growth Des.*, 2020, **20**, 2553–2561.

34 H. Cheng, R. Chabok, X. Guan, A. Chawla, Y. Li, A. Khademhosseini and H. L. Jang, *Acta Biomater.*, 2018, **69**, 342–351.

35 D. Griesiute, L. Sinusaite, A. Kizalaite, A. Antuzevics, K. Mazeika, D. Baltrunas, T. Goto, T. Sekino, A. Kareiva and A. Zarkov, *CrystEngComm*, 2021, **23**, 4627–4637.

36 D. Griesiute, J. Gaidukevic, A. Zarkov and A. Kareiva, *Sustainability*, 2021, **13**, 7859.

37 C. Combes and C. Rey, *Acta Biomater.*, 2010, **6**, 3362–3378.

38 X. Cao, W. G. Harris, M. S. Josan and V. D. Nair, *Sci. Total Environ.*, 2007, **383**, 205–215.

39 X. Guo, X. Liu, H. Gao, X. Shi, N. Zhao and Y. Wang, *J. Mater. Sci. Technol.*, 2018, **34**, 1054–1059.

40 R. G. Carrodeguas and S. De Aza, *Acta Biomater.*, 2011, **7**, 3536–3546.

41 P. N. de Aza, C. Santos, A. Pazo, S. de Aza, R. Cuscó and L. Artús, *Chem. Mater.*, 1997, **9**, 912–915.

42 B. Wopenka and J. D. Pasteris, *Mater. Sci. Eng., C*, 2005, **25**, 131–143.

43 B. L. Jolliff, J. M. Hughes, J. J. Freeman and R. A. Zeigler, *Am. Mineral.*, 2006, **91**, 1583–1595.

44 K. T. Tait, M. C. Barkley, R. M. Thompson, M. J. Origlieri, S. H. Evans, C. T. Prewitt and H. Yang, *Can. Mineral.*, 2011, **49**, 1065–1078.

45 M. Ben Osman, S. Diallo-Garcia, V. Herledan, D. Brouri, T. Yoshioka, J. Kubo, Y. Millot and G. Costentin, *J. Phys. Chem. C*, 2015, **119**, 23008–23020.

46 L. Obadia, P. Deniard, B. Alonso, T. Rouillon, S. Jobic, J. Guicheux, M. Julien, D. Massiot, B. Bujoli and J.-M. Bouler, *Chem. Mater.*, 2006, **18**, 1425–1433.

47 A. T. Grigg, M. Mee, P. M. Mallinson, S. K. Fong, Z. Gan, R. Dupree and D. Holland, *J. Solid State Chem.*, 2014, **212**, 227–236.

48 E. Davies, M. J. Duer, S. E. Ashbrook and J. M. Griffin, *J. Am. Chem. Soc.*, 2012, **134**, 12508–12515.

49 J. M. Hughes, B. L. Jolliff and J. Rakovan, *Am. Mineral.*, 2008, **93**, 1300–1305.

50 C. T. Adcock, E. M. Hausrath, P. M. Forster, O. Tschauner and K. J. Sefein, *Am. Mineral.*, 2014, **99**, 1221–1232.

51 K. S. W. Sing, *Pure Appl. Chem.*, 1985, **57**, 603–619.

52 C.-W. Yang and T.-S. Lui, *Acta Biomater.*, 2009, **5**, 2728–2737.

53 T. T. Eighmy, A. E. Kinner, E. L. Shaw, J. D. Eusden Jr. and C. A. Francis, *Surf. Sci. Spectra*, 1999, **6**, 219–227.

54 G. Duan, L. Yang, S. Liao, C. Zhang, X. Lu, Y. Yang, B. Zhang, Y. Wei, T. Zhang, B. Yu, X. Zhang and F. Wang, *Corros. Sci.*, 2018, **135**, 197–206.

55 L. Wu, L. Zhao, J. Dong, W. Ke and N. Chen, *Electrochim. Acta*, 2014, **145**, 71–80.

56 M. C. Biesinger, B. P. Payne, A. P. Grosvenor, L. W. M. Lau, A. R. Gerson and R. S. C. Smart, *Appl. Surf. Sci.*, 2011, **257**, 2717–2730.

57 C. R. Chandraiahgari, G. De Bellis, P. Ballirano, S. K. Balijepalli, S. Kaciulis, L. Caneve, F. Sarto and M. S. Sarto, *RSC Adv.*, 2015, **5**, 49861–49870.

58 S. Bera, S. Dhara, S. Velmurugan and A. K. Tyagi, *Int. J. Spectrosc.*, 2012, **2012**, 371092.

59 L. Sinusaite, A. Popov, A. Antuzevics, K. Mazeika, D. Baltrunas, J.-C. Yang, J. L. Horng, S. Shi, T. Sekino, K. Ishikawa, A. Kareiva and A. Zarkov, *Mater. Sci. Eng., C*, 2020, **112**, 110918.

60 M. Ikeuchi, A. Ito, Y. Dohi, H. Ohgushi, H. Shimaoka, K. Yonemasu and T. Tateishi, *J. Biomed. Mater. Res., Part A*, 2003, **67**, 1115–1122.

Electronic Supplementary Material (ESI) for CrystEngComm.

Supplementary information

Peculiarities of the formation, structural and morphological properties of zinc whitlockite ($Ca_{18}Zn_2(HPO_4)_2(PO_4)_{12}$) synthesized via phase transformation process under hydrothermal conditions

Agne Kizalaite[1], Vytautas Klimavicius[2], Justina Versockiene[3], Egle Lastauskiene[3], Tomas Murauskas[1], Ramunas Skaudzius[1], Taishi Yokoi[4], Masakazu Kawashita[4], Tomoyo Goto[5,6], Tohru Sekino[5], Aleksej Zarkov[1,*]

[1] *Institute of Chemistry, Vilnius University, Naugarduko 24, LT-03225 Vilnius, Lithuania*

[2] *Institute of Chemical Physics, Vilnius University, Sauletekio 3, LT-10257, Vilnius, Lithuania*

[3] *Institute of Biosciences, Life Sciences Center, Vilnius University, Sauletekio 7, LT-10257 Vilnius, Lithuania*

[4] *Institute of Biomaterials and Bioengineering, Tokyo Medical and Dental University, 2-3-10 Kanda-Surugadai, Chiyoda-ku, Tokyo 101-0062, Japan*

[5] *SANKEN (The Institute of Scientific and Industrial Research), Osaka University, 8–1 Mihogaoka, Ibaraki, Osaka 567–0047, Japan*

[6] *Institute for Advanced Co-Creation Studies, Osaka University, 1-1 Yamadaoka, Suita, Osaka 565-0871, Japan*

*Authors to whom correspondence should be addressed.

Aleksej Zarkov: e-mail: aleksej.zarkov@chf.vu.lt

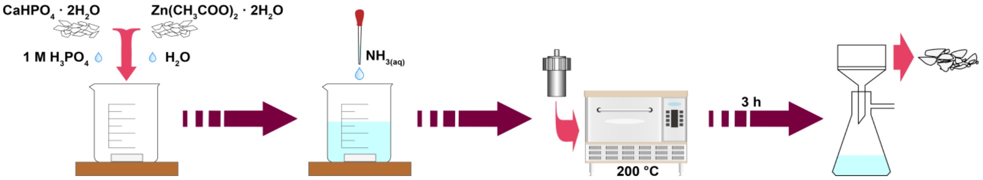

Figure S1. Schematic representation of the synthesis of Zn-WH powders.

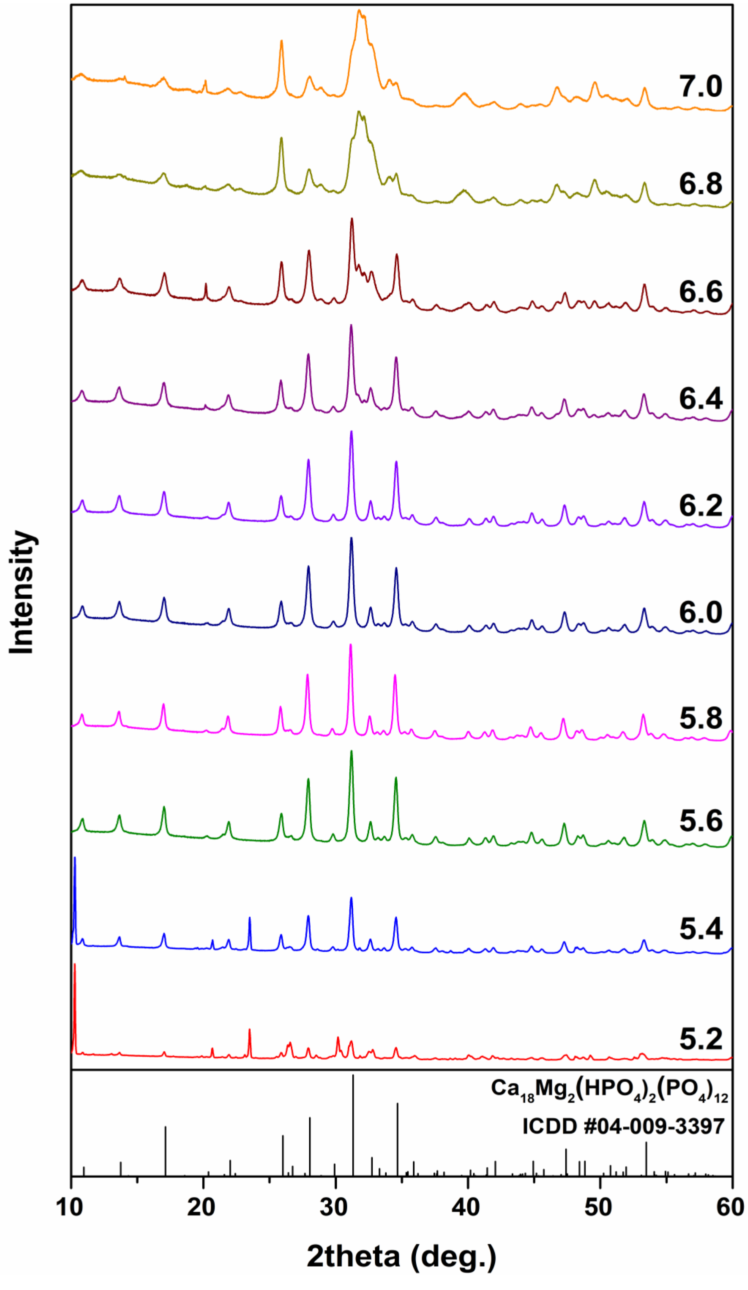

Figure S2. XRD patterns of synthesis products obtained at different pH values (t = 3h; T = 200 °C).

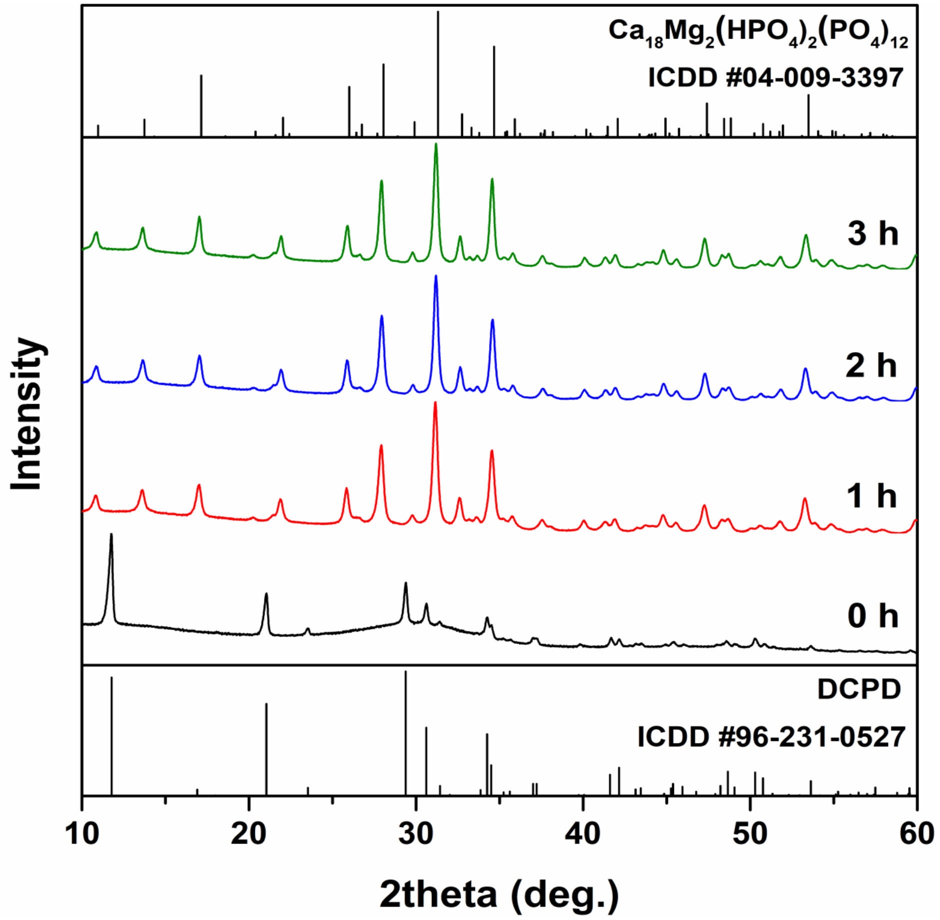

Figure S3. XRD patterns of synthesis products after different reaction times (pH = 5.8; T = 200 °C).

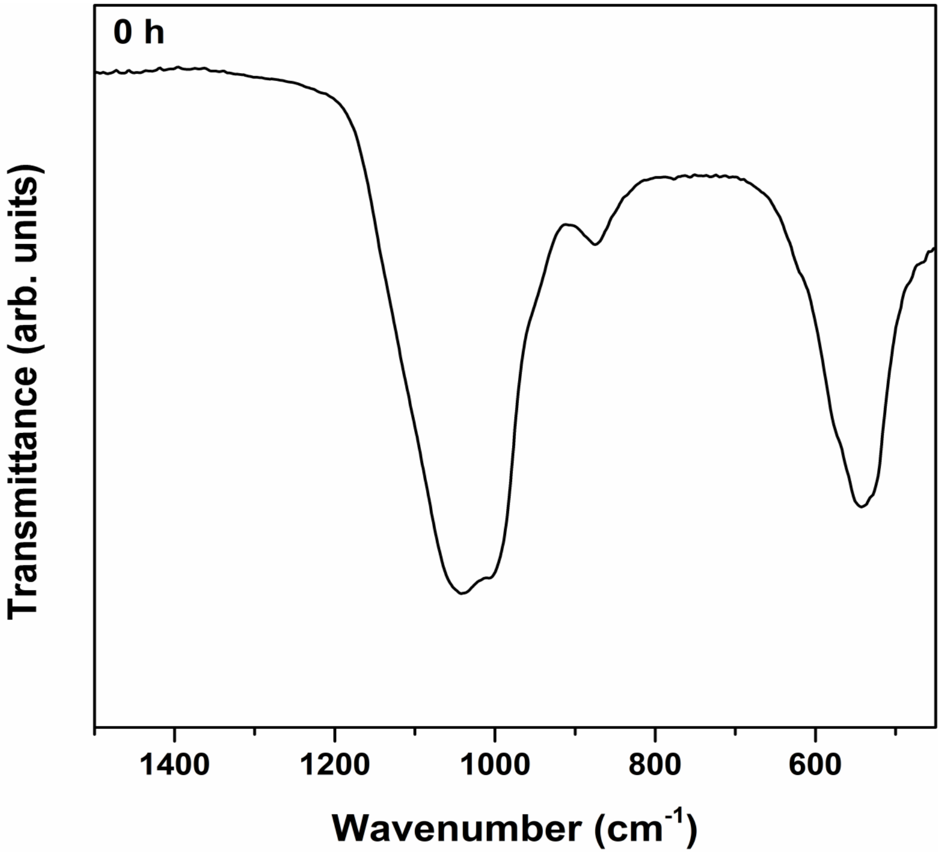

Figure S4. FTIR spectrum of as-precipitated powders.

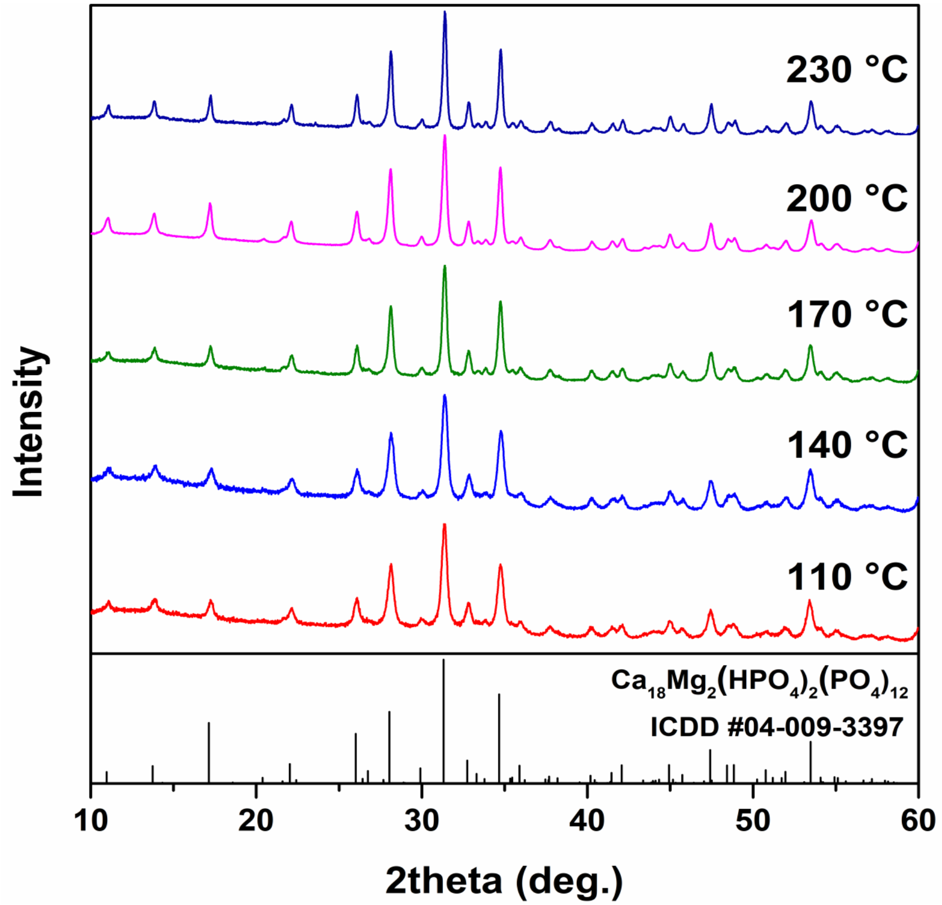

Figure S5. XRD patterns of synthesis products obtained at different reaction temperatures (pH = 5.8, t = 3 h).

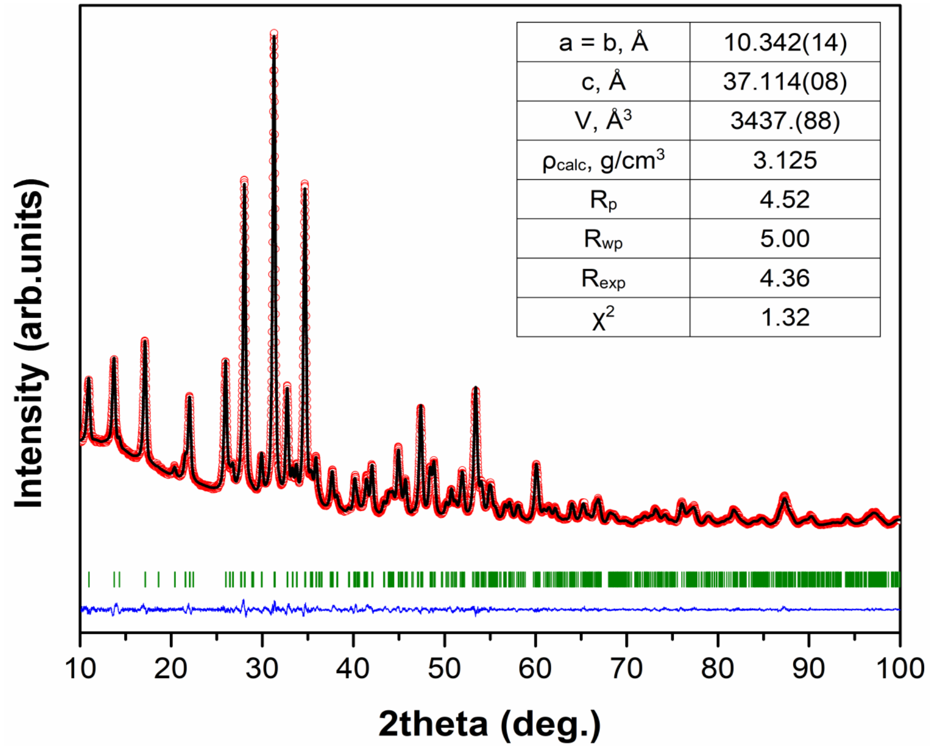

a = b, Å	10.342(14)
c, Å	37.114(08)
V, Å^3	3437.(88)
ρ_{calc}, g/cm^3	3.125
R_p	4.52
R_{wp}	5.00
R_{exp}	4.36
χ^2	1.32

Figure S6. Rietveld refinement of the XRD data obtained for Zn-WH (T = 200°C; t = 3 h; pH = 5.8) refined in space group R3c. The red circle symbols and the black solid line represent the experimental and calculated intensities, respectively, and the blue line below is the difference between them. The green tick marks indicate the positions of the Bragg peaks.

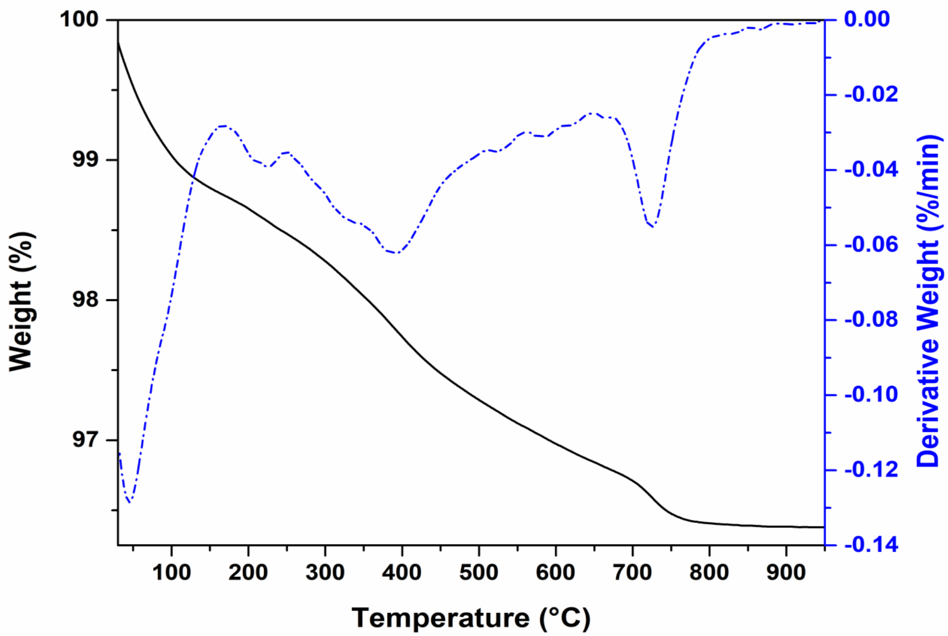

Figure S7. TG-DTG curves of Zn-WH (pH = 5.8, t = 3 h, T = 200 °C).

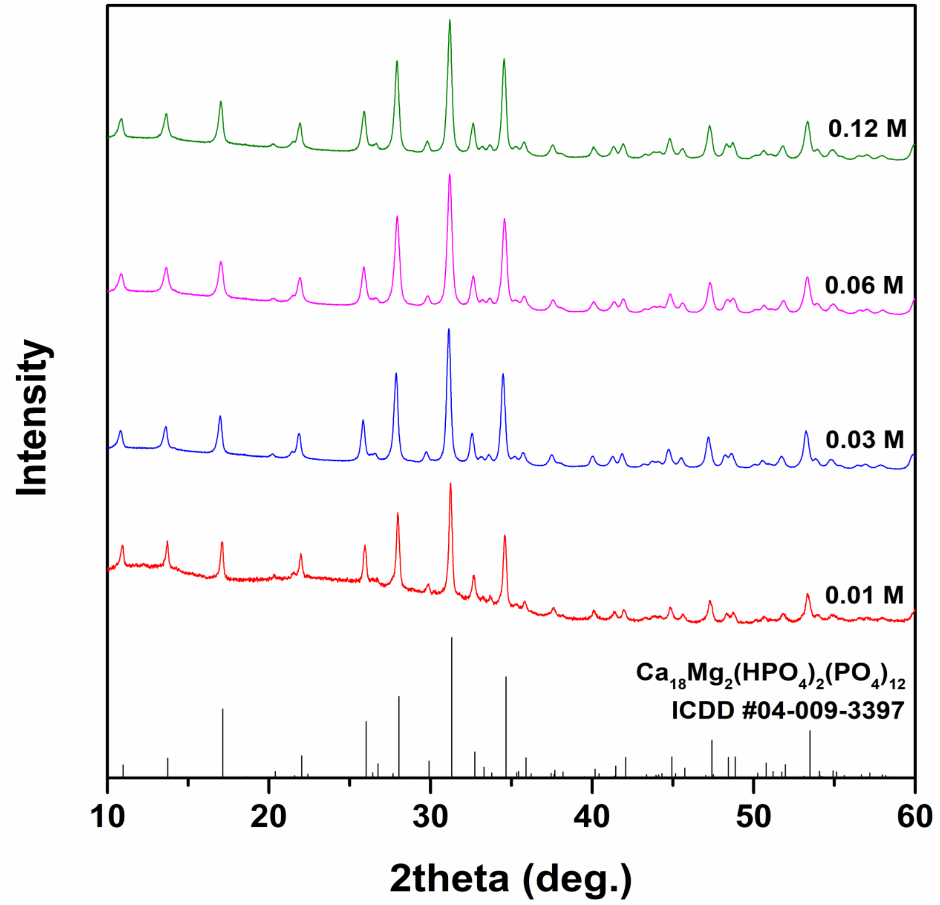

Figure S8. XRD patterns of synthesis products obtained with different concentrations of starting materials (pH = 5.8, t = 3 h, T = 200 °C).

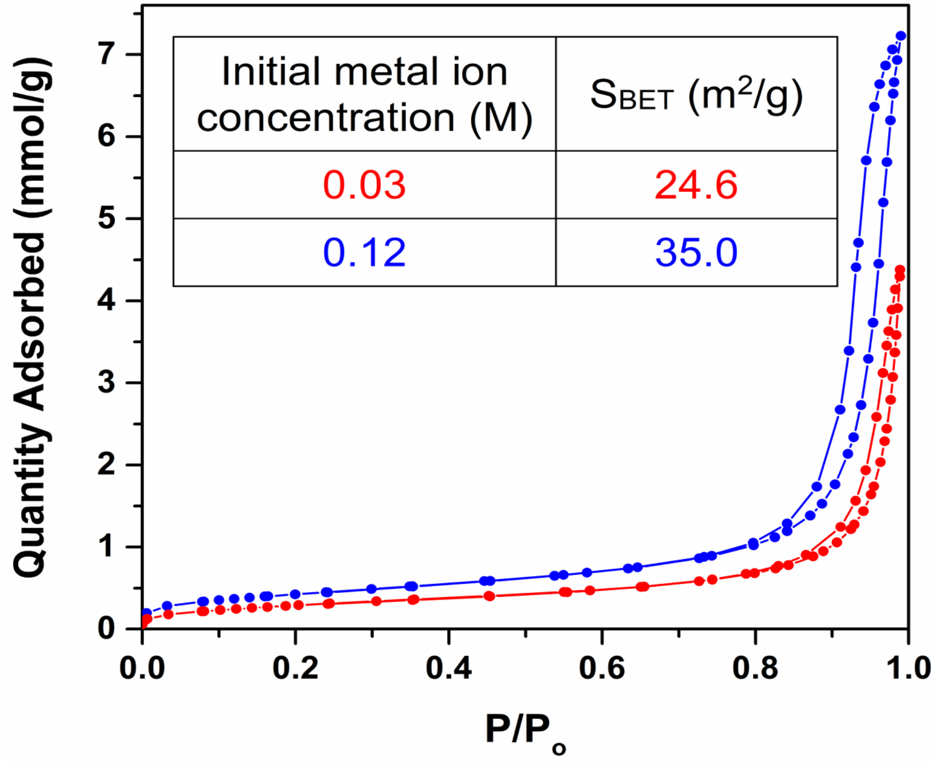

Initial metal ion concentration (M)	SBET (m^2/g)
0.03	24.6
0.12	35.0

Figure S9. N_2 absorbtion-desorbtion isotherms of Zn-WH powders obtained with different total metal ion concentrations.

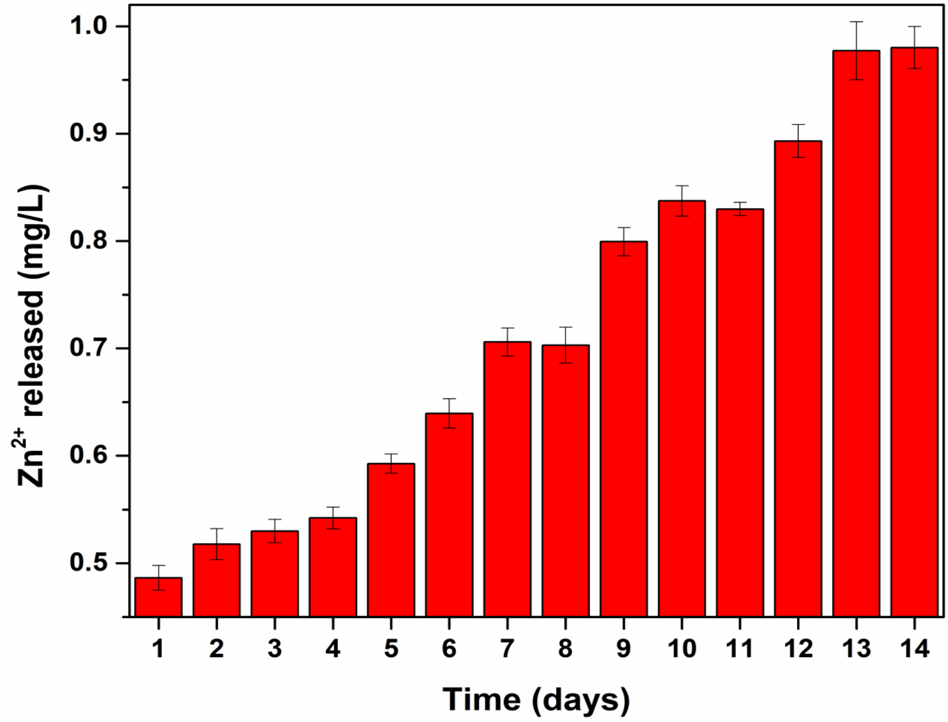

Figure S10. Zinc release in SBF solution.

4th publication

A copper-containing analog of the biomineral whitlockite: dissolution–precipitation synthesis, structural and biological properties

D. Griesiūtė, **A. Kizalaitė**, A. Dubnika, V. Klimavičius, V. Kalendra, V. Tyrpekl, S. H. Cho, T. Goto, T. Sekino, A. Žarkov

Dalton Transactions, 53(4), 2024, 1722-1734
(https://doi.org/10.1039/D3DT03756H)

Dalton
Transactions

ROYAL SOCIETY
OF CHEMISTRY

PAPER

View Article Online
View Journal | View Issue

Cite this: *Dalton Trans.*, 2024, **53**, 1722

A copper-containing analog of the biomineral whitlockite: dissolution–precipitation synthesis, structural and biological properties†

Diana Griesiute,[a] Agne Kizalaite,[a] Arita Dubnika,[b,c] Vytautas Klimavicius,[d] Vidmantas Kalendra,[e] Vaclav Tyrpekl,[f] Sung Hun Cho,[g] Tomoyo Goto,[g,h] Tohru Sekino[g] and Aleksej Zarkov*[a]

In the present work, copper whitlockite (Cu-WH, $Ca_{18}Cu_2(HPO_4)_2(PO_4)_{12}$) was successfully synthesized and comprehensively characterized, founding the base knowledge for its future studies in medicine, particularly for bone regeneration. This material is a copper-containing analog of the well-known biomineral magnesium whitlockite (Mg-WH, $Ca_{18}Mg_2(HPO_4)_2(PO_4)_{12}$). The synthesis of powders was performed by a dissolution–precipitation method in an aqueous medium under hydrothermal conditions. Phase conversion from brushite ($CaHPO_4{\cdot}2H_2O$) to Cu-WH took place in an acidic medium in the presence of Cu^{2+} ions. Optimization of the synthesis conditions in terms of medium pH, temperature, time, Ca/Cu molar ratio and concentration of starting materials was performed. The crystal structure of the synthesized products was confirmed by XRD, FTIR and Raman spectroscopy, ^1H and ^{31}P solid-state NMR, and EPR. Morphological features and elemental distribution of the synthesized powders were studied by means of SEM/EDX analysis. The ion release in SBF solution was estimated using ICP-OES. Cytotoxicity experiments were performed with MC3T3-E1 cells. The study on thermal stability revealed that the synthesized material is thermally unstable and gradually decomposes upon annealing to Cu-substituted β-$Ca_3(PO_4)_2$ and $Ca_2P_2O_7$.

Received 10th November 2023,
Accepted 12th December 2023

DOI: 10.1039/d3dt03756h

rsc.li/dalton

1. Introduction

Synthetic calcium phosphates (CPs) are widely used in medicine for bone regeneration purposes due to their structural and chemical similarities to natural bone.[1] Although CPs are highly biocompatible and have already demonstrated high efficiency, one of the directions of research aimed at achieving the superior performance of CP-based materials considers the partial replacement of Ca by other ions.[2] The ion substitution strategy allows combining the characteristics of CPs with newly obtained substitution-induced properties: antibacterial, optical, magnetic, *etc.*[3] This approach leads to the development of biocompatible multifunctional materials with a wider application range.[4]

One of the most promising substituting ions is Cu^{2+}. Being an essential element in the human body, Cu is involved in numerous physiological functions; however, its relatively high local concentration is toxic.[5] This reason limited the development and application of Cu-containing biomaterials for a long time. Nevertheless, in recent years the number of publications on Cu-modified biomaterials has grown constantly.[6] The reason for this increased interest is the nature and specific biological properties of Cu^{2+} ions. It was confirmed that Cu is exceptionally useful in the development of materials for orthopedic applications. Cu-doped CPs demonstrate antibacterial properties, provide angiogenic ability and favor osteogenesis; these properties represent the key points for ideal biomaterial integration and the healing process.[6]

---

[a] *Institute of Chemistry, Vilnius University, Naugarduko 24, LT-03225 Vilnius, Lithuania. E-mail: aleksej.zarkov@chf.vu.lt*

[b] *Rudolfs Cimdins Riga Biomaterials Innovations and Development Centre of RTU, Faculty of Materials Science and Applied Chemistry, Institute of General Chemical Engineering, Riga Technical University, LV-1007 Riga, Latvia*

[c] *Baltic Biomaterials Centre of Excellence, Headquarters at Riga Technical University, LV-1658 Riga, Latvia*

[d] *Institute of Chemical Physics, Vilnius University, Sauletekio 3, LT-10257 Vilnius, Lithuania*

[e] *Institute of Applied Electrodynamics and Telecommunications, Vilnius University, Sauletekio 3, LT-10257 Vilnius, Lithuania*

[f] *Department of Inorganic Chemistry, Faculty of Science, Charles University, Hlavova 2030/8, 128 43 Prague, Czech Republic*

[g] *SANKEN (The Institute of Scientific and Industrial Research), Osaka University, 8-1 Mihogaoka, Ibaraki, Osaka 567-0047, Japan*

[h] *Institute for Advanced Co-Creation Studies, Osaka University, 1-1 Yamadaoka, Suita, Osaka 565-0871, Japan*

† Electronic supplementary information (ESI) available. See DOI: **https://doi.org/10.1039/d3dt03756h**

The majority of the works investigating Cu-substituted CPs are focused on the most popular synthetic phases including calcium hydroxyapatite (HA, $Ca_{10}(PO_4)_6(OH)_2$),[7] beta-tricalcium phosphate (β-TCP, $Ca_3(PO_4)_2$),[8–10] brushite (DCPD, $CaHPO_4 \cdot 2H_2O$),[11,12] and biphasic CPs (HA + β-TCP).[13] For instance, Cu-doped HA demonstrated an antimicrobial effect against *E. coli* and *C. albicans*.[7] Cu-containing TCP was determined to be biocompatible, revealing no cytotoxic effect regardless of the studied Cu substitution level; moreover, it showed antibacterial properties against *E. coli*, *E. faecalis*, *S. aureus* and *P. aeruginosa*.[10] Cu-loaded DCPD cement was recognized as a suitable material for bone tissue defect-related repair in orthopedic surgeries demonstrating good antibacterial properties and cell affinity.[11]

Magnesium whitlockite (Mg-WH, $Ca_{18}Mg_2(HPO_4)_2(PO_4)_{12}$) is an ion-substituted member of the CP family naturally occurring in the human body. Due to the similarity of the crystal structures of WH and β-TCP, these two names are often used interchangeably and synonymously; however, the structural and compositional differences are well discussed in the literature.[14,15] The data on the presence of Mg-WH in the human body are rather contradictory. While some authors claim that depending on the age Mg-WH can constitute a quite significant part of human hard tissues – up to 25–35%,[16] some research studies show that Mg-WH is found exceptionally in pathological tissues.[17] Nevertheless, synthetic Mg-WH demonstrated superior biological properties and suitability for bone regeneration applications.[18,19] Considering an ion-substitution strategy and the peculiarities of the WH structure, it looks reasonable to investigate synthetic materials with the WH structure, where Mg ions are substituted by other biologically active small cations. In this light, the first row transition metal ions appear to be suitable candidates to form WH structures since their ionic radii are close enough to that of Mg^{2+} ions.[20] To the best of our knowledge, currently there are only a few published reports regarding the synthesis and characterization of transition metal WH, including some on Zn-WH,[21–23] Mn-WH,[24,25] and Co-WH[26] and a recently published report on the feasibility of the formation of Cu-WH.[27]

The main aim of this work was to comprehensively investigate the peculiarities of the formation of Cu-WH and to study its structural, morphological and biological properties in detail. For this purpose, nanodimensional Cu-WH powders were synthesized *via* a dissolution–precipitation process under hydrothermal conditions. The crystal structure and phase purity were confirmed by powder X-ray diffraction (XRD), vibrational and ^1H and ^{31}P nuclear magnetic resonance (NMR) spectroscopy. Electron paramagnetic resonance (EPR) was employed to investigate in depth the structural characteristics. Scanning electron microscopy (SEM) and transmission electron microscopy (TEM) were used to study the morphology of the synthesized materials. The ion release in SBF solution was estimated using inductively coupled plasma optical emission spectrometry (ICP-OES). Finally, the cytotoxicity of the developed Cu-WH samples was evaluated using the MC3T3-E1 pre-osteoblastic cell line.

2. Experimental

2.1. Synthesis

Cu-WH powders were synthesized in hydrothermal autoclave reactors equipped with PTFE liners. For the synthesis, calcium hydrogen phosphate dihydrate (DCPD, $CaHPO_4 \cdot 2H_2O$, 99.1%, Eurochemicals) and copper(II) nitrate trihydrate ($Cu(NO_3)_2 \cdot 3H_2O$, ≥98%, Roth) were used as starting materials. In a typical procedure, appropriate amounts of metal salts were transferred into 90 mL PTFE liners and dissolved at room temperature in 50 mL of deionized water by addition of 10 mL of 1 M phosphoric acid (H_3PO_4, 75%, Roth). After the complete dissolution of precursors under constant mixing on a magnetic stirrer, a clear blue colored solution was obtained. In a standard synthesis, the total concentration of metal ions in the reaction mixture was 0.08 M. Next, concentrated ammonia solution was added to the reaction mixture in order to adjust the pH to a certain value. After the addition of ammonia solution, the instantaneous formation of precipitates was observed. The PTFE liners were transferred into stainless steel jackets, screwed tightly, placed into a preheated oven and heated at different temperatures (110–230 °C) for different periods of time (1–24 h). In this work, the synthesis time was calculated from the moment the hydrothermal reactors were placed in the oven to the moment they were removed to room temperature. After the synthesis, the reactors were cooled down and the resulting blue powders were separated from the solution by vacuum filtering. Afterwards, the powders were washed with deionized water and dried in the oven at 70 °C.

2.2. Characterization

Powder X-ray diffraction (XRD) data of the synthesized specimens were obtained using a Rigaku MiniFlex II diffractometer (Cu-Kα, $\lambda = 1.5419$ Å) working in Bragg–Brentano ($\theta/2\theta$) geometry. The data were collected within the 10–100 2θ angle range at a speed of 1° min^{-1}. The FullProf Suite was used for structural refinement (FullProf Suite software version September-2020).

Fourier transform infrared (FTIR) spectra were obtained in the range of 4000–400 cm^{-1} with a Bruker ALPHA-FTIR spectrometer.

Raman spectra were recorded using a combined Raman and scanning near field optical microscope WiTec Alpha 300 R equipped with a 532 nm excitation laser source.

Thermal decomposition of the synthesized powders was analyzed by thermogravimetric analysis (TGA) using a PerkinElmer STA 6000 Simultaneous Thermal Analyzer. A dried sample of about 20 mg was heated from 25 to 900 °C at a heating rate of 10 °C min^{-1} under dry flowing air (20 mL min^{-1}).

Solid-state nuclear magnetic resonance (NMR) experiments were carried out at 14.1 T on a Bruker Avance Neo 600 NMR spectrometer operating at 600.3 and 243.0 MHz for ^1H and ^{31}P, respectively, using a 2.5 mm Trigamma MAS probe and 2.5 mm zirconia rotors. The temperature was stabilized at 298 K and the MAS rate was set to 20 kHz. For ^1H MAS experiments, a pulse sequence containing two π refocusing pulses with a delay of 2 μs was employed to eliminate the signal from the probe background. The ^1H 90° excitation pulse was 2.1 μs and 16 scans were accumulated using a repetition delay of 10 s. For ^{31}P MAS measurements, a saturation recovery pulse sequence was used. The saturation pulse train consisted of 10 π/2 pulses followed by 100 s delay. The π/2 excitation pulse was equal to 3.6 μs, and 1024 scans were accumulated. $^1H \rightarrow {}^{31}P$ CP MAS measurements were performed with 2 ms CP contact time employing a 100–50% ramp on the ^1H channel, and 4096 scans were accumulated using a repetition delay of 10 s. ^1H and ^{31}P spectra were referenced respectively to TMS using adamantane (δ (^1H) = 1.85 ppm) and 85% H_3PO_4 using ADP (ammonium dihydrogen phosphate, $NH_4H_2PO_4$, δ (^{31}P) = 0.8 ppm).

The electron paramagnetic resonance (EPR) spectra were recorded on a Bruker ELEXSYS E580 EPR spectrometer equipped with a Bruker ER4118X-MD5 (pulsed X-band) microwave resonator. High-power pulses were obtained using a 1 kW TWT (X-band) microwave amplifier. A helium flow cryostat was used to stabilize the temperature. The operating microwave frequency was set to 9.7 GHz to best match the broad band of the strongly over-coupled pulsed resonator. All the pulsed EPR spectra were acquired at 4.5 K. The echo-detected field sweep (EDFS) spectra were recorded using a Hahn echo pulse sequence (π/2–τ–π–τ–echo) with an interpulse delay τ of 140 ns. The echo was integrated over a 60 ns time window that was centered at the maximum of the echo signal. The lengths of the π/2- and π-pulses were 8 ns and 16 ns, respectively. For the two-dimensional (2D) Hyperfine Sublevel Correlation (HYSCORE)[28] spectra, the echo amplitude was measured using the pulse sequence (π/2–τ–π/2–t_1–π–t_2–π/2–echo) with 8 ns and 16 ns lengths for the π/2- and π-pulses, respectively, and a 12 ns detector gate (that is centered at the maximum of the echo signal). The delays in the pulse sequence are defined as the differences in the starting points of the pulses. The echo intensity was measured as a function of t_1 and t_2, where t_1 and t_2 were increased in steps of 16 ns from an initial value of 40 ns and 32 ns, respectively. 256 steps were used for each dimension. The 8 ns time difference between the initial values of t_1 and t_2 was set to account for the difference in the lengths between the π/2- and π-pulses. This provided symmetric spectra in both dimensions. The unwanted echoes were eliminated by applying a 16-step phase cycling procedure. The HYSCORE spectra of the Cu-WH powder sample were recorded at magnetic field of 334.5 mT with an inter-pulse delay, τ, of 174 ns.

The time domain 2D HYSCORE data were processed using MATLAB R2023a. A third-order polynomial baseline was subtracted from the resulting time-domain spectra. The corrected spectra were zero-filled to obtain a [2048 × 2048] matrix and Fourier transformed using a Fast Fourier Transformation (FFT) algorithm. The frequency domain spectra were plotted as the amplitude (absolute value) of the 2D frequency components.

The morphology of the synthesized powders and elemental distribution were analyzed by scanning electron microscopy (SEM) using a Hitachi SU-9000 microscope equipped with an energy dispersive X-ray spectrometer (EDX).

The elemental composition of the synthesized compounds was determined by inductively coupled plasma optical emission spectrometry (ICP-OES) using a PerkinElmer Optima 7000 DV spectrometer.

For the ion release experiment, 0.6 g of Cu-WH powders was soaked in 30 mL of simulated body fluid (SBF), and the samples were investigated in triplicate. An SBF solution was prepared according to the procedure reported by Kokubo *et al.*[29] The samples were kept in closed containers in a shaker incubator (BioSan ES-20/80) at 37 °C for 14 days under constant mixing at 250 rpm. Every day, 1 mL of the solution was taken from the sample for elemental analysis and replaced with the same amount of fresh SBF solution to maintain a constant volume. Quantitative determination of the released Cu^{2+} ions was performed by ICP-OES.

2.3. *In vitro* cytotoxicity studies

The cytotoxicity of Cu-WH powders was assessed using the MC3T3-E1 cell line (preosteoblasts). In the extract test, 4500 cells per well were seeded in a 96-well plate with 100 μL of the cell medium, composed of 89% Alpha Modified Eagle's Medium (α-MEM), 10% fetal bovine serum (FBS) and 1% penicillin/streptomycin (P/S). The plates with the cells were incubated overnight at 37 °C under 5% CO_2 (New Brunswick™ S41i CO_2 Incubator Shaker, Eppendorf, Hamburg, Germany).

The Cu-WH powder sample was suspended in 5 ml of fresh cell medium, resulting in a concentration of 10 mg mL^{-1}. After 24 and 48 hours, all the solution was collected from the samples and replaced with an additional 5 ml of fresh cell medium. The collected solution was then filtered through a 0.2 μm syringe filter and subsequently used for dilution with fresh medium – at extract to cell medium ratios of 1 : 10 and 1 : 100. The tested concentrations were 0.1 mg mL^{-1} and 0.01 mg mL^{-1}. Extract dilutions were immediately applied onto the preincubated cells (100 μL for each well). Untreated cells were used as a positive control and 5% dimethylsulfoxide (DMSO) solution in the medium was applied to cells as a negative control. There were six replicates for each sample and controls.

Cell Counting Kit-8 (CCK-8) assay was used to assess the cytotoxicity of Cu-WH extracts. For both time points, samples were incubated for 24 h and then 10 μL of CCK-8 solution was added to the cultivation media in each well and incubated for 1 h at 37 °C under 5% CO_2. Absorption at 450 nm was measured using an Infinite M Nano microplate reader (Tecan, Männedorf, Switzerland).

3. Results and discussion

The crystal structure of WH is closely related to that of β-TCP,[14,30] which crystallizes in a rhombohedral structure with the space group *R*3*c* (#161).[30] The crystal lattice of β-TCP contains 5 inequivalent Ca sites and 3 inequivalent P sites. These crystallographic positions are distributed between two types of columns arranged along the *c* axis: A and B. The A column has a form of P(1)O_4–Ca(4)–Ca(5), whereas in the B column calcium atoms and phosphate tetrahedra are arranged in the following sequence: P(3)O_4–Ca(1)–Ca(3)–Ca(2)–P(2)O_4. The Ca(1), Ca(2), Ca(3) and Ca(5) sites are fully occupied by calcium, while the Ca(4) site shows an occupancy factor of 0.5. Each A column is surrounded by six B columns, and each B column is surrounded by two A columns on the opposite sides and four B columns. The Ca^{2+} ions in β-TCP can be substituted by a variety of other cations. Foreign ions depending on their ionic radii and substitution levels tend to occupy one or several distinct Ca sites.[31] The crystal structures of natural and synthetic Mg-WH (Fig. 1) are comprehensively investigated by means of XRD analysis and neutron diffraction and the difference between WH and β-TCP structures is explained.[14,15,32]

To some extent, WH can be considered as an ion-substituted β-TCP; however, other structural and compositional differences include metal ion to phosphorus ratio, the presence of a protonated phosphate group (HPO_4^{2-}) and cationic vacancies. The B columns in both WH and non-substituted β-TCP are identical; the difference occurs in the A column. The small cation (*e.g.* Mg^{2+}, Zn^{2+}, and Mn^{2+}) in the WH structure occupies the most energetically favorable six-fold coordinated Ca(5) site, while the Ca(4) site remains vacant. The protons are bonded to the P(1)O_4 tetrahedra, being close to the Ca(4) site.[33]

It is known that in an aqueous medium, CPs can transform from one phase into another phase *via* a dissolution–precipitation process.[22,34,35] In this process, the pH value, temperature and presence of foreign ions are among the most influencing factors;[36] therefore, the optimization of the synthesis procedure was performed in a few steps. The XRD patterns of the synthesized products obtained at different pH values are given in Fig. 2.

It was found that Cu-WH with no visible secondary phases can be obtained in a very narrow pH range from 6.4 to 6.5. At higher pH values, a secondary HA phase was detected; however, it is worth noting that due to the low crystallinity its detection was challenging. The obtained HA does not give any sharp peak and its presence can be observed by the increase of the background at around 32°. The formation of the additional HA at higher pH values was expected, since WH, compared to HA, is a more stable CP phase exactly at relatively low pH.[37] At lower pH values, a copper-rich $Ca_3Cu_3(PO_4)_4$ phase was observed along with Cu-WH. The percentage of this impurity gradually increased with decreasing pH of the synthesis medium. It is surprising that the optimal pH range was so narrow, when compared to the similar synthesis of Zn-WH, where the optimal pH was determined to be in the range from 5.6 to 6.2.[22]

The influence of the reaction time on the formation of Cu-WH was further investigated; the XRD patterns of the products obtained by performing the synthesis for different periods of time are shown in Fig. 3.

The as-precipitated powder (without hydrothermal treatment) was identified as DCPD. The gradual phase transformation into Cu-WH was observed by increasing the reaction time. Although after 1 h of the reaction, Cu-WH was identified as the major crystalline phase and there were not even traces of DCPD, the co-existing HA phase was detected instead. The percentage of HA in the synthesis product decreased with

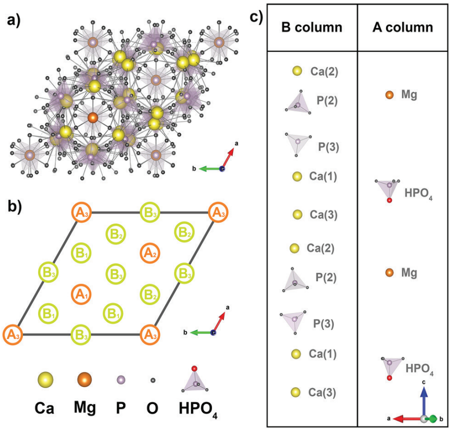

Fig. 1 Unit cell of Mg-WH (a); arrangement of columns in the unit cell (b); arrangement of atoms in structural columns (c).

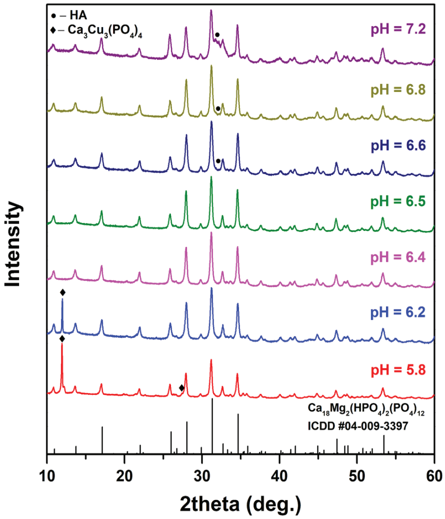

Fig. 2 XRD patterns of the synthesis products obtained at different pH values (*T* = 200 °C, *t* = 3 h, Ca/Cu = 9).

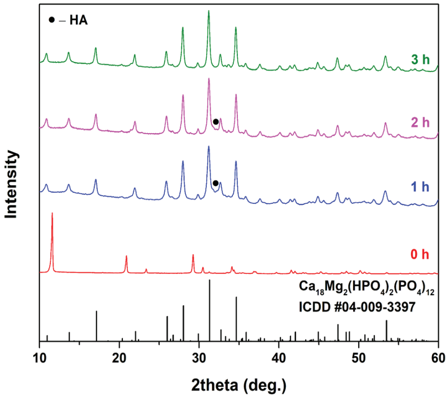

Fig. 3 XRD patterns of Cu-WH powders synthesized for different periods of time (pH = 6.4, T = 200 °C, Ca/Cu = 9).

increasing reaction time; after 3 h of the reaction, there were no visible signals corresponding to HA. Longer reaction times did not result in any detectable changes. Thus, it can be concluded that the synthetic procedure requires at least 3 h. This value is significantly lower compared to those reported for the solvothermal synthesis of Mn-WH[24] or Zn-WH[23] and comparable to the data reported for hydrothermally synthesized Mg-WH.[38,39] On the other hand, previously it was shown that in an aqueous medium, Zn-WH can be formed just in 1 h.[22] The observed time-dependent phase evolution from DCPD to Cu-WH suggests that the transformation *via* a dissolution–precipitation reaction could occur not directly, but in two steps with an intermediate HA phase. Previously, it was shown by Jang *et al.*[37] that under certain conditions HA can be converted into Mg-WH *via* a multistep process; however, it is difficult to compare the phase transformations in certain systems due to plenty of influencing factors such as pH, temperature, pressure, chemical composition of the reaction mixture, *etc.* Future investigation on the observed phase transformation process employing *in situ* X-ray analysis could show the exact reaction pathway.

Next, the effect of the synthesis temperature on the phase purity of Cu-WH was studied. The XRD patterns of the products obtained in the temperature range from 110 to 200 °C are depicted in Fig. S1.† It is evident that Cu-WH was obtained as the major crystalline phase at all temperatures; however, a closer look reveals the presence of a small amount of HA as the secondary phase at lower temperatures. The amount of HA decreased with an increase of the temperature, indicating that the synthesis should be performed at a relatively higher temperature, namely 200 °C.

To further investigate the peculiarities of the formation of Cu-WH, the influence of the concentration of starting materials was studied. In this experiment, the total metal ions' concentration in the reaction vial was varied in the range of 0.02–0.24 M, while in a typical synthetic procedure it was fixed at 0.08 M. The results of XRD analysis (Fig. S2†) revealed that the concentration had only a limited effect on the phase purity of the obtained products. Decreasing the concentration to 0.04 M led to the formation of secondary phases (both HA and $Ca_3Cu_3(PO_4)_4$). There was no significant variation in the width of diffraction peaks, suggesting that the crystallite size of the obtained Cu-WH powders was comparable in all cases.

We were also interested if the variable ratio of metal cations in the initial reaction mixture could lead to the formation of Cu-WH with a variable metal content. Fig. 4 shows the XRD patterns of the products obtained using different initial Ca/Cu ratios.

The results showed 2 different trends. The Cu-rich reaction mixture (Ca/Cu < 9) resulted in the formation of the secondary $Ca_3Cu_3(PO_4)_4$ phase; its percentage in the obtained product increased with increasing initial Cu concentration. In the case of Cu-lean reactions (Ca/Cu > 9), the formation of HA along with Cu-WH was observed. It was observed that the amount of HA increased gradually with the decrease of the Cu concentration. Based on the results of these experiments, it can be concluded that the synthesis of Cu-WH with a variable metal content is impossible under selected conditions. Similar limitations were previously observed for Zn-WH synthesized under hydrothermal conditions.[22]

Rietveld refinement was used to calculate the cell parameters of the synthesized Cu-WH (Fig. 5). The refinement was carried out using a rhombohedral structure (space group $R3c$) adopted from Mg-WH.

The results revealed a good agreement between the calculated and experimental data. The parameter a was calculated as 10.330 Å, while the parameter c was 37.077 Å. These values are slightly lower compared to those previously reported for

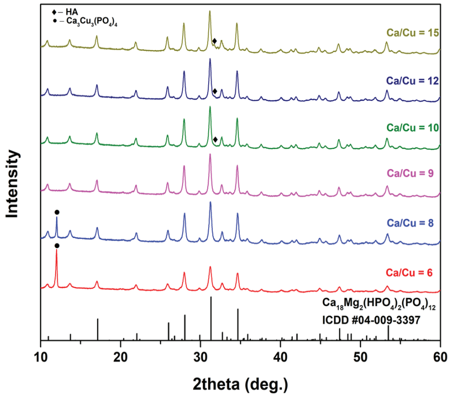

Fig. 4 XRD patterns of Cu-WH powders synthesized with different Ca/Cu ratios (pH = 6.4, T = 200 °C, t = 3 h).

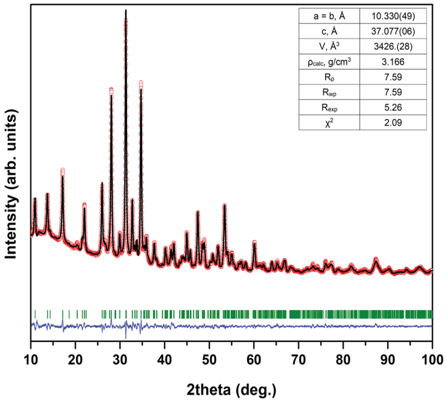

Fig. 5 Rietveld refinement of the XRD data obtained for Cu-WH (T = 200 °C; t = 3 h; pH = 6.4, Ca/Cu = 9) refined in the space group *R*3*c*. The red circle symbols and the black solid line represent the experimental and calculated intensities, respectively, and the blue line below is the difference between them. The green tick marks indicate the positions of the Bragg peaks.

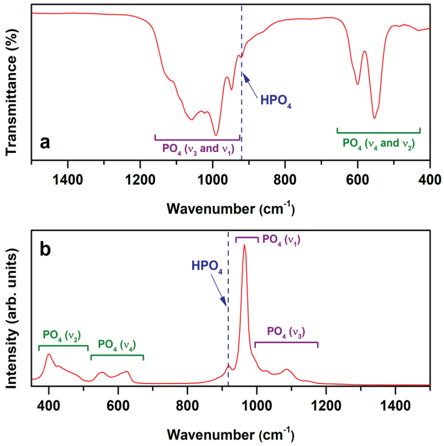

Fig. 6 FTIR spectrum (a) and Raman spectrum (b) of Cu-WH powders (pH = 6.4, T = 200 °C, t = 3 h, Ca/Cu = 9).

Mg-WH,[38,39] Zn-WH[22] and Cu-WH.[27] The Rietveld analysis did not indicate the presence of secondary crystalline phases. Analogically, as in Mg-WH, small Cu^{2+} ions in the WH structure fully occupy the Ca(5) crystallographic site, while the Ca (4) position remains vacant. Although the occupation of the Ca (4) site by small cations is not typical of the WH structure,[32] Konishi and Watanabe reported that Cu^{2+} ions in Cu-WH occupy both Ca(5) and Ca(4) sites.[27] On the other hand, the authors also observed a significant contamination of their product with Mg^{2+} ions. Recent investigations on a closely related Cu-substituted β-TCP structure did not indicate the presence of Cu^{2+} ions at the Ca(4) site. According to Spaeth *et al.*,[8] at the maximal substitution level, Cu^{2+} occupies Ca(5), Ca(2) and Ca(3) sites. These conclusions were confirmed by a recent work by Deyneko *et al.*[10] By contrast, Mg^{2+} ions were shown to occupy both Ca(5) and Ca(4) sites in a heavily doped β-TCP.[40]

As was mentioned above, the crystal structures of WH and β-TCP (or substituted TCP) are in a close relationship, which results in the nearly identical XRD patterns of these two materials; therefore, the reliable identification of WH is impossible without employing vibrational spectroscopy. In this context, FTIR and Raman spectroscopy are superior methods for the characterization of compounds with the WH structure, since both these methods enable the observation of the signals from the $HPO_4{}^{2-}$ group. Only the crystal structure of WH (not β-TCP) contains this structural unit, which can be used as a reliable spectral marker.[39] The FTIR spectrum of the synthesized Cu-WH is given in Fig. 6a; the spectral region from 1500 to 400 cm^{-1} is shown as the most representative. The shape of the spectrum is similar to those of natural and synthetic WH.[22,32] The spectrum exhibits several absorption bands: the bands located in the range from 1170 to 930 cm^{-1} are ascribed to ν_3 and ν_1 stretching modes of PO_4, while the bands ranging from 650 to 410 cm^{-1} correspond to ν_2 and ν_4 bending modes. The band centered at *ca.* 920 cm^{-1} indicates the presence of the $HPO_4{}^{2-}$ group, confirming that the synthesized material is Cu-WH and not Cu-substituted β-TCP.

The Raman spectrum of the same sample is provided in Fig. 6b. In this case, a few bands can also be seen and identified. The bands located in the ranges of 370–495, 520–640 and 990–1170 cm^{-1} correspond to the ν_2, ν_4 and ν_3 vibrational modes of the phosphate group, respectively. The most intense signal peaked at 964 cm^{-1} is ascribed to the ν_1 vibrational mode. Finally, the signal located at 920 cm^{-1} is attributed to $HPO_4{}^{2-}$, which agrees well with the results of the FTIR analysis. Overall, both spectroscopic techniques agree very well with the results reported in the literature in terms of the spectral shape and band wavenumbers.[22,32,39,41]

The ^1H MAS spectra obtained for the Cu-WH sample before and after annealing at 500 °C are shown in Fig. 7. The spectrum of the as-prepared Cu-WH powder looks similar to those previously reported for Zn- and Mg-WH.[22,39] The ^1H spectrum clearly contains a major spectral line at 9.9 ppm, which is attributed to the $HPO_4{}^{2-}$ moiety in the Cu-WH crystal structure (Fig. 1). Additional lines attributed to surface H_xPO_4 and distorted HPO_4 moieties are seen at 12.3 ppm and 6.2 ppm, respectively.[42] Water in the form of bulk and surface species is detected at 4.5–1.5 ppm. As can be seen from Fig. 7, annealing of the sample significantly reduces the amount of the side phosphate species and water. The linewidth of a line attributed to Cu-WH decreases two-fold after annealing, which indicates the formation of the Cu-WH phase with higher crystallinity.

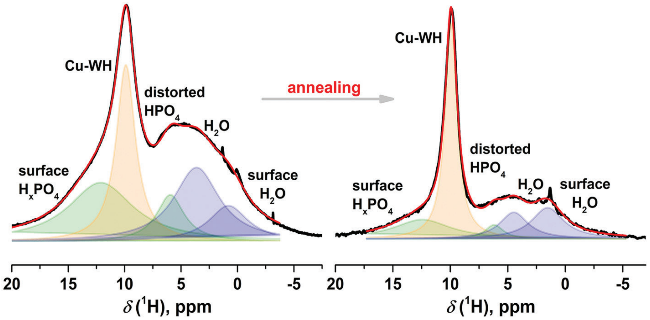

Fig. 7 ^{1}H MAS spectra of Cu-WH before and after annealing at 500 °C. Spectral components attributed to Cu-WH are shown in orange, water in blue, and additional phosphate species in green.

The presence of a relatively higher amount of water could be explained by the trapping of water molecules during the dissolution–precipitation process.

Fig. 8 depicts the ^{31}P MAS and ^{1}H–^{31}P CP MAS spectra of Cu-WH before and after annealing. It is seen that annealing significantly reduces the amount of the amorphous/distorted phase in the sample: before annealing, the signal from the amorphous component highly overlaps with the P(3) signal, which prevents the accurate spectral assignment. Similarly to ^{1}H data, the lines in ^{31}P data after annealing show narrower linewidths, indicating the formation of the Cu-WH phase of higher crystallinity. The ^{31}P MAS spectrum after annealing consists of lines at 2.2, 1.3, and −0.5 attributed to P(2), HP(1)O_4^{2-} and P(3) moieties, which are typical in the WH structure,[22,39]

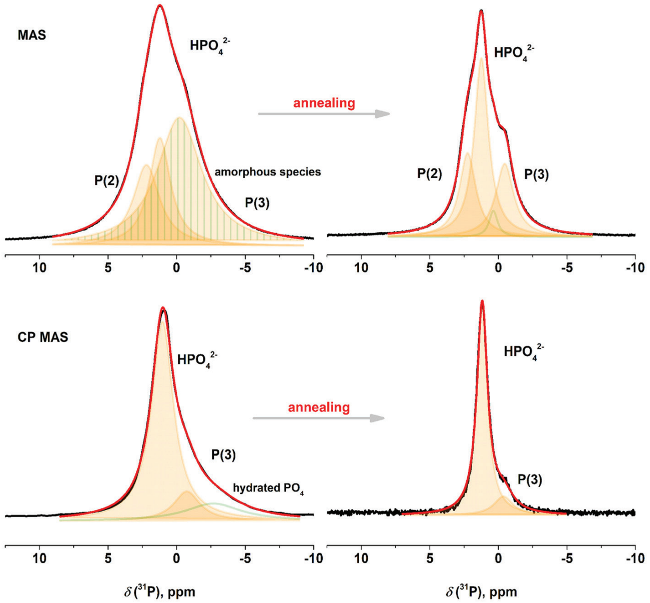

Fig. 8 ^{31}P MAS (upper) and ^{1}H–^{31}P CP MAS (lower) spectra of Cu-WH before and after annealing at 500 °C. Spectral components attributed to Cu-WH are shown in orange and additional phosphate phases in green.

and a line at 0.4 ppm, which is an impure phosphate phase. One more remark has to be made that in comparison with Zn- and Mg-WH, Cu-WH possesses significantly broader lines which is due to the paramagnetic nature of the Cu^{2+} environment. In the ^{1}H–^{31}P CP MAS spectra, the line assigned to HPO_4^{2-} is significantly more enhanced, which corroborates our assignment that the proton is in close vicinity. The line at −2.8 ppm is assigned to the side phase of hydrated PO_4, which vanishes after annealing.

Taking into account the results of X-ray analysis and Rietveld refinement (Fig. 5), it can be concluded that the impurities detected by NMR possess an amorphous nature, since no secondary crystalline phases were detected by XRD. This observation also indicates that ss-NMR is a highly useful method for the comprehensive structural analysis of low-crystalline CPs synthesized at low temperatures. Unfortunately, this technique is rarely employed for the characterization of materials with the WH structure;[22,38,39] this makes the comparison of the experimental results almost impossible. Konishi and Watanabe[38] also observed some additional signals in the ^{1}H NMR spectra of Mg-WH, while XRD did not indicate the presence of secondary phases. The signals in the ^{31}P NMR spectra were better resolved in their study; however, this might be caused by different particle sizes and degrees of crystallinity, and the absence of paramagnetic Cu^{2+} ions. In comparison, in a work by the same group focusing on Cu-WH,[27] the NMR linewidths were comparable to the ones obtained in the present study.

Since Cu-WH possesses copper ions (Cu^{2+}) in the crystal structure, the powders were also characterized by EPR spectroscopy. We recorded the spectrum of Cu-WH powders by using pulsed EPR at low temperature. Fig. 9a shows the field swept spectrum of Cu^{2+}.

Line broadening appears due to hyperfine interaction with nearby copper nuclei. To get more information about the surroundings of the Cu^{2+} paramagnetic center, we used a more advanced pulsed EPR technique – Hyperfine Sublevel Correlation (HYSCORE). The basic advantage of the HYSCORE technique is the formation of the 2D spectra of off-diagonal cross-peaks, whose coordinates are nuclear frequencies from opposite electron spin manifolds. The cross-peaks simplify significantly the analysis of congested spectra by correlating and spreading out the nuclear frequencies. In addition, the HYSCORE experiment separates overlapped peaks along a second dimension and enhances the signal-to-noise ratio through the application of a second Fourier transform. Hyperfine interactions are comprised of the isotropic Fermi contact interaction, A_{iso}, and anisotropic through-space dipolar interaction, T; where A_{iso} provides a measure of the electron spin density at the nucleus, while T reflects the dipole–dipole interaction between the electron and nuclear spins and depends on the distance and orientation of the nucleus relative to the electron spin.[43]

In HYSCORE spectrum (Fig. 9b), we observed a pair of off-diagonal cross-peaks, ^{31}P, at (2.6, 9) and (9, 2.6) MHz in the (+, +) quadrant of the HYSCORE spectrum. The cross-peaks are centered at a ^{31}P Zeeman frequency of 5.77 MHz (at a magnetic field of 334.5 mT) and arise from the hyperfine interactions of the ^{31}P atom (nuclear spin, $I = 1/2$) with the Cu^{2+} paramagnetic center. The separation between the pair of cross-peaks ^{31}P is ~6.4 MHz, which is proportional to the isotropic hyperfine coupling, A_{iso}, of the ^{31}P atom. Simulation of peak positions and shape allowed us to obtain an anisotropic through-space dipolar interaction, T, value of ~1.3 MHz. As dipolar interaction T depends on the distance r between the two centers, we also calculated the r value, which is equal to ~0.3 nm. This value is close to that between the Cu and P(2) atoms in the WH crystal lattice obtained from the XRD data. Moreover, Cu^{2+} ions were observed in only one crystallographic site, which agrees well with the results of Rietveld refinement. Additionally, the experimental spectrum in Fig. 9b also reveals a cross-peak, ^{1}H, on the diagonal (14.3 MHz) which arises from very weak hyperfine couplings ($A_{\mathrm{iso}} < 0.1$ MHz) of the effective electron spin ($S = 1/2$) with surrounding ^{1}H nuclei.

The challenging control of the stoichiometry is a well-known disadvantage of the wet precipitation method, when employed for the synthesis of multicomponent materials. In order to check the chemical composition of the synthesized Cu-WH, the elemental analysis was carried out by means of ICP-OES. The results are summarized in Table 1. It is evident that the experimentally obtained values agree well with the theoretical ones. The Ca/Cu and (Ca + Cu)/P molar ratios were determined to be very close to the theoretical values, being only slightly lower.

The morphological features of Cu-WH were investigated by SEM and STEM. It is known from previous works that the WH

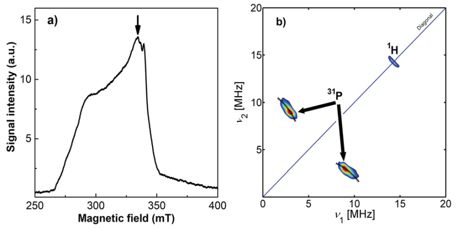

Fig. 9 Electron spin-echo magnetic-field-sweep EPR spectrum of Cu-WH powder. The arrow indicates the magnetic field position of 334.5 mT that was used for the acquisition of the 2D HYSCORE spectrum (a). HYSCORE spectrum of the (+, +) quadrant of the Cu-WH powders. Black dot lines on the top of ^{31}P peaks are obtained from simulation. The spectra were acquired at a temperature of 4.5 K (b).

Table 1 The results of ICP-OES analysis of Cu-WH (pH = 6.4, T = 200 °C, t = 3 h, Ca/Cu = 9)

Sample	Determined Ca/Cu molar ratio	Determined (Ca + Cu)/ P molar ratio	Theoretical Ca/ Cu molar ratio	Theoretical (Ca + Cu)/ P molar ratio
Cu-WH	8.79	1.39	9.00	1.43

structure tends to form particles of a distinctive rhombohedral, hexagonal or octahedral shape.[21,22,37,44] Varying the synthesis conditions in terms of the concentration of starting materials allows one to control the size and shape of WH particles.[22] The SEM images of Cu-WH powders synthesized using different concentrations of starting materials are shown in Fig. 10a and b.

It is seen that the variation of the concentration had only a limited effect on the morphology of the material. The sample synthesized using a 3-fold higher concentration of the starting material consisted of slightly smaller particles (Fig. 10b), compared to those obtained using the standard synthetic conditions (Fig. 10a). Both samples were composed of agglomerated particles of nanoscale dimensions. While most of the particles showed an irregular shape, a closer look allows us to see some particles of well-defined rhombohedral and hexagonal plate-like shapes. The EDS mapping (Fig. 10e–h) indicated a homogeneous distribution of the constituting elements. There were no visible agglomerations of some elements in the absence of others.

It is known that the WH structure is thermally unstable and decomposes upon annealing,[21,39] which is a limiting factor for the fabrication of WH ceramics by conventional routes considering the annealing at elevated temperatures. Thermally induced degradation occurs by the transformation of WH into the mixture of β-TCP and $Ca_2P_2O_7$ (CPP), accompanied by the release of water:

$$Ca_{18}M_2(HPO_4)_2(PO_4)_{12} \rightarrow 6Ca_{2.67}M_{0.33}(PO_4)_2 + Ca_2P_2O_7 + H_2O \quad (1)$$

Although the thermally induced decomposition of Mg-WH was previously investigated in detail,[39] the stability of the synthesized Cu-WH was studied here in order to determine if the origin of small cations in the WH structure could influence the degradation temperature. The results of thermogravimetric analysis in the range from room temperature to 900 °C are depicted in Fig. 11.

It can be seen that the weight loss occurs gradually up to *ca.* 700 °C without any drastic drops. Above 700 °C, the residual mass was nearly constant. The total mass loss was calculated as 4 wt%, while the theoretical weight loss according to eqn (1) was only 0.8 wt%. This mismatch indicates that the as-prepared material contains some adsorbed water and/or other relatively volatile species, which could be trapped during the dissolution–precipitation process. In general, the behavior of the TG curve and the total weight loss are comparable to those observed for Mg-WH[39] and Zn-WH.[22]

In order to investigate the structural changes and the phase evolution upon annealing, the as-prepared Cu-WH powders were annealed at different temperatures in the 500–1000 °C range with steps of 100 °C. The XRD patterns of the obtained samples are presented in Fig. 12a.

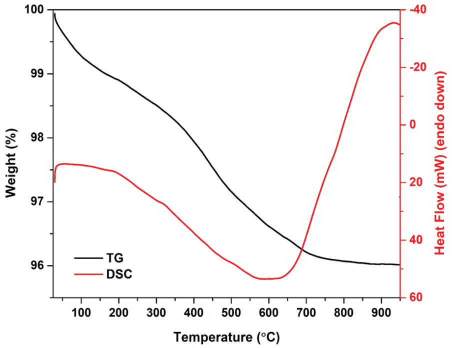

Fig. 11 TG/DSC curves of the Cu-WH powder.

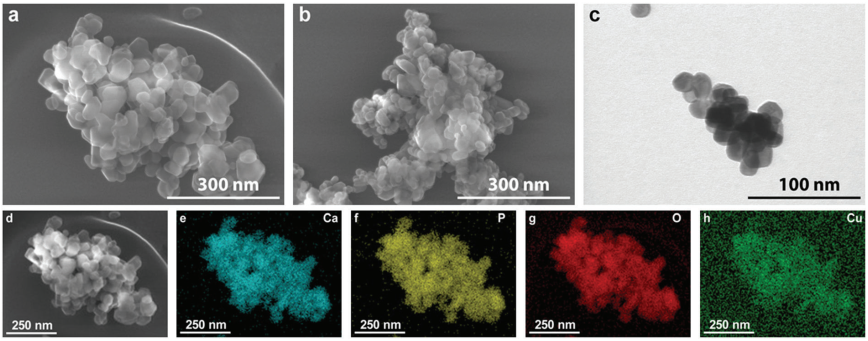

Fig. 10 SEM images of the Cu-WH powders synthesized when the initial concentration of metal ions was 0.08 M (a) and 0.24 M (b); STEM image of Cu-WH synthesized at concentration of 0.08 M (c); SEM image (d) and EDS mapping (e–h) of Cu-WH (pH = 6.4, T = 200 °C, t = 3 h, Ca/Cu = 9).

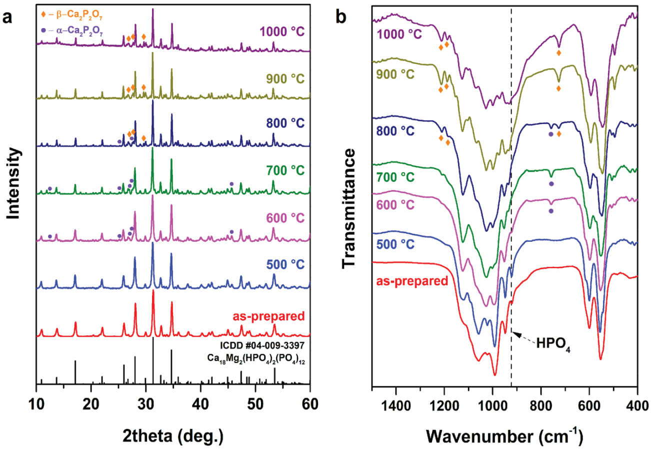

Fig. 12 XRD patterns (a) and FTIR spectra (b) of Cu-WH powders annealed at different temperatures.

It is worth noting that the detection of the transformation of WH into β-TCP is impossible by means of XRD due to their nearly identical patterns;[39] however, XRD is a suitable method for the monitoring of the formation of secondary phases, which can serve as an indicator of the thermal decomposition. The appearance of the secondary crystalline phase starts after annealing at 600 °C. The newly formed phase was identified as α-CPP. The formation of this CPP polymorph was rather unexpected, since α-CPP is assumed to be a high-temperature polymorph;[45] nevertheless, its formation could be explained by the Ostwald step rule.[46] It was demonstrated previously that the amorphous CP (Ca/P ratio 1 : 1) crystallizes as the α-CPP polymorph first; the crystallization temperature was determined as 600 °C.[47] The start of the thermal decomposition of Cu-WH was found to be around 100 °C lower compared to that of Mg-WH,[39] but in good agreement with that of Zn-WH.[21] The thermal treatment at 800 °C resulted in the formation of both α- and β-CPP, while only β-CPP secondary phase was detected in the samples annealed at 900 °C and 1000 °C.

FTIR spectroscopy was employed in parallel with the XRD analysis to monitor the structural changes, since this technique allows for the detection the HPO_4^{2-} group, which serves as a spectral marker for the identification of WH. The presence or absence of this structural unit cannot be detected by XRD. The FTIR spectra are shown in Fig. 12b. After annealing at 500 °C, there were no obvious spectral changes in terms of the appearance or disappearance of absorption bands; however, sharpening of the bands was observed, indicating the increase of the crystallinity of the material. The formation of α-CPP was confirmed after the thermal treatment at 600 °C and 700 °C. The presence and identification of CPP polymorphs can be easily detected by observing the absorption bands at 726 and 754 cm^{-1},[48] since the FTIR spectra of WH and β-TCP do not have any bands in this region. The co-existence of two CPP polymorphs was evident after annealing at 800 °C, while only β-CPP was observed after the thermal treatment at higher temperatures. Overall, the results of FTIR spectroscopy agree very well with the results of XRD analysis; both techniques confirm that Cu-WH is thermally unstable at temperatures above 600 °C.

The ion release experiment was performed in order to estimate the release of Cu^{2+} ions into the SBF solution during the soaking of the as-prepared Cu-WH powder (Fig. 13). The concentration of Cu^{2+} ions monotonously increased during the soaking. It should be highlighted that the drastic release of

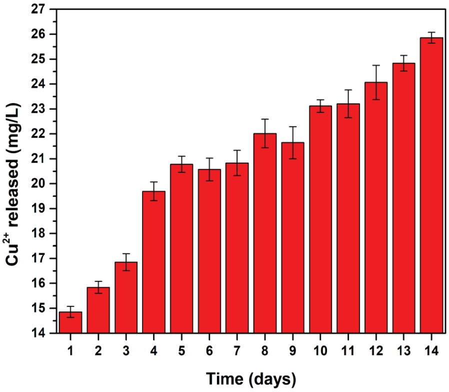

Fig. 13 Cu^{2+} ion release into the SBF solution.

Cu^{2+} was observed just after 1 day. Despite the fact that before the experiment the powder was washed with deionized water, the possible reason for such a behavior is the release of soluble trapped Cu-containing species. The maximal concentration of Cu^{2+} ions was determined after 14 days as 25.8 mg L^{-1}. Although the ion release from Cu-containing biomaterials was investigated in various works,[10,49,50] it is difficult to compare the released amounts of Cu because of the highly varying experimental conditions in terms of Cu content in materials, the sample form, the ratio of sample mass to solution volume, the soaking medium, *etc.*

The comparison of our results with other studies on Cu-WH is currently limited to one report;[27] however, in that study the experiment was performed under significantly different conditions in acetate buffer (pH = 5.5) with powder mass to solution volume ratio being 400 times lower and duration of monitoring of only 180 min. Recalculating the data indicates a noticeably higher release reported in ref. 27. In another work, Deyneko *et al.*[10] investigated the Cu^{2+} release from Cu-doped β-TCP in Tris-HCl buffer solution. The concentration of Cu^{2+} released from the samples with a similar Cu content (9.5 mol%) revealed the same trend upon increasing in time; however, after 30 days of soaking, the concentration was significantly lower compared to our study. It is worth noting that the authors tested the pellets instead of powders, the ion-release medium of different composition and the mass-to-volume ratio (0.4 g in 50 mL) was 2.5 times lower compared to ours. Moreover, the particle size of the initial powders in the mentioned paper was significantly larger as a result of high-temperature synthesis. All these factors could influence the difference in the obtained data. Gomes *et al.*[13] studied the Cu^{2+} release from pelletized biphasic CPs consisting of HA and β-TCP. Depending on the phase composition of the tested samples, the authors determined a comparable or even higher amount of released Cu^{2+} ions, although the doping level of starting materials was lower compared to that in our work. Moreover, the ion release was observed only in the SBF solution, but not in deionized water. Compared to Zn-WH prepared and treated under similar conditions, the amount of Cu^{2+} ions observed in this work was around 25 times higher than that of Zn^{2+}.[22]

The cell viability of Cu-WH samples was assessed using an indirect method by collecting extract solutions. Following the ISO 10993-5:2009 guidelines, the study revealed that none of the tested Cu-WH extract dilutions demonstrated cytotoxic effects after 48 h sample incubation, as these experiments showed cell viability more than 70% (Fig. 14).

Lower cell viability (73.64 ± 9.48%) was noted for Cu-WH extracts at a concentration of 0.1 mg mL^{-1} after 24 h incubation period with a slight increase at 48-hour incubation timepoint. A similar trend of viability increase after 48 h was observed for the extract dilution at a lower concentration of 0.01 mg mL^{-1}. Decreased cell viability in the first 24 hours could be explained by the rapid Cu^{2+} ion release in the medium. Due to its transition between different oxidation states, Cu^{2+} plays a role in numerous physiological processes. Duan *et al.*[51] investigated the effect of Cu-containing alloy on osteoblast proliferation and differentiation, indicating that Cu^{2+} induced the proliferation of osteoblasts at 24 to 72 h timepoints, explaining the increase of cell viability after 48 h. Furthermore, Zhang *et al.*[52] observed that the Cu ion concentration is one of the key factors for switching the biological effects of Cu^{2+} and Cu^{+} from toxicity to activity.

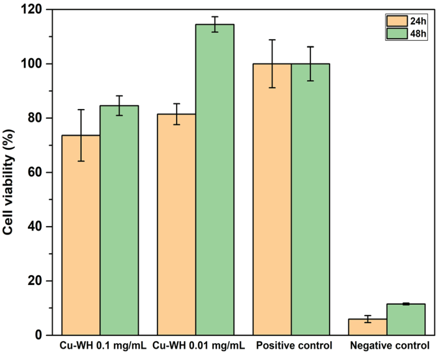

Fig. 14 Cu-WH extract's effect on MC3T3-E1 cell proliferation.

4. Conclusions

In this work, nanodimensional copper whitlockite (Cu-WH) powders were successfully synthesized by a dissolution–precipitation method under hydrothermal conditions. The conversion from brushite to Cu-WH occurred in a slightly acidic medium in the presence of Cu^{2+} ions and required at least 3 h at 200 °C. The optimal pH range was found to be very narrow being from 6.4 to 6.5. The variation of the chemical composition in terms of the Ca/Cu ratio was impossible under the selected synthesis conditions; the initial Ca/Cu ratio of 9, corresponding to the theoretical metal ratio in the WH structure, was determined as optimal. While XRD and vibrational spectroscopy did not indicate the presence of any impurity phase in the as-prepared Cu-WH powders, the NMR studies revealed the co-existence of amorphous/distorted phosphate species. The amount of distorted phosphates was reduced significantly by annealing the powder at a moderate 500 °C temperature. The Cu^{2+} release from the Cu-WH powder monitored for 14 days showed a gradually increasing trend with a drastic release during the first day of soaking. The study on thermal stability revealed that Cu-WH is thermally unstable and gradually decomposes to Cu-substituted β-$Ca_3(PO_4)_2$ and $Ca_2P_2O_7$ upon annealing above 600 °C. The cell viability study revealed that none of the tested Cu-WH extract dilutions demonstrated cytotoxic effects, as all experiments demonstrated cell viability exceeding 70%.

Conflicts of interest

There are no conflicts to declare.

Acknowledgements

This research was funded by a grant WHITCERAM (No. S-LJB-22-1) from the Research Council of Lithuania and by the Joint Research Projects under the Bilateral Program (JSPS), RCL JSPS, No. 120224202. The authors acknowledge the access to the infrastructure and expertise of the BBCE – Baltic Biomaterials Centre of Excellence (European Union's Horizon 2020 research and innovation programme under the grant agreement no. 857287). The authors acknowledge the Center of Spectroscopic Characterization of Materials and Electronic/Molecular Processes ('Spectroversum', **https://spectroversum.ff.vu.lt**) for the use of NMR and EPR equipment.

References

1 W. Habraken, P. Habibovic, M. Epple and M. Bohner, *Mater. Today*, 2016, **19**, 69–87.
2 N. V. Bulina, O. B. Vinokurova, I. Y. Prosanov, A. M. Vorobyev, K. B. Gerasimov, I. A. Borodulina, A. Pryadko, V. V. Botvin, M. A. Surmeneva and R. A. Surmenev, *Ceram. Int.*, 2022, **48**, 35217–35226.
3 M. Gu, W. Li, L. Jiang and X. Li, *Acta Biomater.*, 2022, **148**, 22–43.
4 V. H. M. Doan, D. D. Vu, S. Mondal, T. M. T. Vo, C. D. Ly, V. T. Nguyen, S. Park, J. Choi, T. P. Nguyen, B. Lee and J. Oh, *ACS Biomater. Sci. Eng.*, 2023, **9**, 4607–4618.
5 S. Jin, L. Ren and K. Yang, *J. Mater. Sci. Technol.*, 2016, **32**, 835–839.
6 A. Jacobs, G. Renaudin, C. Forestier, J.-M. Nedelec and S. Descamps, *Acta Biomater.*, 2020, **117**, 21–39.
7 V. Stanić, S. Dimitrijević, J. Antić-Stanković, M. Mitrić, B. Jokić, I. B. Plećaš and S. Raičević, *Appl. Surf. Sci.*, 2010, **256**, 6083–6089.
8 K. Spaeth, F. Goetz-Neunhoeffer and K. Hurle, *J. Solid State Chem.*, 2020, **285**, 121225.
9 D. V. Deyneko, I. V. Fadeeva, E. Y. Borovikova, P. B. Dzhevakov, P. V. Slukin, Y. Zheng, D. Xia, B. I. Lazoryak and J. V. Rau, *Ceram. Int.*, 2022, **48**, 29770–29781.
10 D. V. Deyneko, Y. F. Zheng, K. Barbaro, V. N. Lebedev, S. M. Aksenov, E. Y. Borovikova, M. R. Gafurov, I. V. Fadeeva, B. I. Lazoryak, G. Di Giacomo, C. Cicione, V. Tilotta, F. Russo, G. Vadala and J. V. Rau, *Ceram. Int.*, 2023, **49**, 21308–21323.
11 X. Li, G. Li, K. Zhang, Z. Pei, S. Zhao and J. Li, *J. Biomed. Mater. Res., Part B*, 2021, **109**, 877–889.
12 M. Schamel, A. Bernhardt, M. Quade, C. Würkner, U. Gbureck, C. Moseke, M. Gelinsky and A. Lode, *Mater. Sci. Eng., C*, 2017, **73**, 99–110.
13 S. Gomes, C. Vichery, S. Descamps, H. Martinez, A. Kaur, A. Jacobs, J.-M. Nedelec and G. Renaudin, *Acta Biomater.*, 2018, **65**, 462–474.
14 R. Gopal and C. Calvo, *Nat. Phys. Sci.*, 1972, **237**, 30–32.
15 R. Gopal, C. Calvo, J. Ito and W. K. Sabine, *Can. J. Chem.*, 1974, **52**, 1155–1164.
16 H. Cheng, R. Chabok, X. Guan, A. Chawla, Y. Li, A. Khademhosseini and H. L. Jang, *Acta Biomater.*, 2018, **69**, 342–351.
17 F. A. Shah, *Acta Biomater.*, 2021, **125**, 72–82.
18 H. D. Kim, H. L. Jang, H.-Y. Ahn, H. K. Lee, J. Park, E.-S. Lee, E. A. Lee, Y.-H. Jeong, D.-G. Kim, K. T. Nam and N. S. Hwang, *Biomaterials*, 2017, **112**, 31–43.
19 H. L. Jang, G. B. Zheng, J. Park, H. D. Kim, H.-R. Baek, H. K. Lee, K. Lee, H. N. Han, C.-K. Lee, N. S. Hwang, J. H. Lee and K. T. Nam, *Adv. Healthcare Mater.*, 2016, **5**, 128–136.
20 R. D. Shannon, *Acta Crystallogr., Sect. A: Cryst. Phys., Diffr., Theor. Gen. Crystallogr.*, 1976, **32**, 751–767.
21 A. Kizalaite, I. Grigoraviciute-Puroniene, D. R. C. Asuigui, S. L. Stoll, S. H. Cho, T. Sekino, A. Kareiva and A. Zarkov, *ACS Biomater. Sci. Eng.*, 2021, **7**, 3586–3593.
22 A. Kizalaite, V. Klimavicius, J. Versockiene, E. Lastauskiene, T. Murauskas, R. Skaudzius, T. Yokoi, M. Kawashita, T. Goto, T. Sekino and A. Zarkov, *CrystEngComm*, 2022, **24**, 5068–5079.
23 M. Wang, J. Yao, S. Shen, C. Heng, Y. Zhang, T. Yang and X. Zheng, *Nano Res.*, 2023, **16**, 757–770.
24 C. Heng, W. Liu, X. Zheng, X. Ma, J. Hui and D. Fan, *Colloids Surf., B*, 2023, **222**, 113120.
25 E. Kostiner and J. R. Rea, *Acta Crystallogr., Sect. B: Struct. Crystallogr. Cryst. Chem.*, 1976, **32**, 250–253.
26 S. Y. Stefanovich, B. I. Lazoryak, A. M. Antipin, A. S. Volkov, A. I. Evdokimov, O. A. Gurbanova, O. V. Dimitrova and D. V. Deyneko, *Z. Kristallogr. - Cryst. Mater.*, 2023, **238**, 301–309.
27 T. Konishi and S. Watanabe, *Phosphorus Res. Bull.*, 2022, **38**, 18–24.
28 P. Höfer, A. Grupp, H. Nebenführ and M. Mehring, *Chem. Phys. Lett.*, 1986, **132**, 279–282.
29 T. Kokubo and H. Takadama, *Biomaterials*, 2006, **27**, 2907–2915.
30 M. Yashima, A. Sakai, T. Kamiyama and A. Hoshikawa, *J. Solid State Chem.*, 2003, **175**, 272–277.
31 K. Matsunaga, T. Kubota, K. Toyoura and A. Nakamura, *Acta Biomater.*, 2015, **23**, 329–337.
32 F. Capitelli, F. Bosi, S. C. Capelli, F. Radica and G. Della Ventura, *Crystals*, 2021, **11**, 225.
33 T. Debroise, E. Colombo, G. Belletti, J. Vekeman, Y. Su, R. Papoular, N. S. Hwang, D. Bazin, M. Daudon, P. Quaino and F. Tielens, *Cryst. Growth Des.*, 2020, **20**, 2553–2561.
34 L. Sinusaite, A. Popov, E. Raudonyte-Svirbutaviciene, J.-C. Yang, A. Kareiva and A. Zarkov, *Ceram. Int.*, 2021, **47**, 12078–12083.
35 G. Montes-Hernandez and F. Renard, *J. Phys. Chem. C*, 2020, **124**, 15302–15311.

36 E. Raudonyte-Svirbutaviciene, L. Lukaviciute, Z. Moravec, J. Pinkas, T. Goto, T. Sekino, A. Zarkov and A. Kareiva, *Ceram. Int.*, 2023, **49**, 32816–32825.

37 H. L. Jang, H. K. Lee, K. Jin, H.-Y. Ahn, H.-E. Lee and K. T. Nam, *J. Mater. Chem. B*, 2015, **3**, 1342–1349.

38 T. Konishi and S. Watanabe, *Phosphorus Res. Bull.*, 2021, **37**, 21–25.

39 A. Kizalaite, V. Klimavicius, V. Balevicius, G. Niaura, A. N. Salak, J. C. Yang, S. H. Cho, T. Goto, T. Sekino and A. Zarkov, *CrystEngComm*, 2023, **25**, 4370–4379.

40 R. Enderle, F. Götz-Neunhoeffer, M. Göbbels, F. A. Müller and P. Greil, *Biomaterials*, 2005, **26**, 3379–3384.

41 H. Zhou, L. Yang, U. Gbureck, S. B. Bhaduri and P. Sikder, *Acta Biomater.*, 2021, **127**, 41–55.

42 M. Ben Osman, S. Diallo-Garcia, V. Herledan, D. Brouri, T. Yoshioka, J. Kubo, Y. Millot and G. Costentin, *J. Phys. Chem. C*, 2015, **119**, 23008–23020.

43 A. Schweiger and G. Jeschke, *Principles of pulse electron paramagnetic resonance*, Oxford university press, 2001.

44 X. Guo, X. Liu, H. Gao, X. Shi, N. Zhao and Y. Wang, *J. Mater. Sci. Technol.*, 2018, **34**, 1054–1059.

45 D. Griesiute, E. Garskaite, A. Antuzevics, V. Klimavicius, V. Balevicius, A. Zarkov, A. Katelnikovas, D. Sandberg and A. Kareiva, *Sci. Rep.*, 2022, **12**, 7116.

46 R. A. Van Santen, *J. Phys. Chem.*, 1984, **88**, 5768–5769.

47 Z. Zyman, A. Goncharenko and D. Rokhmistrov, *J. Cryst. Growth*, 2017, **478**, 117–122.

48 D. Griesiute, E. Raudonyte-Svirbutaviciene, A. Kareiva and A. Zarkov, *CrystEngComm*, 2022, **24**, 1166–1170.

49 M. M. Erol, V. Mouriňo, P. Newby, X. Chatzistavrou, J. A. Roether, L. Hupa and A. R. Boccaccini, *Acta Biomater.*, 2012, **8**, 792–801.

50 K. M. Weiss, S. K. Kucko, S. Mokhtari, T. J. Keenan and A. W. Wren, *J. Biomed. Mater. Res., Part B*, 2023, **111**, 295–313.

51 J.-Z. Duan, Y. Yang and H. Wang, *Orthop. Surg.*, 2022, **14**, 758–768.

52 J. C. Zhang, Y. P. Li, K. N. Yang and X. H. Hao, *Chin. J. Inorg. Chem.*, 2010, **26**, 2251–2258.

Electronic Supplementary Material (ESI) for Dalton Transactions.

Copper-Containing Analog of the Biomineral Whitlockite: Dissolution-Precipitation Synthesis, Structural and Biological Properties

Diana Griesiute[1], Agne Kizalaite[1], Arita Dubnika[2,3], Vytautas Klimavicius[4], Vidmantas Kalendra[5], Vaclav Tyrpekl[6], Sung Hun Cho[7], Tomoyo Goto[7,8], Tohru Sekino[7], Aleksej Zarkov[1,*]

[1]*Institute of Chemistry, Vilnius University, Naugarduko 24, LT-03225 Vilnius, Lithuania*

[2]*Rudolfs Cimdins Riga Biomaterials Innovations and Development Centre of RTU, Faculty of Materials Science and Applied Chemistry, Institute of General Chemical Engineering, Riga Technical University, LV-1007 Riga, Latvia*

[3]*Baltic Biomaterials Centre of Excellence, Headquarters at Riga Technical University, LV-1658 Riga, Latvia*

[4]*Institute of Chemical Physics, Vilnius University, Sauletekio 3, LT-10257 Vilnius, Lithuania*

[5]*Institute of Applied Electrodynamics and Telecommunications, Vilnius University, Sauletekio 3, LT-10257 Vilnius, Lithuania*

[6]*Department of Inorganic Chemistry, Faculty of Science, Charles University, Hlavova 2030/8, 128 43 Prague, Czech Republic*

[7]*SANKEN (The Institute of Scientific and Industrial Research), Osaka University, 8–1 Mihogaoka, Ibaraki, Osaka 567–0047, Japan*

[8]*Institute for Advanced Co-Creation Studies, Osaka University, 1-1 Yamadaoka, Suita, Osaka 565-0871, Japan*

*Author to whom correspondence should be addressed. E-mail: aleksej.zarkov@chf.vu.lt

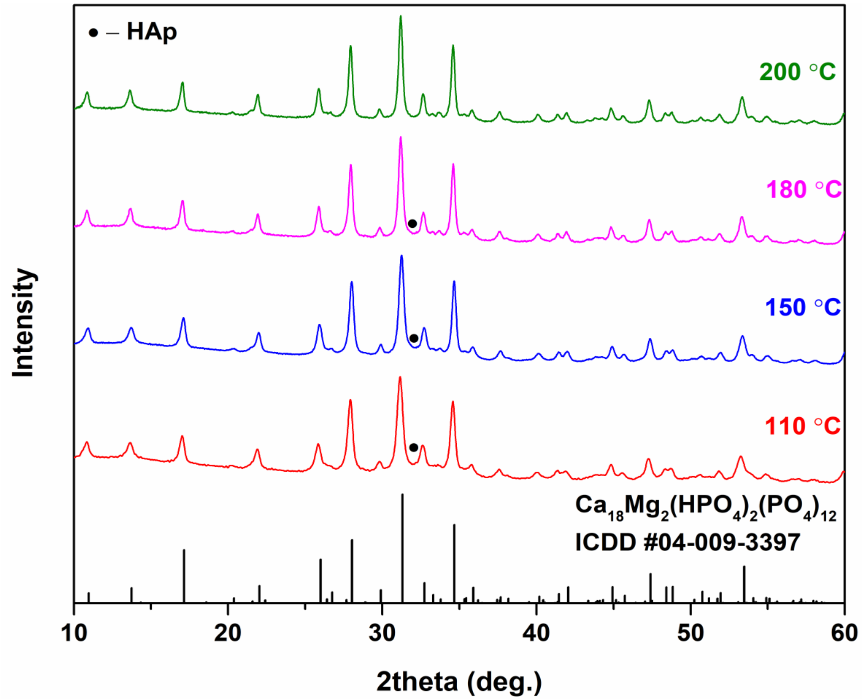

Fig. S1. XRD patterns of Cu-WH powders synthesized at different temperatures (pH = 6.4, t = 3h, Ca/Cu = 9).

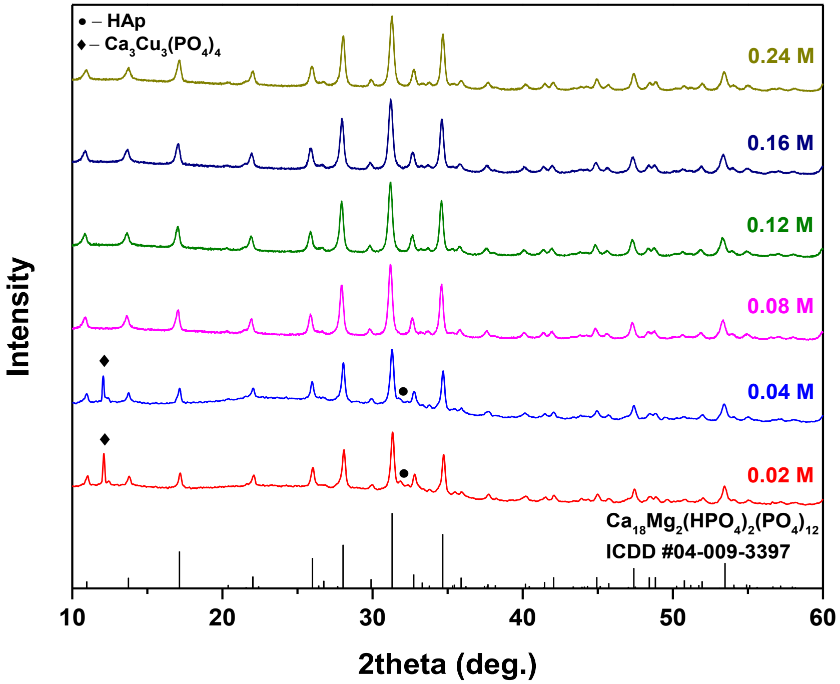

Fig. S2. XRD patterns of Cu-WH powders synthesized with different concentrations of precursors. Standard concentration is 0.08 M (pH = 6.4, T = 200 °C, t = 3 h, Ca/Cu = 9). The increased background in the XRD patterns of 0.02 M and 0.04 M samples arises from the glass sample holder.

5th publication

Low-temperature aqueous synthesis and biocompatibility of manganese whitlockite

A. Kizalaitė, A. Dubnika, A. Antuzevics, T. Murauskas, O. Stewart,
S. L. Stoll, T. Goto, T. Sekino, A. Žarkov

Ceramics International, 50(16), 2024, 28490-28497
(https://doi.org/10.1016/j.ceramint.2024.05.157)

Ceramics International 50 (2024) 28490–28497

Contents lists available at ScienceDirect

Ceramics International

journal homepage: www.elsevier.com/locate/ceramint

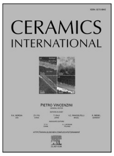

Low-temperature aqueous synthesis and biocompatibility of manganese whitlockite

Agne Kizalaite [a], Arita Dubnika [b,c], Andris Antuzevics [a,d], Tomas Murauskas [a],
Orlando Stewart Jr. [e], Sarah L. Stoll [e], Tomoyo Goto [f,g], Tohru Sekino [f], Aleksej Zarkov [a,*]

[a] Institute of Chemistry, Vilnius University, Naugarduko 24, LT-03225, Vilnius, Lithuania
[b] Institute of Biomaterials and Bioengineering, Faculty of Natural Sciences and Technology, Riga Technical University, Pulka 3, Riga, LV-1007, Latvia
[c] Baltic Biomaterials Centre of Excellence, Headquarters at Riga Technical University, LV-1658, Riga, Latvia
[d] Institute of Solid State Physics, University of Latvia, Kengaraga 8, LV-1063, Riga, Latvia
[e] Department of Chemistry, Georgetown University, 37th and O Streets NW, Washington D.C, 20057, United States
[f] SANKEN (The Institute of Scientific and Industrial Research), Osaka University, 8–1 Mihogaoka, Ibaraki, Osaka, 567–0047, Japan
[g] Institute for Advanced Co-Creation Studies, Osaka University, 1-1 Yamadaoka, Suita, Osaka, 565-0871, Japan

ARTICLE INFO

Handling Editor: Dr P. Vincenzini

Keywords:
Manganese whitlockite
$Ca_{18}Mn_2(HPO_4)_2(PO_4)_{12}$
Dissolution-precipitation
Cell viability

ABSTRACT

In this work, manganese whitlockite (Mn-WH, $Ca_{18}Mn_2(HPO_4)_2(PO_4)_{12}$) was successfully synthesized and comprehensively characterized. This material is a manganese-containing analog of the biomineral magnesium whitlockite (Mg-WH, $Ca_{18}Mg_2(HPO_4)_2(PO_4)_{12}$). The synthesis was performed *via* a low-temperature dissolution-precipitation process in aqueous medium under ambient pressure at 75 °C using dicalcium phosphate dehydrate and manganese acetate tetrahydrate as starting materials. The crystal structure of the synthesized powder was determined by powder X-ray diffraction, FTIR and Raman spectroscopies, demonstrating the presence of characteristic structural units. Morphological features and elemental distribution within the synthesized powder were studied by SEM/EDX analysis. XPS, EPR and magnetic studies confirmed the presence of Mn ions in a divalent state. Temperature-dependent magnetic measurements revealed a paramagnetic behavior of Mn-WH down to 5 K. *In vitro* cytotoxicity experiments were performed with MC3T3-E1 preosteoblastic cell line.

1. Introduction

In recent years magnesium whitlockite (Mg-WH; $Ca_{18}Mg_2(HPO_4)_2(PO_4)_{12}$) has attracted attention of the scientific community due to its potential to be used in bone regeneration and reconstruction. Various sources claim that this material is a biomineral that naturally occurs in both physiological and pathological formations of human body such as dentin [1], alveolar [2] and other bone tissues [3]. On the other hand, the recent study by Shah reveals that the presence of Mg-WH is limited to pathological formulations [4]. Despite the existing contradictions, synthetic Mg-WH is still considered a promising material for medical applications due to its biocompatibility and osteoconductivity. For instance, WH-containing borosilicate bioactive glass bone cements were shown to have great osteogenic properties in biological systems [5]. WH nanoparticles were also shown to induce osteogenesis of human gingival mesenchymal stem cells more effectively than calcium hydroxyapatite (HAp) [6], which is widely used in bone regeneration and tissue engineering [7–9]. Zhang et al. proposed to use Mg-WH as a component in nanocomposite fiber membrane to achieve better angiogenesis and osteogenic differentiation in periosteal tissue [10].

The ion-substitution can significantly enhance the biological performance of synthetic biomaterials and open new fields for application. Although the reports on the modification of chemical composition of Mg-WH are quite rare, several studies on the substitution of Mg in the Mg-WH structure by transition metal ions such as Zn^{2+} [11,12], Cu^{2+} [13,14] or Co^{2+} [15] are already known. These biologically active ions are known for their antibacterial properties as well as enhanced osteogenesis [16–19]. Other dopants like Ce significantly promote osteogenic activity of Mg-WH, increase the implant *in vivo* biodegradation as well as accelerate bone formation and mineralization [20]. Eu- and Tb-codoped Mg-WH nanoparticles possessed fluorescent properties that were successfully applied for bioimaging [21].

Manganese is an essential human dietary element, which is a critical component in dozens of proteins and enzymes [22]. This element is

---

* Corresponding author.
E-mail address: aleksej.zarkov@chf.vu.lt (A. Zarkov).

https://doi.org/10.1016/j.ceramint.2024.05.157
Received 15 March 2024; Received in revised form 26 April 2024; Accepted 10 May 2024

necessary for normal function of nervous and immune systems and aids in defense mechanisms against reactive oxygen species [22,23]. The human body contains about 10–20 mg of Mn, of which 25 %–40 % is found in bones [24]. Even though the exact mechanisms of Mn effect on bone mineralization are not well understood yet, it is known that this mineral plays a role in bone homeostasis [25] and increases osteoblast proliferation [26] as well as the production of osteogenic compounds [27]. At the same time, at high dosages Mn^{2+} intake can be neurotoxic causing symptoms ranging from irritability to dementia [22,28]; therefore, it is important to determine safe amounts of Mn-containing materials when used in biological systems.

To date, the use of Mn in biomaterials is quite limited; however, some of the previously published studies show that Mn-containing materials can be good contrast agents for imaging due to their magnetic properties [29,30]. Various Mn-substituted calcium phosphates, such as HAp [31], amorphous calcium phosphate [32] and others can be used for magnetic resonance imaging (MRI). Additionally, Mn-containing biomaterials were shown to have antibacterial properties [33] and demonstrated a positive effect on osteogenic processes [34].

To this day, we found very few studies of manganese whitlockite (Mn-WH; $Ca_{18}Mn_2(HPO_4)_2(PO_4)_{12}$), which is a synthetic analog of the biomineral described above. The very first report by Kostiner et al. [35] describes the structural properties of Mn-WH that was accidently synthesized while trying to obtain Mn-doped HAp. Just recently Heng et al. reported a purposeful synthesis of Mn-WH nanoparticles by solvothermal method with further successful application for MRI imaging [36]. The same group also synthesized Nd- and Eu-codoped Mn-WH [37, 38] nanoparticles using similar synthesis techniques. In both cases the obtained materials demonstrated promising results for the use in MRI imaging; however, the synthetic procedure requires the use of harmful organic solvents and elevated pressure.

In this study, we present a fast, cost-effective and environmentally benign way to prepare Mn-WH powder in aqueous medium. The synthesis was performed by a low-temperature dissolution-precipitation process at ambient pressure. The obtained material was comprehensively characterized to evaluate its structural, morphological, and biological properties.

2. Materials and methods

2.1. Synthesis

Mn-WH powder was synthesized by a dissolution-precipitation method using calcium hydrogen phosphate dihydrate ($CaHPO_4 \cdot 2H_2O$, 99.1 %, Eurochemicals) and manganese acetate tetrahydrate ($Mn(CH_3COO)_2 \cdot 4H_2O$, ≥99 %, Roth) as starting materials. For the synthesis, the required amounts of precursors corresponding to the Ca-to-Mn molar ratio of 9 were dissolved in a mixture of 100 mL of deionized water and 13 mL of 1 M phosphoric acid (H_3PO_4, 75 %, Roth). The total metal ion concentration of the obtained solution was 0.06 M and the pH was 2.7. Next, a concentrated ammonia solution (NH_4OH, 25 %, Roth) was added to the reaction mixture under a constant stirring and the pH of the reaction medium was raised to 5.6. The increased pH value resulted in the formation of white precipitates with a slight pink hue. The reaction mixture was sealed in a 250 mL glass bottle with a screw cap and placed in a shaker incubator (Biosan ES-20/80) for 3 h at 75 °C with a rotating speed of 220 rpm. At the end of the synthesis, the precipitates were vacuum-filtered, washed with deionized water, and dried at 60 °C in an oven overnight.

2.2. Characterization

The powder X-ray diffraction (XRD) data of the synthesized compound were obtained using a Rigaku MiniFlex II diffractometer (Cu-Kα, $\lambda = 1.5419$ Å) working in Bragg-Brentano (θ/2θ) geometry. The data were collected within 10–100° 2θ angle range with a speed of 1°/min. The FullProf Suite was used for structural refinement (FullProf Suite software version September-2020). As a reference for data fitting, ICSD 143481 was used [39].

Fourier transform infrared spectra (FTIR) were obtained in the range of 4000–400 cm^{-1} with a Bruker ALPHA-FTIR spectrometer.

Raman spectra were recorded using a combined Raman and scanning near field optical microscope WiTec Alpha 300 R equipped with a 532 nm excitation laser source.

The N_2 adsorption and desorption isotherms of samples were obtained at −196 °C by using Brunauer–Emmett–Teller (BET) analyzer TriStar II 3020, Micromeritics. Prior to the gas sorption measurements, all the samples were outgassed in N_2 atmosphere at 100 °C for 2 h.

The microstructure and elemental analysis of the samples were studied by field emission scanning electron microscopy (FE-SEM, SU9000, Hitachi) equipped with an EDX detector.

The Bruker ELEXSYS-II E500 CW-EPR spectrometer was used for electron paramagnetic resonance (EPR) spectra measurements of the sample. The data acquisition settings were: room temperature, 9.836 GHz microwave frequency, 1 mW microwave power, and 0.1 mT magnetic field modulation amplitude.

The XPS analyses were carried out with a Kratos Axis Supra spectrometer using a monochromatic Al K(alpha) source (25 mA, 15 kV). The instrument work function was calibrated to give a binding energy (BE) of 83.96 eV for the Au 4f7/2 line for metallic gold and the spectrometer dispersion was adjusted to give a BE of 932.62 eV for the Cu 2p3/2 line of metallic copper. The Kratos charge neutralizer system was used on all specimens. Survey (wide) scan analyses were carried out with an analysis area of 300 x 700 μm and a pass energy of 160 eV. High-resolution analyses were carried out with an analysis area of 300 x 700 μm and a pass energy of 20 eV. Since Mn is sensitive to ion sputtering and sample might be damaged by cleaning process, the samples were not cleaned before the analysis. The acquired spectra have been charge corrected to the main line of the C 1s spectrum (adventitious carbon) set to 284.8 eV. Spectra were analyzed using CasaXPS software (version 2.3.23rev1.1R).

Magnetic susceptibility data for Mn-WH were obtained using a Quantum Design MPMS3 SQUID magnetometer. The data collection involved a temperature sweep ranging from 5 K to 300 K at a magnetic field strength of 100 Oe. Measurements were conducted in both zero-field cooled (ZFC) and field-cooled (FC) conditions. For ZFC data, the sample was initially cooled to 5 K in a 0 Oe field, and the moment was measured as the sample warmed to 300 K. In the case of FC data, the sample was cooled in an applied field of 100 Oe, and the moment measured as the sample was heated back to 300 K. Additionally, magnetic hysteresis data were collected at 5 K and 300 K over a range of −20000 Oe to 20000 Oe (−2.0 to 2.0 T). Data collection was performed either in vibrating sample magnetometry (VSM) mode with 5 mm scan lengths and 2 s averaging or in direct current (DC) scan mode with 30 mm scan lengths and 5 s averaging. All data were corrected for diamagnetic contributions using Pascal's Constants [40], and for sample shape and radial offset effects using the MPMS3 Sample Geometry Simulator [41].

Thermal analysis of Mn-WH powder was performed by thermogravimetric and differential scanning calorimetric (TG-DSC) analysis using PerkinElmer STA 6000 Simultaneous Thermal Analyzer. Dried sample of about 20 mg was heated from 25 to 900 °C with a heating rate of 10 °C/min in a dry flowing air (20 mL/min).

Elemental composition of Mn-WH was determined by inductively coupled plasma optical emission spectrometry (ICP-OES) using PerkinElmer Optima 7000 DV spectrometer.

2.3. In vitro cytotoxicity studies

Cytotoxicity of Mn-WH powders was assessed using the MC3T3-E1 cell line (preosteoblasts). In the extract test, 4500 cells per well were seeded in a 96-well plate with 100 μL cell medium, composed of 89 % Alpha Modified Eagle Medium (α-MEM), 10 % fetal bovine serum (FBS) and 1 % penicillin/streptomycin (P/S). The plates with the cells were incubated overnight at 37 °C, with 5 % CO_2 (New Brunswick™ S41i CO2 Incubator Shaker, Eppendorf, Hamburg, Germany).

Mn-WH powder was suspended in a fresh 5 ml of cell medium resulting in a concentration of 10 mg/mL. After 24 and 48 h all the solution was collected from the samples and replaced with additional 5 mL of fresh cell medium. The collected solution was then filtered through a 0.2 μm syringe filter and subsequently used for dilution with fresh medium. Tested concentrations were 1 mg/mL, 0.1 mg/mL and 0.01 mg/mL. Extract dilutions were immediately put onto the pre-incubated cells (100 μL for each well). Untreated cells were used as a positive control and 5 % dimethylsulfoxide (DMSO) solution in the medium was applied to cells as a negative control. There were six replicates for each sample and controls.

Cell Counting Kit −8 (CCK-8) assay was used to assess the cytotoxicity of Mn-WH extracts. For both time points samples were incubated for 24 h and then 10 μL of CCK-8 solution was added to the cultivation media to each well and incubated for 1 h at 37 °C, with 5 % CO_2. Absorption at 450 nm was measured using an Infinite M Nano microplate reader (Tecan, Männedorf, Switzerland).

3. Results and discussion

The XRD data showed a successful synthesis of single-phase Mn-WH with no additional crystalline phases (Fig. 1a). All diffraction peaks matched very well with the standard XRD data. Further structural analysis was performed employing Rietveld refinement using the rhombohedral crystal structure with *R3c* space group (#161) as a model. The calculated lattice parameters were $a = 10.358(4)$ Å and $c = 37.077$ (7) Å. These values are similar to those previously reported in literature for both Mn-WH [35] and Mg-WH [39,42,43], though both parameters are slightly smaller. According to the refinement data, in the crystal structure Mn^{2+} ions occupy the Ca(5) crystallographic site, while the Ca (4) remains a vacancy, which is in good agreement with the peculiarities of WH structure [39].

Due to similarities between WH and beta-tricalcium phosphate (β-TCP; $Ca_3(PO_4)_2$) crystal structures, both compounds possess an identical XRD pattern [44]; therefore, vibrational spectroscopy is an essential tool in distinguishing between these two materials. The major difference between β-TCP and WH in their FTIR and Raman spectra is the band at 920 cm^{-1} associated with the HPO_4^{2-} group, which is present in the WH structure, but absent in undoped or Mn-doped β-TCP [45,46]. This distinctive band is clearly visible in both FTIR (Fig. 1b.) and Raman (Fig. 1c) spectra of the obtained material; therefore, we can confirm a successful synthesis of Mn-WH. The positions of other absorption bands can be attributed to the vibrational modes of phosphates characteristic of WH compounds [14,43]. In the FTIR spectrum, the bands in the range from 1170 to 930 cm^{-1} are assigned to the ν_3 and ν_1 stretching modes of phosphate tetrahedra, while the bands in the wavenumber range of 640–500 and at 436 cm^{-1} correspond to the ν_4 and ν_2 bending modes, respectively. Corresponding signals are seen in the Raman spectrum indicating a good agreement between the two spectroscopic techniques.

The BET method was used to measure the surface area of the as-prepared Mn-WH powder. The N_2 adsorption-desorption isotherm (Fig. 1d) was assigned to type IV with a type H3 hysteresis loop. The type H3 hysteresis loop is usually indicative of plate-like particle aggregates, which result in the formation of slit-shape pores [47]. The specific surface area (S_{BET}) was calculated to be 32.3 m^2/g; this value is similar to that of previously reported for WH materials [12,43].

To determine the chemical composition of the synthesized Mn-WH powder, the elemental analysis was performed by means of ICP-OES. The results are summarized in Table 1. Experimentally determined Ca/Mn and (Ca + Mn)/P molar ratios were in good agreement with theoretical values, which reflects the reliability of the proposed

Table 1
The results of ICP-OES analysis of Mn-WH powder.

Determined Ca/ Mn molar ratio	Determined (Ca + Mn)/P molar ratio	Theoretical Ca/ Mn molar ratio	Theoretical (Ca + Mn)/P molar ratio
8.84	1.40	9.00	1.43

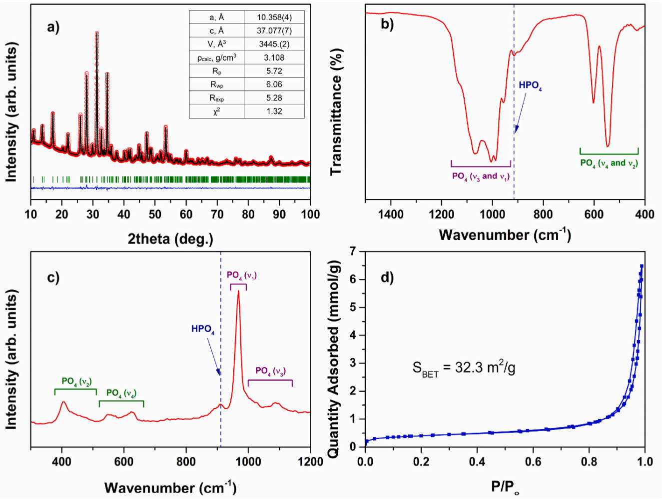

Fig. 1. Results of Rietveld refinement (a), the red circle symbols and the black solid line represent the experimental and calculated intensities, respectively, and the blue line below is the difference between them. The green tick marks indicate the positions of the Bragg peaks; FTIR spectrum (b); Raman spectrum (c); and N_2 absorption-desorption isotherm (d) of the as-prepared Mn-WH powder. (For interpretation of the references to colour in this figure legend, the reader is referred to the Web version of this article.)

synthetic approach.

The SEM image taken under lower magnification (Fig. 2a) demonstrates the homogeneity and uniformity of the obtained powder. A closer look (Fig. 2b) reveals that synthesized powder is composed of agglomerated irregularly shaped particles. The individual particles are of nanoscale dimensions with the size varying in the range of approximately 30–60 nm. Hexagonal or rhombohedral particle shape usually associated with materials having WH structure [11,48,49] was barely visible in the investigated sample with only few particles with a visibly expressed hexagonal shape. The EDX mapping data (Fig. 2c–f) showed that all the elements are uniformly distributed within the sample confirming the formation of single-phase material of a particular chemical composition.

The EPR spectrum of Mn-WH is shown in Fig. 3. It consists of a broad line centered at 349 mT with a peak-to-peak linewidth of 50 mT. The spectrum resembles that of Mn^{2+} ions in highly concentrated systems [46,50–52], which is expected as Mn is the host element of the Mn-WH matrix.

A previous study of a Mn-WH single crystal reported a significantly smaller EPR linewidth (20 G = 2 mT) [35], but no spectrum was provided. However, there are factors, which could explain significant broadening in our case such as orientational disorder, *i.e.*, EPR signal averaging from chaotically oriented crystallites, or structural disorder effects caused by variations in particle size and degree of crystallinity. Therefore, it would be of interest to explore a series of Mn-WH samples with differing grain sizes or solid solutions of Mn-doped Mg-WH with variable content of Mn ions.

The obtained Mn-WH sample was further investigated by XPS analysis, acquiring the low-resolution survey and high-resolution spectra (Fig. 4). Survey spectra (Fig. 4a) revealed that powder was composed of C, Mn, Ca, O, P and traces of Si (measurement contamination). To investigate the oxidation states, high-resolution spectra of all the elements were recorded. The P $2p_{3/2}$ transition peaks were detected at ~133.3 eV, which is the typically reported value for calcium phosphates with WH-related structure [53]. In the Ca $2p_{3/2}$ spectrum the peak was observed at ~347.5 eV, which also agrees well with the values reported for calcium phosphates [54]. Manganese oxidation state was investigated by measuring and modelling Mn $2p_{3/2}$ and Mn 3s spectra. It is known that Mn 2p spectra modeling might be very inaccurate due to small difference in chemical shifts between different manganese oxidation states. The analysis is further complicated due to the multiplet splitting when comparing the oxidation states; however, the Mn^{2+} state is usually observed with distinct satellite peaks. These satellite peaks were observed in the analyzed powder; therefore, $Mn^{2+/3+}$ model was most likely. The dominant Mn^{2+} state in the Mn-WH structure is also supported by previous works by Heng et al. [36,38]. In these studies, magnetic measurements indicated the presence of Mn^{2+} state, although their provided XPS spectra were not of sufficient quality for detailed analysis and fitting of Mn 2p spectra was not reported. There is little reliable data for fitting Mn-WH, so the model was constructed based on manganese oxide models and combining those models together [55]. A higher resolution spectrum with sufficient intensity has been acquired in this work. Using the Mn^{2+}/Mn^{3+} model it was determined that Mn^{2+} amounted for ca. 89 % and the rest of Mn ions were in the Mn^{3+} oxidation state. The observed Mn 3s spectra peak multiplet splitting values (ΔBE) were approximately 5.8 eV. The Mn 3s peak energy difference usually correlates with the oxidation state of manganese, having a ΔBE of approximately 6.1 eV for Mn^{2+} and 5.5 eV for Mn^{3+} [56]. The measured Mn 3s and Mn 2p values in this work suggested that Mn was a mix of Mn^{2+}/Mn^{3+} with a dominant Mn^{2+} state. This observation is in good agreement with the results of structural analysis, since it is known that WH structure is stabilized by relatively small divalent cations such as Mg, Zn, Cu etc. [12,14,43]. To the best of our knowledge, there are no reports on the ability of trivalent ions to stabilize WH; therefore, it can be concluded that Mn^{3+} species observed by XPS analysis are associated with surface defects.

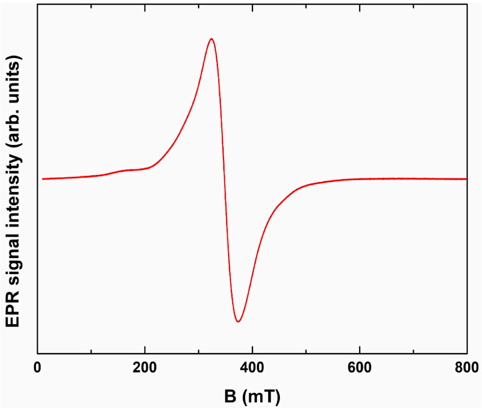

Fig. 3. EPR spectrum of Mn-WH sample.

The magnetic measurement data obtained for Mn-WH are given in Fig. 5. The magnetic data demonstrate an expected paramagnetic behavior as shown by the 1/χ-vs-T graph (Fig. 5a). The data show an

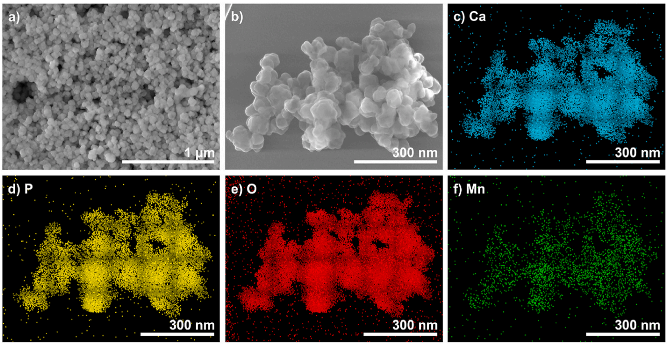

Fig. 2. SEM micrographs (a, b) and EDX mapping (c–f) of the as-prepared Mn-WH powder.

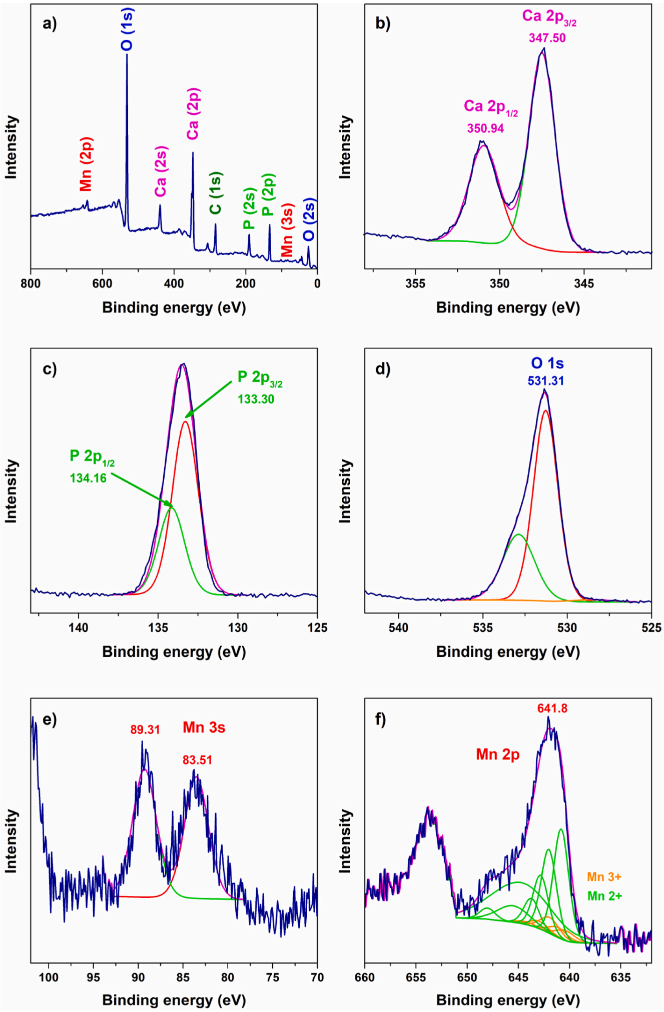

Fig. 4. Survey XPS spectra of Mn-WH (a), high-resolution XPS spectra and fitting results of Ca 2p (b), P 2p (c), O 1s (d); Mn 3s (e) and Mn 2p (f) peaks.

intercept at the origin, typical for paramagnetic materials, and a linear relationship between $1/\chi$ and T over the measured temperature range, demonstrating that this material follows Curie's Law. There was no difference depending on the measurement mode (FC or ZFC). The effective magnetic moment, $\mu_{eff} = (8C)^{1/2}$, was calculated as 6.00 μ_B (μ_B, Bohr magneton) per Mn^{2+} ion. This value is close to the theoretical one, 5.92 μ_B, expected for the free Mn^{2+} ion. These data confirm that Mn ions in the synthesized material are in 2+ oxidation state, which agrees well with the results of Rietveld refinement and XPS. The M vs H curves at 5 K and 300 K also show an expected paramagnetic behavior (Fig. 5b).

The materials with WH structure are known to be thermally unstable and decompose upon annealing resulting in the release of water and the formation of β-TCP and $Ca_2P_2O_7$ [11,43]. The results of thermogravimetric analysis showed that the total weight loss in the range from 30 to 900 °C reached 4.5 wt% (Fig. 6). This value is close to those obtained for Mg-WH or Zn-WH [12,43]. Around 1.2 wt% of this weight loss occurs below 200 °C, which can be attributed to the removal of adsorbed water. At higher temperatures, three weight losses in the ranges of 350–500, 500–600 and 640–680 °C can be seen, which also could be ascribed to the removal of water and/or other trapped volatile species. The residual mass was nearly constant at the temperatures above ca. 700 °C. Thermally induced degradation of Mn-WH and accompanying phase transformations can be predicted based on the data provided in literature for Mg-, Cu- and Zn-WH [11,14,43]. The thermal behavior of all these materials is nearly the same.

The cell viability of Mn-WH powder was assessed by collecting the extract solutions according to the ISO 10993–5:2009 guidelines. The results revealed that none of the tested Mn-WH extract dilutions

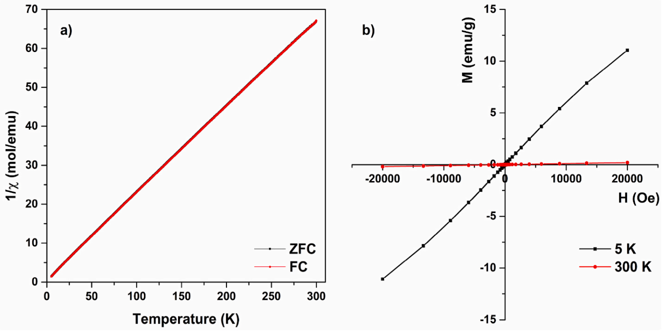

Fig. 5. Inverse magnetic susceptibility of Mn-WH vs T (a); M vs H curves of Mn-WH at 5 K and 300 K (b).

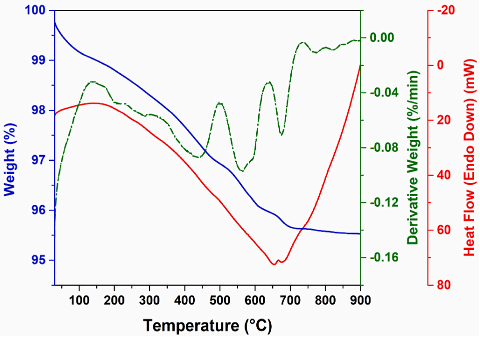

Fig. 6. TG/DTG/DSC curves of the as-prepared Mn-WH powder.

demonstrated cytotoxic effects after 24 h incubation; in all cases the observed cell viability was above 70 % (Fig. 7). The lowest cell viability was determined for the highest Mn-WH concentration (1 mg/mL). The observed trend indicates that the cell viability decreases for all samples after the incubation for 48 h; however, the value does not drop below 70 % with an exception for the dilution with 1 mg/mL of Mn-WH. The comparison of the experimental results with other data on the biocompatibility of Mn-WH is limited to 3 papers by Heng et al. [36–38]. In Ref. [36] the authors investigated cell viability of MG-63 cells for only 24 h; moreover, Mn-WH was studied not in its pure form, but in the form of composites, while the highest total concentration reached only 0.64 mg/mL. In Ref. [37] the viability of hBMSCs cells was higher compared to our study, however, the authors investigated Mn-WH-containing hydrogel. Finally, in Ref. [38] the cell viability of MG-63 and L929 cells was evaluated after the treatment with Eu-doped Mn-WH nanoparticles for 24 h. In that study the cell viability was higher compared to our results; however, the investigated range of nanoparticles concentrations was lower (up to 0.32 mg/mL).

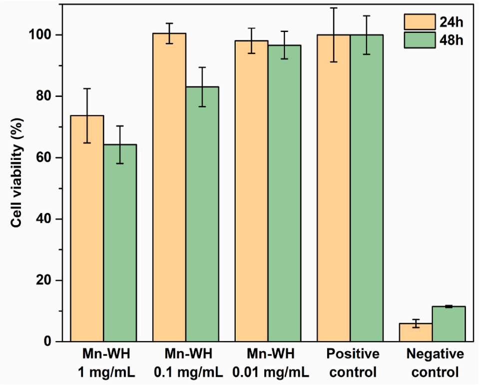

Fig. 7. Mn-WH extract effect on MC3T3-E1 cell proliferation.

Finally, we were also interested in luminescent properties of synthesized Mn-WH powder, since it is known that Mn^{2+} ions are optically active and in different calcium phosphate matrices can possess a broadband luminescence [57,58]. Unfortunately, the obtained material was optically inactive in terms of photoluminescence.

4. Conclusions

In this work, a simple, time- and cost-effective method of Mn-WH synthesis was demonstrated employing a dissolution-precipitation process at low temperature. The proposed synthetic approach does not require the use of harmful organic solvents and elevated pressure. The results of Rietveld refinement indicated that the synthesized material is a single-phase Mn-WH. The powder consisted of uniform particles of nanosized dimensions with evenly distributed elements. The combination of XRD, EPR, XPS and magnetic studies confirmed the presence of Mn ions in the 2+ oxidation state, while temperature-dependent magnetic measurements revealed a paramagnetic behavior of Mn-WH down to 5 K temperature. The material did not exhibit a toxic effect on MC3T3-E1 cells after the incubation period of 24 h for the concentration range of 0.01–1 mg/L; however, the cell viability decreased after the longer incubation.

Conflicts of interest

There are no conflicts to declare.

CRediT authorship contribution statement

Agne Kizalaite: Writing – original draft, Visualization, Methodology, Investigation, Formal analysis, Conceptualization. **Arita Dubnika:** Resources, Investigation. **Andris Antuzevics:** Writing – original draft, Resources, Investigation. **Tomas Murauskas:** Writing – original draft, Investigation. **Orlando Stewart:** Investigation. **Sarah L. Stoll:**

Supervision, Resources, Formal analysis. **Tomoyo Goto:** Resources, Funding acquisition, Formal analysis, Data curation. **Tohru Sekino:** Supervision, Project administration, Funding acquisition, Conceptualization. **Aleksej Zarkov:** Writing – review & editing, Writing – original draft, Supervision, Resources, Methodology, Conceptualization.

Declaration of competing interest

The authors declare that they have no known competing financial interests or personal relationships that could have appeared to influence the work reported in this paper.

Acknowledgements

This research was funded by a grant WHITCERAM (No. S-LJB-22-1) from the Research Council of Lithuania and by Joint Research Projects under the Bilateral Program (JSPS), RCL JSPS, No. 120224202. Institute of Solid State Physics, University of Latvia, Latvia as the Center of Excellence has received funding from the European Union's Horizon 2020 Framework Programme H2020-WIDESPREAD-01-2016-2017-TeamingPhase2 under grant agreement No. 739508, project CAMART^2. A.D. acknowledges the access to the infrastructure and expertise of the BBCE – Baltic Biomaterials Centre of Excellence (European Union's Horizon 2020 research and innovation programme under grant agreement No. 857287). The authors sincerely acknowledge Dr. Justina Gaidukevic and Hanna Klipan (Vilnius University) for assistance.

References

[1] H.L. Jang, G.B. Zheng, J. Park, H.D. Kim, H.-R. Baek, H.K. Lee, K. Lee, H.N. Han, C.-K. Lee, N.S. Hwang, J.H. Lee, K.T. Nam, In vitro and in vivo evaluation of whitlockite biocompatibility: comparative study with hydroxyapatite and β-tricalcium phosphate, Adv. Healthcare Mater. 5 (1) (2016) 128–136.

[2] F.A. Shah, B.E.J. Lee, J. Tedesco, C. Larsson Wexell, C. Persson, P. Thomsen, K. Grandfield, A. Palmquist, Micrometer-sized magnesium whitlockite crystals in micropetrosis of bisphosphonate-exposed human alveolar bone, Nano Lett. 17 (10) (2017) 6210–6216.

[3] T. Sakae, H. Yamamoto, H. Mishima, T. Matsumoto, Y. Kozawa, Morphology and chemical composition of dental calculi mainly composed of whitlockite, Scanning Microsc. 3 (3) (1989) 855–860.

[4] F.A. Shah, Magnesium whitlockite – omnipresent in pathological mineralisation of soft tissues but not a significant inorganic constituent of bone, Acta Biomater. 125 (2021) 72–82.

[5] Y. Chang, R. Zhao, H. Wang, L. Pang, J. Ding, Y. Shen, Y. Guo, D. Wang, A novel injectable whitlockite-containing borosilicate bioactive glass cement for bone repair, J. Non-Cryst. Solids 547 (2020) 120291.

[6] S. Pouraghaei Sevari, J.K. Kim, C. Chen, A. Nasajpour, C.-Y. Wang, P.H. Krebsbach, A. Khademhosseini, S. Ansari, P.S. Weiss, A. Moshaverinia, Whitlockite-enabled hydrogel for craniofacial bone regeneration, ACS Appl. Mater. Interfaces 13 (30) (2021) 35342–35355.

[7] J. Zhang, W. Liu, V. Schnitzler, F. Tancret, J.-M. Bouler, Calcium phosphate cements for bone substitution: chemistry, handling and mechanical properties, Acta Biomater. 10 (3) (2014) 1035–1049.

[8] T. Xu, L. Sheng, L. He, J. Weng, K. Duan, Enhanced osteogenesis of hydroxyapatite scaffolds by coating with BMP-2-loaded short polylactide nanofiber: a new drug loading method for porous scaffolds, Regen. Biomater. 7 (1) (2019) 91–98.

[9] L.A. Rasskazova, I.V. Zhuk, N.M. Korotchenko, A.S. Brichkov, Y.-W. Chen, E. A. Paukshtis, V.K. Ivanov, I.A. Kurzina, V.V. Kozik, Synthesis of magnesium- and silicon-modified hydroxyapatites by microwave-assisted method, Sci. Rep. 9 (1) (2019) 14836.

[10] X. Zhang, W. Liu, J. Liu, Y. Hu, H. Dai, Poly-ε-caprolactone/Whitlockite electrospun bionic membrane with an osteogenic–angiogenic coupling effect for periosteal regeneration, ACS Biomater. Sci. Eng. 7 (7) (2021) 3321–3331.

[11] A. Kizalaite, I. Grigoraviciute-Puroniene, D.R.C. Asuigui, S.L. Stoll, S.H. Cho, T. Sekino, A. Kareiva, A. Zarkov, Dissolution–precipitation synthesis and characterization of zinc whitlockite with variable metal content, ACS Biomater. Sci. Eng. 7 (8) (2021) 3586–3593.

[12] A. Kizalaite, V. Klimavicius, J. Versockiene, E. Lastauskiene, T. Murauskas, R. Skaudzius, T. Yokoi, M. Kawashita, T. Goto, T. Sekino, A. Zarkov, Peculiarities of the formation, structural and morphological properties of zinc whitlockite ($Ca_{18}Zn_2(HPO_4)_2(PO_4)_{12}$) synthesized via a phase transformation process under hydrothermal conditions, CrystEngComm 24 (28) (2022) 5068–5079.

[13] T. Konishi, S. Watanabe, Copper whitlockite synthesized via hydrothermal transformation of calcium hydrogen phosphate dihydrate, Phosphorus Res. Bull. 38 (2022) 18–24.

[14] D. Griesiute, A. Kizalaite, A. Dubnika, V. Klimavicius, V. Kalendra, V. Tyrpekl, S. H. Cho, T. Goto, T. Sekino, A. Zarkov, A copper-containing analog of the biomineral whitlockite: dissolution–precipitation synthesis, structural and biological properties, Dalton Trans. 53 (4) (2024) 1722–1734.

[15] S.Y. Stefanovich, B.I. Lazoryak, A.M. Antipin, A.S. Volkov, A.I. Evdokimov, O. A. Gurbanova, O.V. Dimitrova, D.V. Deyneko, Crystal structures of biocompatible Mg-, Zn-, and Co-whitlockites synthesized via one-step hydrothermal reaction, Z. für Kristallogr. - Cryst. Mater. 238 (9–10) (2023) 301–309.

[16] S. Sprio, L. Preti, M. Montesi, S. Panseri, A. Adamiano, A. Vandini, N.M. Pugno, A. Tampieri, Surface phenomena enhancing the antibacterial and osteogenic ability of nanocrystalline hydroxyapatite, activated by multiple-ion doping, ACS Biomater. Sci. Eng. 5 (11) (2019) 5947–5959.

[17] Y. Su, K. Wang, J. Gao, Y. Yang, Y.-X. Qin, Y. Zheng, D. Zhu, Enhanced cytocompatibility and antibacterial property of zinc phosphate coating on biodegradable zinc materials, Acta Biomater. 98 (2019) 174–185.

[18] A. Jacobs, G. Renaudin, C. Forestier, J.-M. Nedelec, S. Descamps, Biological properties of copper-doped biomaterials for orthopedic applications: a review of antibacterial, angiogenic and osteogenic aspects, Acta Biomater. 117 (2020) 21–39.

[19] D.V. Deyneko, I.V. Fadeeva, E.Y. Borovikova, P.B. Dzhevakov, P.V. Slukin, Y. Zheng, D. Xia, B.I. Lazoryak, J.V. Rau, Antimicrobial properties of co-doped tricalcium phosphates $Ca_{3\text{-}2x}(M'M'')_x(PO_4)_2$ ($M = Zn^{2+}$, Cu^{2+}, Mn^{2+} and Sr^{2+}), Ceram. Int. 48 (20) (2022) 29770–29781.

[20] M. Hu, F. Xiao, Q.-F. Ke, Y. Li, X.-D. Chen, Y.-P. Guo, Cerium-doped whitlockite nanohybrid scaffolds promote new bone regeneration via SMAD signaling pathway, Chem. Eng. J. 359 (2019) 1–12.

[21] Z. Yang, T. Yao, X. Zheng, J. Hui, D. Fan, Eu^{3+}/Tb^{3+}-doped whitlockite nanocrystals: controllable synthesis, cell imaging, and the degradation process in the bone reconstruction, Nano Res. 15 (2) (2021) 1303–1309.

[22] A.M. Brokesh, A.K. Gaharwar, Inorganic biomaterials for regenerative medicine, ACS Appl. Mater. Interfaces 12 (5) (2020) 5319–5344.

[23] J.L. Aschner, M. Aschner, Nutritional aspects of manganese homeostasis, Mol. Aspect. Med. 26 (4) (2005) 353–362.

[24] A.C. Ross, B. Caballero, R.J. Cousins, K.L. Tucker, Modern Nutrition in Health and Disease, Jones & Bartlett Learning, 2020.

[25] Y.-J. Bae, M.-H. Kim, Manganese supplementation improves mineral density of the spine and femur and serum osteocalcin in rats, Biol. Trace Elem. Res. 124 (1) (2008) 28–34.

[26] S. Bose, G. Fielding, S. Tarafder, A. Bandyopadhyay, Understanding of dopant-induced osteogenesis and angiogenesis in calcium phosphate ceramics, Trends Biotechnol. 31 (10) (2013) 594–605.

[27] B. Bracci, P. Torricelli, S. Panzavolta, E. Boanini, R. Giardino, A. Bigi, Effect of Mg^{2+}, Sr^{2+}, and Mn^{2+} on the chemico-physical and in vitro biological properties of calcium phosphate biomimetic coatings, J. Inorg. Biochem. 103 (12) (2009) 1666–1674.

[28] D. Hamai, S.C. Bondy, Oxidative basis of manganese neurotoxicity, Ann. N. Y. Acad. Sci. 1012 (1) (2004) 129–141.

[29] L. García-Hevia, M. Bañobre-López, J. Gallo, Recent progress on manganese-based nanostructures as responsive MRI contrast agents, Chem. Eur J. 25 (2) (2019) 431–441.

[30] J. Lu, S. Ma, J. Sun, C. Xia, C. Liu, Z. Wang, X. Zhao, F. Gao, Q. Gong, B. Song, X. Shuai, H. Ai, Z. Gu, Manganese ferrite nanoparticle micellar nanocomposites as MRI contrast agent for liver imaging, Biomaterials 30 (15) (2009) 2919–2928.

[31] S.S. Syamchand, G. Sony, Multifunctional hydroxyapatite nanoparticles for drug delivery and multimodal molecular imaging, Microchim. Acta 182 (9) (2015) 1567–1589.

[32] L.-H. Fu, Y.-R. Hu, C. Qi, T. He, S. Jiang, C. Jiang, J. He, J. Qu, J. Lin, P. Huang, Biodegradable manganese-doped calcium phosphate nanotheranostics for traceable cascade reaction-enhanced anti-tumor therapy, ACS Nano 13 (12) (2019) 13985–13994.

[33] Q. Nawaz, M.A.U. Rehman, A. Burkovski, J. Schmidt, A.M. Beltrán, A. Shahid, N. K. Alber, W. Peukert, A.R. Boccaccini, Synthesis and characterization of manganese containing mesoporous bioactive glass nanoparticles for biomedical applications, J. Mater. Sci. Mater. Med. 29 (5) (2018) 64.

[34] M.B. Pabbruwe, O.C. Standard, C.C. Sorrell, C.R. Howlett, Bone formation within alumina tubes: effect of calcium, manganese, and chromium dopants, Biomaterials 25 (20) (2004) 4901–4910.

[35] E. Kostiner, J.R. Rea, The crystal structure of manganese-whitlockite, $Ca_{18}Mn_2H_2(PO_4)_{14}$, Acta Crystallogr. B 32 (1) (1976) 250–253.

[36] C. Heng, W. Liu, X. Zheng, X. Ma, J. Hui, D. Fan, Dopamine and DNA functionalized manganese whitlockite nanocrystals for magnetic resonance imaging and chemo-photothermal therapy of tumors, Colloids Surf. B Biointerfaces 222 (2023) 113120.

[37] C. Heng, X. Zheng, J. Hui, X. Ma, D. Fan, Neodymium and manganese ions co-doped whitlockite for temperature monitoring, photothermal therapy, and bone tissue repair in osteosarcoma, J. Colloid Interface Sci. 653 (2024) 1488–1503.

[38] C. Heng, X. Zheng, J. Hui, X. Ma, D. Fan, DNA aptamer functionalized monodisperse Eu/Mn-WH nanoparticle for in vivo magnetic resonance and fluorescence imaging, Ceram. Int. 50 (2) (2024) 2995–3004.

[39] F. Capitelli, F. Bosi, S.C. Capelli, F. Radica, G. Della Ventura, Neutron and XRD single-crystal diffraction study and vibrational properties of whitlockite, the natural counterpart of synthetic tricalcium phosphate, Crystals 11 (3) (2021) 225.

[40] G.A. Bain, J.F. Berry, Diamagnetic corrections and pascal's constants, J. Chem. Educ. 85 (4) (2008) 532.

[41] G. Morrison, H.-C. zur Loye, Simple correction for the sample shape and radial offset effects on SQUID magnetometers: magnetic measurements on Ln_2O_3 (Ln=Gd, Dy, Er) standards, J. Solid State Chem. 221 (2015) 334–337.

[42] R. Gopal, C. Calvo, J. Ito, W.K. Sabine, Crystal structure of synthetic Mg-whitlockite, $Ca_{18}Mg_2H_2(PO_4)_{14}$, Can. J. Chem. 52 (7) (1974) 1155–1164.
[43] A. Kizalaite, V. Klimavicius, V. Balevicius, G. Niaura, A.N. Salak, J.C. Yang, S. H. Cho, T. Goto, T. Sekino, A. Zarkov, Dissolution-precipitation synthesis and thermal stability of magnesium whitlockite, CrystEngComm 25 (30) (2023) 4370–4379.
[44] H.L. Jang, K. Jin, J. Lee, Y. Kim, S.H. Nahm, K.S. Hong, K.T. Nam, Revisiting whitlockite, the second most abundant biomineral in bone: nanocrystal synthesis in physiologically relevant conditions and biocompatibility evaluation, ACS Nano 8 (1) (2014) 634–641.
[45] L. Sinusaite, A. Popov, A. Antuzevics, K. Mazeika, D. Baltrunas, J.-C. Yang, J. L. Horng, S. Shi, T. Sekino, K. Ishikawa, A. Kareiva, A. Zarkov, Fe and Zn co-substituted beta-tricalcium phosphate (β-TCP): synthesis, structural, magnetic, mechanical and biological properties, Mater. Sci. Eng. C 112 (2020) 110918.
[46] L. Sinusaite, A.M. Renner, M.B. Schuetz, A. Antuzevics, U. Rogulis, I. Grigoraviciute-Puroniene, S. Mathur, A. Zarkov, Effect of Mn doping on the low-temperature synthesis of tricalcium phosphate (TCP) polymorphs, J. Eur. Ceram. Soc. 39 (10) (2019) 3257–3263.
[47] K.S.W. Sing, Reporting physisorption data for gas/solid systems with special reference to the determination of surface area and porosity (Recommendations 1984), Pure Appl. Chem. 57 (4) (1985) 603–619.
[48] X. Guo, X. Liu, H. Gao, X. Shi, N. Zhao, Y. Wang, Hydrothermal growth of whitlockite coating on β-tricalcium phosphate surfaces for enhancing bone repair potential, J. Mater. Sci. Technol. 34 (6) (2018) 1054–1059.
[49] H.L. Jang, H.K. Lee, K. Jin, H.-Y. Ahn, H.-E. Lee, K.T. Nam, Phase transformation from hydroxyapatite to the secondary bone mineral, whitlockite, J. Mater. Chem. B 3 (7) (2015) 1342–1349.
[50] I. Mayer, S. Cohen, S. Gdalya, O. Burghaus, D. Reinen, Crystal structure and EPR study of Mn-doped beta-tricalcium phosphate, Mater. Res. Bull. 43 (2) (2008) 447–452.
[51] D. Toloman, L.M. Giurgiu, I. Ardelean, EPR investigations of calcium phosphate glasses containing manganese ions, Phys. B Condens. Matter 404 (21) (2009) 4198–4201.
[52] B. Gabbasov, M. Gafurov, A. Starshova, D. Shurtakova, F. Murzakhanov, G. Mamin, S. Orlinskii, Conventional, pulsed and high-field electron paramagnetic resonance for studying metal impurities in calcium phosphates of biogenic and synthetic origins, J. Magn. Magn Mater. 470 (2019) 109–117.
[53] T.T. Eighmy, A.E. Kinner, E.L. Shaw, J.D. EusdenJr, C.A. Francis, Whitlockite (β-$Ca_3(PO_4)_2$) characterization by XPS: an environmentally important mineral, Surf. Sci. Spectra 6 (3) (1999) 219–227.
[54] C.C. Chusuei, D.W. Goodman, M.J. Van Stipdonk, D.R. Justes, E.A. Schweikert, Calcium phosphate phase identification using XPS and time-of-flight cluster SIMS, Anal. Chem. 71 (1) (1999) 149–153.
[55] M.C. Biesinger, B.P. Payne, A.P. Grosvenor, L.W.M. Lau, A.R. Gerson, R.S.C. Smart, Resolving surface chemical states in XPS analysis of first row transition metals, oxides and hydroxides: Cr, Mn, Fe, Co and Ni, Appl. Surf. Sci. 257 (7) (2011) 2717–2730.
[56] A.J. Nelson, J.G. Reynolds, J.W. Roos, Core-level satellites and outer core-level multiplet splitting in Mn model compounds, J. Vac. Sci. Technol. A 18 (4) (2000) 1072–1076.
[57] D. Griesiute, E. Garskaite, A. Antuzevics, V. Klimavicius, V. Balevicius, A. Zarkov, A. Katelnikovas, D. Sandberg, A. Kareiva, Synthesis, structural and luminescent properties of Mn-doped calcium pyrophosphate ($Ca_2P_2O_7$) polymorphs, Sci. Rep. 12 (1) (2022) 7116.
[58] L. Sinusaite, A. Antuzevics, A.I. Popov, U. Rogulis, M. Misevicius, A. Katelnikovas, A. Kareiva, A. Zarkov, Synthesis and luminescent properties of Mn-doped alpha-tricalcium phosphate, Ceram. Int. 47 (4) (2021) 5335–5340.

Vilniaus universiteto leidykla
Saulėtekio al. 9, III rūmai, LT-10222 Vilnius
El. p. info@leidykla.vu.lt, www.leidykla.vu.lt
bookshop.vu.lt, journals.vu.lt
Tiražas 30 egz.